Nanostructured optical materials for planar photonics

A DISSERTATION PRESENTED
BY
ROBERT DEVLIN
TO
HARVARD, JOHN A. PAULSON SCHOOL OF ENGINEERING AND APPLIED SCIENCES

IN PARTIAL FULFILLMENT OF THE REQUIREMENTS
FOR THE DEGREE OF
DOCTOR OF PHILOSOPHY
IN THE SUBJECT OF
APPLIED PHYSICS

HARVARD UNIVERSITY
CAMBRIDGE, MASSACHUSETTS
AUGUST 2017

Thesis advisor: Professor Federico Capasso Robert Devlin

Nanostructured optical materials for planar photonics

Abstract

How a material interacts with light, whether it is reflective, transparent or absorptive, results form the fundamental properties of the atoms and molecules comprising the material. Adding a suitably-designed geometry to the material allows one to manipulate the light that is interacting with the material—adding curvature to glass allows one to focus light down to a point. However, the set of available responses from naturally-occurring materials is still limited. 'Metamaterials' are materials that have been artificially structured on dimensions smaller than the wavelength of light, allowing one to achieve a set of optical responses beyond traditional materials. Metamaterials, however, are incompatible with fabrication processes standardized by the electronic industry (semiconductor processing) and often have unusably-high losses. This thesis details the use of metasurfaces, the two-dimensional analog of metamaterials, which can be processed using standard production techniques while replicating or expanding on many of the functionalities of conventional optics and metamaterials. A particular emphasis is placed on the realization of metasurfaces at visible wavelengths, where material processing and fabrication challenges are amplified due to the smallness of the wavelength. It is shown that the combination of materials engineering, nanofabrication and device design enable new fundamental physical phenomena—controllable coupling between spin and orbital angular momentum in light—as well as substantial increases in the efficiency of metasurfaces—planar lenses and holograms with orders of magnitude reduction in thickness.

Contents

Listing of figures

For my family

Acknowledgments

My path to my doctorate was in some ways a roundabout, meandering road with more turns than I ever could have imagined. In the moment, such a complicated route can be frustrating but the benefit of taking the long road is that I was able to cross paths with many more people who have added more to my life and taught me more than I ever could have hoped.

My family have always provided me with support, even when I was too stubborn to ask for it on my own. I was certainly not an easy child for my mom and dad and I often had to find out things the hard way (a true experimentalist!). But, my parents gave me every chance to figure things out for myself, again, again and again, even if it meant more gray hairs for them. Their constant nudges and at times full on push made me a better person and ultimately made work to the height of my capability. My brother, being five years older than me, has always been a great source of wisdom in my life and my taste in music has been the biggest beneficiary of his advice. My sister constantly looked out for me as we grew up very close in age and she and my grandmother both claim that my sister taught me math. I don't have any recollection of this but at this point I'll cede the argument and thank her for her help in making me a better physicist. My grandparents, pop-pop and mom-mom also had a profound influence on me. Much of my time after classes and during the summer while I was in grade school was spent with my grandparents. My grandfather introduced me to carpentry and engineering and always pushed me towards what would ultimately be my passion and career path.

My grandmother, whose patience and love knew no bounds, was always incredibly supportive and pushed me to keep going to school even during uncertain times in my life, an opportunity she never had. She is greatly missed and I hope I can make her proud as I continue with my career and life.

At Drexel University, for my undergrad and Masters, I was lucky enough to work in Steve May's group, where I not only learned to do research and meet great scientists but I also made life-long friends. Steve had full confidence in me, even as an undergrad, and often gave me as much latitude as Ph. D. student. This is evidenced by the fact that he had me hack into a $250,000 piece of equipment that he was relying on to get tenure, without any hesitation. (Luckily the tool is still running and producing data). Steve would always take time out of his schedule to provide me with advice and help me with grad school applications, even though I'm sure he had more pressing issues to address. His trust in me and the experience I gained in his lab undoubtedly made me ready for the work that I would carry out during my Ph. D. I am also infinitely grateful to my friends and colleagues from Steve's group. Cole Smith was a great friend, mentor and roommate who was always willing to grab a beer and vent. Rebecca was my first close scientific mentor and her advice and help with papers was invaluable. Alex Krick, besides being a great scientist and friend, provided me with the champion sample, AK22, that would ultimately form the basis of my Master's thesis and first primary author paper. I am also grateful to Mark, Eun Ju, Terry and Amber, all of whom made my time in Steve's lab an invaluable experience.

At Harvard I was lucky enough to continue my scientific career amongst some of the greatest scientist and best people. Early in my Ph. D., I met Alex High. Alex quickly became one of my closest friends and the work we were able to do together is shown in Chapter 2. Without his continued advice and friendship throughout my Ph. D., I am sure that I would not have been able to achieve half of the things that I have during my time here. Alex was just about the best scientific pep-pep anyone could have hoped for–great job! The same goes for Alan Dibos, step-pepper, who as a 'fab guru' and great friend was always willing to put aside what he was doing to help me. Nathalie de Leon was another great friend and influence on me in my early years at Harvard.

Federico Capasso, my advisor, is one of the most passionate people that I have met. He is passionate even for an Italian! It has been an incredible privilege to work in his group and being as influential of a physicist as Federico is has made my time in his group incredibly exciting and fruitful. Federico has, in his words, a bottom up approach. This means that he provides complete autonomy to his students. For an early grad student this can be incredibly frightening but what Federico wants is for the students to become creative scientists in their own right. His policy of allowing his students to follow any intellectual curiosity they find has really led me to a new understanding of how to approach difficult questions. Although he allows his students to follow their own will, once you start pursuing your research Federico becomes intensely involved in your research and life. You will often receive an midnight phone call from him to discuss results or a voice email (one of his most creative inventions) at 3AM and a follow up at 7AM. That's just how passionate he is, even after 40 years of doing science and working amongst the most brilliant minds in the world at Bell Labs, he still gets truly excited about every student's results.

In the Capasso group I continued to meet more great scientists, mentors and friends, all of whom have made my time at Harvard immensely enjoyable. Balthasar Mueller is one of my first friends at Harvard and his influence on Federico is the reason I had a chance to join the

Capasso group in the first place. He is one of the most creative physicists that I have known, a deep intellectual and will be brilliant in whatever he decides to do next. His loyalty to his friends is unmatched. My work with Reza, Wei Ting and Alex has led to everything in Chapters 2-4 and their work ethic and scientific drive are unmatched. Working with Antonio Ambrosio (another passionate Italian) has been one of the greatest joys in my time at Harvard and I am immensely indebted to him for how he has taught me to do thorough science and his introducing me to the subject of optical orbital angular momentum. My work with him is shown in Chapters 4 and 5. I am also incredibly lucky to have worked with Noah Rubin who joined the group shortly after I did. He is one of the most rigorous scientists I know and has become one of my closest friends. He not only is incredibly smart and hardworking, he also makes sure to keep his life and research in perspective. His insistence on taking bike rides during some of the most stressful times of my Ph. D. definitely helped me decompress and I appreciate those times, even if he is able to bike down Mt. Wachusett faster than me. The Capasso group has a large number of great physicists and people and has a ton of moving parts so it is hard to keep track of everyone. I am also grateful to the friendship and help of Paul who was always ready to 'chill', Vincent, whose Belgian humor was guaranteed to stop you in your tracks (out of laughter or shock), Charles, a real 'dude' and amazing scientist, Marco, even if he isn't strong enough to out last me in endurance competitions, Dima, a passionate, hard working scientist and Xinghui, Daniel, Shi, Michele, Kundan, Alan, Shuyan, Lulu, Toby, and Andrea.

A large portion of my thesis work was carried out in the comfort of a bunny suit and white noise of the cleanroom in Harvard's Center for Nanoscale Science (CNS). Working so often in the cleanroom not only made me an expert at identifying friends by their eyes only but it gave me the opportunity to work closely with many passionate members of the staff. In particular I would like to thank Ed Macomber, whose constant battle to keep SP3 in working order enabled much of the work in Chapter 2, Jason Tresback whose upkeep of the AFM tools allowed me to take the beautiful images in Appendix A, Mac Hathaway, who is probably having nightmares about TiO_2 and keeps the CNS safety standards high, Ling Xie for her help with etching and Bill Wilson and JD for keeping CNS running fluidly—an almost impossible task when you see what some of the users will attempt to do to in a piece of equipment.

I am also grateful to Draper Laboratory who funded my Ph. D. for the final 2 years through their Draper Laboratory Fellowship program. Particularly at Draper I am thankful to Steve Byrnes, who I first met during his post-doc and later moved to Draper, who is about the most insightful physicist I know and it was always great to get his input and J.P. Laine whose constant words of encouragement spurred on my research. I would also like to thank my thesis committee, Professor Evelyn Hu and Professor Philip Kim, for taking time out of their busy schedules.

...the more we know, the more ignorant we become in the absolute sense, for it is only through enlightenment that we become conscious of our limitations. Precisely one of the most gratifying results of intellectual evolution is the continuous opening up of new and greater prospects.

Nikola Tesla

1

Introduction

Our entire physical connection with electromagnetic (EM) radiation results from the interaction of light with matter. Whether it is light being transmitted, reflected, or absorbed by objects and ultimately exciting an electron in the photoreceptor of our eye or the radiation of the sun being converted into infrared wavelengths and feeling warm on our face, we require the coupling of light to the medium to detect its presence. Even in the age of electronics and digital cameras, in order for us to detect EM radiation, a photon must first interact with a material (a silicon photodetector, for example).

Light in the visible spectrum has been especially important to us due to the transparency of our atmosphere to these wavelengths. Due to our intimate connection with EM radiation and visible light in particular it is no surprise that the study of light is one the oldest endeavors in the physical sciences[1]. The ability to control and manipulate light naturally closely followed the fundamental pursuit of understanding the physical nature of light. We have since been molding and shaping materials to make reflective and refractive optical components. These components have not only enabled new technologies but also elucidated fundamental questions across all scientific fields. Although our fundamental understanding of the nature of light continued to be refined and we progressively assembled more complex optical systems, the fundamental way manipulated light remained largely the same. In the last 40 years or so, however, there has been a fundamental shift in how we can engineer new optical devices and we can now move from adding shape to materials to engineering the optical properties of the materials themselves.

1.1 Nanophotonics

One of the largest departures in our understanding of optical properties of materials and our ability to manipulate light came, ironically, as a result of an advance in electronics. The invention of the transistor marked a new era in technology[2]. Around these solid state electronics grew a multi-billion dollar industry with a focus on advancing materials science and producing increasingly small transistors and circuits. This pursuit required new equipment for fabricating devices on smaller scales (microns and eventually nanometers) and new techniques for characterizing the processes.

As the fabrication and characterization techniques, which we now refer to generally as microfabrication or nanofabrication, continued to mature, the study of optics would ultimately be the beneficiary. The dissemination of this equipment into universities and research labs, enabled the production of structures with nanoscale dimensions as well as the ability to study and understand the optical phenomena of these nanostructures. This new field, nanophotonics, allowed one to deterministically structure materials with physical dimensions similar to the wavelengths of visible light. These structures with length scales on the order of the wavelength, which became known as photonic crystals, allowed a set of new optical structures to be demonstrated[3]. Additionally, while materials science has always been a critical part of the optical sciences, nanophotonics truly made materials science, optics and fabrication inseparable fields. The continued refinement of nanofabrication techniques has more recently allowed structures with length scales even smaller than visible wavelengths to be readily fabricated.

1.2 Metamaterials

The response of a material to light can be fully characterized by two simple quantities, its electric permittivity, ε, and its magnetic permeability, μ[4]. These two quantities, and how they change with different wavelengths of light, determine whether a material is reflective, transparent, absorptive and the colors that we see from objects. Their effectiveness in describing the richness of the world around us is almost unreasonable, especially considering that the materials they are describing is composed of countless numbers of discrete atoms and molecules, a fact that is largely ignored when deriving these quantities.

The key factor in allowing these simplified descriptions of a material to provide so much utility is the relative length scale of the spacing between the atoms or molecules compared to the wavelength of the particle interacting with the material. For example, the discrete nature of a material cannot be ignored when describing how an electron interacts with the material. This is because the typical wavelength of an electron moving through the material is on the order of the spacing between neighboring atoms or molecules in the material. In contrast, for the majority of the EM spectrum, the atomic spacing in a material is many times smaller than the wavelength of the EM field it is interacting with. Consider specifically silicon, which has a lattice spacing of 0.543 nm[5]. As a result, within one wavelength at visible wavelengths, (400-750 nm) there are nearly 100 spacings and 800 silicon atoms. This allows one to effectively average over the response of all the individual atoms and the wave can 'ignore' the fine, discrete features.

Metamaterials are artificial, engineered materials that exploit this scale difference between EM radiation and the size of materials. In some sense metamaterials are the natural progression of photonic crystals introduced above. By leveraging manufacturing techniques that have allowed precise production of continuously smaller structures, as well as previous knowledge from microwave engineering, it was realized that one could tailor the effective response, ϵ and μ of a material[6]. Using artificial structures, such as resonators, scatterers or composite materials, one could now provide an effective response and produce an artificial homogenous medium—as long as whatever structure introduced was well below the excitation wavelength. This enabled a new set of materials that exhibit phenomena typically impossible in natural materials. For example, it was predicted that a material with simultaneously negative ϵ and μ should exhibit negative refraction[7]—light rays violate Snell's law and bend 'the wrong way' across an interface. This prediction was long held to be a mere intellectual curiosity but through precise design of metamaterials negative refraction was experimentally demonstrated and opened up a new direction of research[8]. Metamaterials have also exhibited a host of interesting phenomena such as subdiffraction imaging[9] and diffractionless propagation[10], to name a few.

One may assume that in order to engineer the optical properties of a material in any meaningful or exceptional way, the structures must be complex. For certain realizations of metamaterials, it is the case where relatively complicated arrays of precisely tuned resonators or 3D patterns are required[11]. However, in some cases a great deal of complexity in the optical response can be derived from a remarkably simple engineered material. This concept, as well as a more detailed demonstration of the concept of the effective medium in general, is illustrated in Fig. 1.1.

Figure 1.1A shows a schematic diagram of a simple metamaterial. This particular metamaterial consists of only two layered materials with permittivities ε_m and ε_d and corresponding layer thicknesses d_m and d_d where $d_m = 1 - d_d$. As discussed above, the most interesting phenomena occurs in the limit where the material structure is much less than the wavelength of light, $d_m + d_d << \lambda$. This condition, sometimes referred to as the quasi-static limit because the electric field does not fluctuate much over a single period of the layered material, allows the material to be treated as an 'effective medium'—the essence of a metamaterial.

In such a case one can derive effective dielectric functions parallel and perpendicular to the plane of the layers as[12]

$$(\varepsilon_{\parallel})^{-1} = \frac{d_m/\varepsilon_m + d_d/\varepsilon_d}{d_m + d_d} \tag{1.1}$$

and the value perpendicular to the plane is

$$\varepsilon_{\perp} = \frac{\varepsilon_m d_m + \varepsilon_d d_d}{d_m + d_d} \tag{1.2}$$

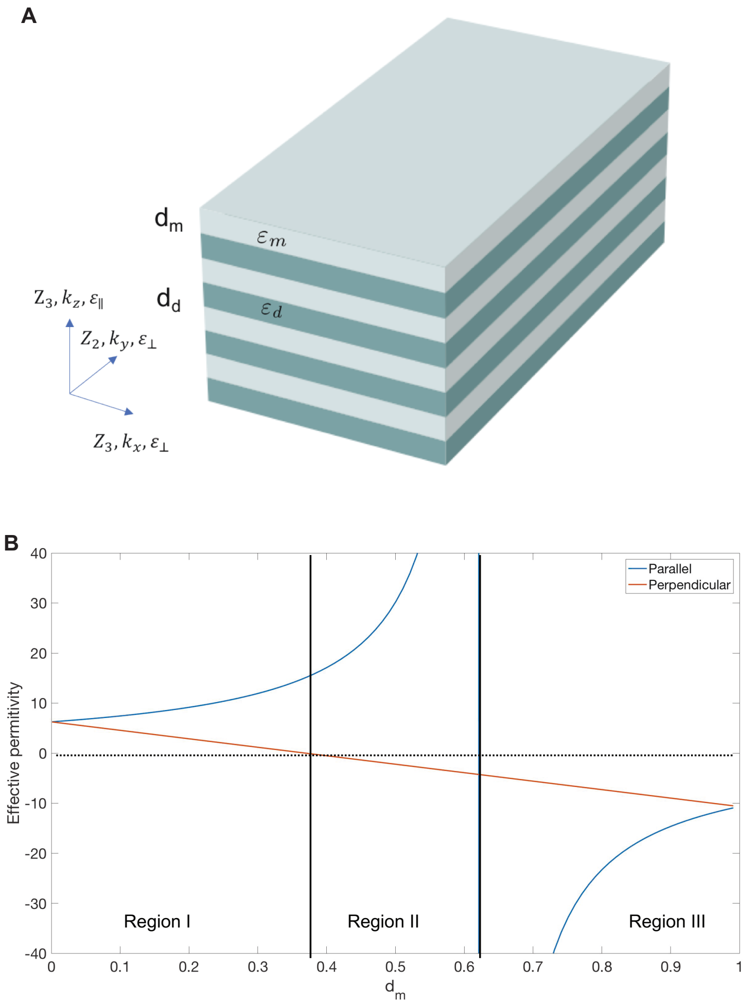

Figure 1.1: Demonstration of the effective medium concept for metamaterials. (A) Schematic diagram of a layered metal-dielectric metamaterial. (B) Effective permittivity in a direction parallel and perpendicular to the anisotropy axis as a function of metal filling factor.

As one can see from Eq. 1.1 and Eq. 1.2, the effective response of the metamaterial is a combination of the two individual material responses and is anisotropic, despite being composed of two isotropic materials. Thus, the simple structure shown in Fig. 1.1A allows both tailorable material response and anisotropy.

A particularly interesting case, both in this example and for metamaterials in general, occurs when the two materials are metals and dielectrics, respectively. The bulk dielectric function of a metal and dielectric, especially in the near infrared to visible frequency range, have opposite signs $\varepsilon_m < 0$ and $\varepsilon_d > 1$.

Figure 1.1B plots the effective dielectric constant as a function of the metal filling fraction d_m (specific materials dielectric constants are chosen to be silver and titanium dioxide at a blue wavelength). This plot further highlights the versatility of this simple metamaterial. Changing the metal filling fraction results in three distinct responses from this metal-dielectric stack. In 'Region I', the dielectric constants along both directions, $\varepsilon_{\|}$ and $\varepsilon_{\perp}$, are both positive. At higher relative metal thickness, as in 'Region III", the dielectric constants are both negative. In 'Region II', a case occurs that is not found in naturally-occurring materials. Here along one direction of the metamaterial, the dielectric constant is positive (dielectric-like), while along an orthogonal direction, the dielectric constant is negative (metal-like). Naturally occurring materials, even anisotropic crystals, tend to be either dielectric or metal at any given wavelength. This metamaterial, however, is able to both a metal and a dielectric at a given wavelength.

This simple demonstration of a resultantly rich metamaterial, which has different signs of the effective dielectric constant along different directions, is referred to as a 'hyperbolic metamaterial'[13] (the origin of this name will be made clear in Chapter 2). More than just exhibiting the unusual characteristic of oppositely signed dielectric constants, this metamaterial also exhibits negative refraction and other properties that only metamaterials can achieve.

While the promise of metamaterials has spawned an entire field, extended the set of possible optical devices and produced creative solutions to a new set of problems in electromagnetics, there has been few examples of widescale applications even after 20 years of research. Metamaterials suffer from several practical problems. Most demonstrations have been in the microwave portion of the spectrum. The wavelength of microwave radiation is on the order of 1 cm so it is much easier to create subwavelength structures, however many important applications require metamaterials to operate at visible wavelengths. Since metamaterials also rely on resonances and propagation of light through the medium, they tend to be very lossy. Additionally, nearly all metamaterials use metals, which are particularly-lossy at visible wavelengths and are difficult to process. Finally, metamaterials do not lend themselves to the well established processing of CMOS fabrication techniques.

1.3 Metasurfaces

Metasurfaces seek to address many of the problems associated with metamaterials and conventional optical elements. These devices are essentially two-dimensional analogs of metamaterials that can replicate and expand upon the function of both metamaterials and conventional optical elements.

The conception of metasurfaces[14], resulted from a simple thought experiment. Instead of relying on phase accumulation via propagation effects as in traditional optics, could one introduce abrupt phase shifts on an incident EM wave directly at an interface? What Yu *et al.* did to answer this question was to simulate, at a particular wavelength, the phase shifts introduced by subwavelength antennae with varied geometrical parameters. As is well known in optics, as long as one can produce any value of phase shift between 0 and 2π any phase only optical device can be reproduced[15]. The antennae were then distributed across an interface to introduce a specific phase shift at a specific spatial coordinate. This is the essence of initial metasurfaces. Find the phase profile of your desired optical element. Find a suitable set of nanoscale phase shifting elements. Discretize and periodically sample the phase profile. For example, the phase profile required to produce a traditional lens is given by

$$\phi(x,y) = \frac{2\pi}{\lambda}\left(f - \sqrt{x^2 + y^2 + f^2}\right) \tag{1.3}$$

To produce a metasurface one would take this function, modulo 2π, and at each subwavelength period period in the $x - y$ plane place a suitable phase shifting element.

To provide context, a top-view of a metasurface is shown in Fig. 1.2A. The inset shows the degrees of freedom that allow a metasurface to carry out a specific function. Phase shifts from 0 to 2π can be introduced by varying the geometrical parameters, w_x, w_y and θ and the continuous phase function is discretized and sampled with periods a_1 and a_2, which are subwavlength. The metasurface is then able to perform some function (Fig. 1.2B), e.g., focusing light to a point, by judicious placement of the elements.

In some sense, metasurfaces can be considered the ultimate conclusion of what was started by Fresnel nearly 200 years ago. Fresnel and others essentially realized that in order to produce a phase-only optical device, one needs only to introduce phase shifts modulo 2π. This means that much of the material along the propagation direction in these traditional optical devices is redundant and can be completely removed. Metasurfaces possess several practical advantages over previous optical devices. They have only nanoscale thickness. They require

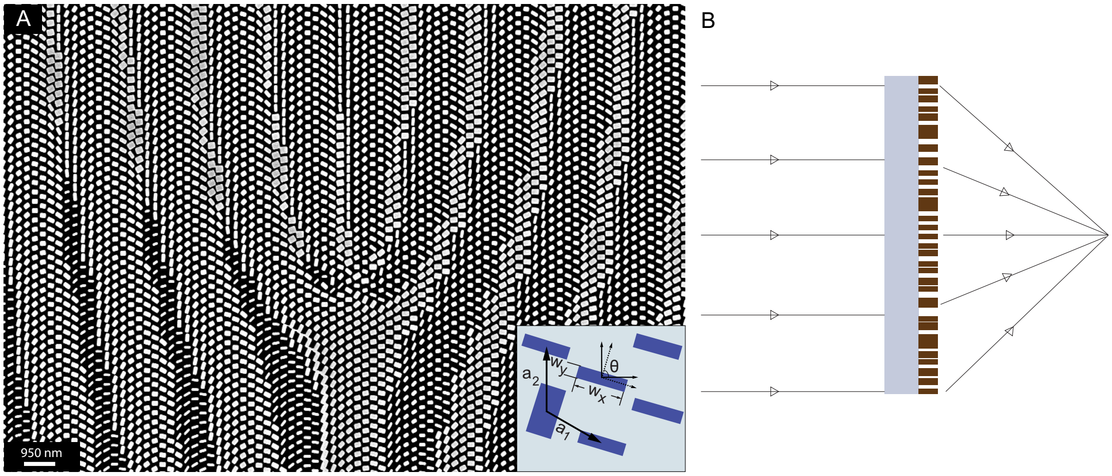

Figure 1.2: An overview of metasurface degrees of freedom and operation. (A) Top-view scanning electron microscope image of a metasurface. The inset shows the available degrees of freedom of a metasurface. (B) Schematic demonstration of a metasurface operating as a lens.

only very simple processing, an entire metasurface can be produced with a single lithographic step. They are planar, which makes them directly-integratabtle with a variety of sensors and solid state light sources. Perhaps most importantly from a practical perspective, they are able to be processed using standard semiconductor fabrication technique. This allows the production of optics to potentially move to the already-present massive infrastructure of the electronics industry. Finally, metasurfaces have recently introduced entirely new optical elements.

Besides just reproducing effects in conventional optics or metamaterials with the practical benefits discussed above, metasurfaces also provide a new solution to a set of previously untenable problems. The new functionality offered once again requires one to reconsider the possible set of responses from a material. In particular, metasurfaces have more recently been shown to allow unprecedented control over the phase and polarization of light[16,17]. One such metasurface has already been introduced in Fig. 1.2A. To provide complete control over both the phase and polarization of light, one requires a medium that has a spatial variation of linear birefringence and the local orientation of the anisotropy axis. No natural crystal provides subwavelength control over both of these parameters. However, a metasurface can provide a discrete approximation to such a crystal by allowing the width along two orthogonal directions and the rotation angle of each element to vary independently (Fig. 1.2A inset). This concept will be described in more detail and utilized in Chapter 6.

Despite the great amount of progress in the field of metasurfaces, there were still outstanding issues to be solved. The first demonstrations of metasurfaces utilized metallic nano-antennae to imprint an arbitrary phase profile onto incident light[18,14,19]. As detailed at the end of the previous section, metals are inherently lossy and furthermore, these nano-antennae have very small scattering cross-sections leading to very low efficiencies of these early devices—most of the light in the early metasurfaces passed through without interacting with the metasurface in any meaningful way. This led to the introduction of dielectric metasurfaces[20]. As compared to metallic metasurfaces, dielectric metasurfaces are transparent, they do not have the heating losses associated with metallic metasurfaces. The first set of demonstrations for dielectric metasurfaces utilized silicon, as this probably the most widely processed material[16,21,14,19]. However, since the bandgap of silicon occurs around a wavelength of 1130 nm, these metamaterials operated in the infrared region of the spectrum or suffered extremely high losses (efficiencies on the order of 1%).

In order to produce metasurfaces that operate with high efficiency at visible wavelengths, new materials must be explored. Fabrication requirements at these wavelengths become particularly challenging, again because the period of the metasurfaces must be smaller than the wavelength of light. Furthermore, at such small wavelengths, the effect of material imperfections become amplified. Grain boundaries and roughness of even few nanometers become significant sources of isotropic scattering and loss. Chapter 3 deals with the current state of metasurfaces for visible wavelengths.

1.4 Optical angular momentum

Thus far, only exceptional properties of engineered materials have been considered. However, some exceptional properties of light, even in the absence of any material, had remained unknown even more than 125 years after Maxwell's unification of EM theory[22].

That light carries angular momentum has been known since Poynting derived the mechanical equivalence of the circular polarization of light and spin angular momentum in 1909[23]. Poynting's derivation came even before the understanding that the energy of light was quantized and that the quanta of light, the photon, possessed $\pm\hbar$ angular momentum per photon for left and right circularly polarized photons, respectively. In a careful yet simple experiment, Beth later experimentally verified the remarkable fact that photons do carry spin angular momentum, (SAM), which is equivalent to mechanical SAM, and agrees with the quantum prediction[24].

That light should also carry orbital angular momentum (OAM), which is differentiated from SAM as angular momentum arising from off-axis rotation, in retrospect, seems as if it should follow naturally. It was suggested as far back as 1932, even before Beth's experiment, that in order to conserve angular momentum in certain atomic transitions, light must carry angular momentum greater than the $\pm\hbar$ attributed to SAM[25]. However, it would not be until 1992, that Allen and colleagues[26] would definitively derive this result.

The result is relatively straightforward and begins in a manner similar to almost all wave equations—the Helmholtz equation. Following ref.[26] and solving the Helmholtz equation in cylindrical coordinates and taking the paraxial limit one finds the following solution for the EM amplitudes

$$u_{p,\ell}\left(r,\phi,z\right)=\sqrt{\frac{2p!}{\pi\left(p+|\ell|\right)}}\frac{1}{w(z)}\left(\frac{r\sqrt{2}}{w(z)}\right)^{|\ell|}L_p^{|\ell|}\left(\frac{2r^2}{w(z)^2}\right)\exp\left(\frac{-r^2}{w(z)^2}\right)\exp\left(\frac{-ikr^2}{2R(z)}\right)$$
$$\exp\left[-i(2p+|\ell|+1)\mathrm{arctan}\left(\frac{z}{z_R}\right)\right]\exp(i\ell\phi) \quad (1.4)$$

where r is the radial coordinate, ϕ is the azimuthal coordinate L_p^ℓ is the Laguerre polynomial, ℓ and p are the azimuthal and radial index, respectively, $w(z)$ is the beam waist and z_R is the Rayleigh range. In many cases, the index p is set to zero, as ultimately, only the index ℓ will contribute to the angular momentum. In the case where ℓ is also set equal to zero, Eq. 1.4 reduces to a normal Gaussian beam associated with a typical laser.

In light, the angular momentum is calculated in a manner completely analogous to mechanics. Angular momentum is the cross product of the radial coordinate and the linear momentum of a system. For EM waves, the linear momentum is given by the time average of the quantity $\epsilon_0\mathbf{E}\times\mathbf{B}$. The angular momentum flux in this beam is then given by $\mathbf{M}=r\times\epsilon_0\mathbf{E}\times\mathbf{B}$ and the flux in the propagation direction is

$$M_z=\frac{\ell}{\omega}|u|^2+\frac{\sigma_z r}{2\omega}\frac{\partial|u|^2}{\partial r} \quad (1.5)$$

the value ℓ is the same as in Eq. 1.4 and notably can take on any integer value from $-\infty$ to $+\infty$ and $\sigma_z=\pm1$ for left and right circular polarization, respectively. Taking the ratio of Eq. 1.5 to the total power in the beam allows one to find

$$J=(\ell+\sigma)\hbar. \quad (1.6)$$

which is the total angular momentum of this beam. Not only does this expression show succinctly that EM waves can posses SAM *and* OAM it provides a direct parallel with atomic systems, where it is natural and well known that the total angular momentum is given by the spin and orbital components $J = L + S$[27]. This analogy to atomic systems, also suggests that there may be other connections between atomic and EM systems such as spin-orbit coupling or spin-orbit interactions of light, where the SAM of light sets its orbit or motion[28,29].

Since the initial description showing that light possess OAM, there has been immense interest in the study of these beams. Much of this research has been based on the fact that, unlike light's polarization, which only provides two orthogonal degrees of freedom, the orbital angular momentum of light, ℓ, provides an infinite orthogonal basis. These extra dimensions, or 'channels' have made OAM beams a prime candidate for increasing optical information capacity[30] or for new quantum information protocol[31,32,33].

In addition to carrying OAM, the beams described in Eq. 1.4 possess other salient features, which have lead to both fundamental studies and potential applications. Specifically, while Eq. 1.4 has a rather long form, the key factor giving rise to many of the interesting phenomena of OAM beams arrises from the final term of the expression, $\exp(i\ell\phi)$. This so called 'aziumuthal phase' term takes the typical plane wave phase profiles one is often more familiar with and twists the phase fronts around the propagation axis, forming a helix of intertwined planes. The number of intertwined planes corresponds to the integer value ℓ or the OAM. Furthermore, the implication of an azimuthally-dependent phase is that as one approaches the origin $(r \rightarrow 0)$ the phase of this beam is undefined and ultimately how quickly the phase becomes undefined depends on the magnitude of ℓ. Through a simple argument, Berry and Nye showed that if the phase is undefined at the beam center the amplitude must be zero at the beam cen-

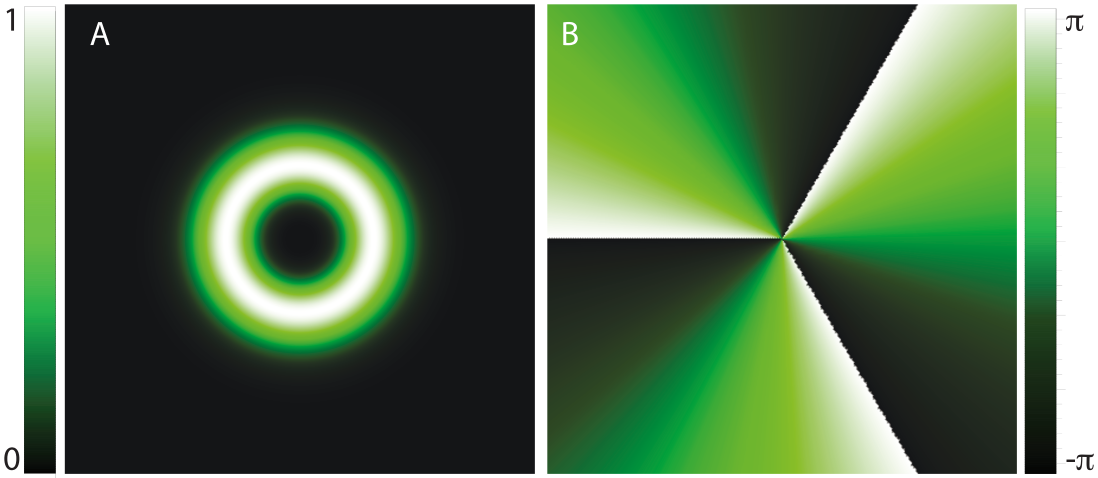

Figure 1.3: (A) Intensity distribution and (B) phase of a beam carrying orbital angular momentum of $\ell = 3$. The bars show normalized intensity from 0 to 1 (A) and phase in radians (B)

ter simultaneously[34].

To provide a more tangible picture of this case, Fig. 1.3 shows a beam with OAM and $\ell = 3$. Figure 1.3A shows the intensity of this beam which can be seen to be a singly-ringed annuli, with zero intensity on the beam axis, as expected. Because of this particular intensity distribution, these beams are often referred to colloquially as 'doughnut' beams. (Strangely the intertwined phase fronts described above are also often referred to as fussili pasta, which hints at a strange underlying theme in this field). The resulting azimuthal phase, projected onto a plane orthogonal to the propagation direction, is shown in Fig. 1.3B. As one can see from the phase map, as a round trip is made about the beam, there are $\ell 2\pi$ phase discontinuities and as one moves towards the beam center, the phase ultimately becomes undefined or singularity, which in the particular case shown here $\ell = 3$.

The intensity and phase of these beams lends various names to this particular class of EM wave: singular beams (because of the phase singularity), vortex beams (because of the circulating power about the beam center) and helical beams (because of the intertwined phase fronts). Additionally, the spatial distribution of the phase and intensity enable a variety of additional applications[35]. Most notably these beams have been used for sub-diffraction limited imaging in stimulated-depletion microscopy[36], which was the subject of a Nobel prize in 2014[37] but have also been used for manipulation of microscopic particles[38].

While EM waves that carry orbital angular momentum can propagate even in the absence of a medium (in free space), how does this concept connect back to the topics of metasurfaces and metamaterials introduced in the previous sections? A key requirement to produce beams of the form Eq. 1.4 is to be able to add an azimuthal phase dependence to a normal plane-wave or Gaussian beam. Thus, one must have a suitably-designed material or device that allows the efficient introduction of this phase. Various techniques for introducing such a phase have been detailed, for example a spiral phase plate or forked hologram, which directly introduce a phase discontinuity onto a plane wave. However, these methods are generally inefficient or require unrealistically precise fabrication requirements—a particular problem for high fidelity quantum systems.

Metasurfaces, introduced in the previous section, are ideal candidates for introducing specific spatial phase distributions onto a beam. Vortex beams have been generated by metasurfaces[19,14] and in essence allow the more complicated, three-dimensional spiral phase plate to be collapsed down to a single plane with nanoscale dimensions. Additionally, as metasurface technology matured, this technique of producing beams with OAM ultimately has become the most efficient method[39,16], with overall efficiency of the incident light acquiring OAM of more than 90%. (Efficient vortex generation with metasurfaces at visible wavelengths will be discussed in greater detail in Chapter 5).

But metasurfaces allow more than just an optimal technique for generating OAM beams, they also enable new physical phenomena in the angular momentum of light. Specifically, because one can judiciously design each nanostructure comprising the metasurface, the device can be made to act as a spatially-inhomogeneous medium[40,41], i.e., a medium that acts as local subwavelength half-wave-plates with spatially-varying fast axes. While the description of optical angular momentum above has shown the spin and orbital angular momentum as independent quantities, when subwavelength structure is introduced into a material, there can be a coupling between the spin and orbital angular momentum[28,42]. Such a process is referred to as the spin-orbit coupling (SOC) or spin-orbit-interactions (SOI) of light, again to draw analogy to atomic or electronic systems. As metasurfaces provide subwavlength structure, with designable control over the polarization response, they provide an ideal platform to produce and study such phenomena in light, as will be first discussed in Chapter 2 and 5 and expanded upon in Chapter 6.

1.5 Overview of the thesis

The theory and experimental results in the following chapters utilize and expand upon some of the concepts introduced in the previous sections. These chapters deal primarily with the design, fabrication and characterization of metasurfaces which are used for both fundamental studies as well as practical applications to optical devices. A focus is placed on addressing some of the remaining challenges that inhibit the wide scale application of metasurfaces. Chapter 2 details a plasmonic metasurface that reproduces many of the results of bulk metamaterials as well as introduces a new physical phenomenon where the spin angular momentum of light couples to specific directions of propagation, and changes with wavelength. Additionally, a process is developed for producing single-crystal silver films, which exhibit some of the lowest optical losses compared to any previous metal film. Chapter 3 introduces all-dielectric metasurfaces. The chapter examines the current state of dielectric metasurfaces and introduces a material and a process that allows high-efficiency dielectric metasurfaces to be demonstrated across the visible spectrum. Additionally this chapter further demonstrates how the spin angular momentum (circular polarization) of light can couple to spatial degrees of freedom. Chapter 4 builds upon the demonstration of Chapter 3 and realizes a planar lens with diffraction-limited focusing and imaging. Again the process is demonstrated across the visible spectrum. Chapter 5 demonstrates how metasurfaces can be used as devices to convert spin angular momentum of light into orbital angular momentum, so called spin-orbit-coupling. Chapter 6 is a culmination of all previous and provides a theoretical and experimental generalization of the spin-orbit-coupling of light introduced in Chapter 5.

2

Visible-frequency hyperbolic metasurface

Metamaterials and plasmonics have held great promise for achieving optical phenomena not possible in natural materials[8]—two hallmarks being negative refraction, where light is bent ‘the wrong way’ across an interface and confinement of light down to nanoscale dimensions. However, the main issue limiting their wide scale application or use in studying fundamental optical phenomena has been material loss—in many of these elements most of the optical energy has decayed only after a few 10s of nanometers. Plasmonics, and most metamaterials, use metals to confine light to small volumes or to locally engineer the optical response of a material. All metals are inherently lossy, especially at visible wavelengths, and this problem is exacerbated by typical techniques used for depositing these metals. In addition to the intrinsic losses, these deposition techniques introduce extrinsic loss mechanisms to the materials such as scattering and absorption at grain boundaries. Additionally, most three-dimensional metamaterials require complex or non standard fabrication techniques which further limits their application and often introduces additional loss mechanisms.

This chapter addresses several of the problems inherent to plasmonic metamaterials. First we introduce a simple technique for depositing single crystal silver. Silver (Ag) has the lowest material absorption from visible to infrared wavelengths and by eliminating grain boundaries and roughness associated with polycrystalline forms of this material we are able to achieve the lowest optical losses reported to date[43]. We also introduce a fabrication technique that allows us to transfer deep subwavelength structures into these Ag films, while maintaining the quality of the films. We are then able to utilize this fabrication technique and intrinsically low material loss to produce a 'hyperbolic' metasurface, the two-dimensional, planar counterpart of a bulk metamaterial, which exhibits orders of magnitude longer propagation lengths than any previous metamaterial (the distance that light propagates before losing 1/e of its intensity). We characterize this hyperbolic metasurface throughout the visible regime (from 450 nm to 700 nm) and show that it exhibits many of the properties of bulk metamaterials. We also show the discovery of a new effect, called the dispersion-dependent plasmonic spin Hall effect, where the spin angular momentum of light couples to specific propagation directions and depends on the wavelength of incident.

Later, Chapters 3-5, discuss all dielectric metasurfaces, which in contrast to this plasmonic metasurface that confines light to the near-field, produce arbitrary radiation patterns in the far-field. While the ultimate function of these two classes of metasurfaces are different, some of the fabrication techniques developed in this chapter are leveraged to produce high-quality dielectric metasurfaces (particularly detailed in Chapter 3). Additionally, the PSHE found in the plasmonic metasurface here has fundamental ties to the spin-orbit-conversion of light that is discussed in Chapter 5 and 6. The remainder of the chapter discusses potential applications of this metasurface, more details regarding the SC-Ag process, and the experimental results from the metasurface.

2.1 Bulk metamaterials

Metamaterials are artificial optical media composed of sub-wavelength metallic and dielectric building blocks that feature optical phenomena not present in naturally occurring materials[9,44,45,46,47,48,49]. While they can serve as the basis for unique optical devices that mold the flow of light in unconventional ways, three-dimensional (3D) metamaterials suffer from extreme propagation losses[11,13]. Two-dimensional (2D) metasurfaces and, in particular, hyperbolic metasurfaces (HMSs) for propagating surface plasmon polaritons (SPPs)[50,51] have the potential to alleviate this problem. Because SPPs are guided at a metal-dielectric interface (rather than passing through metallic components), these SPP-HMSs have been predicted to feature much lower loss while still exhibiting optical phenomena akin to those in 3D metamaterials. Moreover, because of their planar nature, these devices enable the construction of integrated metamaterial circuits as well as facile coupling with other optoelectronic elements. Here, we report the first experimental realization of a visible-frequency HMS using single-crystalline silver nanostructures defined by lithographic and etching techniques. The resulting devices display the hallmark properties of metamaterials, such as negative refraction[9,44,47,48,49] and diffraction-free propagation[45,46] with device performance significantly exceeding those of previous demonstrations. Moreover, HMSs exhibit strong, dispersion-dependent spin-orbit coupling, enabling polarization- and wavelength-dependent routing of SPPs and 2D chiral optical components[52,53,54,55]. These results open the door for realizing integrated optical meta-circuits, with wide-ranging applications in areas from imaging and sensing to quantum optics and quantum information science.

2.2 Single crystal silver properties and fabrication of hyperbolic metasurface for surface plasmon polaritons

Our approach for realizing a visible-frequency HMS involves the definition of a nanoscale silver/air grating on a sputter-deposited, single-crystalline silver film by electron-beam lithography and plasma etching. Unlike focused-ion-beam milling methods[52,49] that produce rough, defect-ridden structures, this new method produces smooth, high-quality silver nanostructures with high aspect ratios, critical for the realization of an SPP-HMS. Figure 2.1 illustrates the materials and structures that form the basis for HMSs. As a starting material, we sputter-deposited a micron-thick silver film on a (111)-silicon substrate at 300° C and at high deposition rate (> 1.5 nm/s)[56,57]. High-resolution transmission electron microscopy (TEM, Fig. 2.1a), X-ray diffraction, atomic force microscopy, and electron backscatter diffraction measurements (see Appendix A, Figs. A.1-A.3, respectively) reveal that these films are single-crystalline and have root-mean-square roughnesses as low as 300 pm. The ellipsometric characterization (Fig. A.4) shows that, over a significant portion of the visible spectrum, the optical loss in our film is significantly lower than those reported previously[43,58] and is lower than recently reported silver films prepared by molecular beam epitaxy (MBE)[59]. Unlike the MBE

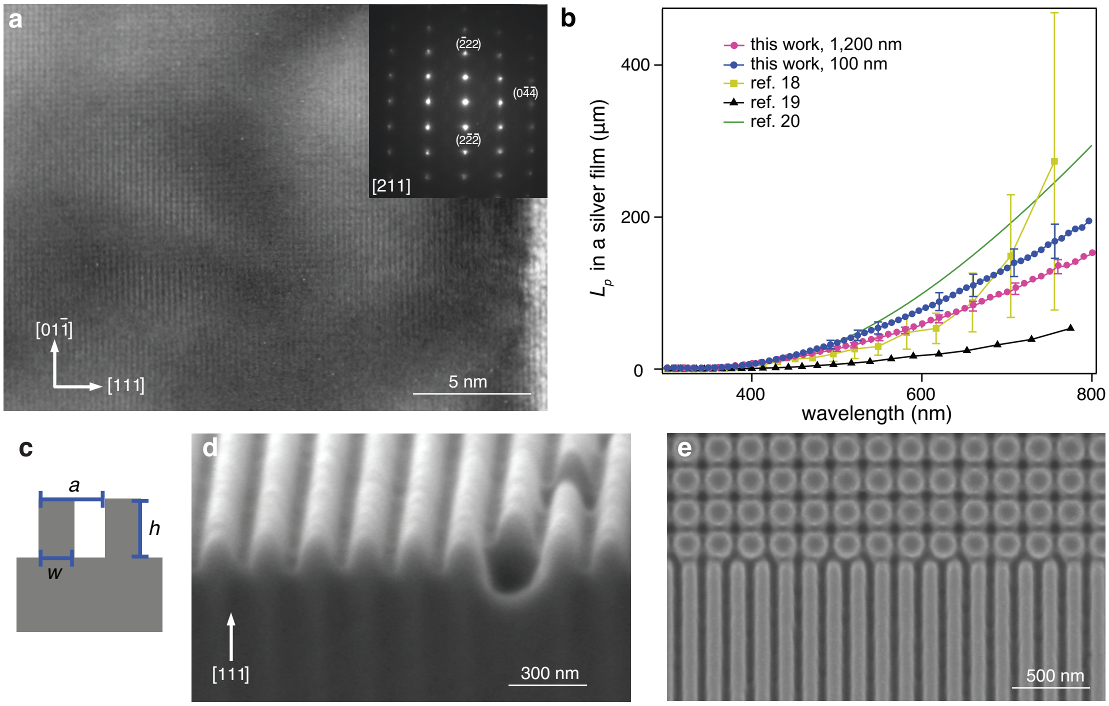

Figure 2.1: Single-crystalline silver film and fabricated devices. **a**, High-resolution TEM image taken down the $[211]$ axis that demonstrate the single-crystalline nature of the sputter-deposited silver. The growth direction is from left to right along the $[111]$ direction with the surface of the silver film shown at the far right of the image. Inset shows the electron diffraction pattern. **b**, SPP propagation length Lp on a silver film derived from measured real and imaginary parts of the dielectric constants for 100 nm (blue circle) and 1200 nmthick (pink circle) sputtered films. For comparison, propagation lengths calculated using the dielectric constants reported in 18-20 (green line) are also shown (error bars are one standard deviation from the average value). **c**, Schematic of HMS, with pitch a, width w, and height h. **d**, A cross-sectional SEM image of a fabricated device. e, Top-down SEM image of a silver/air grating and out-coupling structures (top).

process[59], however, the sputtering process can rapidly grow single-crystalline films of large thicknesses, which is crucial for the realization of an HMS because it prevents SPP absorption by the silicon substrate. From the experimentally measured dielectric constants, we determine that the SPP propagation length $\mathrm{L_p}$ (defined as the length over which the SPP intensity decays by 1/e) in a silver film exceeds 100 μm for far-field wavelengths (λ) greater than 650 nm (Fig. 2.1b).

Beyond exceptional optical performance, single-crystalline silver films offer mechanical and thermodynamic stability, crucial for defining nanoscale features using lithography and etching. We fabricated the silver/air gratings and light in- and out-coupling structures by first defining an Al_2O_3 hard mask with electron-beam lithography and then dry-etching silver with argon plasma (see Appendix A, Fig. A.6 for details). After etching, the residual Al_2O_3 mask was removed with hydrofluoric acid, leaving clean, high aspect ratio silver features. Figures 2.1 and e show scanning electron microscope (SEM) images of representative devices (schematically shown in Fig. 2.1c: silver ridge height h = 80 nm, width w = 90 nm, and pitch a = 150 nm). The smooth surface of our devices, coupled with single-crystalline nature of silver, minimizes extrinsic optical losses originating from grain boundaries and surface roughness.

A recent theoretical work[51] has predicted that a silver/air grating with appropriate subwavelength feature sizes, such as that shown in Figs. 2.1d and e, should exhibit hyperbolic dispersion for propagating SPPs below a critical wavelength, $\lambda = \lambda_T$ (and elliptical dispersion above it). A simple physical picture provides insight into the transition from hyperbolic to elliptical dispersion in this structure. At short wavelengths, the plasmonic modes are tightly confined to the ridges of the grating, qualitatively similar to the situation in an array of parallel nanowires that exhibit hyperbolic dispersion[60]. In the long wavelength limit, on the other hand, the modes are only weakly confined, and the grating can be considered a perturbation to a flat surface, resulting in elliptical dispersion (for discussion, see Appendix A, Figs. A.7 and A.8).

2.3 Experimental verification of hyperbolic dispersion for surface plasmons

To experimentally verify these predictions, we fabricated a series of devices and tested their optical properties. Figure 2.2 presents a device (D1) designed to demonstrate negative refraction of SPPs, a known property of hyperbolic metamaterials[61]. This device consists of a silver/air grating as well as a groove that launches SPPs on flat silver upon far-field excitation (Fig. 2.2a). The angle of refraction at the flat silver/grating interface was determined by collecting scattered light at the in-coupling structure, the silver-film/grating interface, and the corresponding out-coupling structure. As clearly shown in Figs. 2.2b and d (see also Appendix A, Figs. A.9 and A.10), the behavior of D1 changes from normal refraction at $\lambda > 540$ nm to negative refraction at $\lambda < 540$ nm. We note that λ_T at which the device behavior changes from normal to negative refraction (i.e. elliptical to hyperbolic dispersion) can be tuned by varying the device geometry (Fig. A.11a) or by changing the dielectric environment of silver (e.g., by depositing a thin layer of Al_2O_3 on the device, Fig. A.11b).

2.4 Diffraction-free propagation

Figure 2.3 illustrates a second device (D2) with $\lambda_T = 560$ nm that exhibits another remarkable phenomenon—diffraction-free propagation. At λ_T, the flat dispersion curve dictates that all SPPs propagate parallel to the silver ridges[51] (Fig. 2.3b, Fig. A.12 and discussions below)

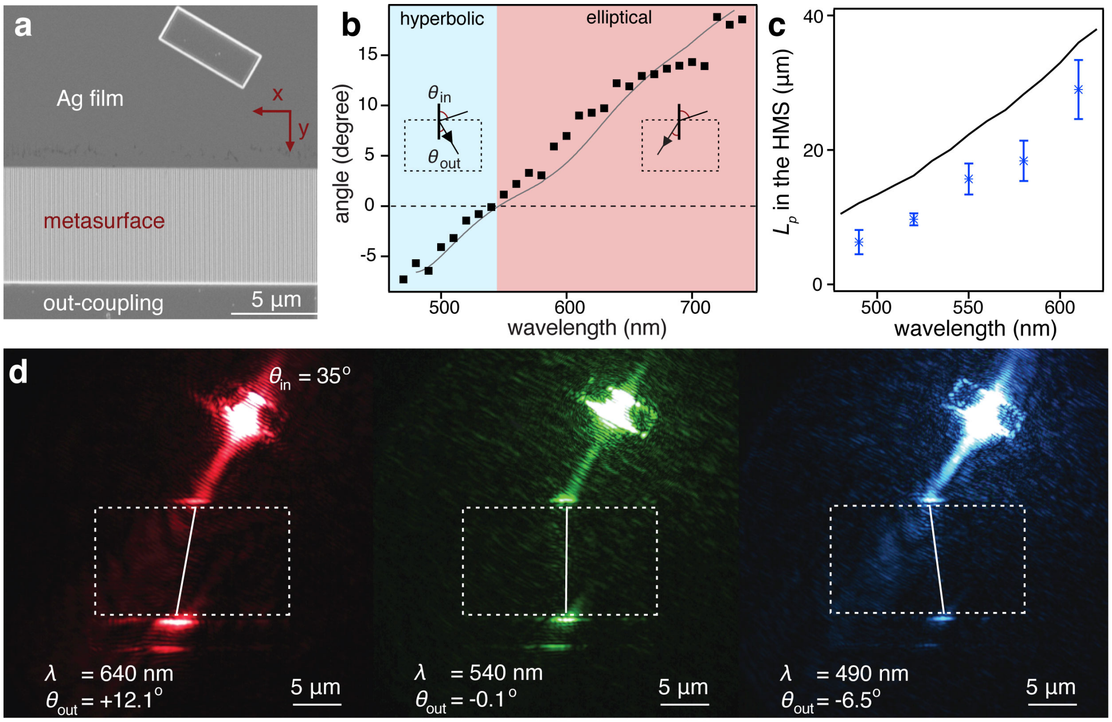

Figure 2.2: Measurement of SPP refraction at a flat silver/HMS interface. **a**, An SEM image of a device D1. Far-field light is converted to SPPs in the silver film via the in-coupling structure at the top of the image. The excitation laser is unpolarized. The SPPs propagate along the silver film, are refracted at the film-metasurface interface, and are then scattered into the far field at the out-coupling structure at the bottom of the image. In this device, the height of the silver ridge is 80 nm, the width is 90 nm, and the pitch is 150 nm. **b**, The angle of refraction as a function of wavelength, with elliptical (red) and hyperbolic (blue) dispersion regimes indicated. The solid line is the simulated angle of refraction from FDTD simulations. **c**, The experimentally measured (blue) and simulated (black) propagation length L_p of SPPs in the HMS (error bars are one standard deviation from the average value). **d**, Images of SPP refraction at the flat silver/HMS interface. The dashed line indicates the region of the HMS.

and thus SPPs excited on a single silver ridge remain primarily confined to the same ridge despite its sub-wavelength width ($\lambda/6$). In device D2, slots defined directly on individual silver ridges serve as in- (out-) coupling structures that convert far-field light to SPPs (or vice versa, Figs. 2.3a-c). As shown in Fig. 2.3d, at $\lambda = 585$ nm, despite being excited by only one in-coupling structure, SPPs scatter off multiple out-coupling structures due to normal, diffractive propagation. However, at $\lambda_T = 560$ nm SPPs primarily scatter off the out-coupling structure located on the same ridge as the in-coupling structure (Fig. 2.3e), signifying diffraction-free propagation. This diffraction-free propagation, coupled with suitably designed 'magnifying' out-coupling structures, enables sub-diffraction-resolution imaging and photon routing[45,46]. Figure 2.3g presents one such demonstration: at $\lambda_T = 560$ nm, despite SPPs being launched at two in-coupling structures separated by a sub-wavelength spacing of 150 nm, SPPs primarily scatter off the two corresponding out-coupling structures staggered along the propagation axis.

2.5 Dispersion-dependent plasmonic spin Hall effect

We next demonstrate a new optical phenomenon supported by the silver/air grating: dispersion-dependent plasmonic spin-Hall effect (PSHE)[62,52,53,63] a plasmonic analogue of the electronic Rashba[64] and photonic spin-Hall effects[65,55]. In electronic systems, spin-orbit coupling arises due to the lack of inversion symmetry (e.g. in the presence of an external electric field) and couples the spin of a charge carrier to its propagation direction. Similarly, in an optical system with tightly confined optical modes, the light propagation direction couples to the electric field rotation, leading to the photonic spin-Hall effect[65,55]. In the HMS, a PSHE arises from three structural features of the silver/air grating. First, this structure lacks inversion sym-

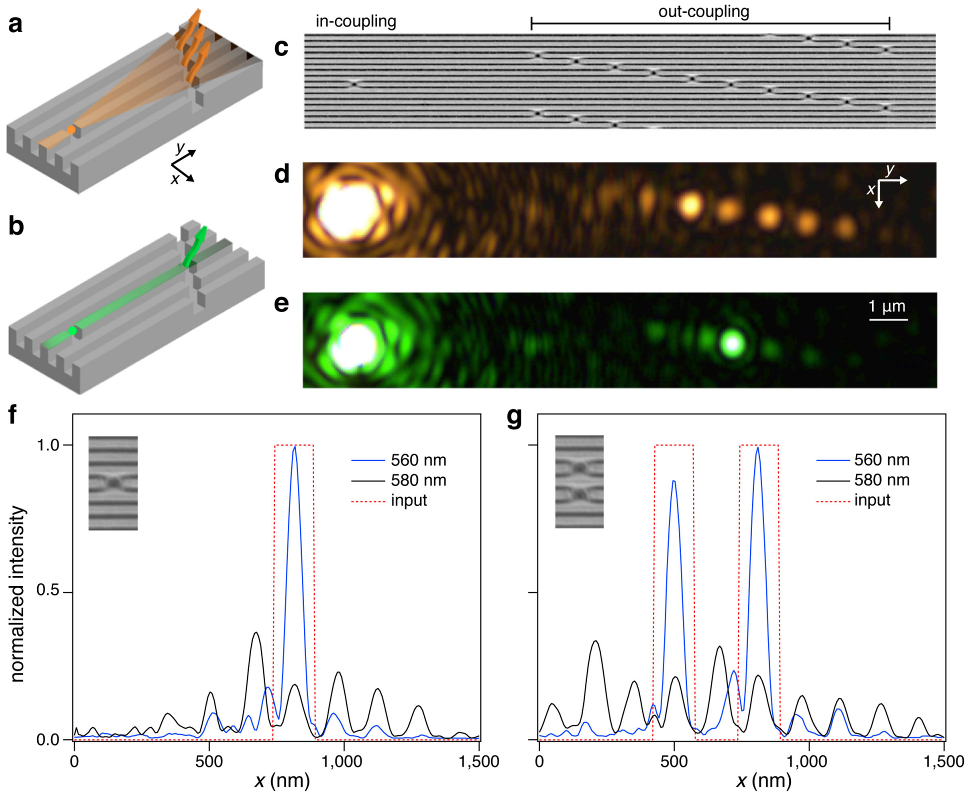

Figure 2.3: Observation of diffraction-free SPP propagation. **a**, A schematic for SPP diffraction in a silver/air grating. **b**, A schematic for diffraction-free SPP propagation in a silver/air grating. In (a) and (b) an in-coupling structure defined on a single ridge (left-hand side) acts as a point source of SPPs. SPPs scatter off at the out-coupling structures on the other side that are staggered along the y-axis for magnification. **c**, An SEM image of a device D2. The height of the silver ridge is 80 nm, the width is 90 nm, and the pitch is 150 nm. The y-axis distance between out-coupling structures is 1 ?m, thus providing the magnification of 6.7. **d-e**, Optical images of SPPs scattering at the out-coupling slots (right-hand side) with SPPs excited with unpolarized light by a single in-coupling structure (Fig. 4f inset) for (d) $\lambda = 585$ nm and (e) $\lambda = \lambda_T = 560$ nm. **f**, Diagonal cross-sections of optical image across out-coupling slots at $\lambda = 560$ nm (blue) and $\lambda = 585$ nm (black), with the input position marked as red. The x-axis coordinate of the cross-section is indicated. **g**, Similar cross-sections obtained when two in-coupling notches (inset) are used. In (f) and (g), the out-coupling intensities are normalized such that the total integrated intensities are equal.

metry and exhibits high optical anisotropy for SPPs propagating parallel and perpendicular to the silver ridges ($y-$ and $x-$axes, respectively, in Fig. 2.4a). Second, due to its nanoscale ridged structure, the HMS can support electric field components perpendicular to the SPP propagation direction (e.g. E_z and E_x for propagation along y), and thus SPPs can exhibit circular polarization. Third, the dispersion of the system is strongly frequency dependent, such that the direction of the SPP group velocity changes when moving from hyperbolic to elliptical polarization. Combined together, these three features enable the dispersion-dependent PSHE in which the SPP propagation direction and helicity are linked to each other in a frequency dependent manner (Fig. 2.4). While the PSHE has been experimentally observed in bulk hyperbolic metamaterials at radio frequencies[54], it has never been realized experimentally in the visible frequency regime.

Figure 2.4c shows a device D3 that demonstrates the PSHE. In this device, a single circular in-coupling structure near the silver/air grating scatters unpolarized far-field light to propagating SPP modes, and an array of vertical silver cylinders on the other side (diameter: 140 nm, height: 90 nm) serves as out-coupling structures that scatter SPPs back to the far field. These out-coupling structures convert the SPP polarization into far-field polarization with minimal distortion (see discussions in Appendix A , Fig. A.13). As shown in Fig. 2.4d, when SPPs are excited by the in-coupling structure, they split into two separate (left- and rightward) beams. Polarization-resolved imaging reveals that these split SPP beams exhibit opposite circular polarizations (one predominantly (80%) $\sigma+$ and the other is $\sigma-$ with $\sigma\pm = E_x \pm iE_z$, Figs. 2.4g and h). Moreover, this helicity-dependent splitting is strongly wavelength-dependent (Figs. 2.4e and f). When the silver/air grating exhibits an elliptical dispersion ($\lambda > 580$ nm), the $\sigma+$ ($\sigma-$)-polarized SPPs deflect to the left (right), with the deflection angle decreasing with

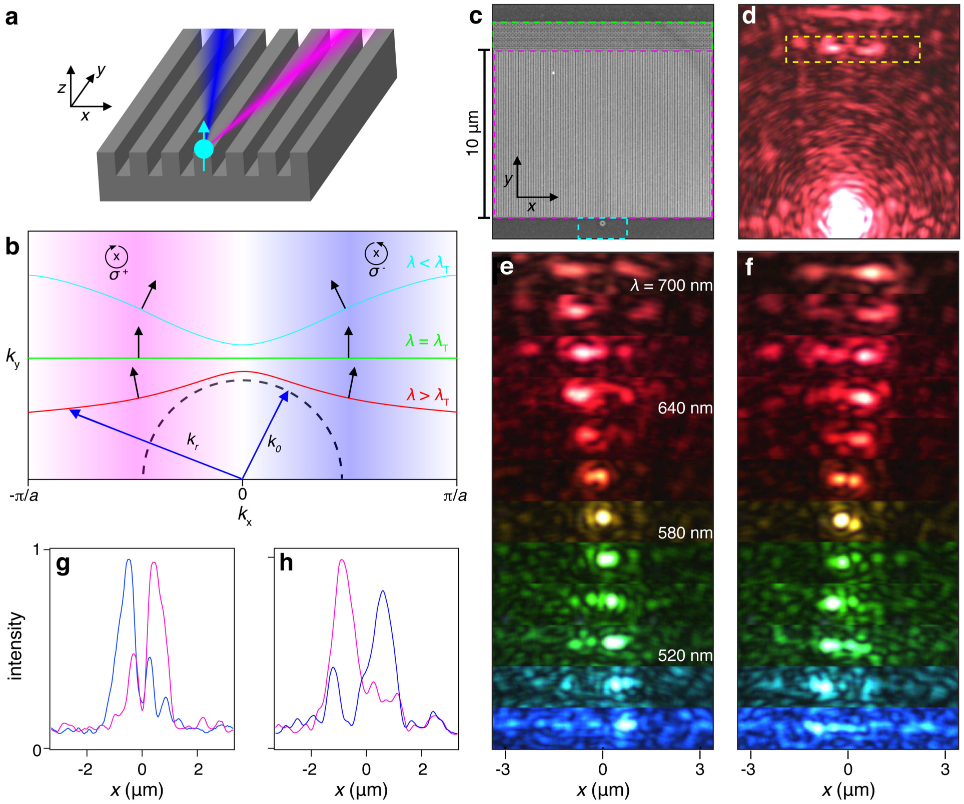

Figure 2.4: The dispersion-dependent plasmonic spin-Hall effect (PSHE). **a**, A schematic of the PSHE. In a silver/air grating, SPPs with different helicities propagate into distinct spatial directions. **b**, Illustration of the origin of the PSHE. Positive k_x corresponds to σ^- (blue shading) and negative k_x to σ^+ (magenta shading). The direction of the group velocity (black arrows) is perpendicular to the isofrequency contours at a given dispersion regime (elliptic (red), diffractionless (green), and hyperbolic (cyan)). The allowed k_x values extend from $-\pi/a$ to $+\pi/a$, where a is the pitch of the silver/air grating. The dotted black line indicates the free-space isofrequency contour at the same frequency as the red curve. **c**, An SEM image of a device D3 used to examine PSHE with an in-coupling structure (cyan rectangle), a silver/air grating (pink rectangle), and out-coupling cylinders (green rectangle). **d**, Image of D3 under unpolarized laser excitation of the in-coupling structure. The out-coupling region is marked by the yellow box. **e-f**, Image from the out-coupling structures as a function of wavelength collecting only (e) σ^+ and (f) σ^- polarized light. From bottom to top, the wavelength increases from 480 nm to 700 nm in increments of 20 nm. **g-h**, Light intensities measured at the out-coupling structures for σ^+- (magenta) and σ^-- (blue) polarized light at (g) $\lambda = 530$ nm and (h) $\lambda = 640$ nm.

decreasing λ. When the silver/air grating enters the hyperbolic regime ($\lambda < 580$ nm), this behavior reverses (similar to the magnetic field switching sign in the electronic Rashba effect), and the $\sigma+$ ($\sigma-$)-polarized SPPs deflect to the right (left). At the diffraction-free propagation point ($\lambda_T = 580$ nm), the splitting between $\sigma+$ and $\sigma-$ helicities vanishes.

The physical origin of this dispersion-dependent PSHE can be understood using the isofrequency contour schematically illustrated in Fig. 2.4b. In the silver/air grating, the SPP helicities are determined by the wave vector that characterizes the electric field. The electric field of an SPP mode is given by $\vec{E} \approx E_r\hat{r} - (k_r/k_z)E_r\hat{z}$, where $k_z = i\sqrt{k_r^2 - k_0^2}$, $k_r = \sqrt{k_x^2 + k_y^2}$ is the plasmonic wavenumber in the direction of $\hat{r}$, $\hat{r}$ is the in-plane direction of , and is the free-space wave number given by ω/c[66,54]. Because the SPPs are evanescent perpendicular to the surface, k_z is imaginary and the field rotates along . Near the center of the Brillouin zone ($k_x = 0$), we have $k_r \approx k_y \approx k_0$, and the SPP wavelength λ_{SPP} in our structures is similar to the far-field wavelength λ (Fig. A.14 and see discussion below). As k_x increases, however, k_r continuously increases due to highly anisotropic dispersion relation, and for $k_r >> k_0$ the modes become circularly polarized in the x-z plane. Near the edge of the Brillouin zone, modes of opposite circular polarization hybridize, and the polarization effects in the $x - z$ plane vanish. These considerations indicate that when projected on the x-z plane, an SPP mode with $k_x < 0$ ($k_x > 0$) exhibits $\sigma+$ ($\sigma-$) polarization (note that an SPP with $k_x = 0$ will exhibit electric field rotation in the y-z plane[55]). The direction of SPP propagation is, however, governed by the group velocity vector that is perpendicular to the isofrequency contour. The small angular spread of the right- and leftward SPP beams is a consequence of the shape of this isofrequency contour that reflects the optical anisotropy of our silver/air grating. As shown in Fig. 2.4b, this simple consideration explains our experimental observations. Specifically, when the device exhibits elliptical dispersion ($\lambda > \lambda_T$), the $\sigma+$ ($\sigma-$)-polarized SPPs deflect to the left (right) because leftward (rightward) group velocity vector is associated with $k_x < 0$ ($k_x > 0$). In contrast, in the hyperbolic dispersion regime ($\lambda < \lambda_T$), the reverse is true, leading to the switching of the deflection directions for $\sigma+$ ($\sigma-$)-polarized SPPs.

A key enabling feature of our approach is dramatic reduction in optical losses in comparison to bulk metamaterials. To directly characterize the optical performance of HMS, we fabricated silver/air gratings of varying lengths with identical light in- and out-coupling structures, and measured the out-coupled light intensity as a function of the grating length at the same in-coupling intensity. By fitting the intensity-length curve by a single exponential at a given λ, we then determined Lp in our devices ranging from 6 μm at $\lambda = 490$ nm up to 29 μm at $\lambda = 610$ nm (Fig. 2.2c, blue, for discussion see Appendix A, Fig. A.15). These propagation length Lp values are two orders of magnitude larger than those measured in bulk visible-frequency hyperbolic metamaterials. To analyze our observations quantitatively, we carried out detailed finite-difference time-domain (FDTD) simulations of SPP propagation in our device geometries (D1 through D3). These FDTD simulations are in a good agreement with the experimental observations in Figs. 2.2, 2.3, and 2.4: negative refraction for $\lambda < \lambda_T$ (Fig. 2.2b, solid line), diffraction-free propagation at λ_T (Fig. A.12), and the dispersion-dependent PSHE (Fig. 2.5 and Appendix A for discussion). The FDTD simulations also indicate that the local polarization of the SPP field reaches 87% for left- and right-propagating circularly polarized SPPs, larger than experimentally observed values of 80%, due to the imperfect polarization conversion of our out-coupling structure (Fig. A.16). The simulated propagation lengths (Fig. 2.2c, black, for discussion see Appendix A) in the HMS are 30% larger than the experimentally determined ones, likely due to residual nanoscale roughness introduced during the fab-

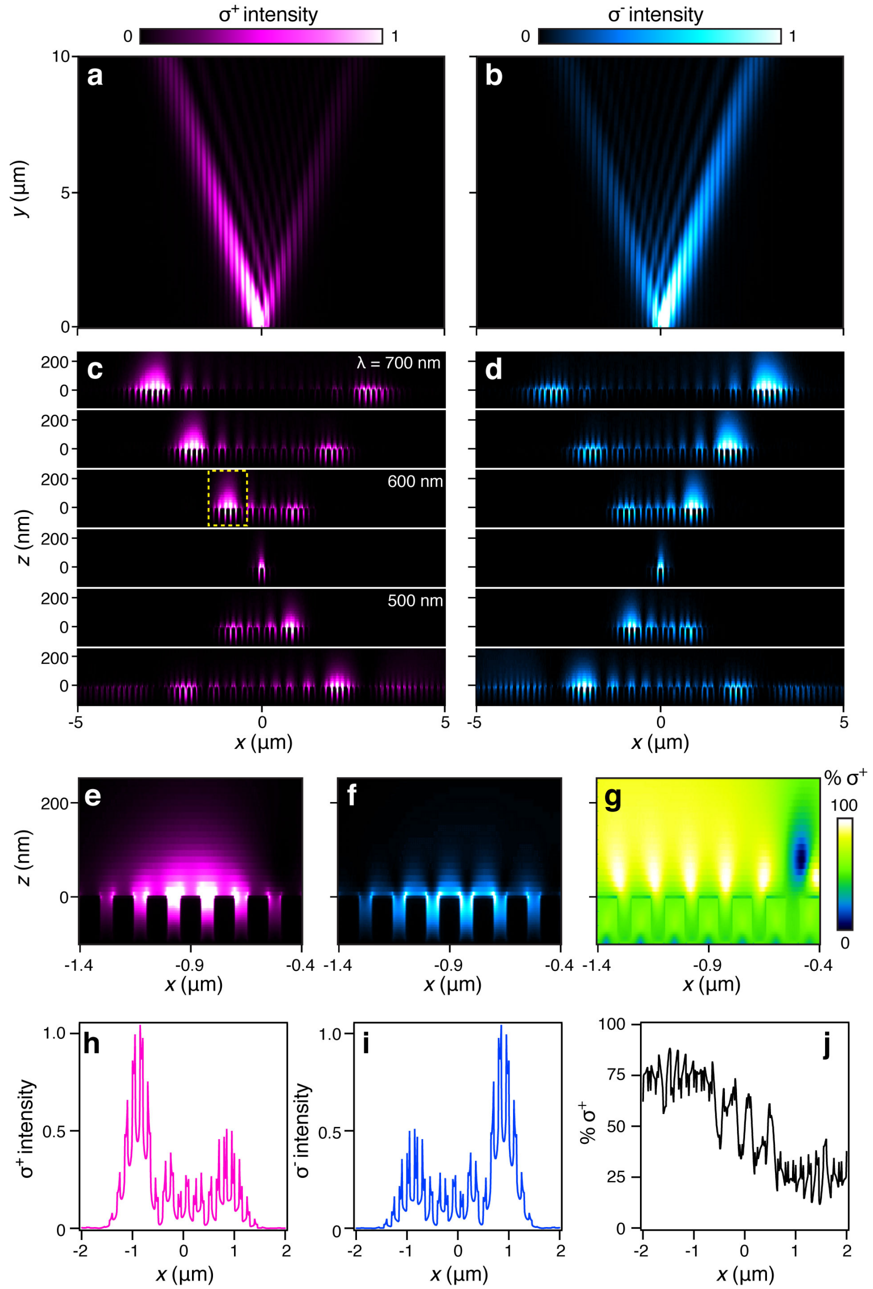

Figure 2.5: Simulations of the PSHE. a,b The simulated electric-field intensity of SPPs propagating on an SPP-HMS at $\lambda = 680$ nm. The intensity is divided in (a) σ^+ and (b) σ^- components. **c,d** the $x - z$ cross sections of the SPP distribution at $y = 10$ μm divided into (c) σ^+ and (d) σ^- components for wavelengths from 450 nm (bottom) to 700 nm (top) $(50$ nm increment). **e-g** A close-up image of the SPP at $\lambda = 600$ nm in the region of yellow box in (c), in (e) σ^+ and (f) σ^- components, and (g) corresponding local degree of σ^+ polarization. The SPP source is a dipole oriented along the $z-$axis at $(x, y, z) = (0, 0, 10)$ nm. The simulated HMS pitch = 150 nm, $w = 90$ nm, and $h = 80$ nm. (h-j) $z-$axis integrated intensity vs. x at $\lambda = 600$ nm and $y = 10$ μm in (h) σ^+ and (i) σ^- components and (j) corresponding integrated polarization vs. x.

rication procedure. Due to increasing SPP confinement, the sensitivity to surface roughness increases at lower wavelengths, resulting in greater scattering losses. Despite these imperfections, the measured propagation distances indicate that the low-loss, 2D nature of our devices offers a substantial improvement over conventional bulk metamaterials in terms of optical loss, thereby opening the door for a wide array of high-performance plasmonic nanostructures.

2.6 CONCLUSION

Although our demonstrations focused on one particular family of metasurfaces, i.e. a silver/air grating, the fabrication strategy is general and compatible with other bottom-up and top-down semiconductor and metal processing techniques. Our method thus opens up the possibility of realizing low-dimensional transformation optics and metamaterial-based devices[67,68]. This same method can be used to generate integrated metamaterial circuits that combine HMSs on-chip with other optoelectronic and plasmonic devices. The HMSs can enable quantum optics applications as well. Because of their small mode volumes and increased plasmonic density of states[50,51], HMSs can be used for enhancing interactions of SPPs with individual quantum emitters—a new pathway for realizing solid-state quantum nonlinear optical circuits. Moreover, the frequency-dependent spin-orbit interaction enables the exploration of a new class of solid-state quantum optical phenomena that involve chiral optical interfaces with quantum emitters. By extending recent demonstrations involving such interactions with 1D waveguides[55] into 2D, this could enable spin-dependent routing of single photons as well as non-trivial topological phenomena that combine spin-orbit interactions with single photon nonlinearities associated with quantum emitters[69].

3

Broadband high-efficiency dielectric metasurfaces for the visible spectrum

Chapter 2 dealt with a particular class of metasurface that confines light to a patterned surface surface (the near field). While near field metasurfaces provide interesting physical phenomena and are an ideal interface for strong coupling to quantum emitters (e.g., color defects in diamonds, quantum dots, exitons in 2D materials), a large class of problems in optics require some specific radiation pattern in the far-field. Transmissive optical elements, the largest subclass of traditional optical elements, are of particular importance technologically. Transmissive metasurfaces are planar optical components that replicate and expand upon the functionalities of traditional optical components and leverage the widespread fabrication techniques of CMOS processing. An outstanding problem, however, is that previous transmissive metasurfaces suffer from high optical loss at visible wavelengths because of the constituent materials and challenges in fabricating high fidelity structures for such small wavelengths (as pointed out in Chapter 1).

This chapter introduces transmissive metasurfaces that operate across the entire visible spectrum with high efficiencies. As the basis of this demonstration, we used a common material which is found in everything from white paint to sunscreen—titanium dioxide. To fabricate these metasurfaces, we use portion of the fabrication technique introduced in Chapter 1 and Appendix A. This chapter also introduces the concept of so called 'Pancharatnam-Berry phase optical elements' (PBOE). These PBOEs produce conjugate phase profiles on incident left- and right-circularly polarized (the spin angular momentum eigenstates), as a result of the relative rotation angles between the constituent nanostructures. While in this Chapter we initially demonstrate the operation of a transmissive metasurface hologram, in Chapter 3 we show that the same principles can be applied to more 'well-behaved' phase profiles such as the hyperbolic phase function of a lens. Additionally, the concept of the SAM (or equivalently, polarization) of light coupling to some spatial degree of freedom, such as phase distribution or propagation direction, connects the demonstration in this chapter to the plasmonic-spin-Hall-effect introduced in Chapter 2. These phenomena are referred to as spin-orbit-interactions (SOI) or spin-orbit-coupling (SOC). The concepts of SOI and SOC will be revisited in Chapter 5 and expanded upon in Chapter 6. The results presented below are important for realizing planar optical components at visible wavelengths—e.g., lenses, holograms and phase plates–with orders of magnitude reduction in thickness compared to traditional refractive optics and practical efficiencies. Finally, the process detailed here has provided the basis for demonstrating a large number of devices within the Capasso group[70,71,72,73,74,75,76,77,78,79,80]

3.1 DIELECTRIC METASURFACES

Transmissive dielectric metasurfaces[21] (DM)–optical devices composed of subwavelength-spaced units and near-flat profiles compared to refractive optics–have allowed unprecedented control over optical wavefronts[16] while circumventing Ohmic losses associated with plasmonic metasurfaces. Due to the scientific and technological importance of visible wavelengths, there has been increasing effort to realize DMs at these wavelengths. For example, silicon nitride dielectric metasurfaces have been realized at a red wavelength[81] ($\lambda = 633$ nm), scattering properties of coupled TiO_2 resonators[82] have been examined and TiO_2 binary diffraction gratings have been fabricated via top-down etching[83]. However, no current dielectric metasurface implementation has been capable of providing arbitrary phase control of an optical wavefront while maintaining high efficiency across the entire visible spectrum (especially at blue and green wavelengths). Furthermore, the typical top-down techniques used to implement these metasurfaces can introduce significant surface roughness and make it difficult to create subwavelength sampling of a desired optical phase profile.

Here we demonstrate amorphous TiO_2 metasurfaces that maintain high efficiency across the entire visible spectrum (from 470 to 700 nm). Our approach to creating DMs utilizes a bottom-up nanofabrication via atomic layer deposition providing high aspect ratio, anisotropic dielectric nanostructures with minimal surface roughness. As a proof of concept that we can provide control of the phase of a wavefront from 0 to 2π a requirement for many optical components, we produced metasurface holograms based on geometric phase. Efficient metasurfaces with metallic components operating in reflection have been demonstrated at red and near infrared wavelengths[84,85] but have efficiencies of <1% and <10% at blue and green wavelengths[86,87]. Thus, the TiO_2 metasurfaces we demonstrate here provide substantial improvement with efficiencies from 78-82%. Additionally, the use of a dielectric material allows our devices to function in transmission with high efficiency, which is necessary for many optical components.

3.2 Constituent material considerations and characterization for metasurfaces

The ability to realize high efficiency dielectric metasurfaces is critically dependent on the optical properties of the constituent material, as characterized by the complex refractive index, $\tilde{n} = n + ik$. The material should have negligible absorption loss $k \approx 0$ with relatively high refractive index ($n > 2$) at visible wavelengths. While a negligible absorption is necessary for high transmission efficiency, a high refractive index ensures strong confinement of the light that ultimately allows full control over the phase of the exiting wavefront (phase changes from 0 to 2π). The material should be optically smooth, having a surface roughness that is much smaller than the wavelength of light. High surface roughness introduces extraneous light scattering, which is a significant source of loss. To minimize roughness, the material must be amorphous or single crystalline, as the grain boundaries in polycrystalline materials increase roughness and act as light scattering centers.

We chose amorphous TiO_2 as our base material because it has a transparency window

($k \approx 0$) for wavelengths longer than 360 nm and its interband transition lies just outside of the visible spectrum, resulting in a sufficiently high index of refraction for strong light-matter interactions. We deposit TiO_2 by atomic layer deposition (ALD) at 90°C with tetrakis (dimethylamido)titanium (TDMAT) as the precursor due to its high deposition rate and absence of defect-driven absorption that is typical of $TiCl_4$-based precursors[88]. Additionally, use of an ALD process offers several advantages. ALD is a self-limiting process providing conformal coverage and monolayer control of the film thickness[89]. The conformal nature of the technique is essential to produce high aspect-ratio nanostructures[90]. The uniform and monolayer coverage yields smooth films with minimal defects compared to those prepared via sputtering or evaporation. Furthermore, the ALD process allows us to precisely control the material phase of the deposited TiO_2, producing amorphous, rutile, or anatase films depending on the deposition temperature[91].

Characterization of the optical properties of our amorphous TiO_2 shows that it is an ideal material for DMs. Figure 3.1a shows the measured optical properties of a TiO_2 film from ultraviolet (243 nm) to near infrared (1000 nm) wavelengths. To extract the TiO_2 optical properties from the collected data, we used a Tauc-Lorentz (TL) oscillator model developed for amorphous materials[92]. Over the visible spectrum the refractive index ranges from 2.63 to 2.34 and remains relatively flat between $\lambda = 570 - 750$ nm ($\Delta n = 0.09$). Below the wavelength of 500 nm the index of refraction increases rapidly, implying the approach of an electronic transition. For wavelengths shorter than 360 nm, the imaginary part of the refractive index, k, begins to take on non-zero values, a result of interband absorption. From the ellipsometry data and corresponding TL model, we determine the bandgap, Eg, to be 3.456 eV (the full set of fitting parameters and raw ellipsometry data are included in Appendix B, Fig. B.1). This

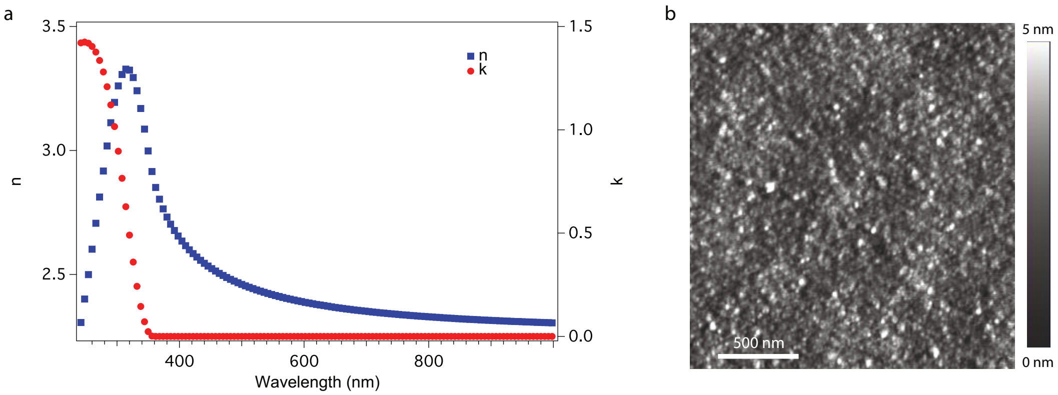

Figure 3.1: Amorphous titanium dioxide material properties. (A) Measured real (blue squares) and imaginary (red circles) part of the refractive index (n and k) as a function of wavelength across the visible spectrum. The full set of ellipsometry data used in obtaining these optical functions is included in Appendix B. **(B)** Atomic force microscope image of a typical TiO_2 film deposited via atomic layer deposition. The film is an atomically smooth surface with RMS roughness of 0.738 nm

value of the bandgap is in good agreement with previously reported values for amorphous TiO_2[93].

Our TiO_2 films also exhibit surface roughness that is much smaller than the incident wavelength, as characterized by atomic force microscopy (AFM). Figure 3.1b shows an AFM scan of a typical TiO_2 film deposited on a fused silica substrate. The scan has a root mean square (RMS) roughness of 0.738 nm, which is on the order of the surface roughness of the underlying substrate (Fig. B.2). Due to the absence of grain boundaries in AFM, coupled with the X-ray diffraction data (Fig. B.3), we conclude that the material is amorphous. The measured roughness of the amorphous TiO_2 is an order of magnitude less than other phases such as polycrystalline rutile or anatase[91]. The latter two phases generally have grain boundaries and RMS roughness as high as 5-10 nm both of which contribute to light scattering loss[94].

3.3 Fabrication process for realizing high efficiency metasurfaces

To achieve highly efficient metasurface devices while preserving the optical properties of ALD-prepared TiO_2, we used the fabrication process1 shown in Fig. 3.2. We spun electron beam resist (EBR) onto a fused silica substrate to produce a layer with thickness, tresist (Fig. 3.2a). Control of tresist is important because it sets the height of our final nanostructures. We patterned the resist using electron beam lithography and subsequent development in solution to remove the exposed EBR. This pattern is the inverse of our final metasurface (Fig. 3.2b). We transferred the exposed sample to an ALD chamber set to 90°C. The purpose of this temperature is twofold: it produces the desired amorphous phase and keeps the EBR below its glass transition temperature (i.e., prevents deterioration of the nanoscale patterns). During the deposition, the gaseous TiO_2 precursor (TDMAT) coated all exposed surfaces, producing a conformal film on the top and side of the EBR as well as on the exposed fused silica substrate (Fig. 3.2c). We allowed the ALD process to reach a specific thickness such that all features had been completely filled with TiO_2. Since the conformal ALD process fills exposed features from both sides the total ALD film thickness required is $t_{\text{film}} \geq w/2$, where w is the maximum width of all gaps (Fig. 3.2d). In practice we allowed the deposition to proceed well beyond the minimum requirement of half the feature width to ensure that TiO_2 had sufficiently diffused into all pores and that there are no voids in the final nanostructures. We removed the residual TiO_2 film that coats the top surface of the resist by reactive ion etching the sample in a mixture of BCl_3 and Cl_2 gas (8:2), similar to a planarization technique. The etch depth was equal to t_{film} so that the etching process exposes the underlying resist and the top of the nanostructures (Fig. 3.2e). We removed the remaining resist and left only the nanostructures that make up our metasurface (Fig. 3.2f). In this way, we obtained structures of heights t_{resist} while only needing to deposit a film of thickness $t_{\text{film}} \geq w/2$, which is timesaving and efficient.

We note that this approach is different from standard liftoff techniques, as one cannot employ conventional liftoff process due to the conformal coating of the ALD films. In addition, creating anisotropic nanostructures via dry etching of TiO_2, similar to other dielectric materials, is difficult and can lead to increased sidewall roughness. This ALD process is different than previous techniques[95,96] where the patterns created are generally fixed by a set template (e.g., anodic alumina or inverse opal). Here we are free to define more complex nanostructures because we use ALD directly onto exposed EBR.

Investigation of the structures, fabricated using the process above, shows that we produce nanostructures (nanofins) with the desired anisotropy and subwavelength dimensions. Figure 3.3 shows SEM images of a fabricated metasurface hologram. As seen in Fig. 3.3a, we can densely pattern large areas with subwavelength-spaced TiO_2 nanofins. This ultimately ensures that the majority of the incident light is imprinted with a desired phase, higher diffraction orders are suppressed and we can produce, in our case, holographic images with high efficiency. Figure 3.3b shows an SEM of the metasurface at high magnification, allowing resolution of individual nanofins. With this process we can also obtain extremely small spacing between individual nanofins, as shown by the 6 nm gap in Fig. 3.3b. The structures in this case have dimensions of 250×90 nm^2 but we can produce structures with dimensions as small as 40 nm (Fig. 3.3c).

Structures that deviate from 90° sidewalls, taking on a more triangular cross section, can introduce phase errors in the metasurface. Similarly, structures with large voids or defects will reduce the effective refractive index of the nanofins. Figure 3.3d shows a cross section SEM of

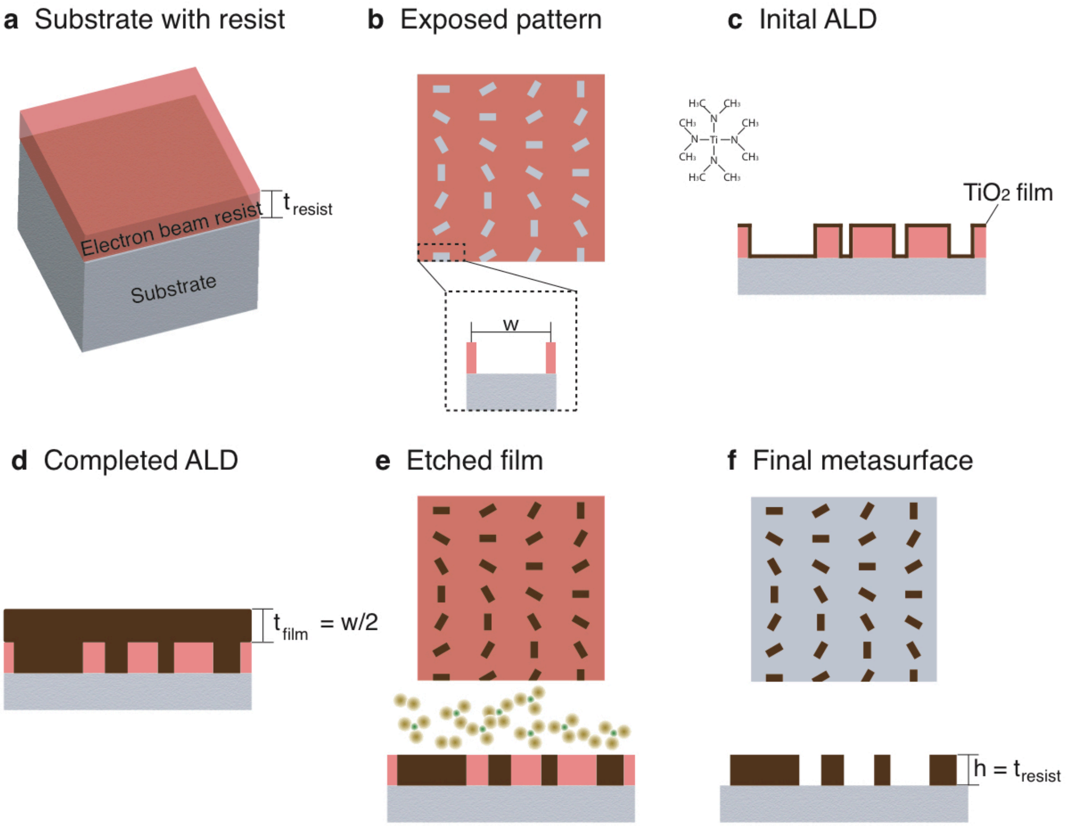

Figure 3.2: Fabrication process for dielectric metasurfaces. **(A)** Electron beam resist (EBR) on fused silica (or equivalent transparent substrate) with thickness tresist that ultimately sets the height of the final structure (perspective view). **(B)** Inverse of the final metasurface pattern imprinted into the EBR by electron beam lithography and subsequent development of the pattern (top view). The boxed area is an expanded cross section of the maximum feature width, w. **(C)** Initial TiO_2 deposition via atomic layer deposition conformally coats sidewalls and top of the EBR and exposed substrate (side view). TDMAT molecule used for atomic layer deposition is also shown. **(D)** Completed deposition of the TiO_2 yields a film thickness greater than half the width of the maximum feature size, $t_{\mathrm{film}} \geq w/2$. **(E)** Exposed tops of the TiO_2 metasurface and residual EBR after reactive ion etching with a mixture of Cl_2 and BCl_3 ions (top and side view). **(F)** Final dielectric metasurface after removal of remaining EBR (top and side view)

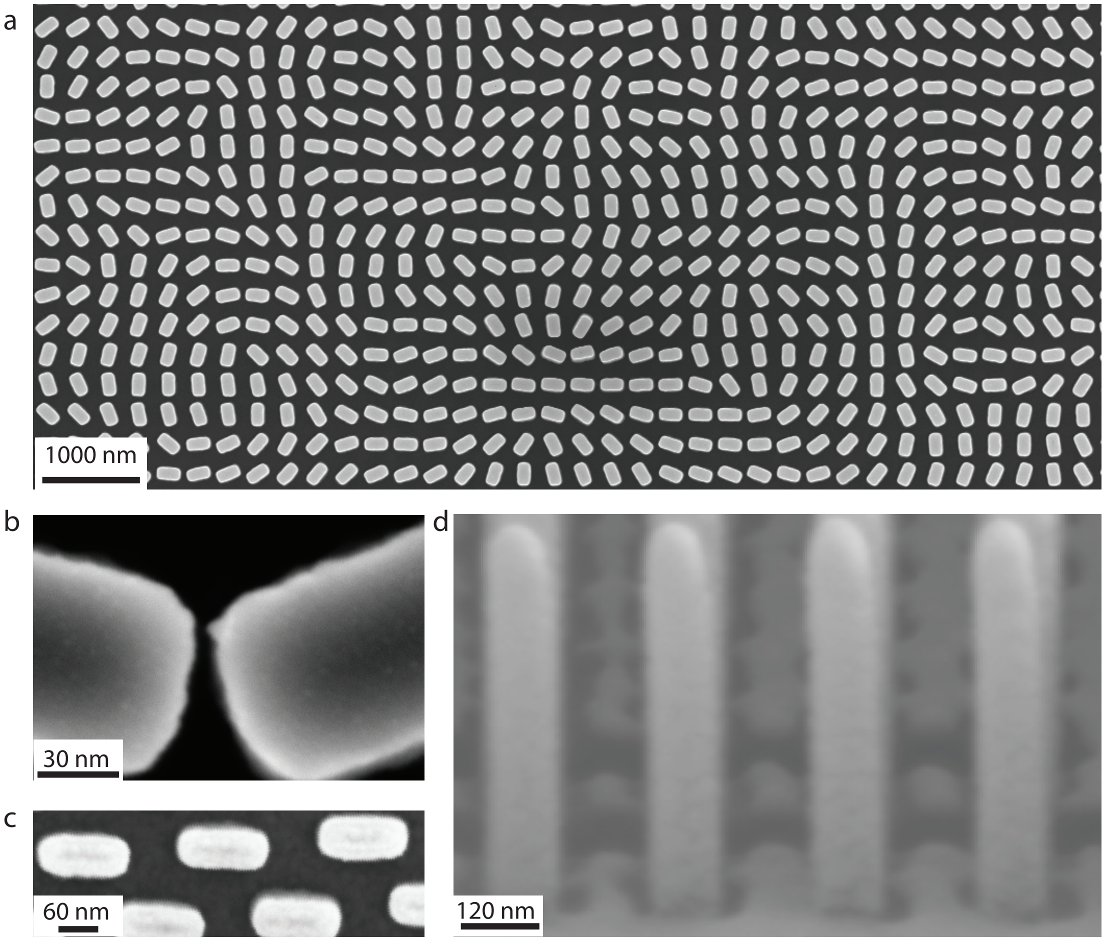

Figure 3.3: Scanning electron microscope images of fabricated structures.(A), Large scale view of a fabricated metasurface hologram composed of $\mathrm{TiO_2}$ nanofins. **(B)** Zoomed top-view of the metasurface showing individual nanofins. The fabricated nanofins are free from residual resist and have dimensions ± 10 nm of the designed dimensions of 250 nm $\times$ 85 nm. It can also be seen that with this fabrication technique we can achieve gaps between structures as small as 6 nm. **(C)** Top view of structures with lateral dimensions of approximately 40 nm. **(D)** Cross section (side-view) of nanofins exhibiting vertical sidewalls with a height of approximately 600 nm. The contrast oscillations between nanofins results from shadowing effects during deposition of a metal film used to prevent charging while we image the samples.

the nanofins (vertical direction in the image is the direction of light propagation). We observe that the angle of the structures in the vertical direction is 89°, that is, the nanostructures are highly anisotropic. This anisotropy is despite the fact that the nanostructures shown here are relatively tall compared to their other dimensions, with heights of 600 nm. Similarly, we do not see any void formation in the center of the nanofins. From the SEMs, it can also be seen that the final nanostructures have minimal surface and sidewall roughness.

3.4 Experimental demonstration of visible wavelength metasurfaces

To demonstrate the efficiency and functionality of our TiO_2 metasurfaces we designed three metasurface holograms (meta-holograms) to have peak efficiencies at wavelengths of 480 nm, 532 nm and 660 nm. We impart the required phase via rotation of the birefringent TiO_2 nanofins shown in Fig. 3.3—known as geometric or Pancharatnam-Berry (PB) phase[97,98,99]. (For more detail on this technique see refs.[98,100] Appendix B). An advantage of the PB phase is that the imparted phase is wavelength independent (only the efficiency changes away from the design wavelength), thus providing an ideal platform to test the performance of our metasurface over the entire visible range. We compute the phase map of a holographic image, the binary Harvard logo, by means of the Gerchberg-Saxton phase-retrieval algorithm(30) (Figure B.4).

Figure 3.4a-c show the measured and simulated efficiencies as a function of wavelength from 480 nm to 800 nm for the meta-holograms designed at $\lambda = 480$ nm, 532 nm and 660 nm, respectively. We define absolute efficiency as the total optical power of the reconstructed Harvard logo divided by the optical power measured through a $300 \times 300\ \mu m^2$ square aperture which is the same size as the hologram. (See Appendix B and Fig. B.6 for measurement details). The experimental results generally follow the simulation data and reach maxima of 82%, 81% and 78% near the design wavelengths of 480 nm, 532 nm and 660 nm, respectively. These values are, to our knowledge, the highest reported to date even compared to reflective metasurfaces[101,50,102]. We note that in certain cases there are discrepancies between the simulated and measured trend. Differences between designed and fabricated nanofin dimensions and the possibility of weak coupling between fins likely cause these discrepancies. Additionally the total efficiency of a geometric phase device depends on the transmission for an electric field polarized along the long or short axis of the individual elements[102]. We see high transmission through the elements (Fig. B.6), especially near the design wavelengths but these transmission values could be further increased by exploring antireflective coatings or by impedance matching techniques.

Since the geometric phase is a wavelength-independent effect, we can generate holographic images across the visible spectrum from a single design. Figure 3.4d-i show the holographic images across the visible spectrum for the hologram with a design wavelength of 480 nm. The subwavelength spacing and oversampling of the phase map can be seen in the images since there is sharp resolution of fine features such as the word 'VERITAS' at the top of the Harvard crest. The bright spot near the center of the cross of the Harvard logo is from the zero-order. However at the design wavelength the ratio of the intensity in the zero order to the total intensity contained in the hologram image is $< 1\%$.

3.5 Conclusion

While we have chosen to demonstrate our process using Panchartnam-Berry phase meta-holograms, the TiO_2 properties and fabrication process are not limited to this specific type of metasurface.

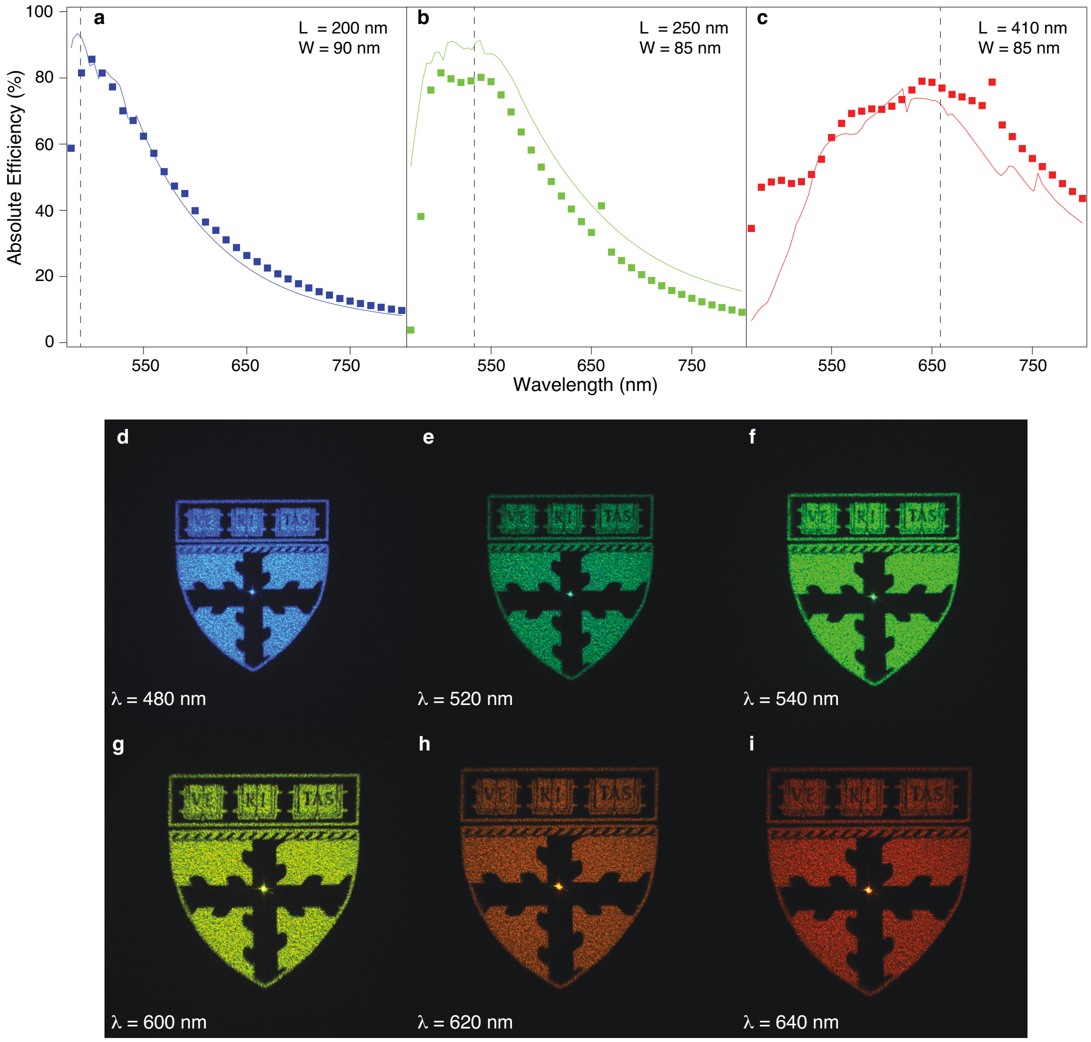

Figure 3.4: Measured absolute efficiencies and holographic images. **(A-C)** Measured (square markers) and simulated (solid line) hologram efficiencies. We define the absolute efficiency as the ratio of the total optical power of the hologram to the total optical power transmitted through an aperture of the same size as the hologram $(300 \times 300\,\mu\mathrm{m}^2)$. The vertical dashed line marks the design wavelengths of each device and device dimensions are given in the top right of each panel. **(D-I)** Holographic images covering the visible spectrum. The input wavelength is shown in the bottom of each panel. All images were obtained from the device designed for 480 nm and show the broadband behavior of a single device. The bright spot in the center of the image is due to the propagation of zero-order light.

For example, simulations using the measured optical constants of our TiO_2 and structural dimensions achievable with our fabrication process show that we can vary pillars dimensions in order to provide full 2π phase coverage rather than using the geometric phase (Fig. B.7). Thus one can also use the results we presented here to produce DMs that use linear birefringent resonators to encode phase information(8). Moreover, the demonstration of full 0 to 2π phase coverage enables the implementation of any DM components with high efficiency at visible wavelengths such as axicons, lenses, gratings and polarization beam splitters.

We have detailed the experimental realization of highly efficient dielectric metasurfaces that span the visible spectrum. We employed ALD to produce smooth amorphous TiO_2 films that are transparent for wavelengths longer than 360 nm and have an index of refraction that is sufficiently high to provide complete phase control over an optical wavefront. The fabrication technique for these metasurfaces, requiring only single-step lithography, provides a simple method to produce the highly anisotropic nanostructures that are necessary for DMs. While we used TiO_2, our process is applicable to any material that can be deposited via ALD. The fabricated metasurface holograms have the highest recorded efficiencies to-date (82%, 81% and 78%) at their respective design wavelengths. The technique presented here is general and can be applied to any type of metasurface. Careful consideration of the optical properties of our base material and the precision of the fabrication technique allowed us to expand the utility of DMs to visible wavelengths. This work can enable the creation of new compact optical systems with thicknesses that are orders of magnitude less than traditional optical systems.

4

Meta-lens for visible wavelengths

The lens is one of the first and the most ubiquitous human-made optical elements (especially in 2017 when approximately 44% of the world population owns a 'smartphone'[103], with approximately 7.2 billion total devices, each of which has approximately 5 lens elements, totaling roughly 35 billion lenses in smartphones alone!) The lens is not only important within the context of consumer technology but has also been the driver of scientific discovery at least notably since Gailileo in 1609. It is natural then to apply the concepts of the metasurface to this crucial optical element. The metasurface approach, however, provides the advantage of using

CMOS fabrication technology, used to produce transistors, sensors and illuminators, to produce lenses that are planar and are 1000s of times thinner than traditional optics. The result provides the potential to directly integrate the optics of a device with the underlying electronics in the same foundry.

In this chapter we examine the performance of a metasurface lens (meta-lens) produced using the underlying principles and fabrication techniques introduced in Chapter 3. Lenses are used for two main, not necessarily independent functions, focusing light to a point and forming an image of a scene or object. Here we examine the performance of the meta-lens for both cases, focusing and imaging. Similar to Chapter 3 we are able to carry out this function with high efficiencies and we demonstrate this for optical devices that imprint a phase profile on an incident beam for a specific circular polarization (SAM). The utility of working with a single polarization is that it we are able to reproduce the desired lens phase function with very high fidelity despite inevitable size variations between the designed and realized nanostructures. However, using the same underlying material system and fabrication process, the meta-lens can work for all incident polarizations[77].

4.1 Planar lenses

Metasurfaces are composed of sub-wavelength-spaced phase nanostructures at an interface, which impose tailorable phase shifts on incident light. These optical elements allow for unprecedented control over the properties of light[50,14] and have enabled a variety functionalities in a planar structure[18,104,105,100,106,101,107,108,109,10,20,110,111,112,50,113,21,114,115,116,117,118,67,119,84,39,14,19,87]. Optical components ranging from lenses, holograms and gratings to polarization-selective devices have been demonstrated using silicon-based[104,105,106,107,109,20,110,111,21,119,39] and plasmonic metasurfaces[18,101,113,117,118,84,14,87]. However, the high intrinsic losses of silicon and plasmonic materials in the visible range (400-700 nm) have prevented the realization of highly efficient metasurfaces in this region. While this challenge can be partially overcome by utilizing dielectric materials with a transparency window in the visible (e.g. GaP, SiN, and TiO_2), achieving full control over the phase of light requires precise, high-aspect-ratio nanostructures, which are in turn restricted by available nanofabrication methods. Recently we have developed a new approach based on titanium dioxide (TiO_2)[108] prepared by atomic layer deposition (ALD)[90] which enables fabrication of high-aspect-ratio metasurfaces that are lossless in the visible spectrum. Here, we demonstrate highly efficient meta-lenses at visible wavelengths (λ = 405 nm, 532 nm, and 660 nm) with efficiencies as high as 86%. They have high numerical apertures (NA) of 0.8 and are capable of focusing light into diffraction-limited spots. At their respective design wavelengths, these focal spots are about 1.5 times smaller than those from a commercially available, high NA objective (100× Nikon CFI 60, NA = 0.8). Imaging using these meta-lenses shows that they can yield sub-wavelength resolution, with image qualities comparable to that obtained by the commercial objective.

4.2 Planar lens design and fabrication

Typical high NA objectives consist of precision-engineered compound lenses which make them bulky and expensive, limiting their applications and hindering their integration into compact and cost-effective systems. Singlet planar lenses with high NA in the visible range are in particularly high demand due to their potential widespread applications in imaging, microscopy, and spectroscopy. Although visible planar lenses can be realized by diffractive components, high NA and efficiency are not attainable because their constituent structures are of wavelength scale that precludes an accurate phase profile. Figure 4.1A shows a schematic of a transmissive dielectric meta-lens. The building blocks of the meta-lens are high-aspect-ratio TiO_2 nanofins (Fig. 4.1, B to E). In order to function like a spherical lens, the phase profile ϕ_{nf} of the meta-lens needs to follow[18]:

$$\phi_{nf} = \frac{2\pi}{\lambda_d}\left(f - \sqrt{x^2 + y^2 + f^2}\right) \tag{4.1}$$

where λ_d is the design wavelength, x and y are the coordinates of the nanofins and f is the design focal length. This phase profile is imparted via rotation of each nanofin at a given coordinate (x, y) by an angle θ_{nf} (Fig. 4.1E). In the case of right-handed circularly polarized incident light, these rotations yield a phase shift $\phi_{nf}(x, y) = 2\theta_{nf}(x, y)$, accompanied by polarization conversion to left-handed circularly polarized light[120,99]. Thus each nanofin at (x, y) is rotated by an angle:

$$\theta_{nf} = \frac{\pi}{\lambda_d}\left(f - \sqrt{x^2 + y^2 + f^2}\right) \tag{4.2}$$

To maximize the polarization conversion efficiency, the nanofins should operate as half-waveplates[100,111,21,87]. This is achieved due to the birefringence arising from the asymmetric cross section of nanofins with appropriately designed height, width, and length (Fig. 4.1, C and D). Simulations using a commercial finite difference time domain (FDTD) solver (Lumerical Inc.) in Fig. 4.1F show that conversion efficiencies as high as 95% are achieved and that the meta-lens can be designed for a desired wavelength via tuning of nanofin parameters. The conversion efficiency is calculated as the ratio of transmitted optical power with opposite helicity to the total incident power.

Three distinct meta-lenses were fabricated with respective design wavelengths (λ_d) of 660

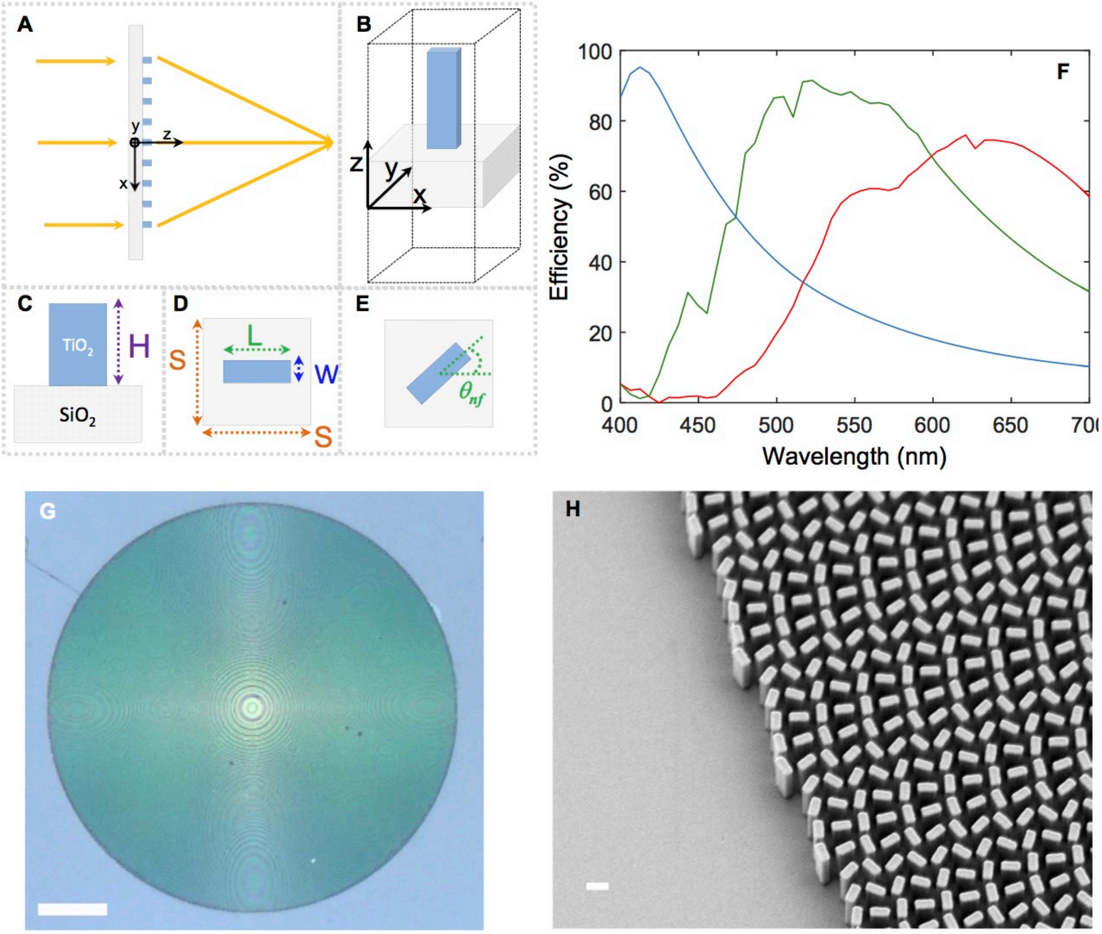

Figure 4.1: Design and fabrication of meta-lenses. (A) Schematic of the meta-lens and its building block, the TiO$_2$ nanofin. **(B)** The meta-lens consists of TiO$_2$ nanofins on a glass substrate. **(C,D)** Side- and top-views of the unit cell showing height H, width W, and length L of the nanofin with unit cell dimensions $S \times S$. **(E)** The required phase is imparted by rotation of the nanofin by an angle θ_{nf} according to the geometric Pancharatnam-Berry phase. **(F)** Simulated polarization conversion efficiency as a function of wavelength. This efficiency is defined as the fraction of the incident circularly polarized optical power that is converted to transmitted optical power with opposite helicity. For these simulations, periodic boundary conditions are applied at the x- and y-boundaries, and perfectly matched layers (PMLs) at the z-boundaries. For the meta-lens designed at $\lambda_d = 660$ nm (red curve), nanofins have $W = 85$ nm, $L = 410$ nm, and $H = 600$ nm with center-to-center spacing $S = 430$ nm. For the meta-lens designed at $\lambda_d = 532$ nm (green curve), nanofins have $W = 95$ nm, $L = 250$ nm, and $H = 600$ nm with center-to-center spacing $S = 325$ nm. For the meta-lens designed at $\lambda_d = 405$ nm (blue curve), nanofins have $W = 40$ nm, $L = 150$ nm, and $H = 600$ nm with center-to-center spacing $S = 200$ nm. (G) Optical image of the meta-lens designed at the wavelength of 660 nm. Scale bar: 40 μm. (H) Scanning electron microscope micrograph of the fabricated meta-lens. Scale bar: 300 nm.

nm, 532 nm, and 405 nm. All of these meta-lenses have the same diameter of 240 μm and a focal length of 90 μm yielding a NA = 0.8. The fabrication process uses electron beam lithography to create the lens pattern in the resist (ZEP 520A). The thickness of the resist is the same as the designed nanofin height, H, and ALD is subsequently used to deposit amorphous TiO_2 onto the developed resist. Amorphous TiO_2 is chosen because it has low surface roughness, no absorption at visible wavelengths, and a sufficiently high refractive index ($n \approx 2.4$). Due to the ALD process being conformal, a deposition thickness of at least $W/2$ (where W is the nanofin width) is required to produce void-free nanofins[108]. However, the deposition also leaves a TiO_2 film of equal thickness on top of the resist, which is then removed by controlled blanket reactive ion etching. Finally, the remaining electron beam resist is stripped and only high-aspect-ratio nanofins remain. Figure 4.1, G and H, show optical and scanning electron microscope (SEM) images of the fabricated meta-lens, respectively. Additional SEM micrographs of the meta-lens are shown in Fig. C.1, Appendix C. Because the geometrical parameters of the nanofins are defined by the resist rather than top-down etching, high-aspect-ratio nanofins with 90° vertical sidewalls are obtained. It is important to note that achieving these atomically smooth sidewalls is very challenging with a conventional top-down approach (e.g. lithography followed by dry etching) since inevitable lateral etching results in surface roughness and tapered/conical nanostructures.

4.3 Characterizing meta-lens performance.

The meta-lenses' focal spot profiles and efficiencies were measured using the experimental setup shown in Fig. C.2. Figure 4.2A shows a highly symmetric focal spot that is obtained for the meta-lens at its design wavelength $\lambda_d = 660$ nm. The vertical cut of the focal spot is also shown in Fig. 4.2G with a diffraction-limited full-width at half-maximum (FWHM), $\lambda/2NA$, of 450 nm. Figure 4.2, B and H, show the focal spot of the meta-lens designed at the wavelength of 532 nm and its corresponding vertical cut. Moreover, this meta-lens design can be extended to the shorter wavelength region of the visible range, which is of great interest in many areas of optics such as lithography and photo-luminescence spectroscopy. Figure 4.2C depicts the intensity profile of the focal spot from the meta-lens designed at the wavelength $\lambda_d = 405$ nm with a FWHM of 280 nm (Fig. 4.2I). Although this wavelength is very close to the band gap of TiO_2, $\lambda_g = 360$ nm, the absorption loss is still negligible[108].

In order to compare the performance of our meta-lenses with a commercially available lens, we selected a state-of-the-art Nikon objective. This objective has the same NA as our meta-lenses (0.8) and is designed for visible light. Focal spot intensity profiles of the objective at wavelengths of 660 nm, 532 nm, and 405 nm were measured using the same set-up in Fig. C.2 (see Fig. 4.2D to F). A comparison of the corresponding focal spot cross sections in Fig. 4.2, G to I, and Fig. 4.2, J to L, reveals that the meta-lenses provide smaller (about 1.5 times) and more symmetric focal spots. This can be understood as conventional high NA objectives are designed to image under broadband illumination. That is, wavefront aberrations need to be corrected for multiple wavelengths over a range of angles of incidence to meet industry standards for the required field of view. This is typically implemented by cascading a series of precisely aligned compound lenses. Fabrication imperfections in each individual optical lens and residual aberration errors, particularly spherical aberration, result in a focal spot size larger than theoretical predictions. In contrast, our meta-lens is designed to have a phase profile free of spherical aberration for normally incident light which results in a diffraction-limited spot at a specific design wavelength[121]. For example, the theoretical root mean squares of the

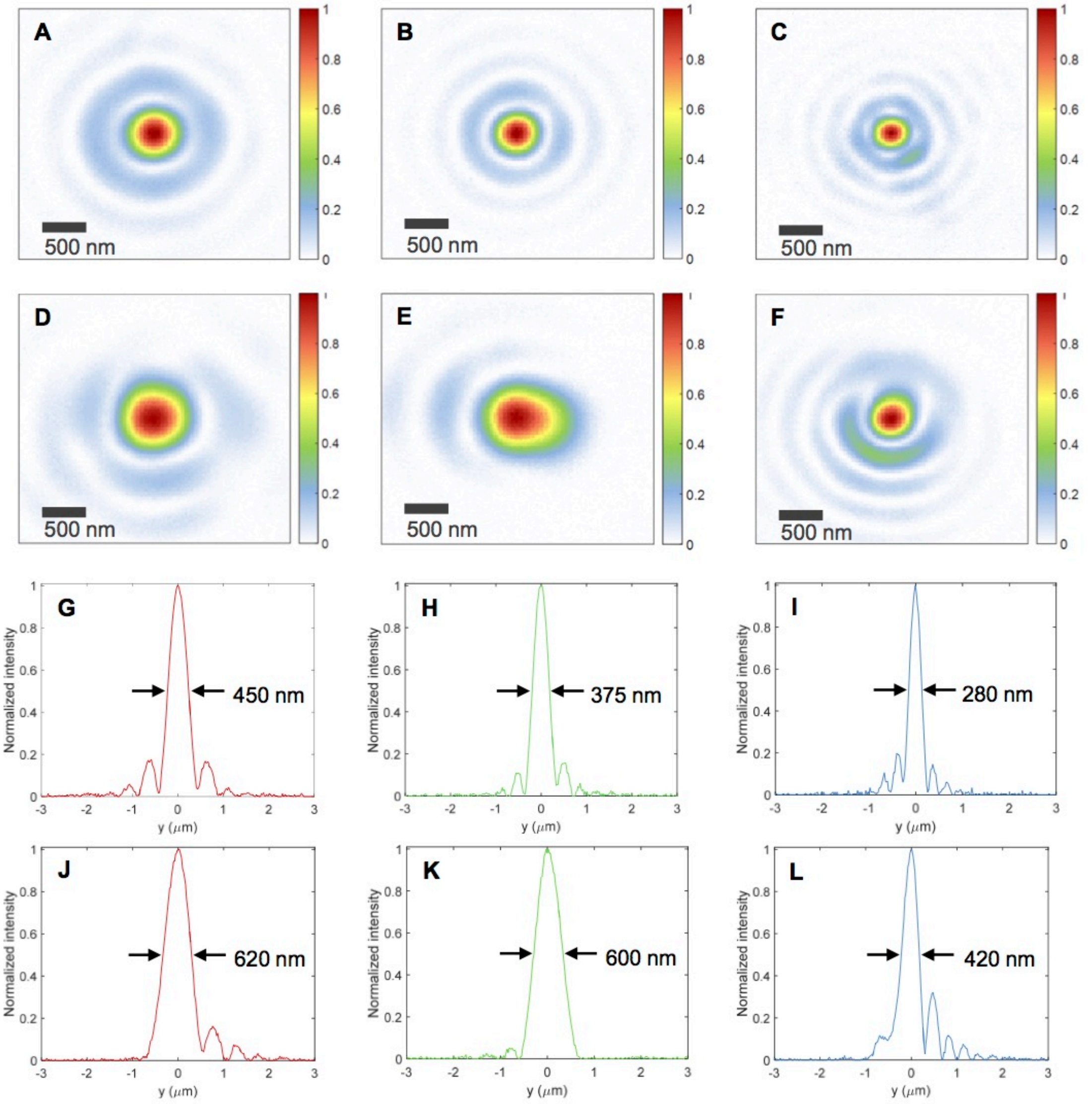

Figure 4.2: Diffraction-limited focal spots of three meta-lenses ($\mathrm{NA} = 0.8$) and comparison with a commercial objective. **(A-C)** Measured focal spot intensity profile of the meta-lens designed at (A) $\lambda_d = 660$ nm, (B) $\lambda_d = 532$ nm, and (C) $\lambda_d = 405$ nm. **(D-F)** Measured focal spot intensity profiles of the objective ($100\times$ Nikon CFI 60, $\mathrm{NA} = 0.8$) at wavelengths of (D) 660 nm, (E) 532 nm, and (F) 405 nm. **(G-I)** Corresponding vertical cuts of the meta-lenses' focal spots. Meta-lenses designed at wavelengths of 660 nm, 532 nm, and 405 nm have full-width at half-maximums $\mathrm{FWHM} = 450$ nm, 375 nm, and 280 nm, respectively. The symmetric beam profiles and diffraction-limited focal spot sizes are related to the quality of the fabricated meta-lenses and accuracy of the phase realization. **(J-L)** Corresponding vertical cuts of the focal spots of the objective, at wavelengths of (J) 660 nm (K) 532 nm, and (L) 405 nm. FWHMs of the focal spots are labeled on the plots. These values are 1.5 times larger than those measured for the meta-lenses.

wave aberration function (WAFRMS) for the meta-lenses designed for 405 nm, 532 nm, and 660 are 0.049λ $0.060\lambda$and 0.64λ respectively. These values are very close to the condition for a perfect spherical wavefront[121]. We also calculated the Strehl ratio from the measured beam profiles for the three meta-lenses at their design wavelengths and found that they are close to 0.8 (see Appendix C and Fig. C.3), consistent with the observed diffraction-limited focusing. In addition, due to the use of the geometric phase, the phase profile of the meta-lens is only dependent on the rotation of the nanofins. This is controlled with very high precision as is characteristic of electron beam lithography. Alternatively, other high throughput lithography methods such as deep-UV can provide similar fabrication accuracy.

It is important to note that although the meta-lenses were designed at specific wavelengths, we still observe wavelength-scale focal spots at wavelengths away from the design. For example, for the meta-lens designed at $\lambda_d = 532$ nm, we measured focal spot sizes of 720 nm and 590 nm at wavelengths of $\lambda = 660$ nm and 405 nm , respectively (Fig. C.4). The broadening of the focal spot with respect to the theoretical diffraction-limited values comes from chromatic aberration since metasurfaces are inherently dispersive. Chromatic aberrations in our meta-lens are more pronounced than the lenses based on refractive optics, resulting in a wavelength-dependent focal length (Fig. C.5A). This is generally not an issue for laser-related imaging, microscopy, and spectroscopy because monochromatic sources with narrow linewidths are used. For example, in Raman microscopes/spectrometers, a 532 nm laser with a linewidth of a few picometers is common. In this case, the linewidth-induced broadening of the focal spot size and change in focal length is negligible.

We also measured the focusing efficiency of the meta-lenses. As shown in Fig. 4.3A, the meta-lens designed at $\lambda_d = 660$ nm has a focusing efficiency of 66% which remains above

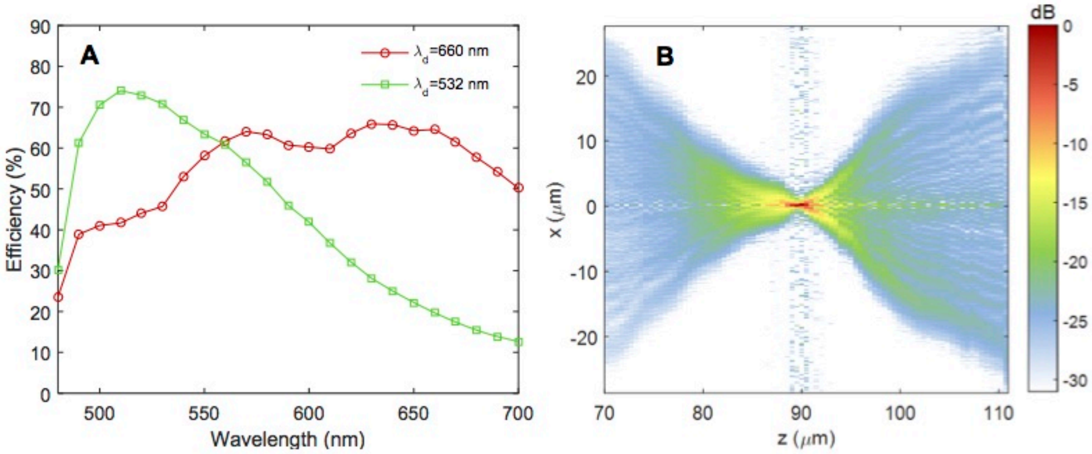

Figure 4.3: Characterization of the meta-lenses. (A) Measured focusing efficiency of the meta-lenses designed at wavelengths of 660 nm and 532 nm. **(B)** Intensity distribution in dB of the $x - z$ plane showing the evolution of the beam from 20 μm before and 20 μm after the focus. This measurement was performed on the meta-lens designed at $\lambda_d = 532$ nm. The wavelength of incident light was 532 nm.

50% in most of the visible range. Figure 4.3A also shows the measured focusing efficiency of the meta-lens designed at $\lambda_d = 532$ nm. This meta-lens has a focusing efficiency of 73% at its design wavelength. In addition, we measured the beam intensity profile of this meta-lens in the $x - z$ cross-section within a 40 μm span around the focal point (Fig. 4.3B). Details of this measurement are discussed in the Appendix C (35) (see Fig. C.2 and Appendix C). The negligible background signal not only demonstrates excellent phase realization, where the beam converges to a diffraction-limited spot, but also shows the high conversion efficiency of each nanofin. For the meta-lens designed at the wavelength of 405 nm, a measured focusing efficiency of 86% is achieved. The latter measurement was done using a diode laser as the shortest wavelength that our tunable laser can provide was 470 nm. All of the efficiency measurements were performed using right circularly polarized incident light. However, the polarization sensitivity of the design can be overcome by implementing the phase profile using circular cross section nanopillars in which the phase is controlled via changing their diameters.

4.4 Imaging demonstration

In order to demonstrate the use of our meta-lens for practical imaging, we fabricated a meta-lens with diameter D = 2 mm and focal length f = 0.725 mm giving NA = 0.8. First, we characterized the imaging resolution using the 1951 United States Air Force (USAF) resolution test chart as the target object. The measurement configuration is shown in Fig. C.6. Figure 4.4A shows the image formed by the meta-lens. The light source was a tunable laser set at 530 nm with a bandwidth of 5 nm. Because the resulting image was larger than our CCD camera, we projected the image onto a translucent screen and took its photo with a Canon digital single-lens reflex (DSLR) camera. The smallest features in this object are lines with widths of 2.2 μm and center-to-center distances of 4.4 μm (the bottom element in the highlighted region). A similar image quality is achieved at wavelengths covering the visible spectrum (Fig. C.7). Images of the smallest features were taken with a CCD camera shown in Fig. 4.4, B to E, at wavelengths of 480 nm, 530 nm, 590 nm, and 620 nm, respectively. It is clear that the meta-lens can resolve these micrometer-sized lines. We repeated a similar experiment using a Siemens star target and showed that all features can be resolved over the whole visible range (Fig. C.8). As mentioned previously, the focal length of the meta-lens varies as the wavelength changes resulting in different levels of magnification (Fig. C.5B). In our experimental setup, we used the meta-lens together with a tube lens (f = 100 mm) giving a magnification of 138× (100/0.725) at 530 nm. For wavelengths of 480 nm, 590 nm, and 620 nm, magnifications of 124×, 152×, and 167× are obtained, respectively, by comparing the ratio of the image sizes formed on the camera to the known physical size of the USAF test object.

To characterize the effects of chromatic aberration, we imaged the same object at 530 nm

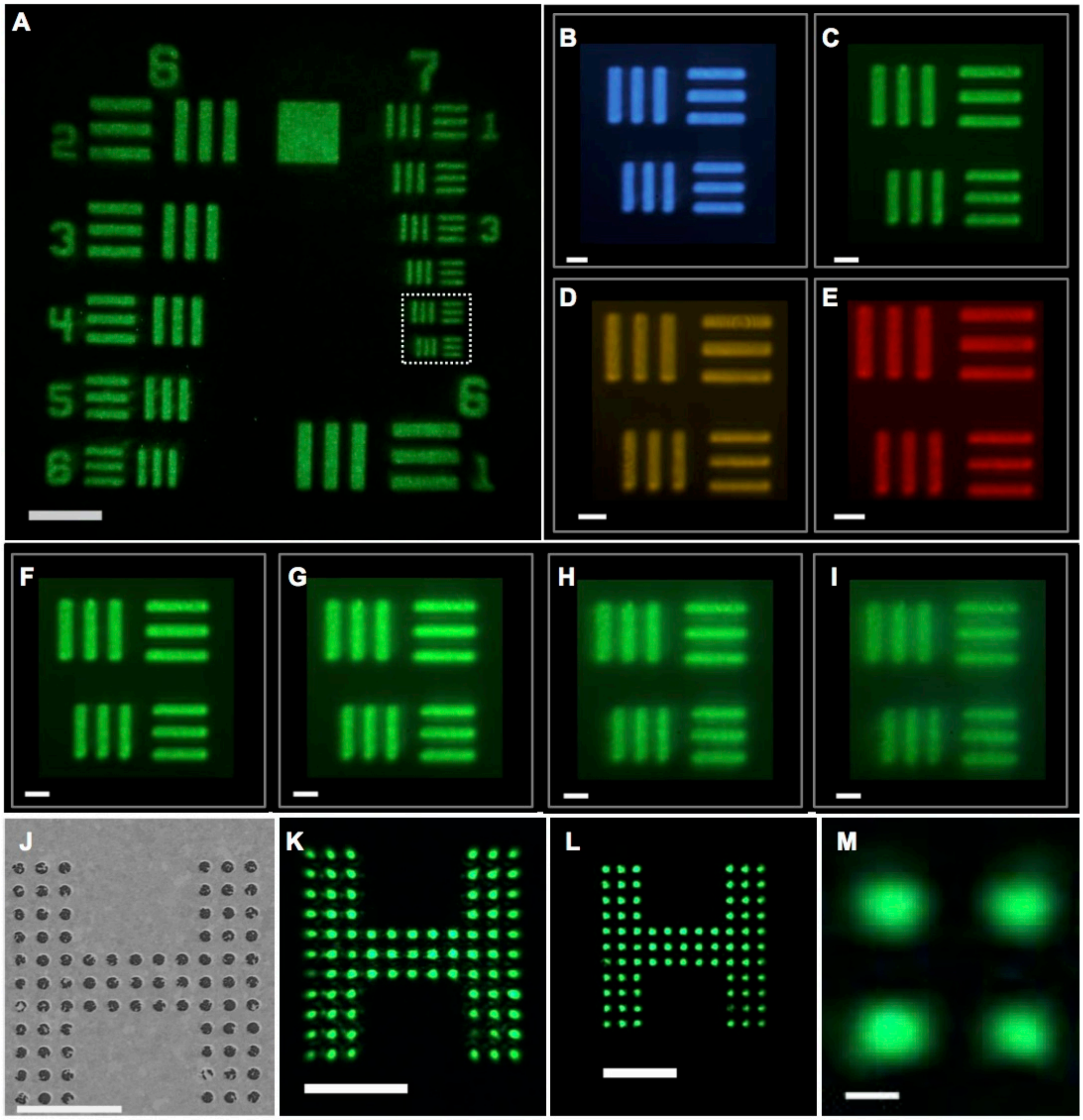

Figure 4.4: Imaging with a meta-lens designed at $\lambda_d = 532$ nm with diameter $D = 2$ mm, and focal length $f = 0.725$ mm. **(A)** Image of 1951 USAF resolution test chart formed by the meta-lens taken with a digital single-lens reflex (DSLR) camera. Laser wavelength is set at 530 nm. Scale bar: 40 μm. **(B-E)** Images of the highlighted region in (A) at wavelengths of (B) 480 nm, (C) 530 nm, (D) 590 nm, and (E) 620 nm. Scale bar: 5 μm. **(F-I)** Images of the highlighted region in Fig. 4A at a center wavelength of 530 nm and with different bandwidths: (F) 10 nm, (G) 30 nm, (H) 50 nm, and (I) 100 nm. Scale bar: 5 μm. **(J)** Nanoscale target prepared by focused ion beam. The gap between neighboring holes is 800 nm. **(K)** Image of target object (Fig. 4J) formed by the meta-lens. **(L)** Image of target object formed by the commercial state-of-the-art objective. Scale bar: 10 μm (J- L). **(M)** Image formed by the meta-lens shows that holes with sub-wavelength gaps of 480 nm can be resolved. Scale bar: 500 nm.

without changing the distance between the meta-lens and the object while varying the bandwidth of the source from 10 nm to 100 nm (the limit of our tunable laser). These results are shown in Fig. 4.4, F to I. Although the quality of the image slightly degrades from increasing the bandwidth, the smallest features are still resolvable even at the maximum bandwidth of 100 nm. Finally, for comparison of the imaging quality to that of a conventional objective, we fabricated a H-shaped object composed of arrays of holes with gaps of $\sim$ 800 nm using focused ion beam (FIB). An SEM micrograph of the object is shown in Fig. 4.4J. The image formed by the meta-lens (Fig. 4.4K) has comparable quality to the one formed by the 100× Nikon objective (Fig. 4.4L) with the same NA = 0.8. The change in the image sizes comes from the difference in the magnification of the imaging systems. We also tested the resolution limit of our meta-lens: four holes with sub-wavelength gap sizes of $\sim$ 450 nm can be well resolved (Fig. 4.4M). This value agrees with the measured modulation transfer function (MTF) of our meta-lens (Appendix C, Fig. C.9).

4.5 Conclusion

The demonstrated visible-range meta-lenses using TiO_2 with NA = 0.8 and efficiencies as high as 86% show that they are able to provide diffraction-limited focal spots at arbitrary design wavelengths, which make them ideal devices for use in optical lithography, laser-based microscopy, and spectroscopy. Providing a magnification as high as 170× and capable of resolving structures with sub-wavelength spacing, the compact configuration of our meta-lenses can enable portable/handheld instruments for many applications. Although our meta-lenses are subject to chromatic aberrations, the latter can be corrected with approaches such as dispersive phase compensation demonstrated in[104,112]. The single-layer lithographic fabrication of the meta-lenses can make use of existing foundry technology (deep UV steppers) used in the manufacturing of integrated circuits, which is crucial for high throughput.

5

Spin-to-orbital angular momentum conversion in dielectric metasurfaces

The use of the spin angular momentum of light to couple to another degree of freedom (propagation direction, spatial phase or intensity distribution) has been detailed in Chapters 2 through 4. This chapter deals with a particularly interesting case of utilizing the SAM of light, so called spin-to-orbital angular momentum conversion (SOC). That left and right circularly polarized light possesses SAM has been known since the Poynting derived this result in 1909.

Only much more recently in 1992 was it shown that light also possesses orbital angular momentum (OAM). In SOC, the incident SAM of light is converted into OAM. Traditionally, these devices have been fabricated through ‘mechanical rubbing’ of liquid crystal droplets on a glass substrate. By rotating the orientation of the liquid crystal axes, the desired SOC can be carried out and these devices have found applications in stimulated-emission-depletion microscopy, quantum optics, optical forces and optical information. These liquid crystal based devices, however, are limited in several senses. First they tend to produce distorted and aberrated intensity distributions in the output beam. Second, only the simplest cases of beams with orbital angular momentum values of between $1\hbar$ and $2\hbar$ can be produced.

In this chapter, we expand on the functionality of the liquid crystal devices. By making use of the high fidelity fabrication technique for dielectric metasurfaces that we introduced in Chapter 3, we are able to, in a simple repeatable manner, produce devices with high values of orbital angular momentum which are particularly useful for quantum optics. Additionally, we demonstrate a device that is capable of producing two different values of orbital angular momentum for a single input polarization, a function that is not possible with previous device designs. While this initial demonstration provides a useful set of devices on its own, in Chapter 6 we present theoretically and demonstrate experimentally a generalization of the concept of SOC.

5.1 Spin and orbital angular momentum of light

A helical mode of light is an optical field whose azimuthal phase evolution around the propagation axis (z) has the form $\exp(i\ell\phi)$, ϕ being the azimuthal coordinate and ℓ (an integer) called topological charge of the beam. The wavefront of a helical mode of charge ℓ is constituted by $|\ell|$ helical surfaces twisted together, whose handedness is set by the sign of ℓ, resulting in a topological singularity (optical vortex), along the propagation axis[34]. Such vortex beams carry an average of $\ell\hbar$ orbital angular momentum (OAM) per photon[26,122]. Additionally, circularly polarized modes carry a spin angular momentum of $\pm\hbar$ per photon, depending on the polarization handedness. Such beams are central to the field of singular optics[123] and have found numerous applications such as optical trapping[124] where the angular momentum is a powerful manipulation tool to spin the trapped object[38,125] as well as to control its orientation[126].

The characteristic screw-type dislocation of a helical mode can be imposed on the wavefront of a propagating beam by means of different devices, for example, pitch-fork holograms[127,128] or cylindrical and axicons lenses and reflectors[129,130]. Additionally, helical modes can be also produced by exploiting the geometrical phase (also known as Pancharatnam-Berry (PB) phase)[97,131,99], to create inhomogeneous gratings for the wavefront reshaping[132,133]. In these spin-orbital angular momentum converters (SOC) the OAM of the vortex beam is coupled with the spin angular momentum of the illuminating light: switching the handedness of the illuminating beam polarization (spin angular momentum) flips the handedness of the vortex (orbital angular momentum). Locking the OAM to the spin angular momentum has unique applications in quantum computing and communications, allowing high dimensionality encoding of quantum units[134] and fast switching related to the modulation of the incident polarization of light[135,136,137].

More recently, the wavefront manipulation allowed by metasurfaces[14] has been used to produce a variety of PB optical elements, e.g., lenses[138,21] and vortex beam generators in the near-infrared[139,19]. Similar approaches have allowed working with visible light although with low transmission efficiency in the bluest part of the spectrum[140,141,142,143,144,145]. To date, the most versatile spin-orbital angular momentum converters for visible light are the liquid crystal devices developed by Marrucci et al. in 2006 and known as q-plates[41]. They have found numerous applications in quantum optics although they are limited by degradation effects and resolution in defining the extent of the topological singularity region[146,147,148,149,150].

5.2 Nanostructured dielectric spin-to-orbital angular momentum converter

In order to describe some general features of a SOC based on PB phase, it is useful to define the orientation angle $\alpha(x, y)$ of the optical axis (fast or slow) of each element of the device in the transverse plane ($x - y$ plane). Regardless of the constituents, if each element imposes a π phase delay between the field transverse components, an incident uniform left-circularly polarized beam $E_{\text{in}} = [1, i]$ is turned into the beam $E_{\text{out}} = \exp(i2\alpha)[1, i]$ that is right-circularly polarized with a geometrical phase 2α in the transverse plane. Analogously to what was reported in the first description of a q-plate[41], if the azimuthal variation of the angle α in the PB-device follows the relation $\alpha = q\phi + \alpha_0$ the incident wave front is then turned into a helical wavefront composed of $|2q|$ intertwined helical surfaces which carries an orbital angular momentum , where the sign depends on the handedness of the incident light polarization (α_0 is a constant). For instance, if $q = 1$ and the incident light is left-circularly polarized (spin angular momentum of $+\hbar$), the out coming light is right-circularly polarized (spin angular momentum of $-\hbar$) with an OAM per photon of $2\hbar$ and zero net angular momentum transferred to the device (Fig. 5.1 (a)). For $q \neq 1$ there will be a net angular momentum exchange with the PB-device to preserve the total angular momentum of the system.

In our devices, the constitutive elements (nanofins) are subwavelength dielectric resonators[105,16,111,151]

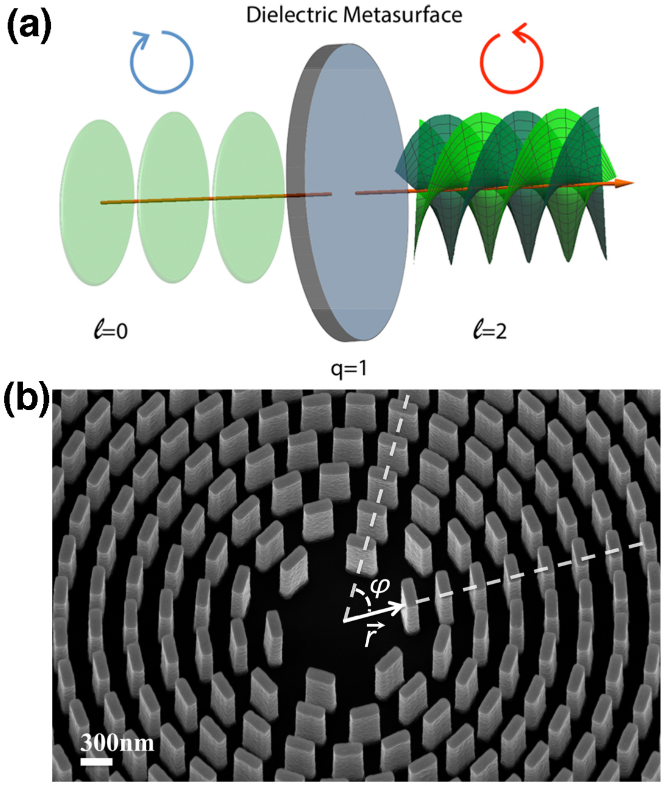

Figure 5.1: Operation and structure of the dielectric spin-orbit-converter(a) Schematic of the working principle of a spin-orbital angular momentum converter. A left circularly polarized beam with plane wavefront is turned into a right circularly polarized helical mode. In this representation the helical mode has a topological charge equal to 2, as the wavefront is composed of two intertwined helices. **(b)** Angled-view SEM image of one of our devices ($q = 1$) showing the orientation of the TiO$_2$ nanofins on the glass substrate, φ is the azimuthal angle and $|r|$ is the distance from the center.

made of TiO_2[108] (Appendix D). Each nanofin is 250 nm long, 90 nm wide and 600 nm tall. The radial distance between two fins is of 325 nm (Fig. 5.1 (b)). Figure 5.2 (a) and (b) show the scanning electron microscope (SEM) images of the devices with $q = 0.5$ and $q = 1$ ($\ell = 1$ and $\ell = 2$, respectively). The insets of Fig. 5.2(a) and (b) show the devices as imaged in cross-polarization. The first polarizer sets the incident polarization direction. Each nanofin works as a half waveplate for the incident light: the nanofin rotates the incident polarization according to its orientation. The cross polarizer after the metasurface filters out the polarization opposite to that of the light incident on the metasurface thus creating intensity lobes in the camera image.

In order to fully characterize the vortex beams, we used a Mach-Zehnder interferometer as shown in Figure 5.2(c). In this configuration, the source beam (a solid-state laser emitting at 532 nm with power lower than 2 mW) is split in two linearly polarized beams by means of a 50/50 beam splitter. Half of the light (upper arm of the interferometer) passes through a quarter waveplate (QWP1) to produce a circularly polarized beam incident on the device. The vortex beam created by the device then passes through a polarization filter made of a quarter waveplate (QWP2) and a linear polarizer (LP2) in cross-polarization with respect to QWP1. This polarization filter is used to eliminate non-converted light passing through the device (see Appendix D for discussion). The reference beam propagates in the lower arm of the interferometer and passes through a half waveplate (HWP) to acquire the same polarization of the helical mode in port 1 (as well as in port 2). This maximizes the intensity modulation (thus the contrast) in the interference pattern.

Figure 5.2(d) shows the intensity distribution of a vortex beam with $|\ell| = 1$ generated by the device in Fig. 5.2(a), in a transverse plane (plane of the camera at port 1 of the setup)

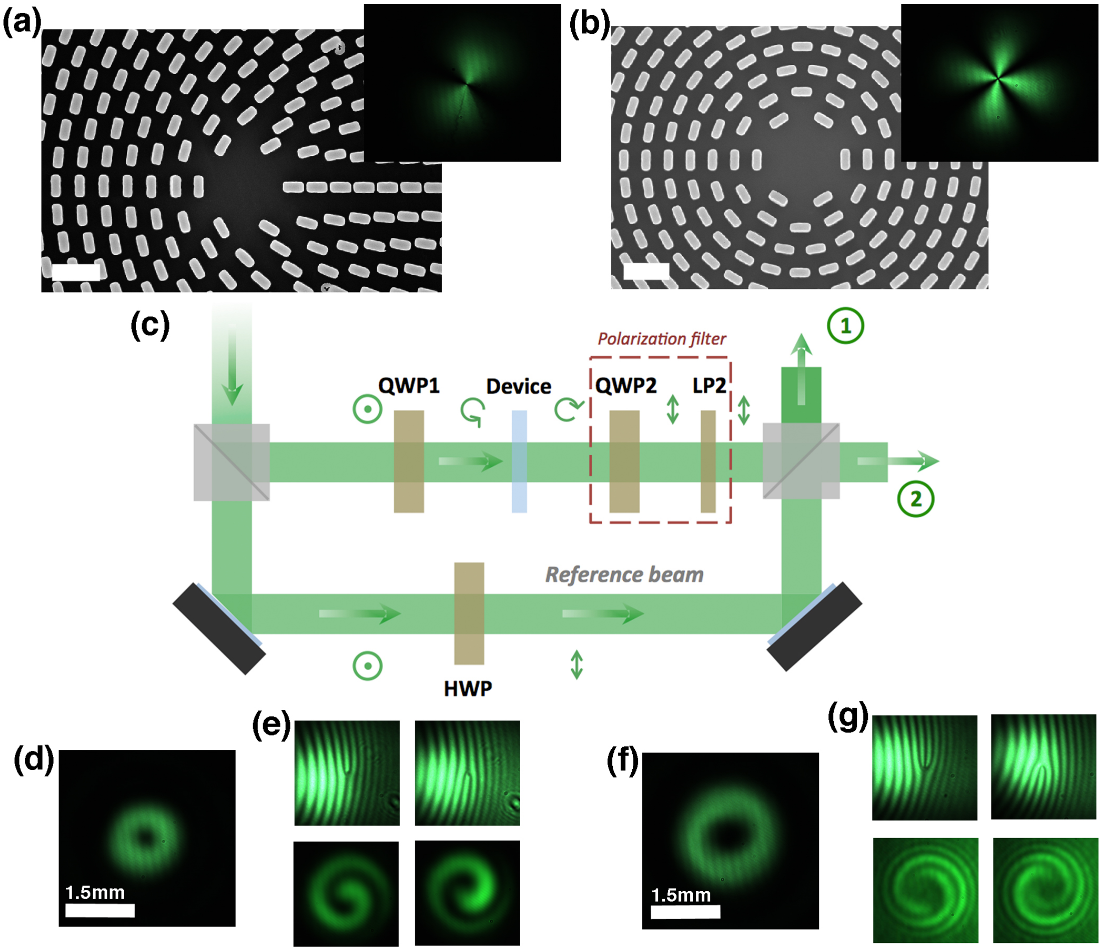

Figure 5.2: Demonstration of spin-orbit-conversion for $q = 0.5$ and $q = 1$. **(a, b)** Scanning electron microscope image of TiO_2-based spin-orbital angular momentum converters with and respectively (scale bar = 650 nm). The insets show the devices observed in cross-polarization at the design wavelength of 532nm. **(c)** Sketch (top view) of the interferometric setup used to characterize the devices. The interference of the helical mode and the reference beam was monitored at port 1 by means of a CCD. The polarization state of the beam after each optical element is sketched. The laser polarization is linear and perpendicular to the optical table. Light becomes circularly polarized after the first quarter waveplate (QWP1). The helical mode generated by the device is circularly polarized with opposite handedness. The helical mode after the polarization filter (QWP2 followed by LP2) is linearly polarized parallel to the optical table. The reference beam in the lower arm of the interferometer becomes also linearly polarized parallel to the optical table after passing through a half waveplate (HWP) that rotates the polarization direction by 90°. **(d)** Transverse intensity distribution of the vortex beam generated by the device of Fig. 2 (a). This beam has a topological charge equal to 1. **(e)** Interference patterns obtained with tilted reference beam (pitchforks) or collinear reference beam (spirals) in the setup of Figure 2 (c). The flipped features result from opposite handedness of the beam that illuminates the device. **(f, g)**, Same as (d) and (e) for the device in Figure 2 (b)

at about 45 cm from the device exit plane, when the reference beam is blocked. Figure 5.2(f) shows the intensity profile for the vortex beam with $|\ell| = 2$ generated by the device of Figure 5.2(b). The four insets of Figure 5.2(e) and (g) show the intensity patterns produced in the plane of the camera by interfering the vortex beam with the reference beam. Such interference experiments are widely used to reveal phase singularities[123]. The pitchfork-like interference is obtained when a vortex beam and a Gaussian beam interfere with an angle between their propagation axes, which sets the fringe spacing. If the vortex beam is collinear with the reference beam from the lower arm of the interferometer, a spiral is obtained as an interference pattern, with the number of arms equal to the topological charge of the vortex beam. The handedness of the incident circularly polarized light sets the orientation of the pitchforks and spirals.

Figure 5.3 shows how our approach can be used to produce optical vortices with higher values of topological charge, $|\ell| = 5$ (Fig. 5.3(a-d)) and $|\ell| = 10$ (Fig. 5.3(e-h)). Each individual device is 500 μm in diameter and all devices are on the same glass substrate of 1 inch diameter (Appendix D, Fig D.2). This allows mounting the device on standard opto-mechanical components and to select the desired topological charge just by translating the corresponding device into the laser beam path. Another important feature of our devices is related to the localization of the beam singularity. The fabrication process is based on atomic layer deposition (ALD) and electron beam lithography (EBL) (Appendix D). This guarantees high resolution and reproducibility, resulting in precise definition of the singularity region and improving the vortex beam quality. For example, the $q = 0.5$ device has a singularity region smaller than 3 μm.

In our devices we reached absolute efficiencies (the amount of light from the illuminating

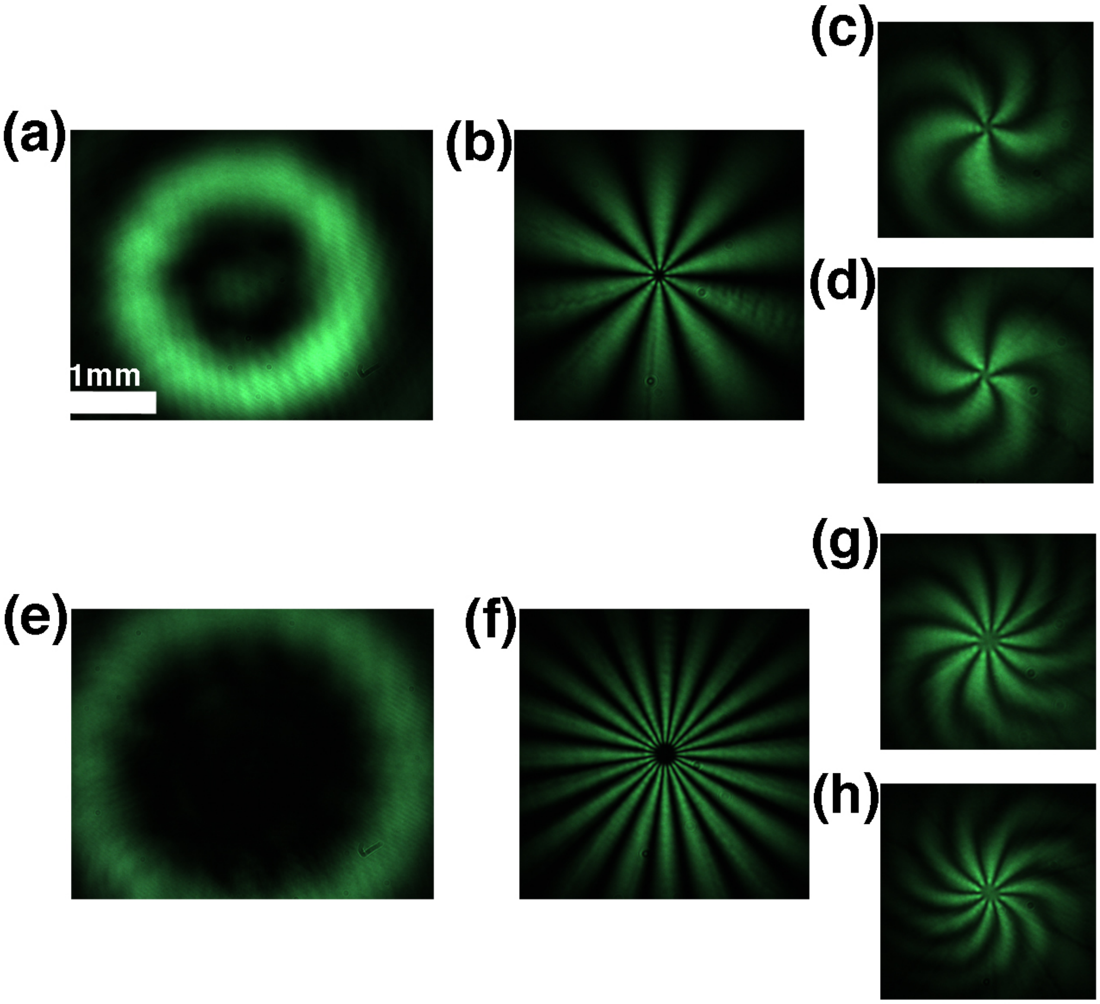

Figure 5.3: Higher order vortices from dielectric q-plates. **(a)** Transverse intensity profile of a beam with topological charge 5 generated by means of our $q = 2.5$ spin-orbital angular momentum converter. **(b)** The $q = 2.5$ device imaged in cross-polarization. **(c, d)** Images of the interference patterns obtained with a collinear reference beam (Figure 2 (c)) for incident left or right circular polarized light. **(e-h)** Same as for (a-d) for the topological charge 10 beam and the $q = 5$ device. Scale for (e) is same as shown in (a).

beam that is actually converted into the helical mode while also accounting for absorption and reflection from the device/substrate) of 60%. Since TiO_2 is ideally transparent at these wavelengths and the nanofins are only 600 nm in height, this measured efficiency is limited mainly due to reflections at the air-substrate and substrate-metasurface interfaces and error between the fabricated and designed nanofin dimensions. Thus this device provides a substantial improvement in efficiency as compared to previous metallic metasurface q-plate devices with conversion efficiencies of 8.4% at an operating wavelength of 780 nm[140]. The simulated phase delay between the $x-$ and $y-$component of the electric field and resulting conversion efficiency as a function of wavelength are shown in Fig. D.5 and while the efficiencies we reported here were for 532 nm illumination, high efficiencies can be achieved at any visible wavelength simply by re-optimizing the lengths and widths of the individual TiO_2 nanofins, as we showed in ref.[108]. Finally, the fact that these devices are fabricated using lithography and etching allows many devices with different topological charge to be placed on a single substrate—this is not easily-achievable with liquid crystal devices.

5.3 FRACTIONAL AND INTERLACED SPIN-TO-ORBITAL ANGULAR MOMENTUM CONVERTERS

As a further demonstration of the versatility of our approach, we designed a SOC that produces a vortex beam with fractional topological charge. This is possible when a non-integer phase discontinuity is introduced in the azimuthal evolution of the helical mode. In this case, Berry described the optical vortex as a combination of integer charge vortices with a singularity line in the transverse plane surrounded by alternating optical single charge vortices[152,153]. From a quantum optics point of view, the average angular momentum per photon has a distribution peaked around the nearest integer value of the topological charge and a spread proportional to the fractional part of the charge[33]. We fabricated a SOC producing a 6.5 topological charge vortex beam. Figure 5.4(a) shows the intensity distribution of the resulting helical mode at about 55 μm from the device plane (Fig. D.3 and Fig. 5.4(b) shows pitchfork-like interference obtained in the Mach-Zehnder configuration of Figure 5.2(c). The phase singularity line predicted for such vortices is evident. The interference pattern (Figure 5.4(b)) also shows the line of alternating vortices (single line pitchforks) along the singularity line. For half odd-integer values of the OAM, two helical modes with same OAM but phase singularities lines with a relative π orientation are orthogonal[153]. This has been used, for instance, to observe high-dimensional photon entanglement[154,155]. Our approach to SOC enables a new and unique feature, the generation of collinear beams from a single device with arbitrary and different OAM. In contrast, a detuned q-plate (i.e., a q-plate with phase delay not equal to π) can only produce a beam with OAM of 2q and a 0th order Gaussian beam with zero OAM, which is unconverted light.

To demonstrate this concept, we designed an interlaced $q = 2.5$ and $q = 5$ device (Figure 5.5(a)). Two metasurfaces with different azimuthal patterns are interleaved by placing the nanofins at alternating radii. Although they have different topological charges the beams emerge collinearly from the device, interfering in the plane transverse to the propagation direction. Figure 5.5(b) and (c) show the intensity patterns recorded in transverse planes (far from the device) for opposite handedness of the incident light. It is evident that the two interference patterns are flipped according to what is expected for beams with opposite topological charges. Figure 5.5(c) and (d) show the calculated interference patterns of two collinear helical modes of topological charges 5 and 10 with opposite handedness. These interference

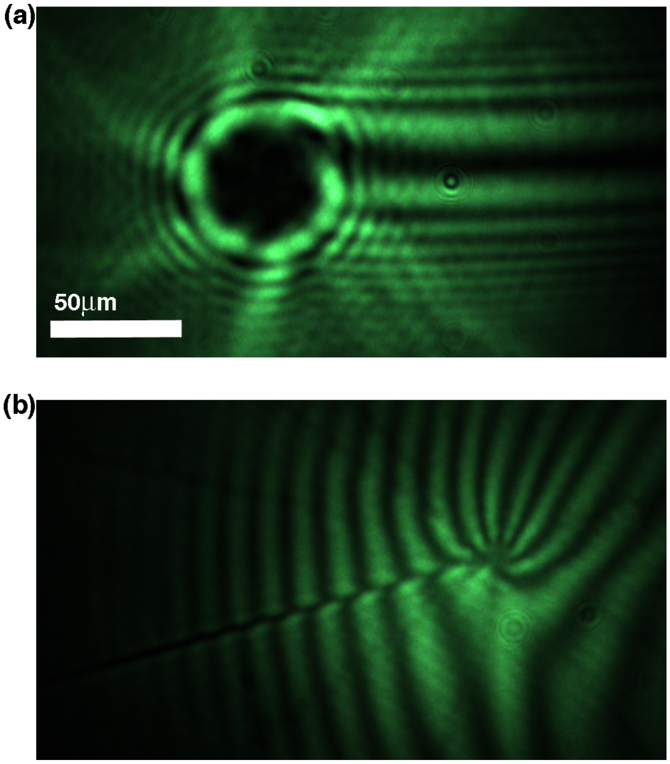

Figure 5.4: Fractional vortex from a dielectric q-plate. **(a)** Transverse intensity distribution of a beam with topological charge 6.5 at 55 μm from the device exit plane. **(b)** Interference pattern arising from the interference with a reference beam at oblique incidence. The resulting pitchfork pattern shows the singularity line surrounded by alternating single charge vortices, a characteristic feature of fractional helical modes. The direction of the singularity line in (a) and (b) is the same although in these figures they are on opposite directions due to the camera orientation during the experiment.

patterns are close to what we found experimentally if we assume for the charge 5 beam a Rayleigh range three times greater than for the charge 10 beam. In the calculations this accounts for the different divergence of the two experimental beams. While the interlaced designs allow for multiple values of OAM to be imprinted on a single beam, the measured efficiency for the interlaced device is 20%, which is less than the single topological charge. This drop in efficiency results from the spatial multiplexing of two devices?the period of each individual device is doubled leading to higher orders of diffraction.

It is important to note that each nanofin in our device has two interfaces, glass-TiO_2 and air-TiO_2. Illuminating one side or the other, as in Figure 5.5(f), does not alter the phase delays imposed by the nanofins (Appendix D) but only slightly affects light coupling into the latter, due to the different reflectance of the air-TiO_2 and glass-TiO_2 interfaces. We measured a small decrease ($< 5\%$) in the device efficiency when illuminating from the air-side, due to the larger refractive indices difference with TiO_2.

5.4 Conclusion

In the setup of Figure 5.5(f), the beams illuminating the sample from opposite interfaces have opposite handedness. The double-face characteristic of our devices together with the illumination configuration of Figure 5.5(f) allows one to simultaneously generate similar beams with opposite topological charges. This configuration was also used to obtain the intensity distributions of Figure 5.5(b) and (c) representing the helical modes at optical ports 3 and 2 respectively.

Although we limited our interlaced design to two collinear beams, it is possible to produce three or more collinear vortices simultaneously as well as $\pm\ell$ collinear vortices (Appendix).

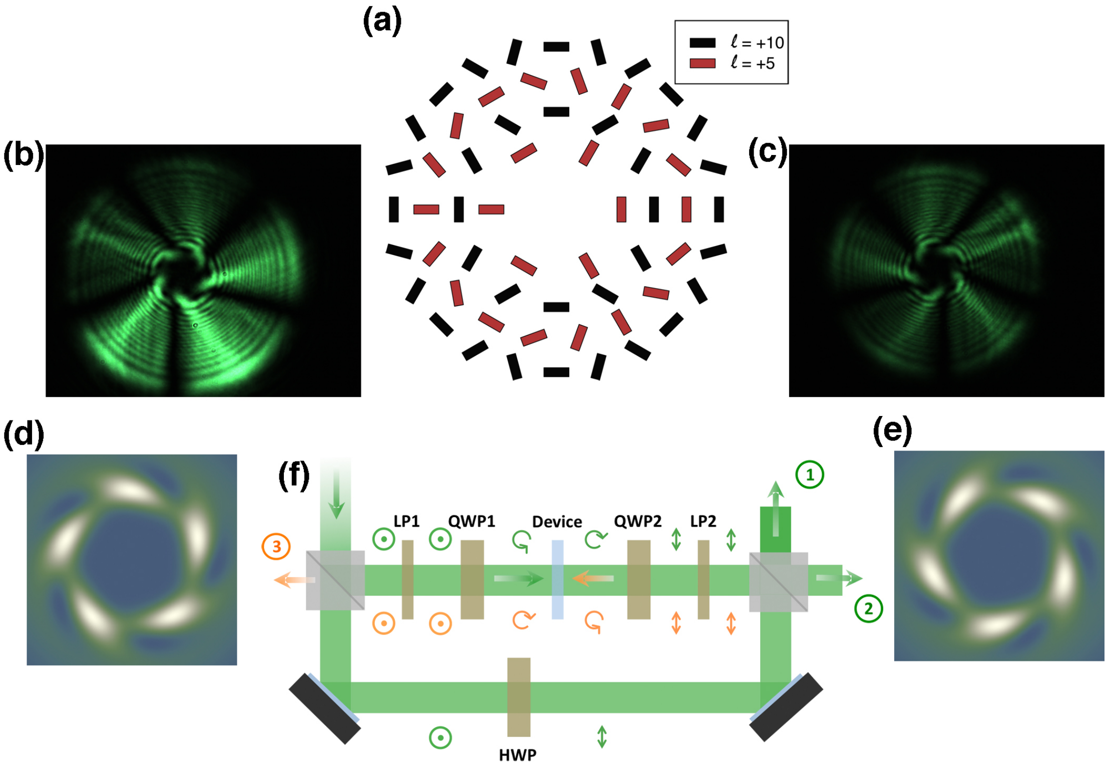

Figure 5.5: Generation of multiple vortices from a single metasurface. **(a)** Schematic of the nanofins azimuthal distribution in the inner part of metasurface device with interleaved patterns that generate collinear beams having topological charges $|\ell| = 5$ and $|\ell| = 10$. The device has a 500 μm diameter and contains more than 700 interleaved radial rows of nanofins. **(b-c)** Transverse intensity distributions of the light emerging from the metasurface for opposite handedness of the incident light. **(d, e)** Simulated intensity patterns for collinear 5 and 10 topological charge beams. **(f)** Sketch of the setup that allows illumination of the transparent devices from the glass and air side simultaneously with circularly polarized beams of opposite handedness. In this case, there are two light beams, whose power can be made equal by suitably balancing the two arms, circularly polarized with opposite handedness that simultaneously illuminate the device from opposite sides at normal incidence. In this configuration, the helical modes propagating towards optical port 2 and 3 have also opposite wave-front handedness. This setup was also used to obtain the intensity distributions of Fig. 5 (b) and (c).

This can find important applications in entanglement and quantum computing experiments. Moreover, the quantum description of a device simultaneously generating co-propagating vortex beams with different topological charges has never been investigated and represents a stimulating direction for future work. Finally, we expect good tolerance to heating since TiO_2 has an intensity damage threshold of 0.5 J/cm^2 in the femtosecond regime[156]; thus we envision using such devices for non-linear optics with pulsed lasers. We actually exposed one of our devices to a CW laser (532 nm wavelength) with a power of 1W over the device area for 5 hours without observing any change in the device efficiency and beam quality.

We have demonstrated that the interaction of light with designer metasurfaces can lead to the generation of complex wavefronts characterized by arbitrary integer and fractional topological charges and co-propagating beams with different orbital angular momenta. Our approach represents a major advance in design with respect to liquid crystals devices and as such has considerable potential in several areas of optics and photonics, ranging from quantum information processing to optical trapping and complex beam shaping.

6

Arbitrary spin-to-orbital angular momentum conversion of light

As we pointed out in Chapter 5, spin and orbital angular momentum are fundamental quantities of light. The transfer between these two quantities gives rise to many physical phenomena and applications in classical and quantum optics. Two key caveats of devices that rely purely on varying the rotation angle between identical nanostructures (like those in Chapter 5), is that the two design polarization states of the device must be left and right circular polarization and the output values of orbital angular momentum are not independent (they are conjugate values $\ell = \pm 2q\hbar$). Thus the previous spin-orbit converters (SOC), first demonstrated in 2006 by Marruci *et al*[41,136] only act on two out of an infinite set of input states and no single device has provided controllable, arbitrary coupling between the spin and orbital angular momentum of light.

In this chapter, we demonstrate how arbitrary coupling between spin and orbital angular momentum of light can be achieved by design of a single optical element, leading to arbitrary states of total angular momentum. This design process, the implementation of the device and the underlying physics are a culmination of the work detailed in all previous chapters. Specifically, we again utilize the fabrication process that we presented in Chapter 3, as it provides us with an ideal way to transfer an arbitrary metasurface design into a high efficiency device for visible wavelengths. The theory introduced in this chapter provides a generalization of the devices in Chapter 5, which we discuss below and prove in Appendix E. Even in the case of the plasmonic-spin-Hall effect, introduced in Chapter 2, the coupling of spin to propagation direction was conjugate for left and right circular polarization. Thus this demonstration is also a generalization for all types of spin-orbit-interactions of light. For the remainder of this chapter, we experimentally verify the operation of this theory for two cases: the transfer from left- and right-circularly polarized light to two independent values of orbital angular momentum, and for incident orthogonal elliptical polarizations in general. These devices allow us to create superpositions of total angular momentum states of light with independently controlled phases and amplitudes. The results presented here show a deep fundamental connection between SAM and OAM of light and may find applications in quantum and classical information.

6.1 Spin-to-orbit angular momentum conversion of light

Circularly polarized light carries spin angular momentum (SAM)[23] of $\pm\hbar$ per photon depending on the handedness, while the most general state of polarization (elliptical) is a superposition of ± 1 spin states. Electromagnetic fields with an azimuthal phase dependence of the form $\exp(i\ell\phi)$, where ℓ is any integer, carry orbital angular momentum (OAM)[26]. Beams with this azimuthal structure, known as helical waves or optical vortices, have ℓ discontinuities in the phase, which is undefined at the beam center, resulting in a 'doughnut' intensity profile[34]. In contrast to SAM, the OAM can take on any integer value from $-\infty$ to $+\infty$ corresponding to $\ell\hbar$ angular momentum per photon[157]. In analogy to atomic physics, a paraxial, circularly polarized, helical beam has been shown to carry a total angular momentum (TAM) of $J = (\sigma + \ell)\hbar$, where $\sigma = \pm 1$, per photon[26,158,159] .

In the more than 25 years since the discovery that light carries OAM[26], optical vortices have led to a deeper fundamental understanding of light as well as a number of potential applications due to the complex field distribution of helical beams and their infinite set of orthogonal basis states[160]. Classical applications include high capacity optical information transfer[161,30,162], optical forces and manipulation[163,38], super resolution imaging[36]. The quantum nature of the photon's OAM has also been exploited through entanglement[122,32] and allows for new quantum communication schemes with higher dimensional quantum states[164,165]. In general, one can generate beams with OAM through a variety of different techniques: laser mode conversion[166], forked holograms[167], spiral phase plates[168] and spatial light modulators. Such techniques rely on introducing a phase discontinuity in the wavefronts but generally establish no connection between the SAM and OAM of the beam.

In contrast, geometric phase optical elements provide a direct connection between the SAM and OAM of light[40]. These devices are composed of identical subwavelength-spaced halfwave plates with a spatially-varying orientation and are often referred to as q-plates[41] since they perform the transformations

$$|L\rangle \rightarrow \mathrm{e}^{i2q\phi}\,|R\rangle \tag{6.1}$$

and

$$|R\rangle \rightarrow \mathrm{e}^{-i2q\phi}\,|L\rangle \tag{6.2}$$

where the input SAM state (left or right circular polarization) is converted to an output TAM state of opposite spin and $\pm 2q\hbar$ OAM. This process is often referred to as spin-orbit-conversion (SOC) and it falls into a more general class of phenomena spin-orbit-interaction (SOI) of light, where the SAM degree of freedom couples to a spatial degree of freedom or propagation direction. In addition to providing a fundamental connection between the SAM and OAM of light, these devices have broadened the applications of angular momentum in light including direct generation of OAM from lasers[169] and new quantum devices[134]. However, due to the symmetry of the devices—only the rotation angles of the elements vary—all SOC demonstrated thus far have two inherent limitations. First, the output OAM states are not independent but are conjugate values ($\pm 2q\hbar$). Second, the mapping from SAM is limited to left- and right-circular polarization, which represent only two of an infinite set of possible polarizations. Even in the broader context of SOI of light, the coupling is generally conjugate for the two input polarizations[28].

Here, we demonstrate the design of an optical element that overcomes the above limitations by providing conversion from any orthogonal SAM states to independent OAM states. We implement this design using metasurfaces because of their ability to control both polarization and phase[16,17]. We stress, however, that this element can be implemented by any medium that allows both birefringence and orientation angle of the fast axis to vary spatially. We examine the full set of output states of the device and show that this technique provides a way to produce arbitrary superpositions of TAM states of light. To experimentally verify this new design, we demonstrate devices that map SAM to OAM for two cases. First we show that we can convert two circularly polarized beams of opposite handedness, into helical beams with independent values of OAM, a freedom not afforded by any previous device. We also demonstrate the conversion of arbitrary and orthogonal elliptical polarizations into two TAM states with independent values of OAM—the most general form of spin-to-orbit conversion. Because of its ability to map SAM to two arbitrary output TAM, we refer to this device as a *J-plate*.

6.2 DESIGN OF ARBITRARY SPIN-TO-ORBITAL ANGULAR MOMENTUM CONVERSION.

Figure 6.1A and B show a schematic of the generalized mapping we would like to perform with the J-plate element. We consider an incident paraxial beam in cylindrical coordinates (r, ϕ, z), propagating along the $+z$-direction. If the incident beam is in some arbitrary polarization state $|\lambda^+\rangle$ (Fig 6.1A), which in general is an arbitrary superposition of photon SAM states (circular polarizations), we require the device to perform the transformation

$$\left|\lambda^+\right\rangle \to \mathrm{e}^{im\phi} \left|\left(\lambda^+\right)^*\right\rangle \tag{6.3}$$

that is, the output polarization state has flipped handedness to $|(\lambda^+)^*\rangle$ indicated by the complex conjugate $*$[170], and the beam has acquired an azimuthally-dependent phase factor $\mathrm{e}^{im\phi}$, where m is any integer. Because of this azimuthal phase factor, the output beam has m helically-intertwined phase fronts resulting in $m2\pi$ phase discontinuities in a round-trip about the optical axis and an annular intensity profile (Fig. 6.1A, right inset). Thus, the beam acquires $m\hbar$ OAM. Now, if a beam in an orthogonal SAM state, $|\lambda^-\rangle$, is incident on the same device we require that the conversion from SAM leads to an independent OAM state. This case is shown in Fig. 6.1B, where the mapping carried out is

$$\left|\lambda^-\right\rangle \to \mathrm{e}^{in\phi}\left|\left(\lambda^-\right)^*\right\rangle . \tag{6.4}$$

For this case, the output beam has acquired an azimuthal phase factor of $\mathrm{e}^{in\phi}$ corresponding to OAM of $n\hbar$, which is in general different from m.

To implement this mapping in practice we must be able to create a single device that independently controls the phase shift imprinted on two orthogonal input polarizations states (See Appendix E for more discussion). This amounts to finding a single operator (device matrix)[17] that will act independently on the two input SAM states. First, we consider the two arbitrary, orthogonal polarization states introduced above in the linear polarization basis

$$\left|\lambda^+\right\rangle = \begin{bmatrix} \cos\chi \\ e^{i\delta}\sin\chi \end{bmatrix} \qquad \left|\lambda^-\right\rangle = \begin{bmatrix} -\sin\chi \\ e^{i\delta}\cos\chi \end{bmatrix} \tag{6.5}$$

where χ and δ set the ellipticity and handedness of the chosen polarization state. To carry out the mapping from these SAM states to OAM states, Eq. 6.3 and 6.4, we must know the action of the device in relating the desired input states to the desired output state. The connection of an input state and output state of an optical device can be related through its Jone's

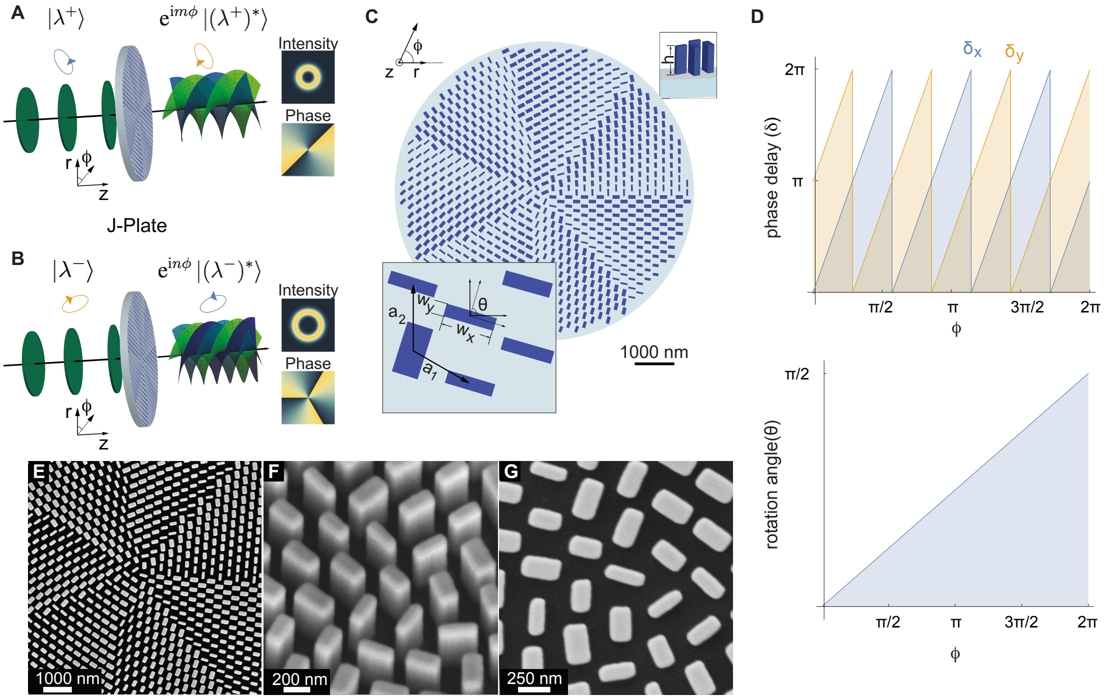

Figure 6.1: Concept for arbitrary spin-to-orbital angular momentum conversion. (**A**) Schematic diagram of the concept for arbitrary SOC. Light with an arbitrary spin state (elliptical polarization), $|\lambda^+\rangle$, propagating along the z-axis is incident on the J-plate (top). The J-plate imprints a helical phase profile on the output beam resulting in an optical vortex with orbital angular momentum (OAM) $m\hbar$, where m is any integer, and flips the handedness of the incident polarization. (**B**) For light incident on the same device with an orthogonal polarization state $|\lambda^-\rangle$, the device imprints OAM of $n\hbar$, where in general n is independent of m and again flips the handedness of the polarization (bottom). (**C**) Schematic of typical J-plate design used to carry out the function in (A). The units have a given height, h, (top inset) and by changing their width along the x- and y-directions, $\mathrm{w_x}$ and $\mathrm{w_y}$ (bottom inset) the structures implement phase shifts given by δ_x and δ_y, respectively. Each unit is also allowed to have an independent orientation angle, θ. (**D**) Required phase shifts, δ_x and δ_y (top) and rotation angle (bottom) as a function of the azimuthal coordinate ϕ. The particular case plotted here is for designed input spin states that are left and right circularly polarized and for OAM values of $m = +3$ and $n = +4$. (**E**-**G**)Scanning electron micrographs of fabricated device for the case of mapping from circularly polarized states to helical beams with OAM values of $m = +3$ and $n = +4$. The SEMs show a top view (E) angled view (F) and zoomed view of the device center (G).

matrix[171] and we can show[170] that for the case of arbitrary SOC, using only linearly birefringent elements, this matrix must be

$$J(\phi) = \begin{bmatrix} e^{i\delta}\left(e^{im\phi}\cos^2\chi + e^{in\phi}\sin^2\chi\right) & \frac{\sin 2\chi}{2}\left(e^{im\phi} - e^{in\phi}\right) \\ \frac{\sin 2\chi}{2}\left(e^{im\phi} - e^{in\phi}\right) & e^{-i\delta}\left(e^{im\phi}\sin^2\chi + e^{in\phi}\cos^2\chi\right) \end{bmatrix} \tag{6.6}$$

where δ and χ define the polarization states in Eq. 6.5, m and n are any real numbers and set the output OAM and ϕ is the azimuthal coordinate. This device matrix provides the most general mapping from orthogonal SAM to independent OAM states and makes no assumptions on the specific values. To see that Eq. 6.6 carries out the mapping, we need only to look at the output state from the device, which can be found as $|E_{\text{out}}\rangle = J(\phi)\,|E_{\text{in}}\rangle$. When the input polarization is chosen to be $|E_{\text{in}}\rangle = |\lambda^+\rangle$ the output can be found to be $e^{im\phi}\left|(\lambda^+)^*\right\rangle$. Similarly, for the orthogonal input state $|\lambda^-\rangle$ the output is $e^{in\phi}\left|(\lambda^-)^*\right\rangle$.

While we have only considered the two orthogonal design polarization states, the device works for any input polarization, $|E_{\text{in}}\rangle = \alpha\,|\lambda^+\rangle + \beta\,|\lambda^-\rangle$, where α and β are complex coefficients. In such a case, the output state is a superposition of the two eigenstates,

$$\begin{aligned} |E_{\text{out}}\rangle &= J\,|E_{\text{in}}\rangle \\ &= \alpha e^{im\phi}\left|(\lambda^+)^*\right\rangle + \beta e^{in\phi}\left|(\lambda^-)^*\right\rangle \end{aligned} \tag{6.7}$$

For simplicity we considered above the case where the incident beam has zero OAM, that is, the device transfers an incident beam with only SAM to an output with OAM. However, the device is equally capable of acting on an incident beam with OAM. In such a case, the mapping is

$$\begin{aligned} \mathrm{e}^{i\ell\phi}\left|\lambda^{+}\right\rangle &\rightarrow \mathrm{e}^{i(m+\ell)\phi}\left|\left(\lambda^{+}\right)^{*}\right\rangle \\ \mathrm{e}^{ip\phi}\left|\lambda^{-}\right\rangle &\rightarrow \mathrm{e}^{i(n+p)\phi}\left|\left(\lambda^{-}\right)^{*}\right\rangle \end{aligned} \tag{6.8}$$

where again ℓ and p are also arbitrary integers and for the case that $m = n = 0$ the case discussed above is recovered.

Given the form of the Jones matrix producing arbitrary conversion from SAM to OAM, we now need to transfer this into a physically-realizable optical element. Since Eq. 6.6 only assumes linear birefringence, we can determine the orientation angle of the fast axis and birefringence as a function of the coordinate ϕ by finding its eigenvectors and eigenvalues, respectively. No optical element can provide continuous spatial variation of both linear birefringence as well as the orientation angle of the fast axis. Metasurfaces, however, which are composed of subwavelength-spaced, birefringent phase-shifters, allow one to discretize a continuous phase function. This concept is shown schematically in Fig 6.1C. Discrete optical elements are arranged periodically in two dimensions with periods $\mathbf{a}_1$ and $\mathbf{a}_2$. For some fixed height, h (top inset), changing the element widths $\mathrm{w_x}$ and $\mathrm{w_y}$ (bottom inset) allows us to control the the phase shifts δ_x and δ_y. The orientation angle of each element, θ, can also be independently varied (bottom inset) and thus, each element acts as a local, subwavelength waveplate with designable birefringence and orientation. An important distinction, compared to SOCs based on the geometric phase, is that by allowing *both* the phase shifts and orientation angle vary as a function of coordinate ϕ (as opposed to orientation angle alone) we are able to decouple the output OAM states and any input SAM state.

For the specific case of circular polarization, $\chi = \pi/4$ and $\delta = \pi/2$, but for any two values of OAM, m and n we can easily find analytical solutions for the required phase shifts and orientation angles as a function of azimuth

$$\theta = \frac{1}{4}(m - n)\phi \tag{6.9}$$

$$\delta_x = \frac{1}{2}(m + n)\phi \tag{6.10}$$

$$\delta_y = \frac{1}{2}(m + n)\phi - \pi \tag{6.11}$$

These equations give us the prescription to map left and right circular polarizations to any two values of OAM, m and n. In Fig. 6.1D, we plot these equations as a function of ϕ for a specific case where $m = +3$ and $n = +4$. In the top panel of Fig 6.1D, we plot the variation of the phase shifts δ_x and δ_y, modulo 2π. We can clearly see $(m + n)2\pi$ phase jumps in the plot. This can readily be observed in the device itself, which is the schematic that we already introduced in Fig. 6.1C, where there are $m + n = 7$ segments. For the more general case of elliptical polarizations the solutions are not amenable to such succinct expressions but must be calculated numerically for specific values of m, n, χ, and δ. This case will be discussed in more detail below.

6.3 Experimental demonstration of circular polarization coupling to arbitrary orbital angular momentum states.

For the experimental realization of the J-plate, we fabricate the devices using a process that we have detailed elsewhere[108]. This process allows us to produce devices with high fidelity and high efficiency that operate at visible wavelengths[75,73] with TiO_2 as a material platform.

We optimized the devices to operate at a wavelength of 532 nm but the same design principle can be applied for any wavelength. To fully characterize a beam with OAM, one needs to characterize both the intensity and phase distributions of the beam. As such we carry out interference measurements in a standard Mach-Zehnder configuration (See Appendix E, Fig. E.1 and surrounding discussion).

To provide the most direct comparison to previous geometric-phase SOCs, we first demonstrate a device that provides a transfer from circularly-polarized input states to two output helical beams with independent values of OAM. We also examine the full set of superposition states that this device can create. We choose the specific mapping to be $|R\rangle \rightarrow |L\rangle |{+4}\rangle$ and $|L\rangle \rightarrow |R\rangle |{+3}\rangle$, carried out by the device in Fig 6.1. Note that here and below we write the azimuthal phase factor as $|m\rangle$, for brevity and to show more explicitly that the output of the J-plate is a TAM state, a direct product between SAM and OAM states.

The full set of output states from this J-plate can be most succinctly represented on a sphere whose poles are the two output TAM states and all other points are superpositions of these two states. This sphere that combines both SAM and OAM is called the higher order Poincaré sphere (HOPS)[172,173] in contrast to the traditional Poincaré sphere for polarization states. While the original HOPS was derived for conjugate states of OAM on the poles, due to the previous availability of devices, it remains valid even when these states are completely independent, as is the case here. Figure 6.2A shows the HOPS for the two design states introduced above. We label all the cardinal points of the sphere and one can see that the poles correspond to states $|R\rangle |{+3}\rangle$ and $|L\rangle |{+4}\rangle$, respectively. All other possible outputs from this device corresponds to a point on the HOPS represented by the angular coordinates Φ and Θ (marked inside the sphere of Fig. 6.2A). Thus any TAM state of the device can be written as $|\Psi\rangle = \cos(\Theta)\,|L\rangle\,|{+4}\rangle + \sin(\Theta)\exp(i2\Phi)\,|R\rangle\,|{+3}\rangle$, where Θ ranges from 0 to $\pi/2$. The states along the equator of the sphere are equal weights of the eigenstates $1/\sqrt{2}\,(|R\rangle\,|{+3}\rangle + \exp(i2\Phi)\,|L\rangle\,|{+4}\rangle)$.

Figure 6.2B-E show the measured and calculated results verifying the operation of the J-plate device. The labels on each figure (i-vi) correspond to the states indicated by the blue circles on the HOPS of Fig. 6.2A. Figure 6.2B(i) and (vi) and Fig. 6.2C(i) and (vi) show the measured and calculated intensities for incident left and right circularly polarized light, respectively. These intensity profiles are a single-ringed annuli with zero intensity as $r \to 0$. The radius of maximum intensity, r_{max}, is larger in Fig 6.2B(vi) as compared to Fig 6.2B(i) indicating that the magnitude of OAM for the prior case is greater than the latter. In order to verify the OAM of a beam, however, one must carry out interference measurements. The measured interference pattern corresponding to the intensities in Fig. 6.2B(i) and (vi) are shown in Fig. 6.2D(i) and (vi). We clearly observe 3 and 4 arms, respectively, in the spiral interference patterns, which converge on the beam axis. Fig 6.2E(i) and (vi) show the calculated phase distribution of the two states, which have 3 and 4 phase discontinuities, respectively. These observations are consistent with the two states being pure OAM states, rather than superpositions, and consistent with the two intended output OAM states for this J-plate, $|{+3}\rangle$ and $|{+4}\rangle$. Notably, these values of OAM are not conjugate values.

To further verify the operation of the device, we also explored the evolution of an equal superposition of the two design states on the HOPS. To produce this state, we input linearly polarized light into the J-plate, which results in an equal superposition of the two eigenstates for any angle of the input linear polarization. Changing the angle of the linear polarization introduces a relative phase shift between the two TAM states and corresponds to changing

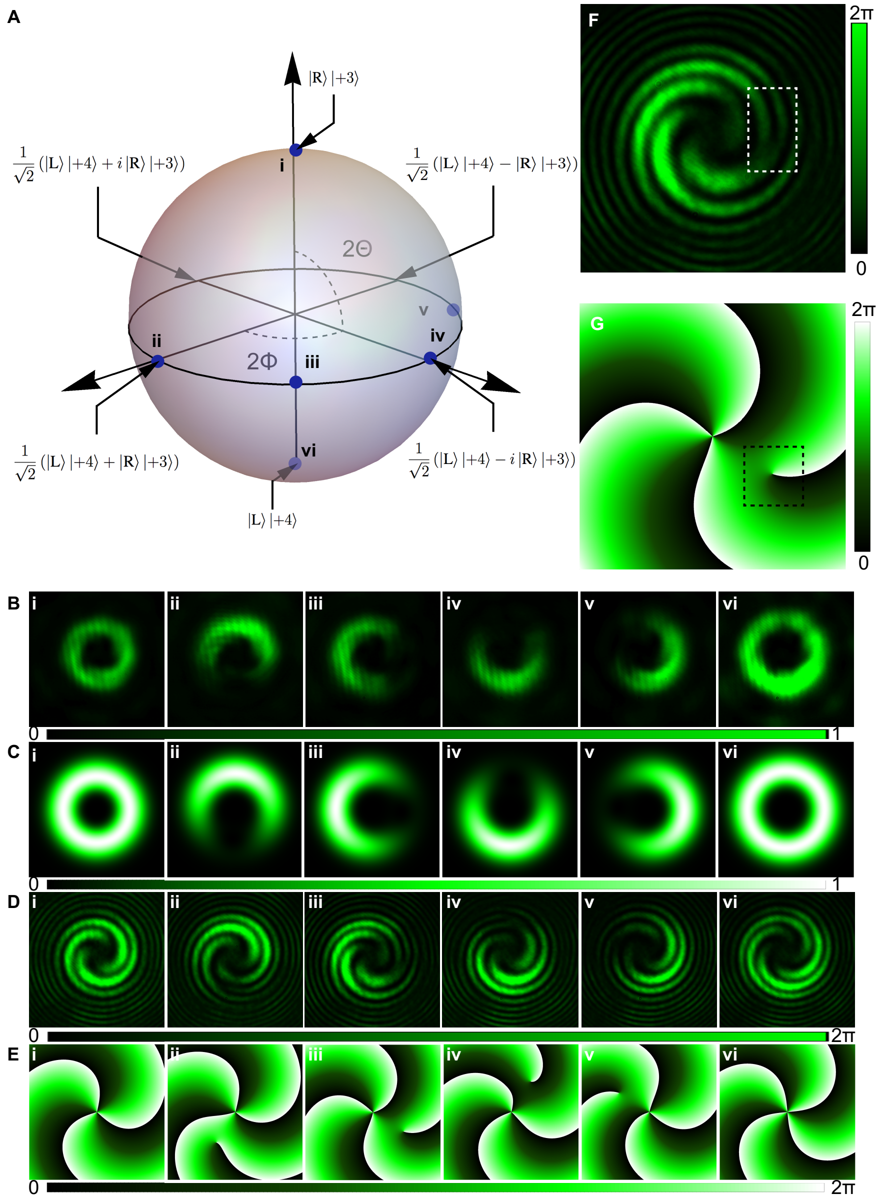

Figure 6.2: Experimental demonstration of mapping from two circular polarizations to two arbitrary values of orbital angular momentum.(**A**). Higher order Poincare sphere (HOPS) representing all possible spin and orbital angular momentum states produced by a device that carries out the mapping $|R\rangle \rightarrow |L\rangle\,|{+4}\rangle$ and $|L\rangle \rightarrow |R\rangle\,|{+3}\rangle$. (**B**,**C**). Measured and calculated intensity of output state . (**D**,**E**) Measured interference and calculated phase of output state, respectively, indicated by blue dots on HOPS. Scale bars below show the phase value. The states in (B-E) i-vi are marked as blue circles on the HOPS in (A). (**F**,**G**) Magnified view of measured interference and calculated phase of intensity of output state in (D)iii and (E)iii. The dashed boxes highlight an additional phase discontinuity that results from the equal superposition of $|{+3}\rangle$ and $|{+4}\rangle$ states. This phase discontinuity results in an off-axis fork in the interference pattern (F) and an additional off-axis 0 to 2π phase jump (G). The scale bar shows the value of phase

longitude at a fixed lattitude on the HOPS. The measured intensity for these cases are shown in Fig. 6.2B(ii-v). Since these states are a superposition of two beams with different values of OAM, we expect an additional $|m - n|$ zeros to develop in the intensity away from the beam center[174], or in this specific case $|3 - 4| = 1$. As can one can see from the measured and calculated intensities in Fig 6.2B and C(ii-v), in addition to the zero in intensity at the beam center, an additional zero has developed at a radially-off-axis position. This zero in intensity is also an optical vortex and for the superposition of two OAM beams where $m \neq n$ and $m < n$ there should be m vortices at the beam center and $|m-n|$ vortices off axis, which again for this specific case corresponds to $m = 3$ and $|3 - 4| = 1$. This is exactly the phase structure of the beam we observe from the interference measurements and phase calculations, e.g., Fig. 6.2D(ii-v) and E(ii). Figure 6.2F and G show expanded views of the measured interference and calculated phase for one of these equal superpositions in order to illuminate the more subtle features of the phase. As we change the angle of the input linear polarization from 0° (horizontal) to 66.75°, which corresponds to changing the relative phase $\exp(i2\Phi)$ between the two states from $\Phi = 0 - 3\pi/4$, we see all of the features (zero in intensity and additional off-axis vortex) rotate (this corresponds to moving from (ii) to (v) in Fig. 6.2B-E). We can understand this qualitatively by noting that the relative phase shift changes the angle where destructive interference occurs; the positions of the intensity minima agree with quantitative expectations[174].

We have verified that the device does indeed produce the two independent TAM states and the effect of a phase difference between equal superpositions of the $|R\rangle\,|{+3}\rangle$ and $|L\rangle\,|{+4}\rangle$ TAM states. However, we can also continuously vary the superposition of these states in both magnitude and phase. Figure 6.3 depicts the continuous evolution from the $|R\rangle\,|{+3}\rangle$ to $|L\rangle\,|{+4}\rangle$

state as a function of changing input polarization to the J-plate. To vary the input polarization, we simply change the angle of the fast axis of a quarter wave plate (QWP) in front of a horizontally-polarized laser. The resulting path taken on the HOPS is shown as the black line in Fig. 6.3 and winds from the north pole, $|R\rangle\,|{+3}\rangle$, to the south pole in a half figure eight pattern, $|L\rangle\,|{+4}\rangle$. We can derive[170] the output state as a function of the QWP fast axis angle, β, and show that total output state is given by $|\Psi(\beta)\rangle = \sin\left(\frac{\pi}{4}-\beta\right)|\mathrm{L}\rangle\,|{+4}\rangle + \mathrm{e}^{i2\beta}\cos\left(\frac{\pi}{4}-\beta\right)|\mathrm{R}\rangle\,|{+3}\rangle$. Note that for the cases of $\beta = +45°$ and $\beta = -45°$ the input polarization is left or right circular polarization and the TAM state corresponds to one of the design eigen-polarizations. We can also relate the angle β of the QWP back to the coordinates on the HOPS as $\Theta = \pi/4 - \beta$ and $\Phi = \beta$. The measured intensity and interference images for 10 values of β are shown surrounding the sphere in Fig. 6.3. As the value of β is changed from $+45°$ to $-45°$ the interference pattern, initially composed of 3 on axis spiral arms, develops an extra vortex at the periphery of the image. Ultimately, as β approaches $-45°$ this additional vortex moves closer and closer to the beam center until, ultimately at $-45°$, the spiral interference pattern has 4 arms, indicating that the state now has OAM of +4. This shows the continuous evolution between the two design states.

This demonstration is the first case where SOC has been carried from two input circular polarization states to two independent TAM states. In addition to producing an arbitrary TAM state with polarization controllable phase and amplitude, we can see from the results in Fig. 6.2 and 6.3 that, due to the spatial intensity profile of the two OAM beams, this device also allows us to produce and control the complex spatial intensity profiles. Although we have chosen to demonstrate this arbitrary SOC with a relatively simple case where the two output OAM values differ only by one, $|m - n| = 1$, there is nothing that prevents us from creating

$$|\Psi(\beta)\rangle = \sin\left(\frac{\pi}{4} - \beta\right)|\mathrm{L}\rangle\,|{+4}\rangle + \mathrm{e}^{\mathrm{i}2\beta}\cos\left(\frac{\pi}{4} - \beta\right)|\mathrm{R}\rangle\,|{+3}\rangle$$

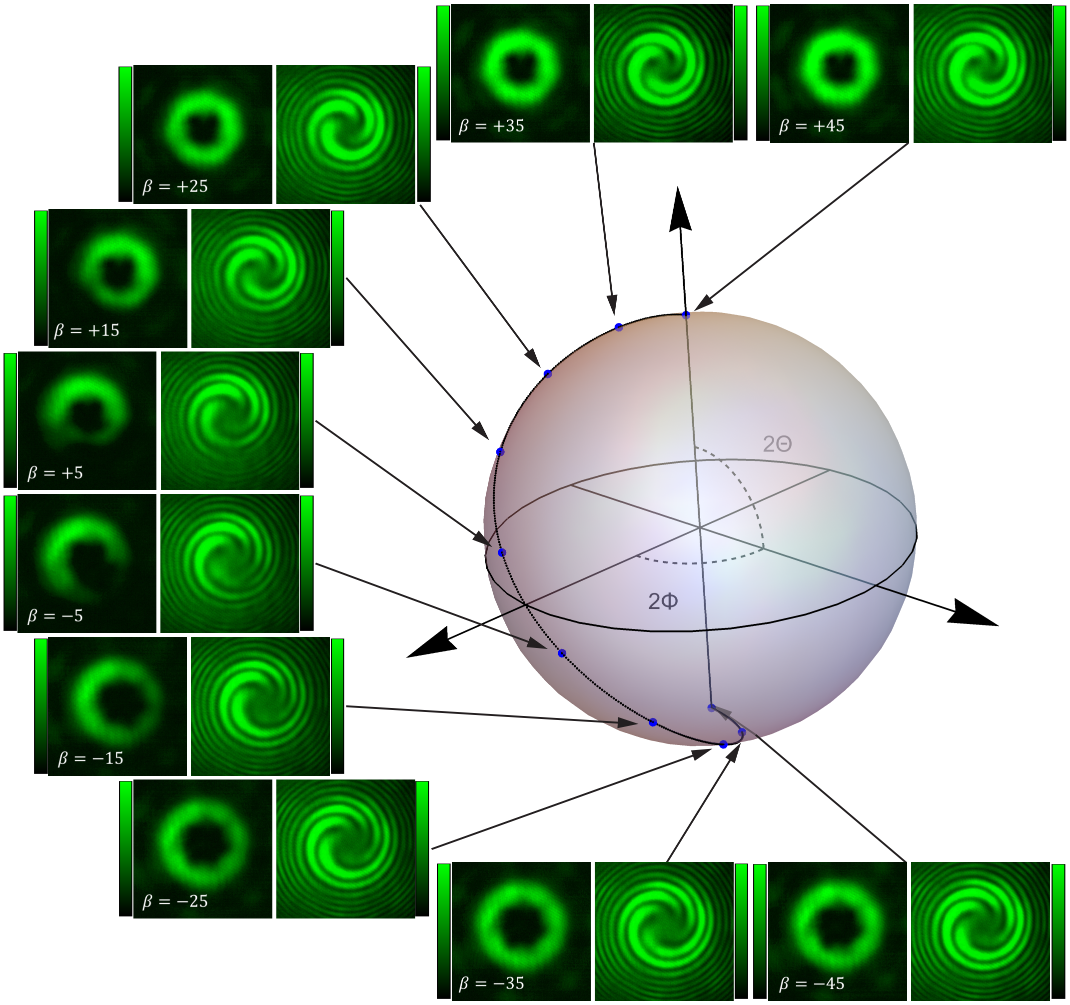

Figure 6.3: Evolution of J-plate output along a path on the higher order Poincaré sphere. The images show measured output intensities (left) and interference (right) for the device in Fig. 2, as the angle of the fast axis of a QWP is varied in front of a horizontally-polarized laser. The angle is varied from $\beta = 45^{\circ}$ to -45° which transfers the output state from the north pole to the south pole while continuously changing both the weights and phases of the superposed states. The QWP angle for each intensity and interference image is displayed in the bottom left. The scale bars for the normalized intensity (left image) range from 0 to 1 and interference (right image) range from 0 to 2π. The output state $|\Psi\rangle$ as a function of β, is shown at the top. The resulting path taken on the HOPS is shown as the black line and the blue circles correspond to the measured points.

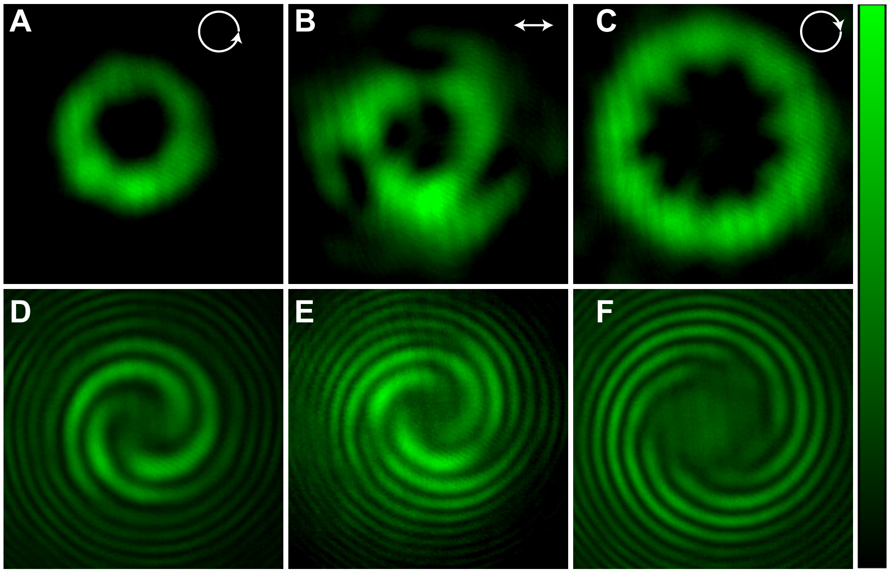

Figure 6.4: Device output for conversion to OAM states with $m = 6$ and $n = 3$. (**A-C**) Measured output intensities for input polarizations: (A) left circular, (B) horizontal, and (C) right circular. (**D-F**) Measured interference patterns corresponding to the intensities in (A-C), respectively. Input left circular polarization produces three arms in the spiral interference pattern (D). Input horizontal polarization produces an intensity pattern with three additional minima off-axis (B) and an additional vortex in the interference pattern at the location of each intensity minima (E). Input right circular polarization produces a larger beam radius (C) and six arms in the spiral interference pattern (F). The scale bar to the right shows normalized intensity from 0 to 1.

outputs with any two values of OAM. To demonstrate this experimentally, we also created a device that converts circular polarizations to OAM states of $m = 3$ and $n = 6$. The results are summarized in Fig. 6.4 with Fig 6.4A-C showing the output intensity for input left circular, horizontal and right circular polarization, respectively and Fig. 6.4D-F showing the corresponding interference patterns. (For a complete description of this device see Appendix E, Fig. E.2-E.4). Finally, we note that while in Fig. 6.3 we chose a relatively simple path along the HOPS, with the same setup, a QWP followed by a J-plate, we can generate any output any state on the HOPS. This is achieved by allowing the J-plate axis to also rotate independently with respect to the QWP angle β, as has been previously demonstrated for the q-plate[169].

6.4 EXPERIMENTAL DEMONSTRATION OF GENERAL SPIN-TO-ORBITAL ANGULAR MOMENTUM CONVERSION

Having demonstrated mapping from input circularly polarized states to two unique output OAM states, we now move to the most general case of SOC–a mapping from an arbitrary, orthogonal SAM states (elliptical polarization) to two independent output TAM states. For this demonstration we choose input polarizations in Eq. 6.5 corresponding to $\chi = \pi/6$ and $\delta = 3\pi/10$ and map to two OAM states $m = -3$ and $n = +4$. Figure 6.5A shows a schematic of the device that we use to experimentally verify this mapping. In addition to the normal azimuthal phase factor that imprints OAM onto the output field, we add an additional constant phase gradient that causes each output beam to be deflected by ±10° from the z-axis, respectively. This is in contrast to the device measured in Figs. 6.2 and 6.3 where the two output states always propagate co-linearly after exiting the J-plate. Spatially separating the two TAM states allows us to vary the input polarization $|E_{\text{in}}\rangle$ and to independently monitor the intensity at each output angle. The advantage of this approach is that we can perform Stokes polarimetry and unequivocally determine the realized eigen-polarizations of the device and compare it to the designed eigen-polarizations polarizations.

The results of this measurement are shown in Fig. 6.5(B-G). We first must verify that the two output beams contain the designed values of OAM. Figure 6.5B shows the measured intensity distribution for six input polarizations (shown at the bottom of each set of images). We collected the images at angles of $+10°$ and $-10°$ away from the z-axis corresponding to the designed OAM states of $|+4\rangle$ (Fig 4B top) and $|-3\rangle$ (Fig 6.5B bottom), respectively. First, we note that the beam radii of two outputs are different, with the max intensity cor-

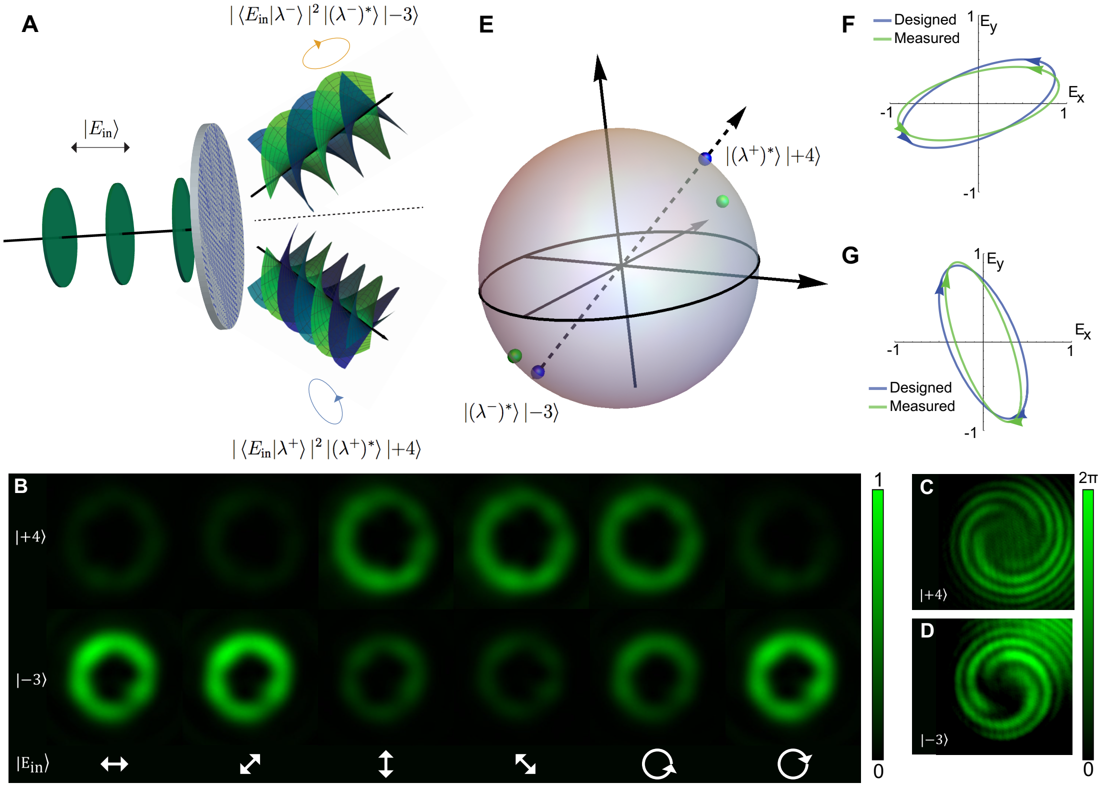

Figure 6.5: Demonstration of SOC for arbitrary spin state. (**A**) Schematic diagram of the device that maps elliptically-polarized input states to two independent values of OAM. An input beam with polarization state $|E_{\rm in}\rangle$ is incident on the J-plate and is mapped to a superposition of orbital angular momentum where the weights are given as a projection of the input polarization onto the two designed output polarizations. An additional constant phase gradient is added to the device so that the two output states are also spatially separated by an angle of $\pm10^{\rm o}$. This spatial separation allows the intensity of each OAM state be probed independently. (**B**)Stokes polarimetry to measure the designed polarization. The beam intensities are shown for the two OAM states, $|+4\rangle$ and $|-3\rangle$, and the input polarizations for each image is shown below. (**C**,**D**) Interference pattern for the $|+4\rangle$ and $|-3\rangle$ states collected at angles $\pm10^{\rm o}$ from the z-axis. The number of arms in the spiral interference pattern corresponds are 4 (C) and 3 (D), indicating that the output beams have the designed values of OAM. The sense of rotation of the spirals, however, is opposite for (C) and (D) due to the sign difference of the two states. (**E**) Designed (blue) and measured (green) polarization of the output states on the HOPS. (**F**,**G**) The designed (blue) and measured (green) polarization ellipses for the input states $|\lambda^+\rangle$ and $|\lambda^-\rangle$, respectively.

responding to $|+4\rangle$ occurring at a larger radius than the case of $|-3\rangle$, as expected. The fact that these two beams carry the two designed, independent values of OAM is confirmed through interference measurements (Fig 6.5C and D). We observe 4 arms in the spiral interference pattern of Fig 6.5C while Fig 6.5D clearly has 3 arms in the interference pattern. Additionally, because of the sign difference between the two OAM states, we expect the phase fronts of the two OAM beams to have opposite handedness. This is confirmed as one can see that the sense of rotation of the two interference patterns in Fig 6.5C and D are opposite.

To verify that the device is performing the desired SOC from an elliptically-polarized input to two TAM states, we measure the power at each output angle, $\pm 10°$ and for each input polarization in Fig. 6.5B and perform Stokes polarimetry. As the input polarization to the device is changed from horizontal to diagonal through to circular, one can clearly observe that the relative output intensities of the two beams vary. We then measure the power of each beam for each input polarization and calculate the eigen-polarizations for the actual device (see Appendix E). Figure 6.5E shows the HOPS corresponding to the device measured here. The blue circles on the HOPS are the two designed output TAM states and the dashed arrow passing through these two points highlights that the designed polarization states no longer correspond to circular polarizations. The green circles on the sphere are the measured polarizations states which have numerical values of $\chi = \pi/6.04$ and $\delta = 3.43\pi/10$ and closely correspond to the desired design polarization. Figure 6.5F and G show plots of the two polarization ellipses for the designed and measured eigenpolarizations. Coupled with the intensity measurements (Fig. 6.5B) and the interference measurements (Fig. 6.5C and D), this shows that we have carried out the most general form of coupling from arbitrary SAM states to two independent TAM states.

6.5 Discussion

We have demonstrated a design technique for converting an arbitrary and orthogonal SAM states of light to an arbitrary superposition of states with independent values of OAM. This design currently represents the most general material-mediated connection between the spin angular momentum and orbital angular momentum of light and can produce arbitrary superpositions of TAM states of light. We have experimentally demonstrated the operation of the J-plate for spin-orbit conversion from two input circular polarizations to two independent output states and for input elliptical polarizations in general. In addition to demonstrating this general mapping, we have shown that with a single optical device, we are able to create controllable structured light, such as complex optical vortex patterns, where the input spin angular momentum uniquely determines these output spatial distributions.

The generalized spin-orbit-coupling that we have presented here, as a new fundamental connection between SAM and OAM of light, has the potential to influence a number of current applications and lead to several interesting future research directions. The compact nature of the J-plate, consisting of only a single-layer of material to produce arbitrary TAM states, makes the device easily integrateable in a variety of platforms. For example the device can be directly integrated into a laser cavity to produce high purity[169], independent TAM states. These states that use both polarization and spatial structure of the field have the potential to increase classical information transfer. The complex, tunable intensity profiles can be used for laser fabrication of materials, optical micromanipulation, and imaging in STED microscopy. While we have only investigated macroscopic fields, the device physics will still hold at the single photon level. Thus, the J-plate can provide a new tool for quantum communications protocol, especially cases that rely on transfer from polarization entanglement to OAM entanglement, rather than parametric down conversion[32]. This device could potentially be used as an analogue to study complex spin-orbit interactions in atomic systems[175]. Finally, we have only considered here the case of a single J-plate. However, cascading devices, especially those designed for different input polarizations, offers an interesting area of future study, as we believe it will allow us to create a plurality of independent OAM modes.

A

Supplemental material: Visible-frequency hyperbolic metasurface

A.1 Silver growth and characterization

In this section we detail our silver growth process that produces ultra-smooth, single-crystalline silver films via standard wafer preparation and deposition techniques. The entire silver growth process takes approximately 1-2 hours and is reproducible in a standard cleanroom environ-

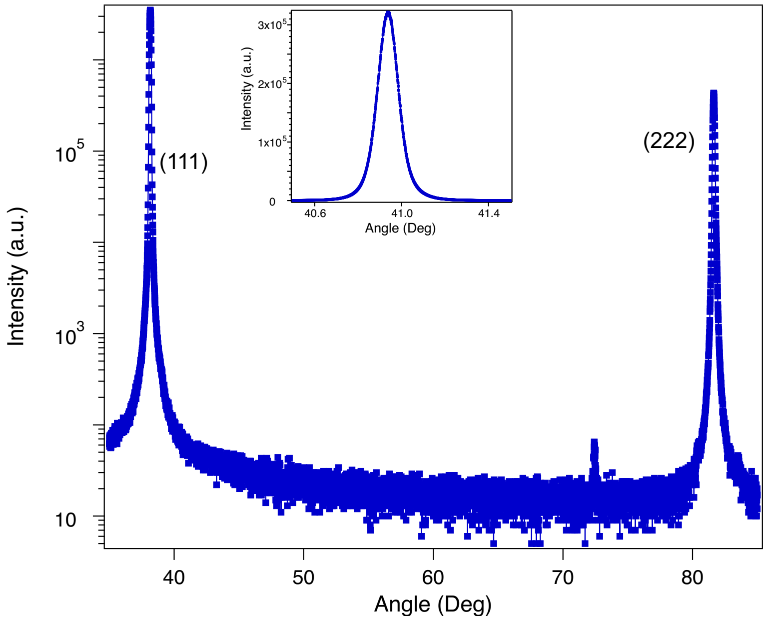

Figure A.1: XRD measurement of a silver film on (111)-Si. An XRD scan showing the (111) and (222) Ag peaks. The inset shows a rocking curve of the (111) peak with a full width at half maximum of 0.116 degree.

ment. Single-crystalline silver films were grown via direct current plasma sputtering (AJA International Orion 3) with 99.99% pure silver targets (Kurt Lesker Inc.) on prime-grade, degenerately doped (111)-Si wafers (0.0015-0.005 Ω-cm). We first ultrasonically cleaned the wafers in acetone, followed by further cleaning in a 2:1 sulfuric acid: hydrogen peroxide solution to eliminates organics. Finally, we placed the wafers in 49% hydrofluoric acid for approximately 10 s to remove the native oxide layer. After oxide removal, we immediately transferred the wafers into the sputtering tool and pumped the system down to limit oxide growth. After a typical base pressure of 5×10^7 Torr was achieved, the substrate was heated to 300$\circ$ C (determined from the temperature calibration sheet of the system), and silver was deposited at a rate of 1.5-1.7 nm/s16,17. Following the growth, we utilized multiple techniques to test the quality of the deposited films and determined their suitability for metasurface fabrication. We

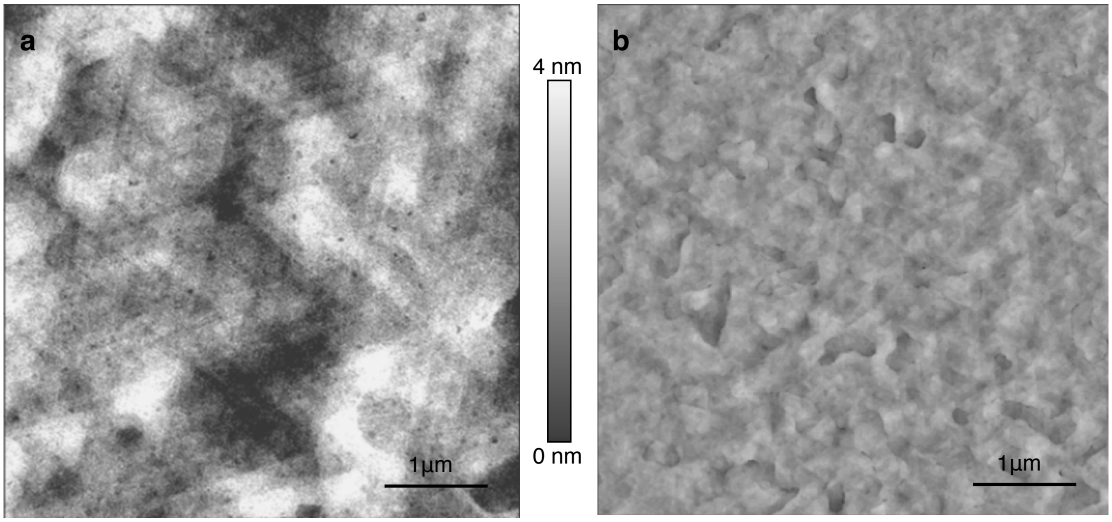

Figure A.2: AFM scans. a, 100 nm and b, 1200 nm thick silver films sputtered on (111) Si. The RMS roughness of these films are 300 pm and 900 pm, respectively.

probed the crystallinity of the films via X-ray diffraction (XRD) and transmission electron microscopy (TEM). In the XRD scan for a 1200-nm-thick Ag film (Fig. A.1), only (111)- and (222)-Ag peaks are present, consistent with (111)-Ag grown on (111)-Si. A rocking curve with a full width at half maximum of 0.116 degree indicates that the film is high quality with minimal defects (Fig. A.1, inset). The TEM image in Fig. 2.1a confirms that the silver films are single-crystalline.

As a further test of the silver quality, we utilized atomic force microscopy (AFM: Asylum MFP3-D, tapping mode) to characterize the surface roughness of the film. Rough surfaces and grain boundaries result in the scattering of surface plasmon polaritons (SPPs) that is detrimental to the performance of any SPP-based device, and as such their presence should be minimized. Figs. A.2a and b show AFM scans for 100 nm and 1200 nm films, respectively (we measured film thicknesses with optical profilometry, Taylor Hobson CCI HD). The AFM scans confirm that the films are ultra-smooth with root-mean-square (RMS) roughness 300 pm (100-

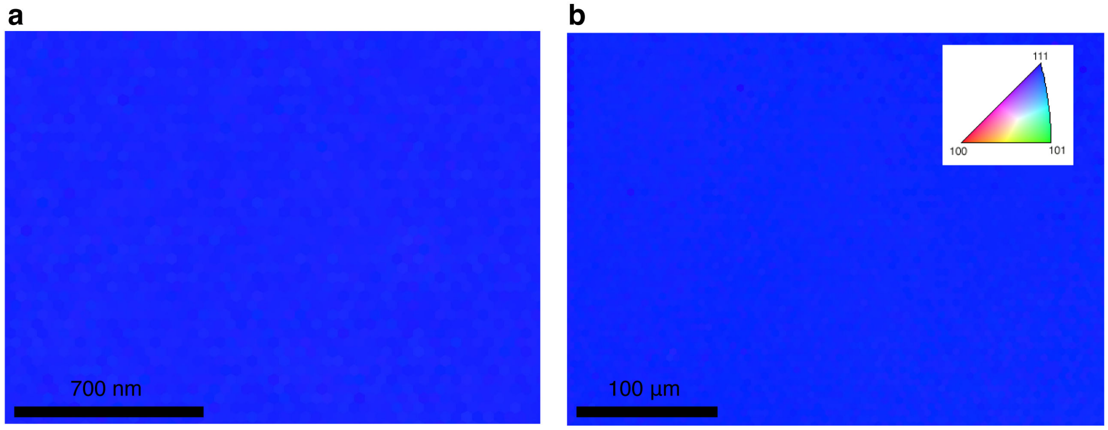

Figure A.3: Electron backscatter diffraction images of 1 μm-thick silver film a Image taken over a short length scale with no grain boundaries. **b** Image taken over a larger length scale still with no grain boundaries.

nm thick film) and 900 pm (1200-nm thick film). We did not observe grain boundaries within the 10 10 μm scan region. The measured surface roughness is comparable to that of silver films grown by molecular beam epitaxy[59].

Finally, we used electron backscatter diffraction to examine the domain structures of our films: as shown in Fig. A.3, only a single domain is observed in both small-scale 2 μm and large-scale 400 μm scans, confirming the quality of our silver films.

A.2 Measurement and calculation of SPP propagation properties of the silver film

The ultra-smooth, single crystalline nature of our silver films results in lower SPP scattering losses and improved optical performance. In general, the optical performance of a film is determined by its dielectric function (or equivalently index of refraction, n, and loss, κ given as

$$\varepsilon(\omega) = \varepsilon(\omega)' + i\varepsilon(\omega)'' \tag{A.1}$$

where

$$\varepsilon' = n^2 - k^2 \tag{A.2}$$

and

$$\varepsilon' = 2nk \tag{A.3}$$

We experimentally determined the dielectric functions of our films using variable angle, spectroscopic ellipsometry (J.A .Woolam Co., WVASE32). Fig. A.4 presents $\varepsilon(\omega)'$ and $\varepsilon(\omega)''$ for films of 100-nm and 1200-nm thickness from the present work as well as typical optical constants derived from literature. For our silver films, the lossy part of the dielectric function, ε'', is lower than previously reported data18,19 and is comparable to those recently reported in films grown by molecular beam epitaxy[59]. Because our film thickness is much greater than the skin depth of silver, the substrate effects are negligible in our study. Consequently, the pseudo-dielectric constants taken from the WVASE software correspond directly to the real and imaginary part of the dielectric function.

From the experimentally determined optical constants, we determined the SPP propagation vector and propagation length. For $|\varepsilon'| >> \varepsilon''$, which is valid for our silver films in the visible frequency range, the dispersion relationship of a silver/air SPP is given by

$$k_{SPP} = k + ik'' = k_0\sqrt{\frac{\varepsilon'}{1+\varepsilon}} + ik_0\left(\frac{\varepsilon'}{1+\varepsilon''}\right)^{3/2}\frac{\varepsilon''}{2(\varepsilon')^2} \tag{A.4}$$

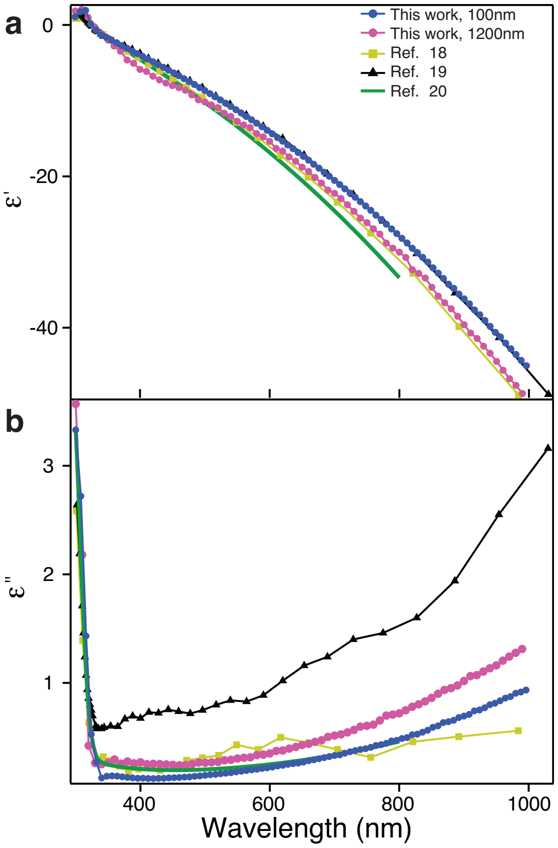

Figure A.4: Optical constants of silver films. **a**, The real and **b**, imaginary parts of the measured dielectric function for 100 nm (blue circles) and 1200 nm-thick (pink circles) silver films. The values reported in 19 (yellow squares), 20 (black triangles), and 21 (green line) are also shown.

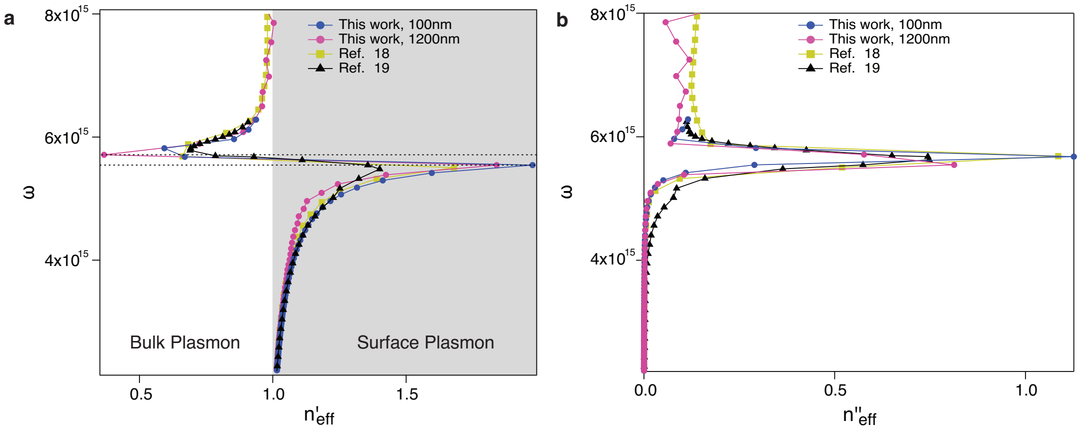

Figure A.5: Plasmon dispersion in silver films. **a**, The real and **b**, imaginary parts of the effective SPP index on various silver films.

Figs. A.5a and b plot the calculated real and imaginary part of the SPP dispersion relationship normalized to k_0, defined as ω/c. The complex wave vector leads to exponential SPP decay with a characteristic SPP propagation length L_p (defined as the distance over which the SPP intensity decays to $1/e$ of its original value) given by

$$L_p = \frac{1}{2k''} \tag{A.5}$$

The results of this calculation using our experimental values, as well as several other literature values are presented in Fig. 2.1b of Chapter 2 text.

A.3 Metasurface fabrication

Due to the thermodynamic stability inherent to single-crystalline silver films, we are able to fabricate metasurfaces in a top-down fashion using electron-beam lithography (EBL) and reactive ion etching (RIE). Such lithographic processing avoids undesirable side effects inherent to focused ion beam (FIB) milling such as unintentional doping, roughened surfaces, and gallium poisoning. Our unique fabrication process relies on the transfer of lithographically defined, anisotropic, high-aspect-ratio features into silver. Since the fabrication does not rely on chemical reactions specific to silver, this process should be broadly applicable to any metal system (e.g., gold and intermetallics) where losses can greatly affect plasmonic device performance. The metasurface fabrication process is summarized in Fig. A.6. We first grew, via atomic layer deposition (ALD), 50-nm-thick alumina on top of as-deposited Ag films (Fig. A.6a). Next, we etched back the alumina by approximately 40 nm using inductively coupled plasma reactive ion etching in select areas defined by EBL. For all EBL process, we used ZEP-520A electron-beam resist at a dilution of 1:1 ZEP-520A:Anisole. For alumina etching we used a gas mixture of BCl_3-Cl_2. This EBL and etching procedure creates 10-nm-thick alumina rectangles within the 50-nm-thick alumina background (Fig. A.6b). Again using EBL, we wrote desired device patterns over the rectangular recess defined in the previous step. This writing step produces the device patterns that will eventually be transferred into the Ag film. Following development of the device pattern, we deposited 150 nm of alumina via ALD onto the resist. Due to the conformal nature of the ALD process, any feature with a width less than twice the deposited alumina thickness will be filled in. The resulting thickness of the alumina film in the filled-in regions will therefore be greater than that of the unpatterned regions by approximately the thickness of the electron-beam resist, as shown schematically in Fig. A.6c.

With the pattern of the desired devices defined, we proceeded to transfer the pattern into the silver film. We removed the 150-nm-thick alumina film on top of the resist using RIE, leaving only the unexposed resist and the alumina that fills the exposed areas of the resist (Fig. A.6d). The residual electron-beam resist was then removed, and another BCl_3-Cl_2 etch

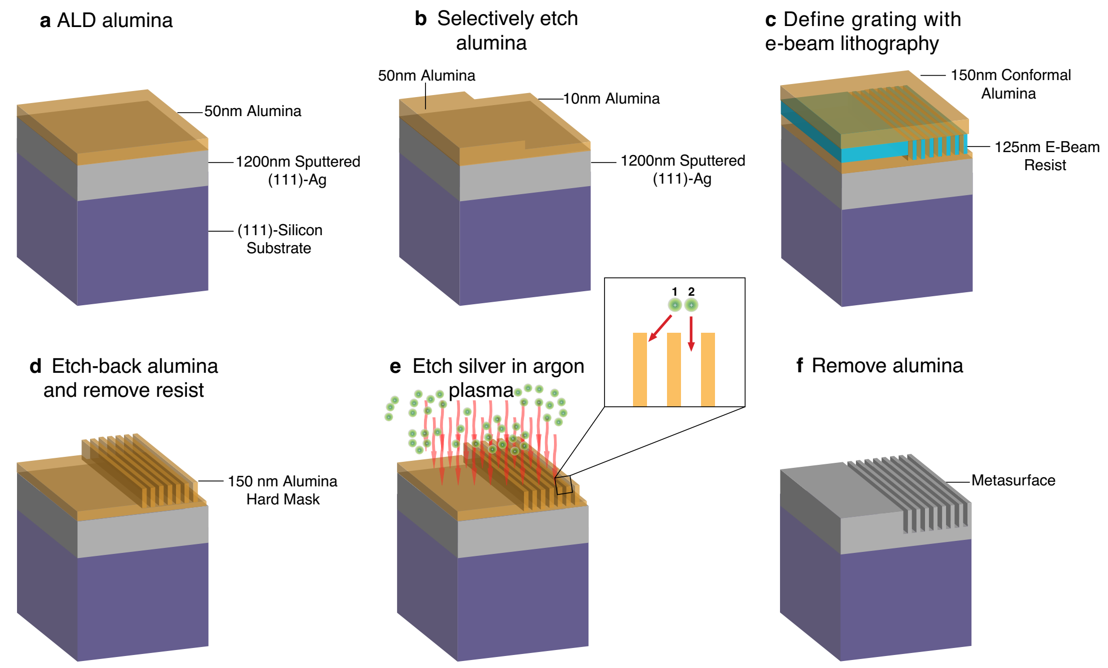

Figure A.6: Schematic of device fabrication process. **a-f**, The process for fabricating HMSs. Refer to the text for description.

step was used to thin the 10-nm-thick alumina between the slabs to approximately 2-nm thickness. Next, the pattern defined by the alumina hard mask was transferred into the silver film using argon plasma. Along with low pressure (4 mTorr) and high bias voltage, the height of the alumina mask was crucial in achieving requisite anisotropy in the etched silver. This process is shown schematically in the inset of Fig. A.6e: ion 1, with lateral momentum, collides with the alumina slabs rather than the silver film, while ion 2, with mainly vertical momentum, impacts the silver film, causing the pattern transfer. In the final step of the process, the alumina hard mask was removed in 49% hydrofluoric acid (Fig. A.6f).

A.4 Analysis of the HMS with a coupled mode theory

We can gain physical insight into the transition from hyperbolic to elliptical dispersion using a simple physical picture. At short wavelengths, the plasmonic modes are tightly confined to the ridges of the grating. This situation is qualitatively similar to an array of parallel nanowires, which constitutes an HMS. In the long wavelength limit, on the other hand, the modes are only weakly confined and the grating can be considered a perturbation to a flat surface. This suggests that the dispersion of the grating will be elliptical at long wavelengths. In between the two regimes, there must exist an intermediate wavelength at which the isofrequency contour becomes relatively flat leading to a minimally dispersive medium.

We use a coupled mode theory to show that an array of nanowires indeed exhibits hyperbolic dispersion. Here we consider an array of parallel nanowires of radius r separated by a distance a as illustrated in Fig. A.7. In isolation, each nanowire supports a number of plasmonic modes depending on the radius of the nanowire. At sufficiently small radii, the dynamics are dominated by the lowest order mode owing to high propagation loss of the higher order

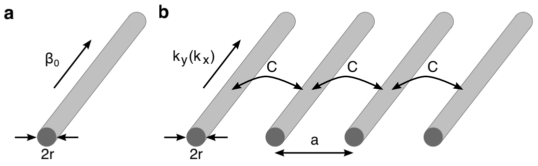

Figure A.7: Model of an HMS as coupled nanowires. **a**, A single nanowire of radius r supports a plasmonic mode with propagation constant β_0. b, An array of parallel nanowires separated by a distance a. Each wire is coupled to its nearest neighbor with a coupling constant C, giving rise to the dispersion $k_y\left(k_x\right)$ in Eq. (3).

modess[176]. Assuming that the wires are only weakly coupled, it is possible to describe the propagation using a coupled mode theory. The starting point of the coupled mode theory is to approximate the electric field of the coupled waveguides by

$$\vec{E}(\vec{r})=\sum_j b_j(y)\vec{E}_j(x,z)e^{i\beta_0 y} \tag{A.6}$$

where $\vec{E}_j(x,z)$ is the transverse mode profile of the j^{th} and β_0 is the propagation constant associated with the mode. The coefficients $b_j(y)$ satisfy the differential equation

$$-i\frac{d}{dy}b_j(y)=C\left[b_{j-1}(y)+b_{j+1}(y)\right] \tag{A.7}$$

The equation can be readily solved by setting $b_j(y)\propto\exp\left(i\beta(k_x)y+ik_xja\right)$, where $\beta(k_x)=2C\cos(k_xa)$. By substituting back into the differential equation, we obtain the dispersion relationship

$$k_y(k_x) = \beta_0 + 2C\cos(k_x a) \tag{A.8}$$

The coupling parameter C can be computed from the mode profile of a single nanowire. One obtains $C = \kappa/P$, where

$$\kappa = \frac{1}{4}\omega\varepsilon_0 \left(\varepsilon_{Ag} - \varepsilon_{air}\right) \int \vec{E}_j^* \cdot \vec{E}_{j_1} dxdz \tag{A.9}$$

and

$$P = \frac{1}{4}\int \left(\vec{E}_j^* \times \vec{H}_j + \vec{E}_j \times \vec{H}_j^*\right) \hat{y} dxdz \tag{A.10}$$

Both integrals are to be taken over the cross-section of the j^{th} wire. A numerical evaluation of the above expressions is shown in Fig. A.8. Since the coupling constant is negative, the propagation constant $k_x(k_y)$ is at a minimum at $k_x = 0$ and the dispersion is therefore hyperbolic. We point out that the negative coupling constant is not specific to nanowires but can also be found in different geometries such as parallel plates.

A.5 Difference in far field scattering rates at input and output of D1

At the entrance of D1, the bulk silver is at the same height as the top of the ridges of the HMS. At the output, the bulk silver is etched down such that its height corresponds to the base of the ridges. Since the SPPs are concentrated at the top of the ridges, this leads to increased scattering efficiency at the output, resulting in the greater measured intensity at the output versus the input for $\lambda > 550$ nm (Fig. 2.2, Fig. A.9).

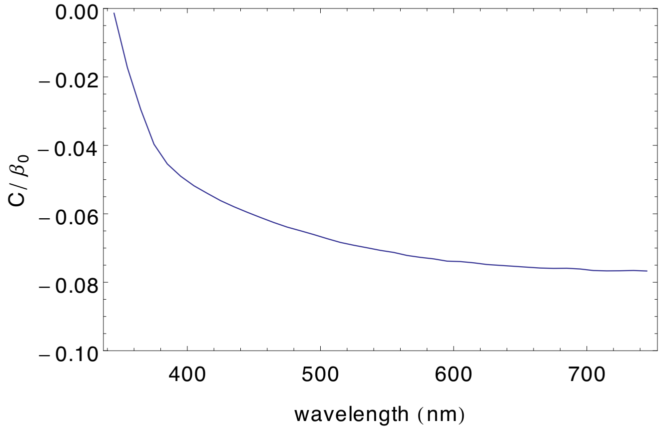

Figure A.8: Ratio of the coupling constant C to the propagation constant β_0 of a nanowire array. The calculation was performed for $r = 45$ nm and $a = 150$ nm.

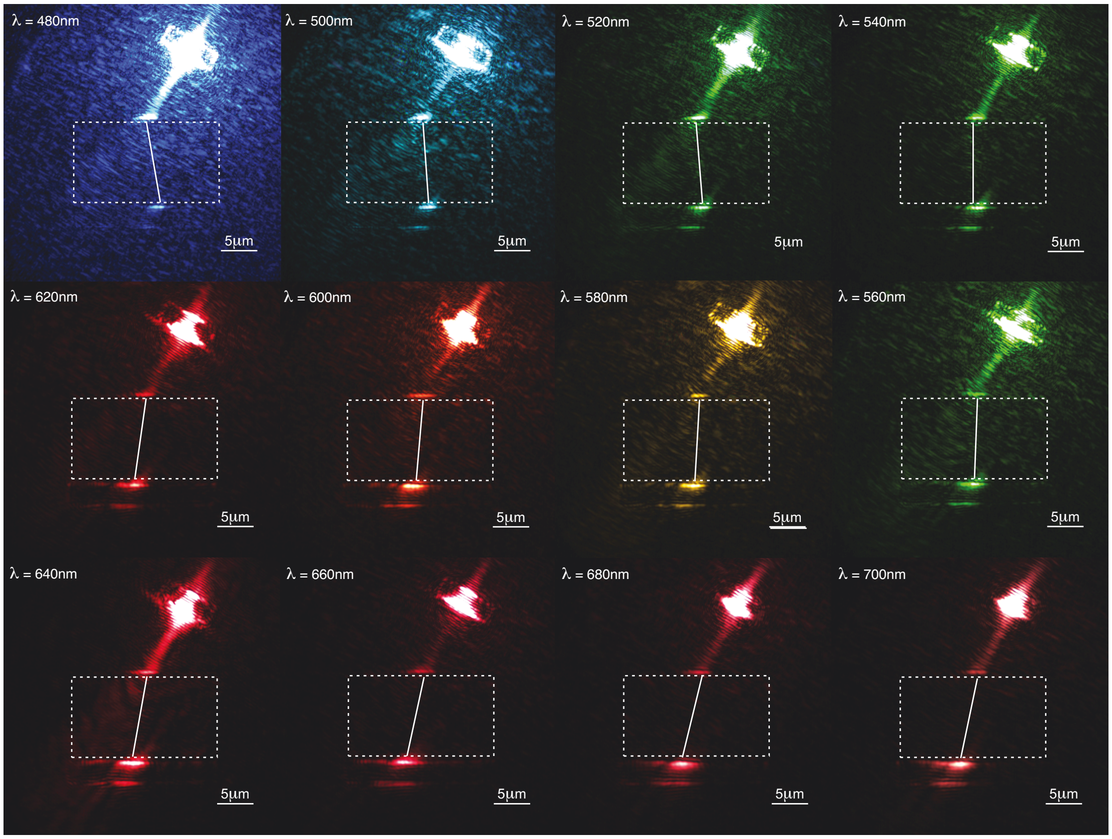

Figure A.9: Compiled refraction images. A compilation of images showing refraction at the flat silver film/SPP-HMS interface for an input angle of 35° and wavelengths ranging from 480 nm to 700 nm.

A.6 Refraction from an SPP-hyperbolic metasurface

To rigorously quantify the angle of refraction of the device D1 presented in Fig. 2.2b, the image from a CMOS camera were processed using Image-J and MATLAB. The entire set of images used in this process is presented in Fig. A.9. Specifically, the intensity profiles over the full width of the flat silver film-metasurface interface were extracted using Image-J (see Chapter 2 Fig. 2.2a for an SEM image of D1). This intensity profiles were then fit to a Gaussian function with a constant intensity offset to account for the laser-speckle background. From these fits, we determined the $x-$coordinates of in- and out-coupling spots, which were then used to calculate the angle of refraction. The experimentally measured refraction angles were in close agreement with those from the finite-difference time-domain (FDTD) simulations (Fig. 2.2b). Just like bulk hyperbolic metamaterials, HMSs are predicted to exhibit all-angle negative refraction11. To test this prediction in our SPP-HMS device, we fabricated additional structures similar to D1 but with varied SPP incident angle (Fig. A.10). As shown in Fig. A.10, we observe negative refraction for $\lambda < 540$ nm when the incident angles are 15° and 25° (in addition to 35° presented in Chapter 2 (Fig. 2.2d)).

A.7 Tuning of metasurface properties

The modes of the SPP-HMS are tightly confined surface waves; therefore, the optical response should be strongly affected by modifications of the local dielectric environment and geometry of the metasurface. This suggests straightforward tuning of the SPP-HMS dispersion via varying fabrication parameters (i.e., slab width, pitch or depth) or subsequent dielectric deposition. This tuning provides control over the HMS properties.

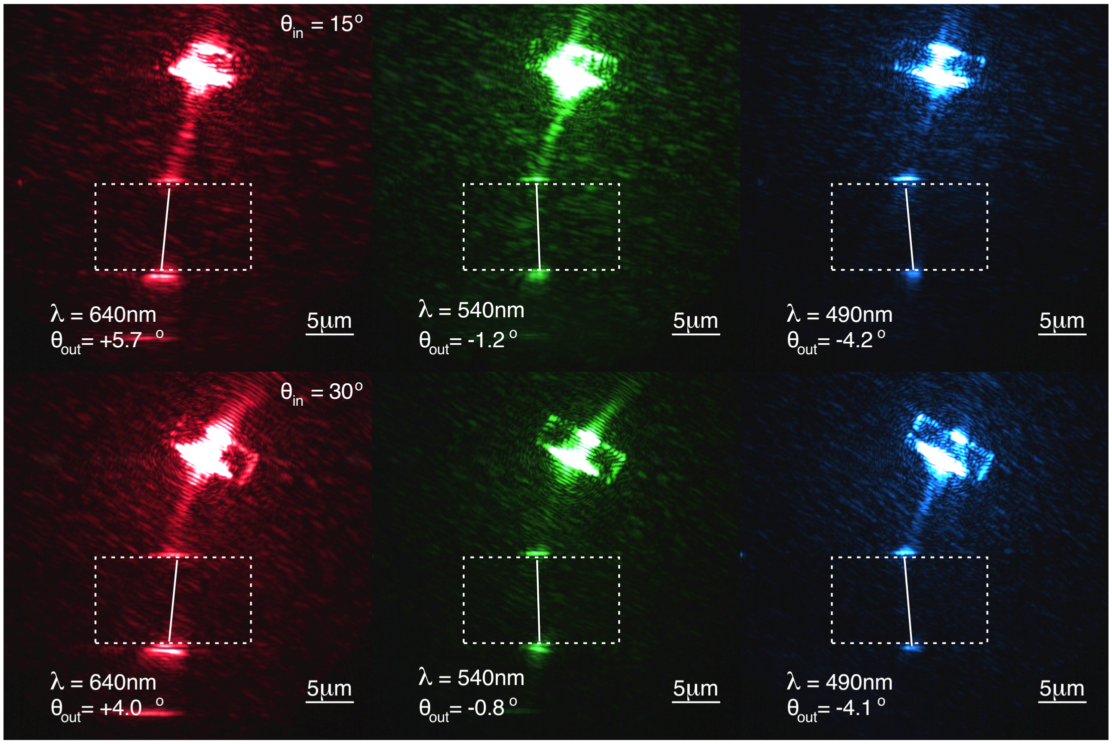

Figure A.10: Dependence of refraction on input angle at the silver-HMS interface. A set of images showing refraction from an SPP-HMS for input angles of 15° (top) and 30° (bottom). We observe the same three regimes—elliptical, flat and hyperbolic—seen for the input angle of 35° (Fig. 2.2c).

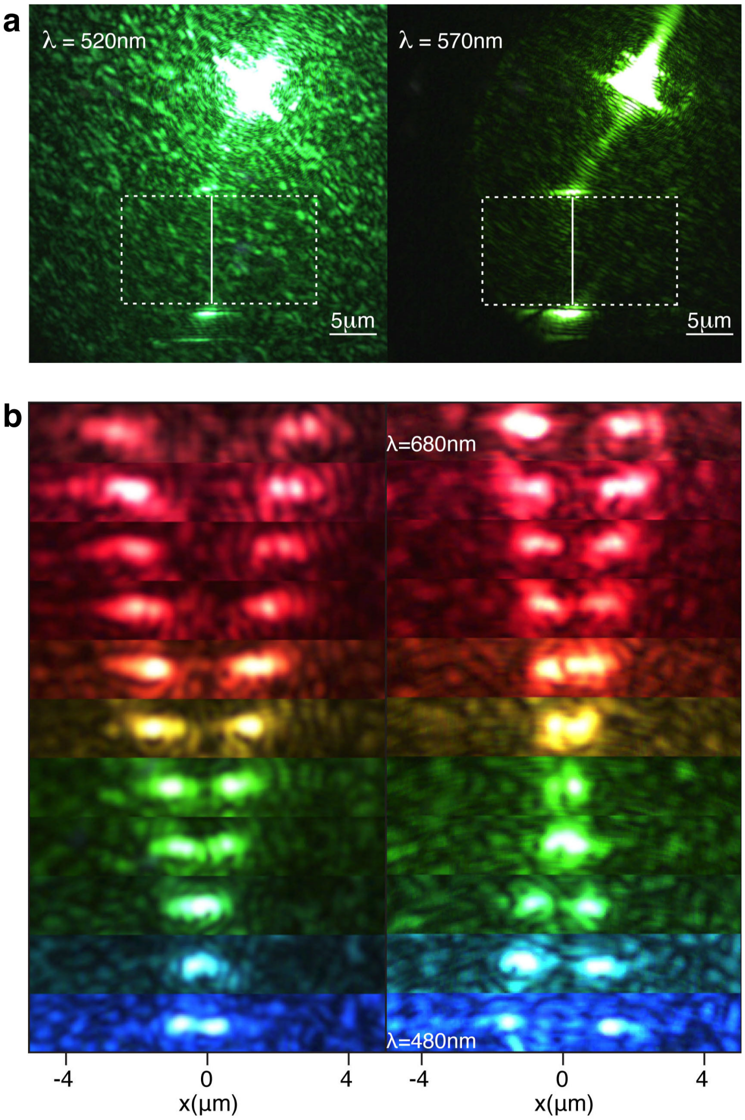

Figure A.11: Tuning of λ_T. **a**, λ_T tuned by pitch difference: 150 nm and 175 nm for left and right respectively. **b**, The spin-dependent propagation before (left) and after (right) the deposition of 5 nm-thick alumina.

Figure A.11a shows λ_T (at which the dispersion relation changes from elliptic to hyperbolic) for two different device geometries. The device shown in the left panel of Fig. A.11a has a pitch of 150 nm, whereas the device in the right panel has a pitch of 175 nm (the ratio of silver to air in both devices are approximately equal). Owing to the larger pitch and therefore deeper etching profile, λ_T for the 175-nm pitch device is red-shifted with respect to the 150-nm pitch device. To probe the effect of dielectric deposition on an SPP-HMS, we first characterized the SPP dispersion for a bare silver/air grating (Fig. A.11b, left panel) and determined that the hyperbolic-to-elliptical transition occurred at $\lambda_T \approx 500$ nm. We then deposited 5 nm of alumina (refractive index = 1.63) on top of the device via ALD on the metasurface. This alumina deposition produced a red shift of λ_T by 70 nm (Fig. A.11b, right panel), confirming the high sensitivity of the SPP-HMS to dielectric modifications.

A.8 Simulations

At λ_T, the flat dispersion curve dictates that all SPPs propagate parallel to the silver ridges (Fig. 2.4b) and SPPs excited on a single silver ridge stay confined to the same ridge despite its sub-wavelength width ($\lambda/6$). This effect is observed experimentally in Fig. 3. FDTD simulations confirm diffraction-free propagation, Fig. A.12. In the simulations, a z-axis (out-of-plane) dipole was evanescently coupled to the central ridge of the metasurface to excite SPPs with all k-vectors in the metasurface. After 10-μm propagation, 80% of the SPP intensity remains confined to the central ridge.

In device D3, we used an array of cylindrical rods to out-couple propagating SPPs into the far field. In principle, if the out-coupling structure has the same $x-$, $y-$, and $z-$dimensions, it should scatter E_x, E_y, and E_z with equal strength, and preserve the phase relationships

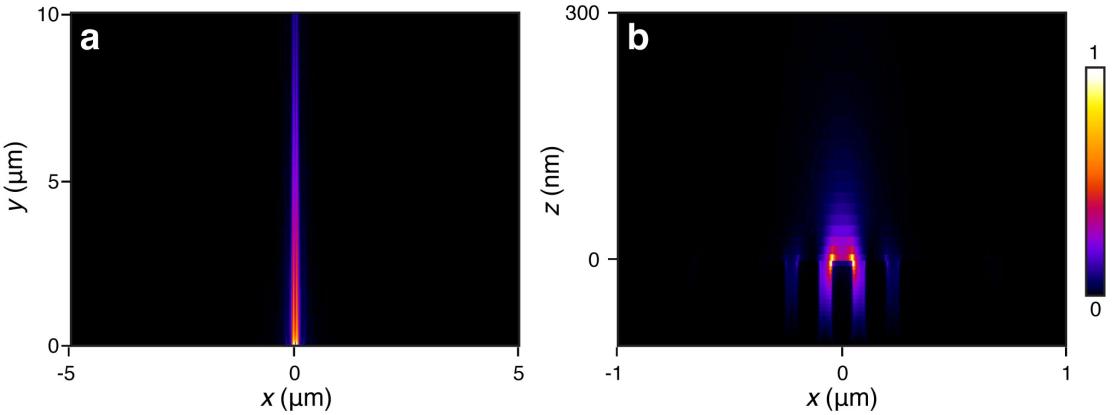

Figure A.12: Diffractionless propagation of SPPs. **a** The simulated electric-field intensity of SPPs propagating on an SPP-HMS at $\lambda_T = 547$ nm. The dipole source is located at $(x, y, z) = (0, 0, 10)$ nm **b**, An $x - z$ cross-section of the SPP intensity after $10 - \mu$m propagation.

between them. Additionally, this effect should be wavelength independent. Therefore, an SPP with $\sigma^{\pm}_{SPP} = E_x \pm iE_y$ incident on the array should scatter to the far-field with electric field $\sigma^{\pm}_{FF} = E_x \pm iE_y$.

We used FDTD simulations to study the performance of our out-coupling structures, which consisted of cylindrical rods with a diameter of 140 nm and a height of 90 nm (Fig. A.13). In the simulations, a plane wave propagating along the y-axis with polarization $\sigma^{\pm} = E_x \pm iE_y$ was scattered off the array, and we monitored the far field polarization. These results indicate that over the range of experimentally measured wavelengths (480 to 700 nm), our out-coupling structure indeed converts $\sigma\pm_{SPP}$ to $\sigma\pm_{FF}$ with fidelity as high as 90%. Simulated mode index of SPPs in the HMS

In metamaterials, losses are characterized by the figure of merit $|n/\kappa|$. We performed FDTD simulations with the optical constants measured from ellipsometry to determine the complex mode index of SPP plane waves propagating parallel to the silver ridges. From those values we determined the wavelength dependent quantity $|n/\kappa|$ Figs. A.14a-c). In the hyperbolic

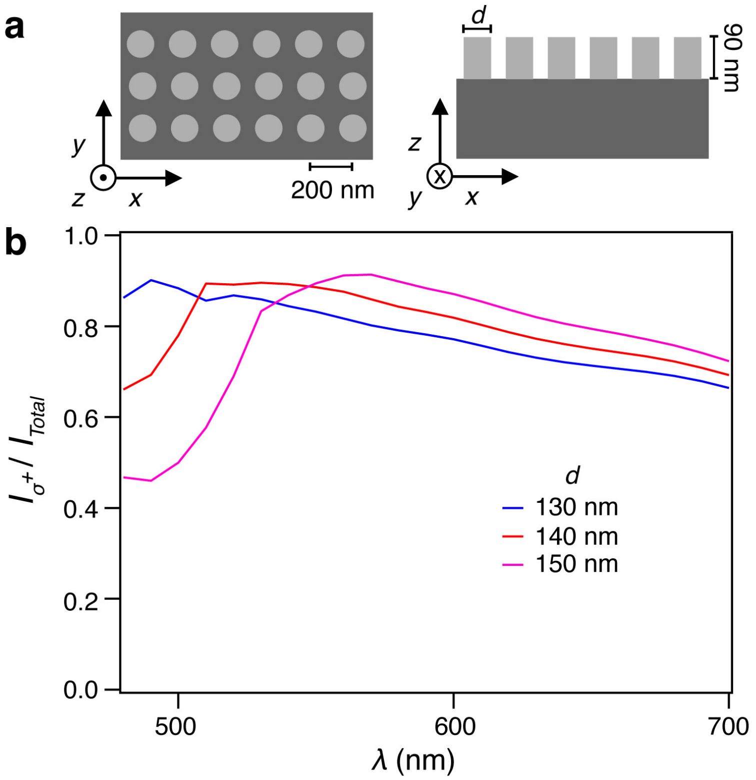

Figure A.13: Out-coupling geometry for scattering SPPs to the far field. **a** A diagram of out-coupling structure; light grey indicates silver rods with diameter d, dark grey indicates silver substrate. **b** The simulated degree of far-field circular polarization defined as ratio of σ^+ scattered intensity to the total scattered intensity.

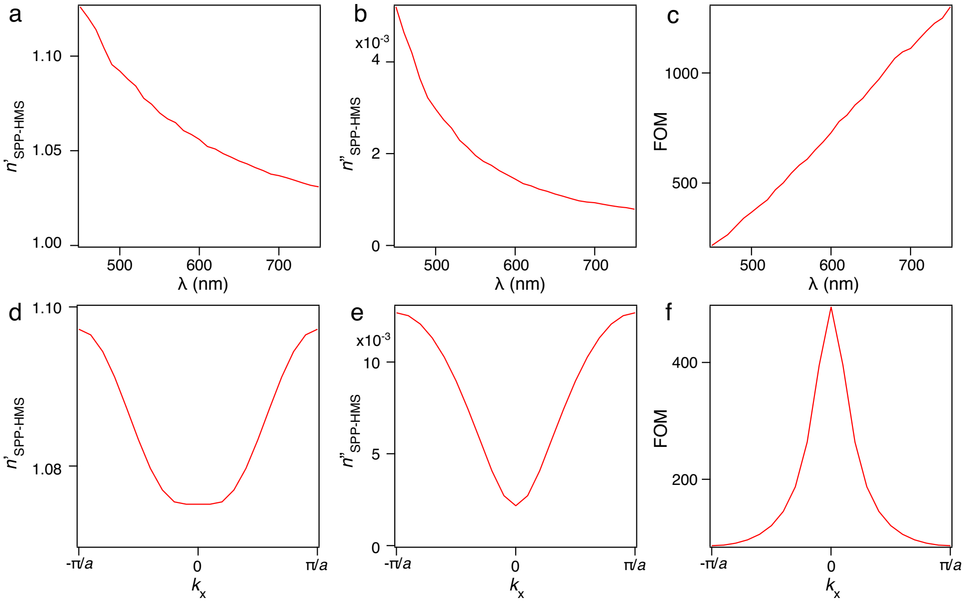

Figure A.14: Simulated mode indexes of our HMS and ratio of real to imaginary parts of the mode index. a,d The simulated real part and **b,e** imaginary part of SPP effective mode index in our SPP-HMS. **c**, The corresponding ratio of real to imaginary mode index $|n/\kappa|$ vs. wavelength λ at $k_x = 0$ and **f**, k_x at $\lambda = 540$ nm. The simulated HMS pitch $a = 150$ nm, $w = 90$ nm, and $h = 80$ nm.

regime, $\lambda \leq 550$ nm, this quantity reaches a value of 500, two orders of magnitude higher than values reported in other metamaterials[11].

Since our SPP-HMS is highly anisotropic, we expect $|n/\kappa|$ to have wavevector dependence. Simulated values of the k_x-dependent complex mode index and $|n/\kappa|$ at $\lambda = 540$ nm are shown in Figs. A.14d-f, with values of $|n/\kappa|$ ranging from 80 at the Brillouin zone edges to 500 at $k_x = 0$.

A.9 Experimental measurement of the propagation lengths of SPPs in the HMS

To measure the propagation length L_p of SPPs in the HMS, we fabricated HMSs of varying lengths, with identical in- and out-coupling structures on both edges of the HMS (illustrated schematically in Fig. A.15a). A SEM image of a typical structure is presented in Fig. A.15b. We utilized a cylindrical lens to elongate the excitation laser along the $x-$axis to preferentially excite SPPs with $k_x = 0$. We illuminated the in-coupling structures with identical input intensity and recorded an image of the far-field scattering at the out-coupling structure. Representative experimental data at $\lambda = 550$ nm is presented in Fig. A.15c-e. The images were captured with a CMOS camera and analyzed with Imagej and Igor Pro. The intensity was integrated over the entire out-coupling structure. To account for variation in the in- and out-coupling structures of each device, the measurement was performed on 5 different devices for each HMS length. Then, the propagation length was determined by an exponential fit to the data, Fig. A.15f. Results of these measurements are presented in Fig. 2.2c. We find that the SPP propagation length reaches up to 16 μm in the hyperbolic regime. This is reduced from a simulated maximum of 22 μm. However, this value is two orders of magnitude larger than in bulk visible-frequency hyperbolic metamaterials, which exhibit propagation lengths on the order of 100 nm[48].

A.10 Simulation of the plasmonic spin-Hall effect (PSHE)

FDTD simulations reproduce the experimental observation of the PSHE, as shown in Fig. 2.5. In the simulations, a $z-$axis (out-of-plane) dipole was evanescently coupled to the metasur-

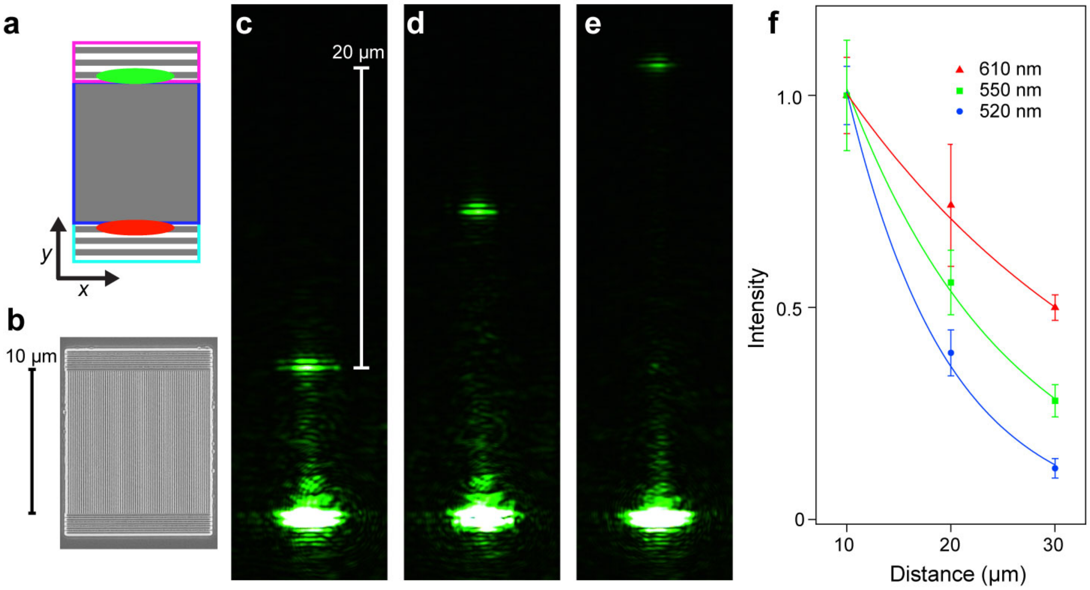

Figure A.15: Measurement of the propagation length of SPPs in our HMS. **a** A schematic of the devices used to measure propagation length. The cyan box indicates the in-coupling structure, the blue box the region of the silver/air grating, and the magenta box the out-coupling structure. The red ellipse indicates the laser excitation spot, and the green ellipse indicates the out-coupling spot. **b** An SEM image of a device with a $10\ \mu$m-long silver/air grating. **c,d,e** Far-field imaging of scattered SPPs after (c) 10 μm, (d) 20 μm, and (e) 30 μm propagation in the silver/air grating at $\lambda = 550$ nm. **f** The integrated intensity at the out-coupling structure as a function of silver/air grating length. The markers indicate experimentally measured values at $\lambda = 610$ nm (red), $\lambda = 550$ nm (green), and $\lambda = 520$ nm (blue). The solid lines are exponential fits to the data, which are used to determine propagation lengths, (Fig. 2c, blue). For each wavelength, the intensities are normalized to the value at 10 μm.

face to excite SPPs with all k-vectors in the metasurface. To illustrate the plasmonic spin-Hall effect, we plot the electric field value of the propagating SPPs with a 2D $x - y$ electric-field monitor, 10 nm above the metasurface. From the total field collected via the monitor, we divided the SPP electric field into its respective circularly-polarized components σ^+ and σ^- and determined the intensity

$$I_\sigma^\pm = |E_x + iE_z|^2 + |E_y|^2. \tag{A.11}$$

At $\lambda = 680$ nm σ^+-polarized SPPs propagate in the +y, -x direction (Fig. 2.5a), while σ^- polarized SPPs propagate in the +y, +x direction (Fig. 2.5b). Figures 2.5c and d present the $x - z$ cross sections of the SPP intensity at $y = 10$ μm for multiple wavelengths. The simulations show that the sign of the spin-Hall effect changes at $\lambda_T = 550$ nm, in agreement with experimental observations in Figs. 2.4e-h.

The FDTD simulations also allow us to probe the local field intensity of the SPPs in detail. Figures. 2.5e and f present a close-up of the SPP field at $\lambda = 600$ nm, while Fig. 2.5g presents the degree of polarization defined as $I_{\sigma+}/I_{total}$ The circular polarization varies spatially and is strongest 30 40 nm above the grating, reaching values as high as 98%. Figures 2.5h and i present the intensity of the SPP field integrated over the $z-$axis at $\lambda = 600$ nm, and Fig. 2.5j presents the resulting integrated polarization, which is as high as 87%.

A.11 DEFINITION OF SPP CIRCULAR POLARIZATION IN THE HMS

The standard definition of circular polarization is the electric field rotation in a plane orthogonal to the direction of propagation. Due to the equifrequency contours of the HMS, SPPs are restricted to propagate almost entirely along the $y-$axis, with maximum deviation of $\pm 10°$.

Therefore, the $x - z$ plane is nearly perpendicular to the plane of propagation for all frequencies, and we define the SPP circular polarization as rotation in the $x - z$ plane. If we take into account the small deviation in propagation from the $y-$axis, the integrated degree of polarization increases slightly from 87% to 88% at $\lambda = 600$ nm.

A.12 Simulation of scattered far-field intensity from circularly polarized SPPs.

The degree of far-field circular polarization is determined by both the magnitude of SPP circular polarization and the fidelity with which the out-coupling array transfers the polarization into the far field. We used FDTD to simulate this whole process (Fig. A.16). SPPs were excited by a dipole polarized along the $z-$axis and evanescently coupled to the metasurface (Fig. A.16a, red circle). The spatial separation of the σ^+ and σ^- modes allowed us to individually probe their scattering off the out-coupling array (see Fig. A.13) via far-field intensity monitors (FFIMs) placed at $x = \pm 3$ μm (+xFFIM and -xFFIM, Fig. A.16a). Data from $-x$FFIM shows that σ^+ SPPs maintain their polarization in the far-field (Figs. A.16a and b). The reciprocal case is shown in Figs. A.16d and e. The simulations show that the measureable far-field polarization is up to 78%, in close agreement with our experimentally observed 80% polarization (Figs. 2.4g and h)

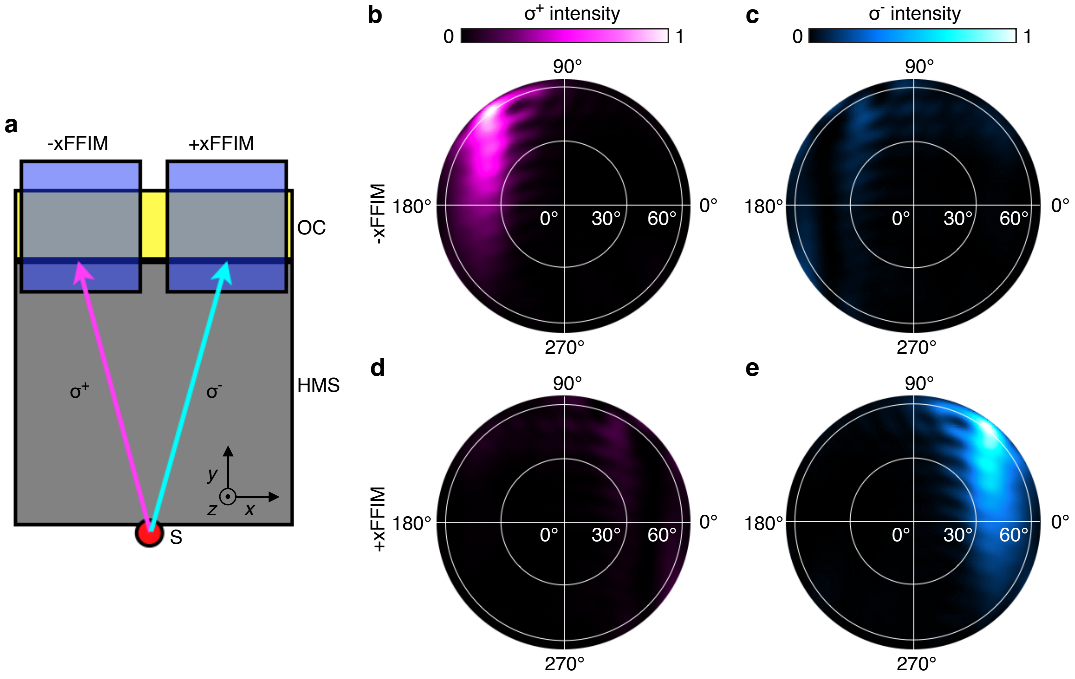

Figure A.16: Simulation of circularly polarized SPP scattering off our out-coupling array. **a** A schematic showing the simulated geometry. SPPs are excited with a dipole source at $\lambda = 640$ nm. The σ^+ (magenta) and σ^- (cyan) SPPs propagate on the HMS (gray) and scatter off the out-coupling structure (yellow). The far-field intensity monitors (FFIM) are placed at $x = -3$ μm (-xFFIM) and $x = 3$ μm (+xFFIM) (blue shaded regions) to record the scattered far-field electric-field intensity. b-e, Far-field intensity of the scattered electric field taken from (b, c) -xFFIM and (d, e) +xFFIM, and measured in (b, d) σ^+ and (c, e) σ^-.

A.13 Simulation of the propagation lengths of SPPs in the HMS

From the simulated mode index, Fig. A.14a,b, we can determine the propagation length Lp of SPPs in the HMS for $k_x = 0$, defined as

$$L_P = \frac{\lambda_0}{4\pi\kappa} \tag{A.12}$$

where λ_0 is the free space wavelength. Results of the calculation are presented Fig. 2.2c, black. In the hyperbolic regime, $\lambda \leq 550$ nm, the simulated L_o reaches a maximum of 22 μm.

A.14 Effect of rounded edges on the HMS dispersion

Due to imperfect fabrication, there is rounding of the edges of the silver ridges that constitute the HMS (Figs. 2.1d and e). The effect of rounded edges and non-vertical sidewalls on the dispersion of individual ridges was previously addressed[51], and no significant impact on the dispersion was observed. We extended this previous work with full FDTD simulations of our HMSs with and without rounded edges to determine the effect on the isofrequency contours (Fig. A.17). With the edges of the ridges rounded with a radius of curvature of 15 nm, the simulations clearly show that the resulting isofrequency contour still exhibits hyperbolic and elliptical dispersion regimes. The simulations also show that the main effect of the rounding is a slight blue-shift of the hyperbolic-to-elliptical transition by 10 nm (from 550 nm to 540 nm).

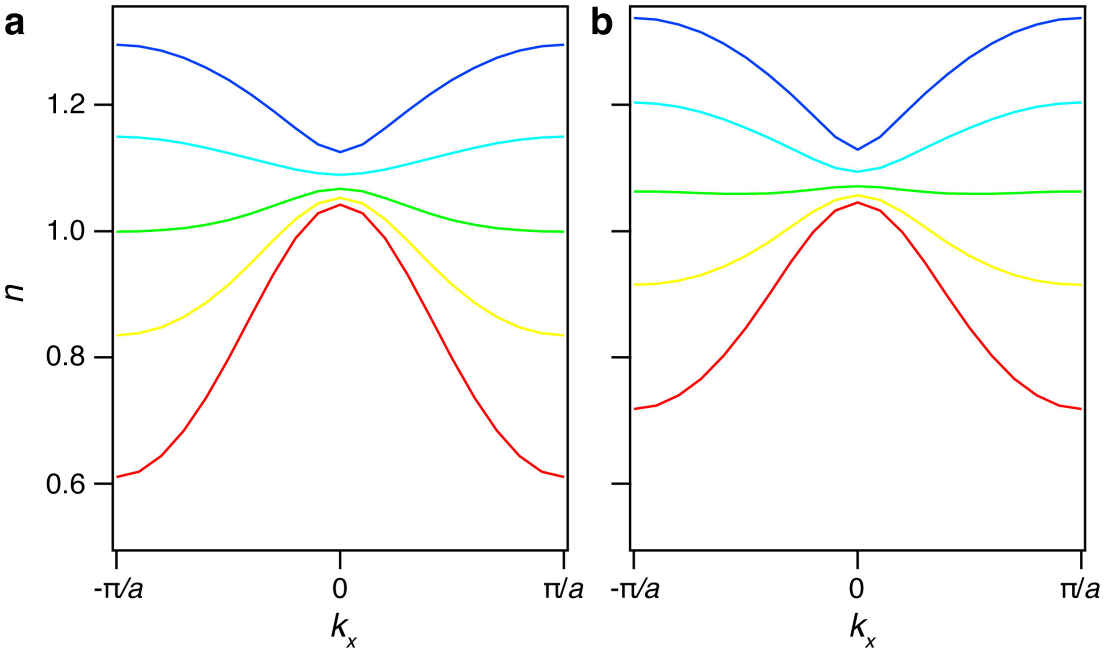

Figure A.17: Effect of rounded edges on the HMS dispersion. a,b Isofrequency contours at $\lambda = 450$ nm (blue), 500 nm (cyan), 550 nm (green), 600 nm (yellow) and 650 nm (red) for a HMS (a) with and (b) without rounded edges. The simulated HMS pitch $a = 150$ nm, $w = 90$ nm, and $h = 80$ nm. In the simulations, the edges are rounded with a radius of 15 nm.

B

Supplemental information: Broadband high-efficiency dielectric metasurfaces for the visible spectrum

B.1 OPTICAL CHARACTERIZATION

We deposit blanket TiO_2 films via ALD onto silicon substrates in order to prepare samples for spectroscopic ellipsometry (SE) measurements. When more than one material is present for SE measurements, a model must be developed in order to extract the complex refractive index, $\tilde{n}(\omega) = n(\omega) + ik(\omega)$, of a specific layer. In our case, we use a standard model for the substrate and we apply the Tauc-Lorentz (TL) model for amorphous materials to the TiO_2 film.

The TL model that we use to extract the optical constants of our ALD TiO_2 is a combination of the normal quantum mechanical Lorentz oscillator and the model Tauc derived for the imaginary part of the dielectric constant for amorphous materials above the bandgap. Tauc derived this model assuming a set of N non-interacting oscillators per unit volume and arrived at the following expression for the imaginary dielectric constant

$$\varepsilon_2 = \frac{A_t \left(E - E_g\right)^2}{E^2} \tag{B.1}$$

where E is energy, E_g is the transition energy and A_T is the amplitude of the oscillator.

For the Lorentz oscillator, the imaginary part of the dielectric function is given by

$$\varepsilon_2 = 2nk = \frac{A_L E_0 C E}{\left(E^2 - E_0^2\right)^2 + C^2 + E^2} \tag{B.2}$$

where A_L is the oscillator amplitude, E_0 is the central energy of the resonator and C accounts for broadening around E_0. Jellison and Modine combined Eq. (B.1) and (B.2) in order to account for the short comings present in each model, leading to the Tauc-Lorentz model for the dielectric constant

$$\varepsilon_2 = \begin{cases} \frac{A E_0 C (E-E_g)^2}{\left(E^2-E_0^2\right)^2 + C^2 + E^2}, & E > E_g \\ 0, & E \leq E_g \end{cases} \tag{B.3}$$

where $A = A_L A_T$ and we have defined the other fitting parameters above. The real part of the dielectric function is then obtained through Kramers-Kronig integration. The values of the four fitting parameters as well as the thickness of the film are shown in Table S1.

Table B.1: Ellipsometry fitting parameters for amorphous TiO_2

Thickness (nm)	67.43 ± 0.034
A (eV)	422.4 ± 18.4
C (eV)	1.434 ± 0.294
E_0 (eV)	3.819 ± 0.0304
E_g (eV)	3.456 ± 0.0079

Figure B.1 shows the raw ellipsometry data Ψ and Δ and the corresponding generated data based on the model discussed above. In addition, we tabulate the entire set of collected and for our TiO_2 film, from 242 nm to 1800 nm, included as a data sheet.

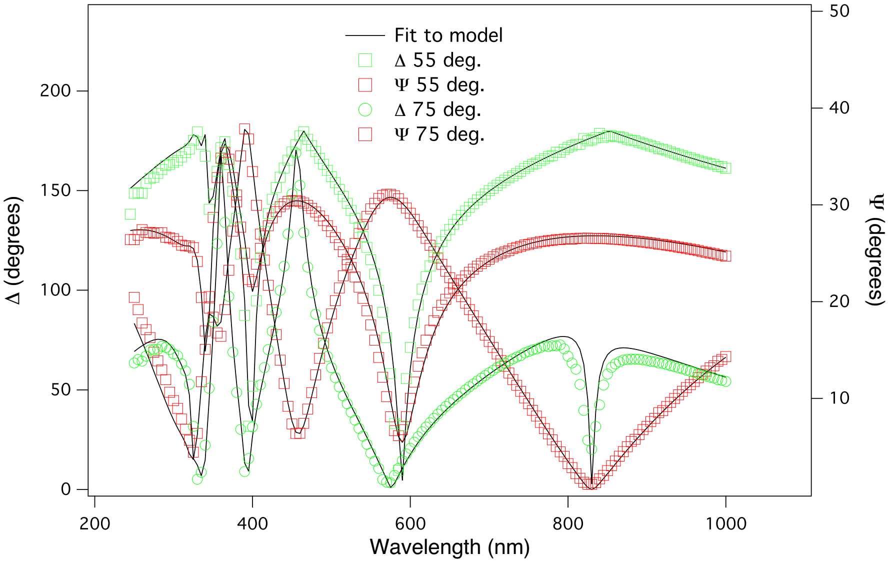

Figure B.1: Raw ellipsometry data used to determine the TiO_2 optical constants, Ψ and Δ, for the TiO_2 film on a silicon substrate as a function of wavelength. The green squares and circles are the values of Δ for angles of 55° and 75°, respectively. The red squares and circles are the Δ values for angles of 55° and 75°, respectively. The black lines are generated data from the model described above.

B.2 STRUCTURAL CHARACTERIZATION OF TiO_2 FILMS

As stated in in the 3 (discussion surrounding Figure 1b), the measured surface roughness of the TiO_2 films is on the order of surface roughness of the underlying substrate. Figure B.2 shows an AFM scan of the fused silica substrates used throughout this study. From the image, we extract an RMS roughness of 0.600 nm. This value is comparable to the measured surface roughness of a fused silica substrate with a film deposited on top (0.738 nm).

To determine the atomic structure of the ALD TiO_2, we use X-ray diffraction (D8 Discover, Bruker). As can be seen from Figure B.3, there are no signs of any diffraction peaks from TiO_2, even over the large angle scan. We measure this diffraction spectrum for a TiO_2 film on a 1 inch diameter fused silica substrate and align the substrate to the center of the x-ray

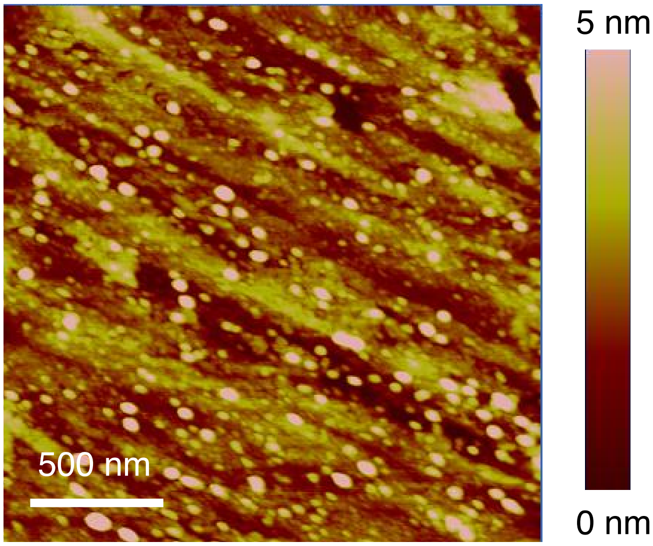

Figure B.2: Atomic force microscope image of bare glass substrate with a root mean squared roughness of 0.698 nm.

beam via a laser alignment mark. The absence of diffraction peaks indicates that the TiO_2 films that we deposit are amorphous. In contrast, if the film was polycrystalline the different polymorphs would generate diffraction peaks at 27.35° for rutile or 25° for anatase, for example.

B.3 Geometric phase

We use Pancharatnam-Berryphase optical elements (PBOE) to implement the holograms, as first detailed by Bomzon et al[100]. In our case, the individual elements are TiO_2 nanofins that act as discrete uniaxial crystals—they posses a structural birefringence that leads to a fast and slow optical axis, which introduces a phase difference between orthogonal components of the incident electrical field. It is then a spatially varying rotation of the fast axis of each nanofin that gives rise to the geometric phase accumulation, as detailed by Pancharatnam and Berry. Mathematically, in Jones calculus a waveplate with spatially varying fast axis, in the

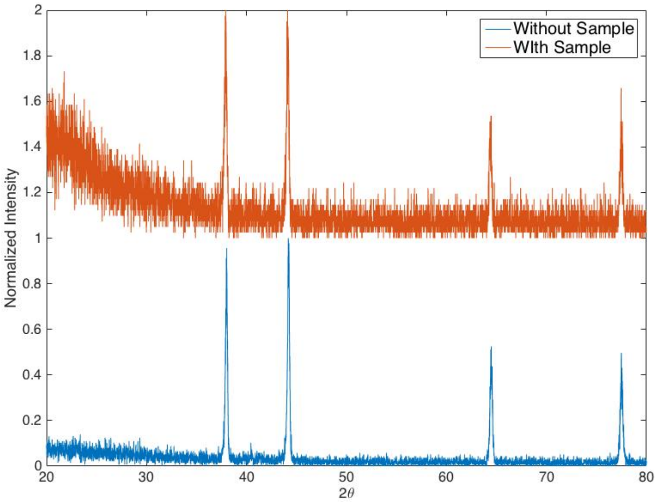

Figure B.3: X-ray diffraction of ALD TiO_2. There are no observable diffraction peaks from any TiO_2 polymorphs (red line). The peaks that appear in the scan result from the XRD stage as can be seen from comparing the scan with (red) and without (blue) the sample.

basis of left and right circularly polarized light (LCP and RCP, respectively), can be represented by the matrix

$$\mathbf{T}(x,y) = \cos\left(\frac{\phi}{2}\right)\begin{bmatrix} 1 & 0 \\ 0 & 1 \end{bmatrix} - i\sin\left(\frac{\phi}{2}\right)\begin{bmatrix} 0 & \exp\left[i2\theta(x,y)\right] \\ \exp\left[i2\theta(x,y)\right] & 0 \end{bmatrix} \tag{B.4}$$

Where ϕ is the retardance of the waveplate and $\theta(x,y)$ represents angle of rotation of a waveplate at position (x,y). The matrix above allows one to take a beam of arbitrary input polarization, $\mathbf{E_i}$, and find the output state as

$$\begin{split}\mathbf{E_0} = \mathbf{TE_i} = \cos\left(\frac{\phi}{2}\right)\mathbf{E}_i - \\ - i\sin\left(\frac{\phi}{2}\right)\left[\langle\mathbf{E}_i|R\rangle\exp\left(-i2\theta\right)|L\rangle + \langle\mathbf{E}_i|L\rangle\exp\left(i2\theta\right)|R\rangle\right]\end{split} \tag{B.5}$$

Where R and L represent the left and right circularly polarized basis vectors and $\langle \mathbf{E}_i | R, L \rangle$ is the projection of the input state onto right and left circular polarization basis, respectively. As shown by Bomzon *et al*, a particular case of interest occurs when the polarization of the input beam is RCP or LCP and the retardance is $\phi = \pi$ in this particular case, the efficiency of the system goes to unity and the output state for an input of RCP light becomes

$$\mathbf{E}_0 = \exp\left(-i2\theta\right) |L\rangle \tag{B.6}$$

Which shows that the output polarization is the inverse of the input polarization and the output of the beam has acquired a phase of -2θ. By the symmetry of the half waveplate, the angle θ can only vary from 0 to π but the additional factor of 2 means that by locally rotating the TiO_2 nanofins we are able to achieve full 2π phase coverage.

B.4 META-HOLOGRAM DESIGN, SIMULATION AND MEASUREMENT

In order to create the holographic images shown in the main text, we first take a binary image and produce a phase map via the Gerchberg-Saxton algorithm (Fig. B.4). We then run simulations (3D FDTD, Lumerical), using the measured TiO_2 optical data shown in Fig. 3.1a of the main text. At a fixed height of 600 nm, we optimize the length and widths of the nanofins to provide π phase difference between two orthogonal components of the electric field ($\mathbf{E}_x$ and $\mathbf{E}_z$), as required for maximum efficiency. As can be seen from Fig. B.5, at the design wavelengths of 480 nm, 532 nm and 660 nm, the TiO_2 nanofins provide a π phase delay between the x- and z-components of the electric field and thus act as a half waveplate.

While each individual nanofin must introduce a π phase shift to have a maximum conver-

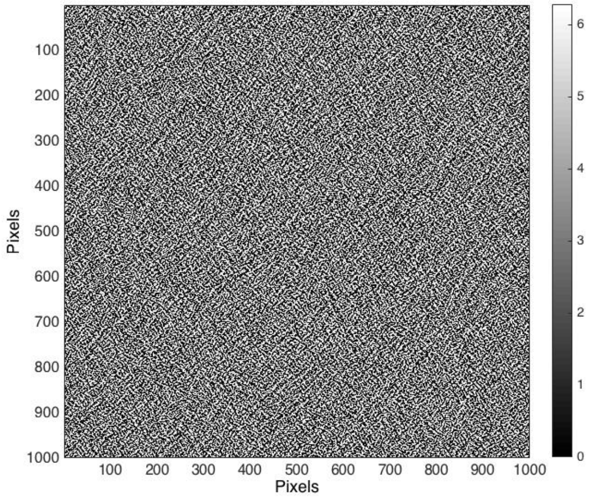

Figure B.4: Computed phase map of Harvard logo used to generate holograms for design wavelength of 480 nm. This phase information was translated to pillar rotations.

sion efficiency (ratio of power in the output circular polarization and the power in the input circular polarization with opposite handedness) the total efficiency of the devices also depends on the transmission of each of the nanofins. Figure B.6 shows the simulated transmission spectra of the TiO_2 nanofins used for design wavelengths of 480, 532 and 660 nm. The simulations were run with a source polarized parallel to the long or the short axis and the simulation setup is identical to that used in Figure B.7. The transmission remains relatively high for most designs throughout the entire visible. However, the design for 660 nm has relatively low transmission at shorter wavelengths. This is reflected in the measured efficiency and could be amended by allowing the optimization algorithm of the structures to search more exhaustively for a structure with higher transmission. Additionally, one could include antireflective coatings, taper the nanofins or explore using overlapping electric and magnetic resonances (Huygens metasurfaces) in order to maximize the efficiency of all devices. This is beyond the

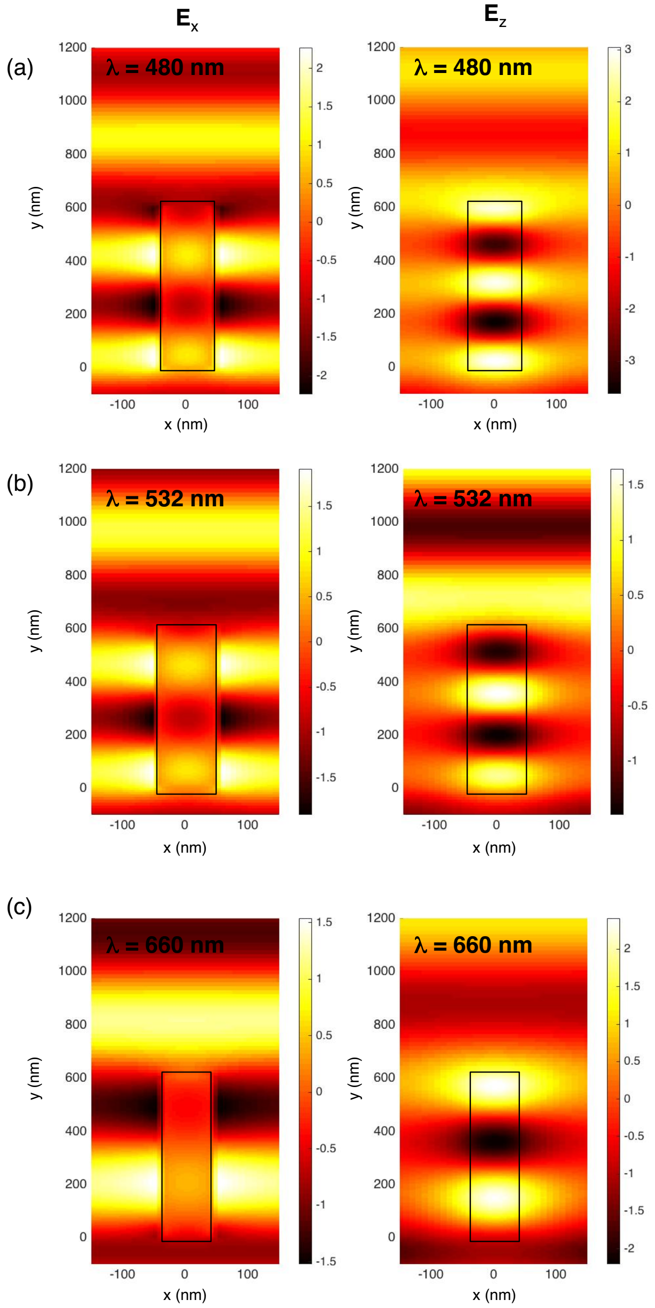

Figure B.5: Simulated electric field profiles at design wavelength. Real part of the $x-$component (left) and $z-$component (right) of the electric field at design wavelengths (a) 480 nm, (b) 532 nm and (c) 660 nm. All fields are shown through a cross section of the nanofin width and the nanofin is highlighted in each panel with a black box. One can see that the $x-$ and $z-$ components of the electric fields exiting the pillar, at each wavelength, are out of phase by π radians, as required for Pancharatnam-Berry phase. The TiO_2 pillars are placed on simulated on a glass substrate that occupies the half space below $y = 0$ and the wave propagates in the $+y$ direction scope of the current work.

We collect the holographic images shown in Fig. 3.4 of the Chapter 3 using the schematic shown in Fig. B.7. A super continuum laser provides access to wavelengths from 470 nm to 800 nm and is sent through a collimator, linear polarizer and quarter waveplate in order to inject circularly polarized light, as required by the PB phase (see discussion above). The circularly polarized light is then incident on the $300 \times 300\ \mu\text{m}^2$ meta-hologram contained on the sample and is converted to a holographic image with the opposite handedness of the input light. The light that passes through the sample is then sent through a 100× objective with a numerical aperture of 0.9. Because the spot of the collimated beam is larger than the area of the hologram, as well as to filter out any light that passes through the hologram but does not get converted (due to the TiO_2 nanofin not working as a perfect half waveplate, e.g.), we place a filter in cross polarization with respect to the input light after the objective. In the case of efficiency measurements, the intensity is then measured using a power meter. For the case of collecting the holographic images, we pass the light through a Bertrand lens in order to magnify the hologram.

B.5 SIMULATIONS FOR GENERAL TiO_2 METASURFACE

The process and TiO_2 material properties demonstrated in the main text are not limited to metasurfaces implemented using PB phase. In order to show that we can produce different types of metasurfaces, e.g., those shown by Arbabi et al[16], we simulate structures with the collected n and k data of our TiO_2 and nanostructure dimensions achievable with our process. The simulation results are shown in Fig. B.8. As we vary the diameter of a TiO_2 pillar, fixed at a height of 600 nm, we can produce phase differences from 0 to 2π without using geometric

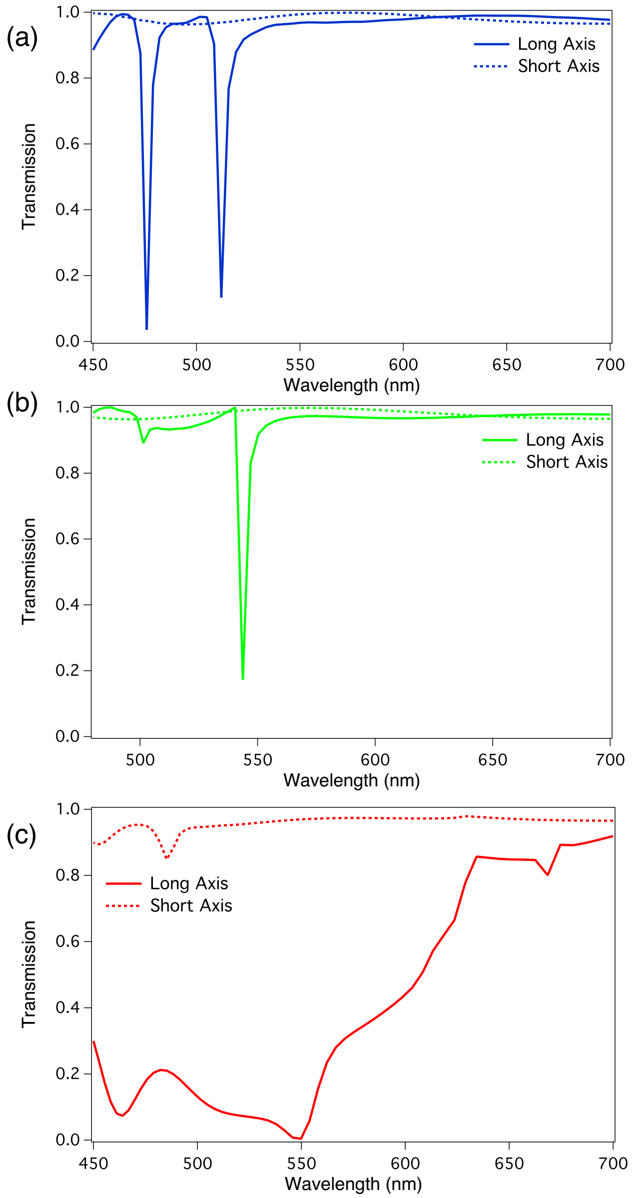

Figure B.6: Simulated transmission spectra for TiO$_2$ nanofins on a periodic lattice at design wavelengths of (a) 480 nm, (b) 532 nm and (c) 660 nm. In each panel, the solid (dashed) line corresponds to an incident plane wave source polarized along the long (short) axis of the rectangular nanofins.

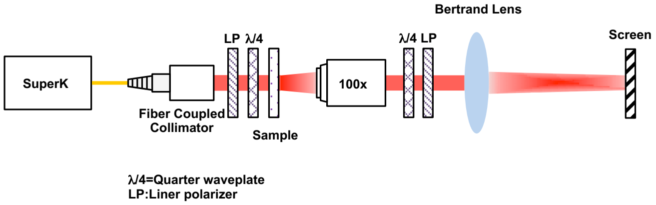

Figure B.7: Schematic of measurement setup for collecting holographic images. LP = linear polarizer; $\lambda/4$ =quarter waveplate; SuperK = Super continuum laser

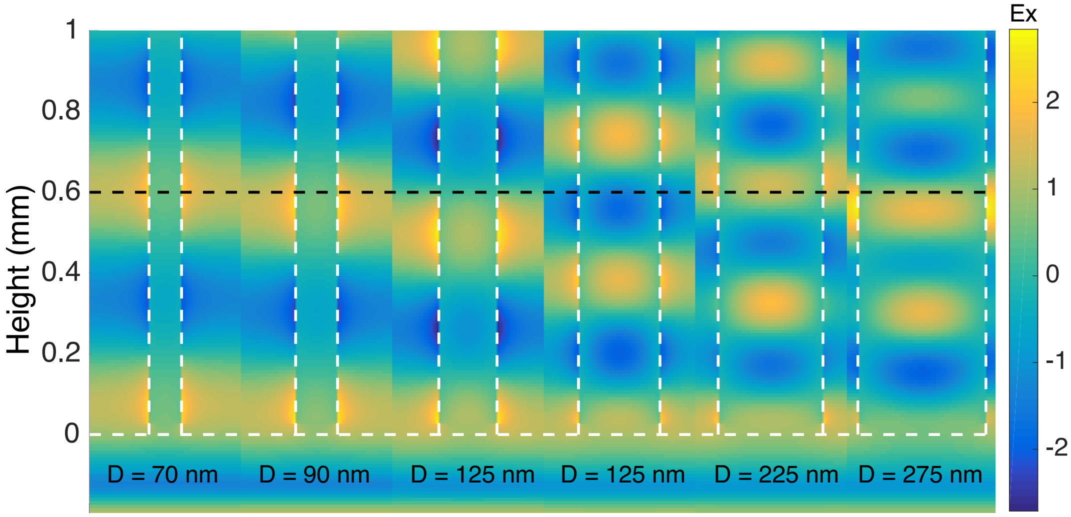

Figure B.8: Simulation of full 2π phase coverage using TiO_2 nanopillars with varied diameters. The white dashed lines show the placement of the TiO_2 nanopillars and the diameter of each pillar is listed below. Around each pillar a 325 nm cross section of the $x-$component of the electric field is included. The black dashed line is set to 600 nm, the height of the nanofins that we presented in the main text.

phase.

C

Supplemental material: Meta-lens at visible wavelengths

C.1 EXPERIMENTAL SETUP USED FOR FOCAL SPOT CHARACTERIZATION AND EFFICIENCY MEASUREMENT

The focal spots of the meta-lenses were characterized using a custom-built microscope consisting of a fiber-coupled laser source, linear polarizer, quarter-waveplate, and Olympus objective

(100×, NA = 0.9) paired with a tube lens (f = 180 mm) to form an image on a CMOS camera (Edmund EO-5012). The sources used were lasers (Ondax Inc.) with linewidths less than 100 MHz. For efficiency measurements, we used a supercontinuum laser (SuperK) as the source. The efficiency is defined as the ratio of the optical power of the focused beam to the optical power of the incident beam, as captured by a photodetector (Thorlabs S120C) located at the same position as the CMOS camera. The incident optical power was measured as the light passing through an aperture (aluminum on glass) with the same size as the meta-lens.

C.2 Measurement of intensity distribution at x-z plane

First, the Olympus objective is focused on the plane 20 μm in front of the focal plane ($z = 70$ μm) to capture the first image. The objective lens and tube lens are then successively moved toward the focal plane. An image is captured at each 500 nm increment. This process is repeated up to $z = 110$ μm, 20 μm beyond the focal plane. Finally, the intensity distributions of all captured images, along the $x - z$ plane, are stitched together to visualize light propagation in the vicinity of the focal point.

C.3 Strehl ratio calculation

The Strehl ratios are calculated by comparing the measured intensity distributions in the focal spots to the calculated profiles, assuming diffraction-limited focusing with a full-width at half-maximum FWHM = $\lambda/(2NA)$ for $NA = 0.8$ (i.e. Airy disks). The intensities of the measured profiles are then normalized to the calculated ones to achieve the same energy within a given area. The Strehl ratio is the ratio of maximum peak value of the measured intensity curve to that of the calculated one (1). Strehl ratios of 0.76, 0.78 and 0.77 are achieved for meta-lenses designed for wavelengths of 405 nm, 532 nm and 660 nm, respectively, at their design wavelengths.

C.4 Experimental setup used for imaging with meta-lens

For imaging, we paired our meta-lens with a tube lens ($f = 100$ mm), Fig. C.6. A collimated beam was passed through a diffuser to reduce laser speckles before being focused by a Mitutoyo objective (10×) to illuminate the target object. We adjusted the distance between the object and meta-lens based on the illumination wavelength.

C.5 Modulation transfer function (MTF) measurement

The MTF measurement was performed using a standard slant-edge test (Thorlabs R2L2S2P) and is shown in Fig. C.9. The MTF value of 0.1 is a good guide to the limit of the resolving power of the meta-lens. Figure C.9 shows that this occurs at the spatial frequency of 1000 line pairs per millimeter (lp/mm). This cut-off value corresponds to a resolution limit of 500 nm ($10^6/(2\times$ cut-off spatial frequency)).

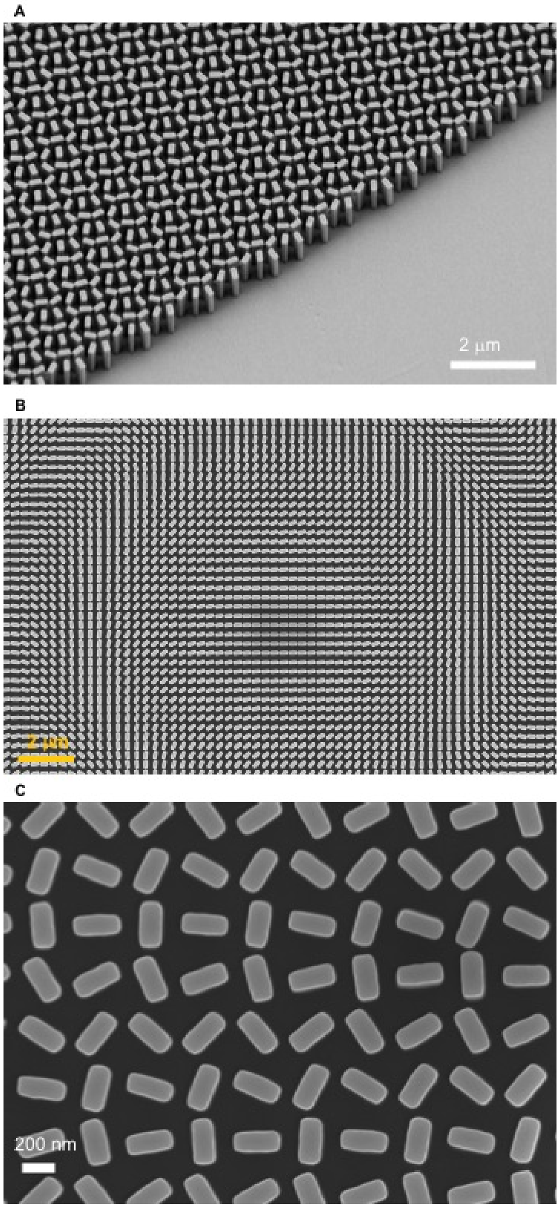

Figure C.1: Scanning electron microscope micrographs of fabricated meta-lenses with diameter $D = 240\,\mu$m and focal length $f = 90\,\mu$m. (A) Tilted view of the meta-lens edge. (B) Top view of the center of the meta-lens. (C) High magnification image of the meta-lens at the edge.

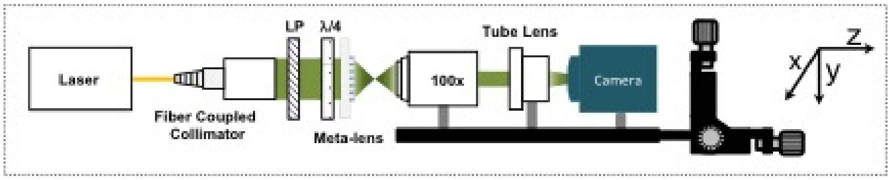

Figure C.2: Schematic of the experimental setup used for measuring the size of the focal spot. The laser beam is collimated by a fiber collimator (Thorlabs RC04APC-P01) with a beam size diameter of 4 mm. The collimated beam then passes through a Glan-Thompson polarizer (Thorlabs GTH10) and a quarter waveplate (Thorlabs AQWP05M-600) to generate circularly polarized light. An Olympus objective ($100\times$ magnification, NA$=0.9$) was used to image the light focused by a meta-lens. A tube lens with focal length f = 180 mm was used to form an image on a CMOS camera (Edmund EO-5012).

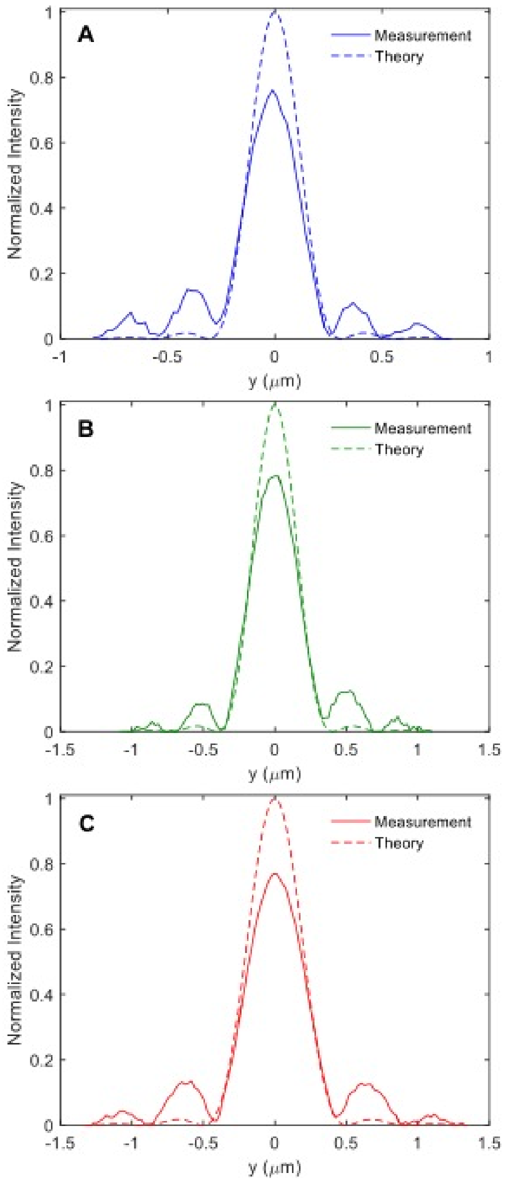

Figure C.3: Strehl ratio calculation. Diffraction-limited (theory) and measured focal spot intensity distributions for three meta-lenses designed at wavelengths of (A) 405 nm, (B) 532 and (C) 660 nm. Focal spots are measured at corresponding design wavelengths.

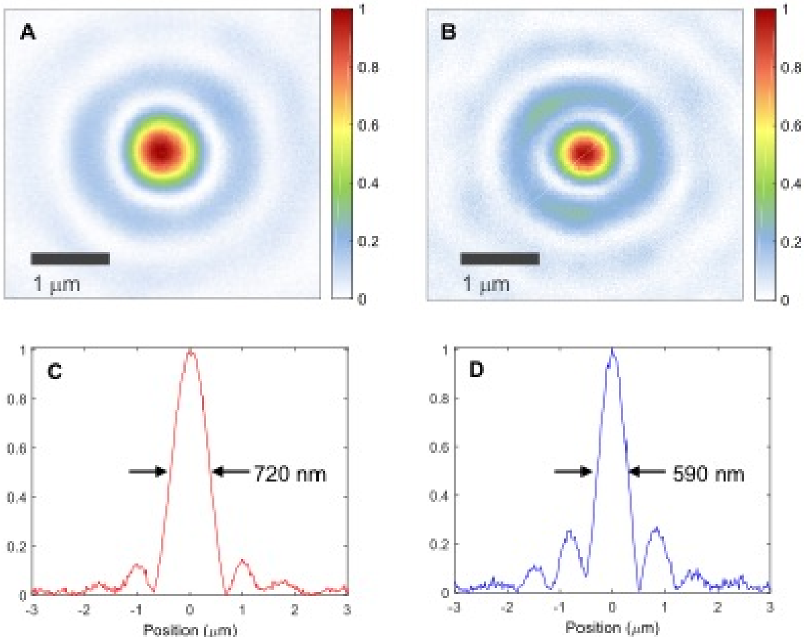

Figure C.4: Focal spot of a meta-lens at wavelengths away from the design wavelength of 532 nm. (A to D) Measured focal spot intensity profile and its corresponding vertical cut at 660 nm (A and C) and 405 nm (B and D) for a meta-lens designed for 532 nm. .

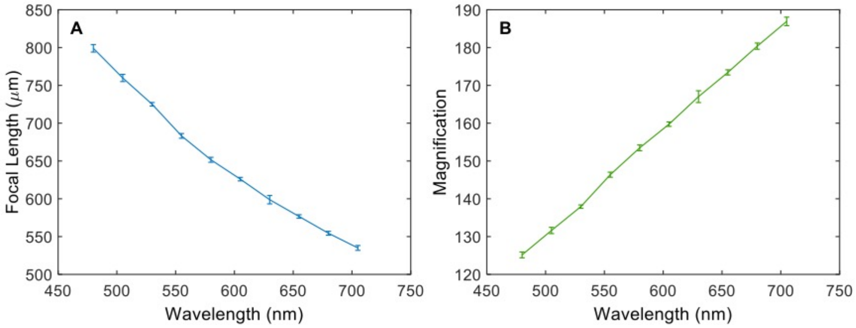

Figure C.5: Focal length and magnification of the meta-lens at different wavelengths. (A) Measured focal length of the meta-lens as a function of wavelength. (B) Magnification corresponding to these focal lengths are also calculated and shown after taking into consideration the tube lens with focal length of 100 mm. The meta-lens here has diameter $D = 2$ mm and focal length $f = 0.725$ mm with the design wavelength of 532 nm.

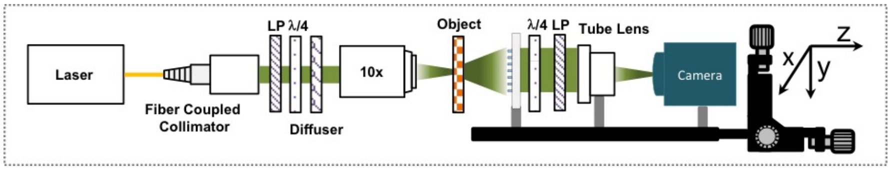

Figure C.6: Measurement set-up used for imaging. Schematic diagram of the experimental setup used for imaging by the meta-lens. The laser beam is collimated by a fiber collimator (Thorlabs RC04APC-P01) with a beam size diameter of 4 mm. The collimated beam then passes through a Glan-Thompson polarizer (Thorlabs GTH10) and a quarter waveplate (Thorlabs AQWP05M-600) to generate right circularly polarized light. This beam is passed through a diffuser to reduce speckles and then focused by a Mitutoyo objective ($10\times$ magnification, $NA = 0.28$) on the target object. The meta-lens is placed a focal length away from the object and paired with a tube lens ($f = 100$ mm) to form an image on CCD camera (Point Grey, GX-FW-28S5C-C). To reduce background signals, we use a polarizer paired with a quarter waveplate in cross polarization.

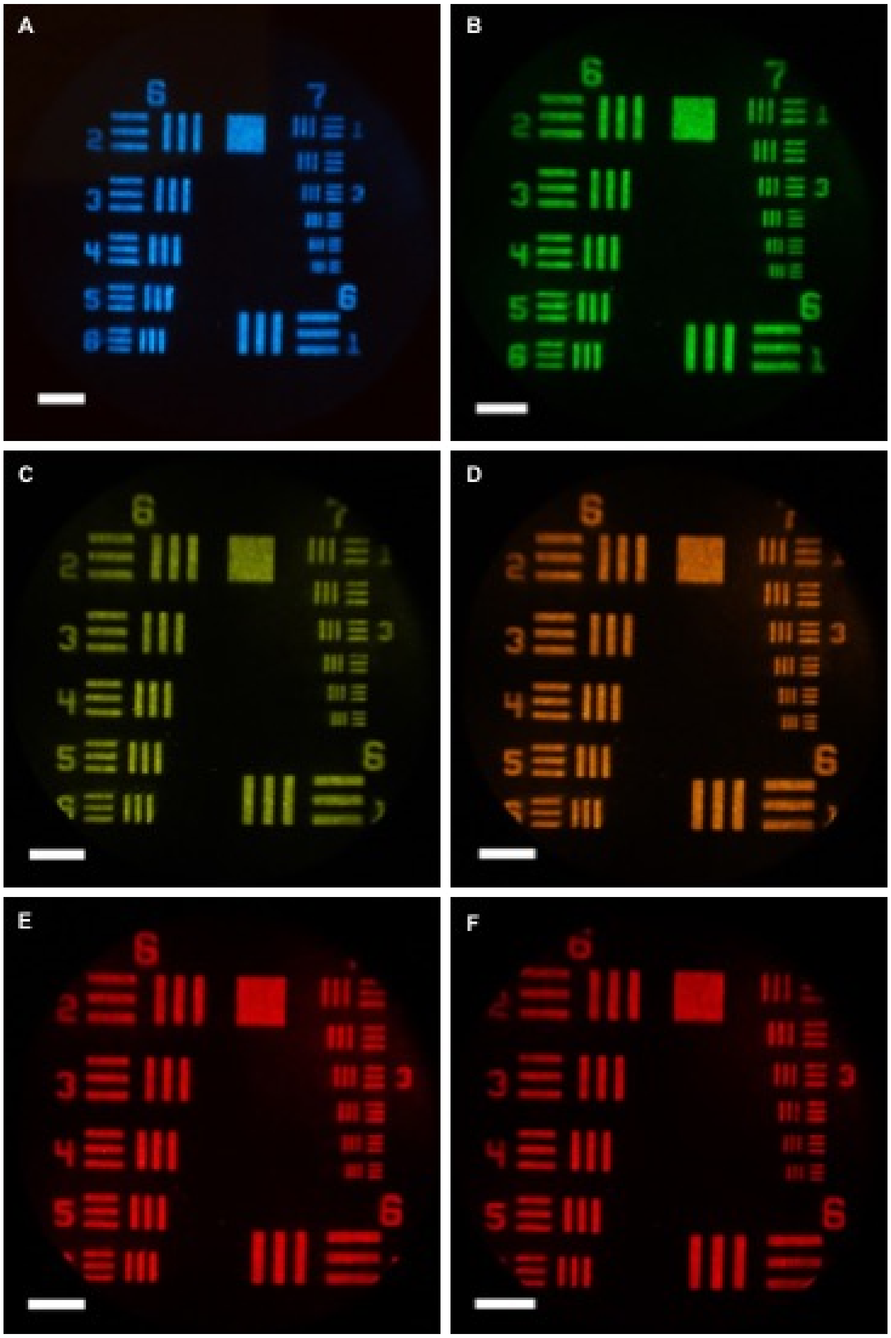

Figure C.7: Imaging with a meta-lens designed at $\lambda_d = 532$ nm with diameter $D = 2$ mm, and focal length $f = 0.725$ mm using a Cannon DSLR camera. Image of the 1951 USAF resolution test chart formed by the meta-lens taken with a Cannon DSLR camera at wavelengths of (A) 480 nm, (B) 550 nm, (C) 580 nm, (D) 590 nm, (E) 620 nm and (F) 640 nm. Scale bar: 40 μm.

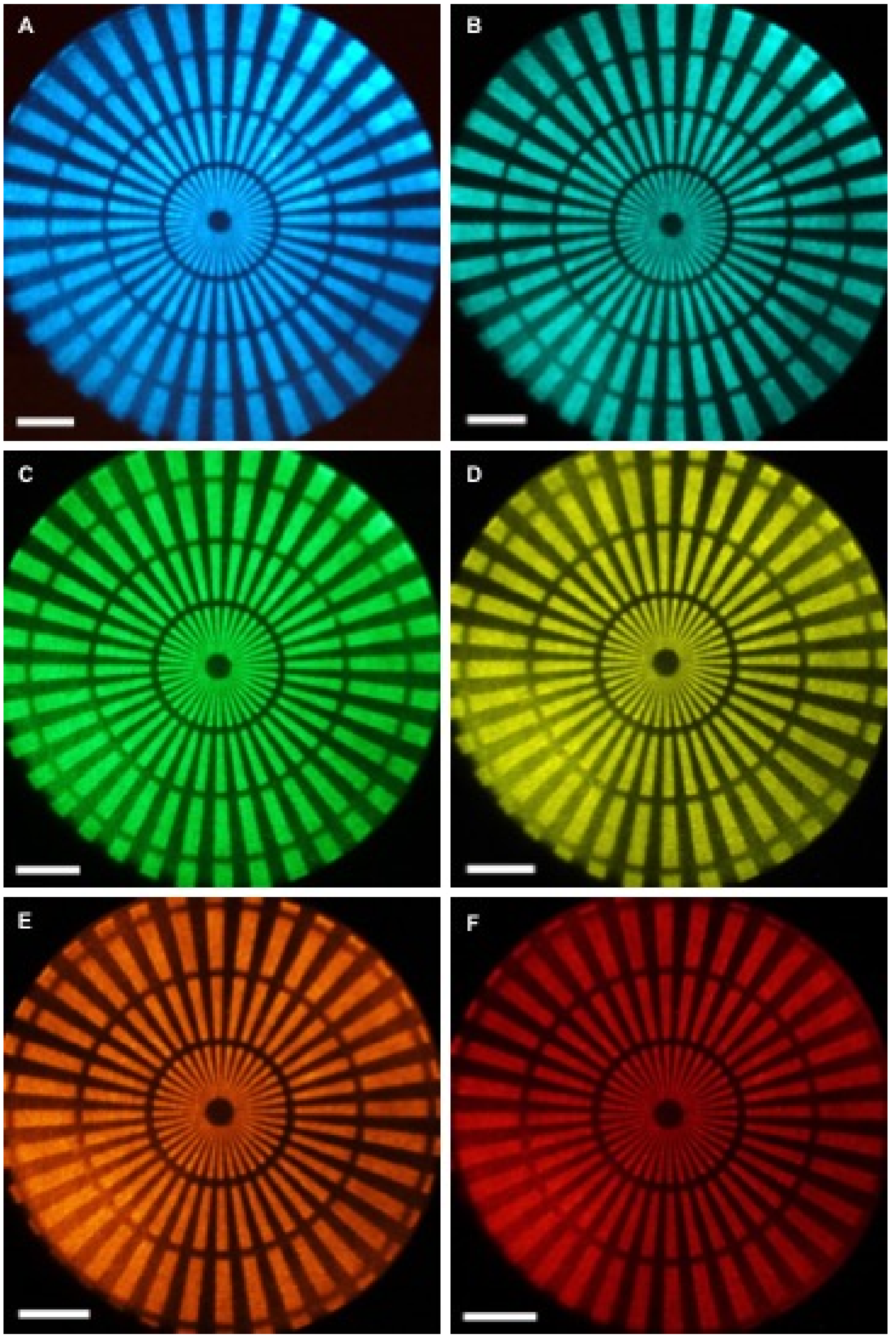

Figure C.8: Imaging with a meta-lens designed at $\lambda_d = 532$ nm with diameter $D = 2$ mm, and focal length $f = 0.725$ mm using a Cannon DSLR camera. Image of a Siemens star formed by the meta-lens at wavelengths of (A) 480 nm, (B) 500 nm, (C) 540 nm, (D) 580 nm, (E) 600 nm and (F) 620 nm. Scale bar: 50 μm. The blurring near the center results from projecting the images onto a translucent screen.

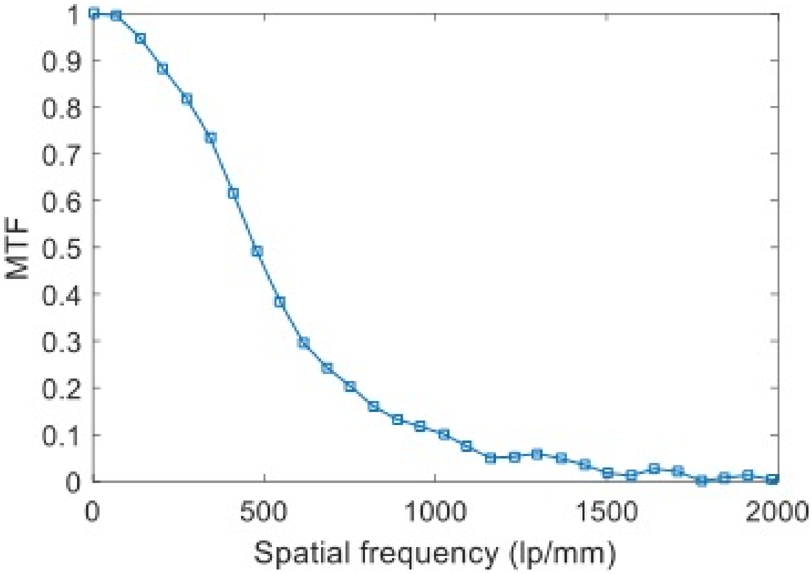

Figure C.9: Measured modulation transfer function as a function of spatial frequency in line pairs per millimeter (lp/mm). The slant-edge target was imaged using the meta-lens designed at ?d = 532 nm with diameter D = 2 mm and focal length $f = 0.725$ mm. The line is to guide the eye.

D

Supplemental material: Spin-to-orbital angular momentum conversion in dielectric metasurfaces

D.1 THE DEVICE CONSTITUTIVE ELEMENT

The individual units of the devices demonstrated in the main text are TiO_2 nanofins, shown schematically in Fig. D.1(a) and (b). These units were fabricated using electron beam lithography and atomic layer deposition of TiO_2 onto the electron beam resist, as was previously described by our group in reference[108]. The low temperature deposition yields amorphous TiO_2 that has minimal surface roughness, which minimizes scattering losses. Additionally the TiO_2 has a high refractive index, ranging from 2.64 at $\lambda = 400$ nm to 2.34 at $\lambda = 700$ nm and a bandgap of 3.46 eV, which lies outside of the visible portion of the spectrum. At the design wavelength ($\lambda = 532$ nm) for the devices described in the main text the measured TiO_2 refractive index is 2.43. This value of refractive index is sufficiently high to confine the incident light to individual nanostructures and the bandgap occurring in the ultraviolet ensures there is no absorption at visible wavelengths.

In order to impose a geometric phase on an incident light field while maximizing the efficiency [16], the nanofins must possess structural birefringence so that a π phase delay can be imparted on orthogonal components of the incident electric field (the $x-$ and $y-$components of the electric field in the example shown here). With our nanofins this birefringence is implemented for a fixed height (h), Fig. (D.1), by varying the length (L) and width (W), Fig. D.1(b). In this way, different each component of light experiences a different effective refractive index, i.e. the nanofins are acting as waveplates with a fast and slow axis.

As stated in the main text, a waveplate with a spatially-varying fast axis (Pancharatnam-Berry phase optical elements [PBOE]), can impart a geometry-dependent phase on an incident circularly polarized light field. The imparted phase arises due to rotation of individual elements causing incident light to traverse two different paths on the Poincar sphere. When the paths form a closed loop, the phase of the exiting light is then equal to half the solid angle of the loop. For our nanofins, which act as half waveplates, spatial rotation of each nanofin by an angle α (Fig. D.1(b)) allows us to imprint the geometric phase and ultimately achieve the phase profile for producing a vortex beam, $\alpha = q\phi + \alpha_0$.

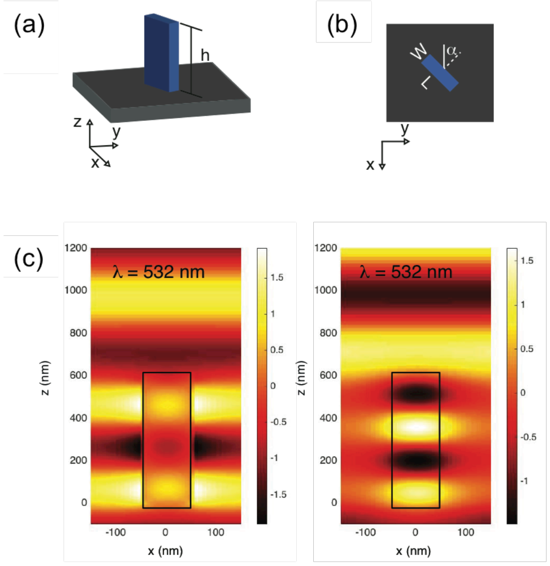

Figure D.1: (a) Perspective view of a single nanofin that makes up our devices. The fabrication process produces fins with a given height, h, which is 600 nm for all devices. (b), Top view of the TiO_2 nanofin. The fins are designed with width, W, length, L and rotation angle with respect to the $x-$axis, α. The length and width of the nanofin sets the relative phase delay between orthogonal components of an incident electric field and the rotation provides the geometric phase. (c), Cross section through the width of a single nanofin, showing the simulated electric field components. The real part of the x-component (left) and y-component (right) of the electric field. At the design parameters of W $=$ 90 nm, L = 250 nm, h = 600 nm, there is a π phase delay between the $x-$ and $y-$components.

The geometric parameters of the fins, W and L, were determined using 3-dimensional finite difference time domain simulations (Lumerical). At a fixed height of 600 nm, W and L were allowed to vary so that for an incident wavelength of $\lambda = 532$ nm, there would be a π phase shift between the $x-$ and $y-$components of the incident electric field. From this optimization, it was found that fins with W $=$ 90 nm and L $=$ 250 nm provided the desired phase shift as can be seen from the simulated electric field profiles in Fig. D.1(c)[108].

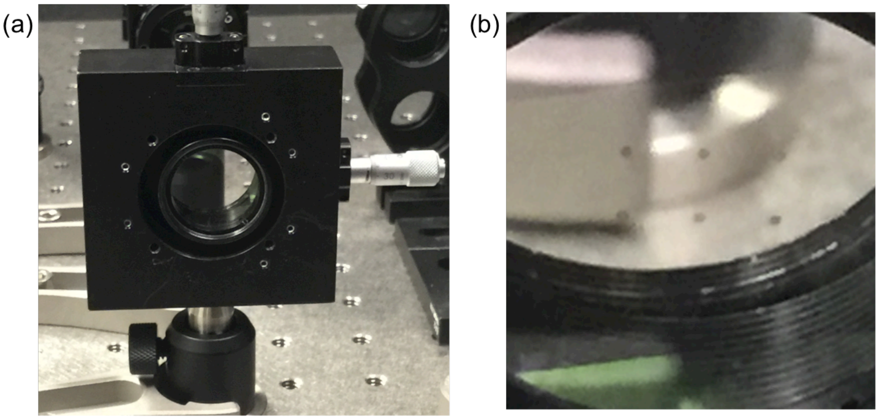

Figure D.2: (a) The devices are produced on a circular 1-inch diameter fused silica wafer, which is then integrated into a commercial opto-mechanic component. (b), Magnified view of the 1-inch wafer in (a) showing six devices on the same substrate. The devices are placed in a rectangular array across the wafer, which allows easy selection of a device by moving it into the illuminating beam path.

D.2 The device

The devices described in the main text have been designed such that they can be easily integrated into manual or automatic positioning systems. Fig. D.2(a) shows a 1-inch fused silica substrate that has been patterned with TiO_2 metasurfaces. The sample sits on a manual translation stage but automatic translation stages could be used for faster switching. Such design allows SOCs producing different topological charges to be arrayed on a single device at regular distances, (Fig. D.2(b)) and easy switching between an output beam with a desired topological charge.

D.3 Imaging at a distance from the device exit plane

In order to produce an image of the transverse light distribution at different distances from the sample plane, the upper arm of the interferometer was slightly modified. In particular the source beam was focused on the device by means of a 75 mm aspherical lens. The light emerg-

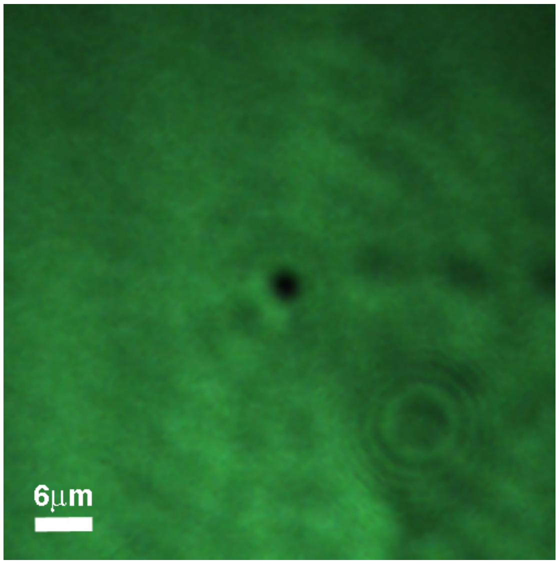

Figure D.3: Image of the singularity region of a $q = 0.5$

ing from the device was then collected by means of a 4× infinity corrected microscope objective. The objective has 0.10 NA and works in confocal configuration with the aspheric lens. The sample is mounted on a translation stage that allows changing the distance from the objective. This configuration has been used, for instance, in Fig. 5.4(a) that shows a fractional optical vortex at 55 μm from the device exit plane. Fig. D.3 shows the image of the center of the device when the device plane is in focus. This image is what is sometimes referred to as near-field image although does not contain any near-field component. The image shows that the singularity localization in the device plane is smaller than 3 μm. In ref.[142] device singularities of 750 nm are reported. The physical dimension of the device singularity (region with no nanofins) in these metasurface devices is 1200 nm, however the fabrication technique used here can produce devices with controlled vacancies (i.e., lack of nanofin) on the order of the unit cell dimension of a few hundred nanometers. As pointed out in [28] this is an advantage of the metasurface q-plates

D.4 DEVICE EFFICIENCY AND CONVERSION OVER THE VISIBLE RANGE

The polarization filter of Fig. 5.2(c) is used to eliminate the light that passes unperturbed through the device. This light has opposite handedness with respect to the helical mode and is absorbed by the polarization filter. It is known that when a waveplate that introduces a phase delay Γ between the transverse field components is illuminated by circularly polarized light, the out coming field has two components with opposite handedness:

$$E_{out} = \frac{1}{2}\left(1 + \mathrm{e}^{-i\Gamma}\right)\sigma^{+} + \frac{1}{2}\left(1 - \mathrm{e}^{-i\Gamma}\right)\mathrm{e}^{i2\alpha}\sigma^{-} \tag{D.1}$$

Note that the first time has the same handedness of the incident beam whereas the second term has the opposite handedness and has acquired an additional phase factor of $\exp(i2\alpha)$, where α the rotation angle of each nanofin.

In some experiments in literature, the percentage of light with flipped handedness is reported as the beam purity since it represents the fraction of total outcoming light converted into the desired helical mode to the unconverted light. This feature, though, does not account whatsoever for the device transmittance since the purity can be close to 100% even if the transmittance is as low as a few percent. This is a particularly important point for communication and quantum optics applications where for high fidelity systems it is necessary that both the transmission efficiency and conversion efficiency of the transmitted light be maximized.

We designed our devices for a π phase delay at $\lambda = 532$ nm. The transmittance of TiO_2 in the visible is greater than 80%. The efficiency that we report in our paper is the amount of light that is converted in a helical mode with respect to the light incident on the device. We

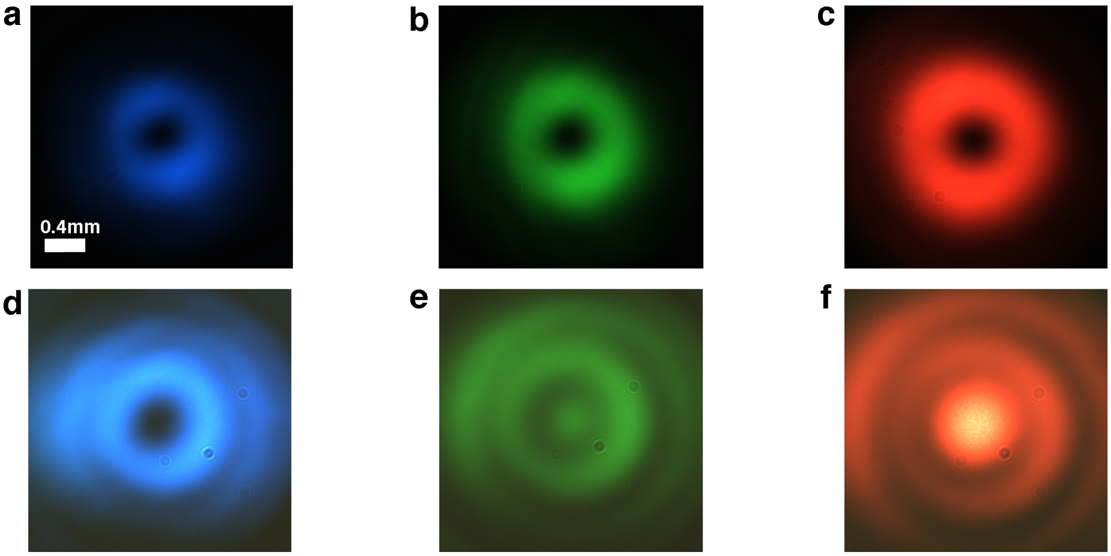

Figure D.4: Images of the donut beams at three different wavelengths from a supercontinuum laser: 480 nm ((a) and (d)), 550 nm ((b) and (e)) and 633 nm ((c) and (f)). The images in the upper row are taken with the setup of Fig. 2 (c) while the images in the lower row are taken by removing the polarization filter. The scale bar of 0.4 mm in Fig. 9 applies to all the panels.

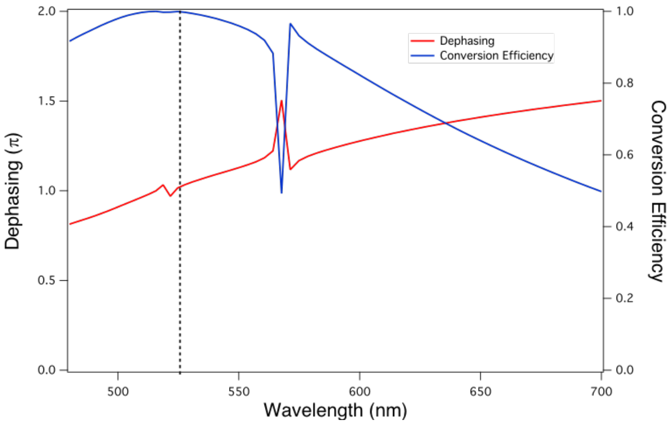

Figure D.5: Nanofin dephasing and conversion efficiency as a function of wavelength. Simulated dephasing between the x- and y- components of the electric field after passing through the nanofins (red line) and the resulting ideal conversion efficiency (blue line).

think that this value (experimentally measured to be up to 60%) is more useful for practical uses since it takes into account the fact that in a real device with discrete features like our TiO_2 nanofins, a certain amount of light just passes through non-modulated. Furthermore, in a real experiment there are also reflections at the interfaces. These effects are all included in the figure of merit that we measured.

An inhomogeneous grating design with densely packed grooves can in principle allow reducing the amount of light that passes through the device without acquiring the proper phase delay. This could result in even higher efficiency values at the designed wavelength. However, such design is limited to cylindrically symmetric structures like those necessary to generate a topological charge 2 vortex and cannot be applied to generate arbitrary vortex beams.

The wavelength dependence of the phase delay Γ imposed by the constitutive elements of spin-orbital momentum converters based on metasurfaces limits the efficiency bandwidth of such devices. The actual phase delay is equal to π only at the designing wavelength. The farther the wavelength is from the designed wavelength the larger the amount of unperturbed light. However, the Pancharatman-Berry phase is path-length independent and does not change with the wavelength of the incident light. Fig. D.4 shows a single charge helical mode obtained at different wavelengths from a supercontinuum laser with our 532 nm optimized device.

The simulated phase shift between the x- and y- components of the electric field after passing through the nanofin and resulting as a function of wavelength is shown in Fig. D.5. As can be seen from the figure, the conversion peaks around the design wavelength (532 nm) and is lower away from the design wavelength since the nanofin no longer acts as a half wave plate. Changing the design parameters of the nanofins would allow optimizing the device operation

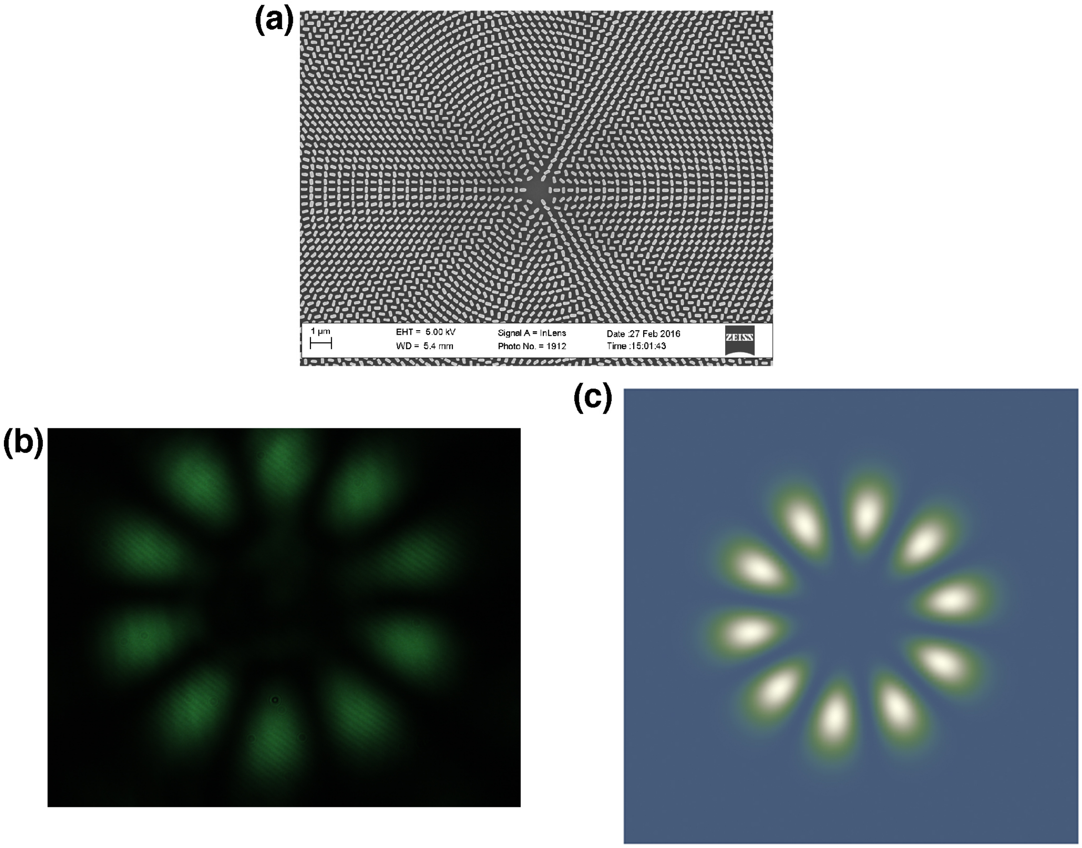

Figure D.6: (a), Scanning Electron Microscopy micrograph of an interlaced device. (b), light distribution at 45 cm from the device exit plane. (c), simulated interference pattern of two collinear beams with topological charges +5 and -5.

at other wavelengths[108].

D.5 Fractional vortex

Figure D.6 shows the light distribution of the fractional 6.5 vortex beam at the camera plane, about 45cm from the device exit plane. The singularity line visible at 55 μm from the device (Fig. 5.4(a)) is no longer visible.

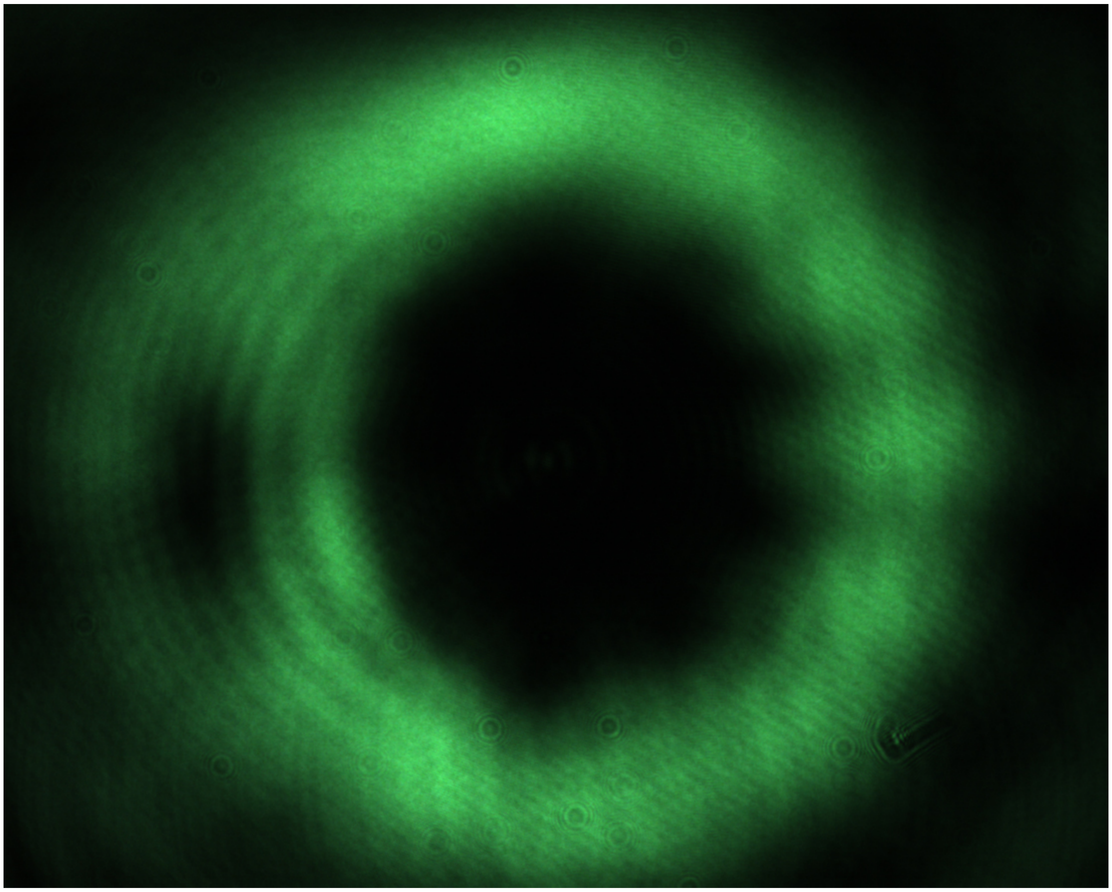

Figure D.7: Far-field image of the 6.5 topological charge vortex beam.

E

Supplemental material: Arbitrary spin-to-orbital angular momentum conversion of light

E.1 DERIVATION OF THE J-PLATE DESIGN MATRIX

In order to allow the J-plate to be realized with a straightforward fabrication process and a single layer of material, we consider only phase modulation of an incident beam (no amplitude modulation). Due to fabrication constraints we work only with locally-varying linear birefringence and rotation of the fast axis. We can realize any two independent phase profiles with only two caveats: the two independent phase profiles can only be placed on orthogonal design polarizations and the output polarization is the complex conjugate of the input polarization (i.e., the handedness is flipped after passing through the device). For two input polarizations arbitrary input polarizations in the linear polarization basis $\{|H\rangle, |V\rangle\}$ given as

$$\left|\lambda^{+}\right\rangle = \begin{bmatrix} \cos\chi \\ e^{i\delta}\sin\chi \end{bmatrix} \qquad \left|\lambda^{-}\right\rangle = \begin{bmatrix} -\sin\chi \\ e^{i\delta}\cos\chi \end{bmatrix} \tag{E.1}$$

where χ and δ control the ellipticity of the beam. Taking these general polarization states and two independent azimuthal phase factors, $m\phi$ and $n\phi$ as the desired phase profiles yields the following equation

$$J(\phi) = \begin{bmatrix} \mathrm{e}^{im\phi}\left(\cos\chi\right)^{*} & \mathrm{e}^{in\phi}\left(-\sin\chi\right)^{*} \\ \mathrm{e}^{im\phi}\left(\sin\chi\mathrm{e}^{i\delta}\right)^{*} & \mathrm{e}^{in\phi}\left(\cos\chi\mathrm{e}^{i\delta}\right)^{*} \end{bmatrix} \begin{bmatrix} \cos\chi & -\sin\chi \\ \sin\chi\mathrm{e}^{i\delta} & \cos\chi\mathrm{e}^{i\delta} \end{bmatrix}^{-1} \tag{E.2}$$

Suppressing the ϕ-dependence for brevity (here and below) and carrying out the matrix multiplication gives

$$J = \mathrm{e}^{-i\delta} \begin{bmatrix} \mathrm{e}^{i\delta}\left(\mathrm{e}^{im\phi}\cos^2\chi + \mathrm{e}^{in\phi}\sin^2\chi\right) & \frac{\sin 2\chi}{2}\left(\mathrm{e}^{im\phi} - \mathrm{e}^{in\phi}\right) \\ \frac{\sin 2\chi}{2}\left(\mathrm{e}^{im\phi} - \mathrm{e}^{in\phi}\right) & \mathrm{e}^{-i\delta}\left(\mathrm{e}^{im\phi}\sin^2\chi + \mathrm{e}^{in\phi}\cos^2\chi\right) \end{bmatrix}. \tag{E.3}$$

After disregarding the global phase factor, this is the matrix presented in Eq. 4 of Chapter 6.

To understand how the Jones matrix for the device controls the output, we simply use the normal Jones matrix formalism that relates input electric field to output polarization as $|E_{\text{out}}\rangle = J\,|E_{\text{in}}\rangle$ and take $|E_{\text{in}}\rangle$ to be one of the two arbitrary orthogonal polarizations above.

In matrix form this is

$$\begin{aligned}
\left|E_{\mathrm{out}}\right\rangle &= \begin{bmatrix} \mathrm{e}^{i\delta}\left(\mathrm{e}^{im\phi}\cos^2\chi + \mathrm{e}^{in\phi}\sin^2\chi\right) & \frac{\sin 2\chi}{2}\left(\mathrm{e}^{im\phi} - \mathrm{e}^{in\phi}\right) \\ \frac{\sin 2\chi}{2}\left(\mathrm{e}^{im\phi} - \mathrm{e}^{in\phi}\right) & \mathrm{e}^{-i\delta}\left(\mathrm{e}^{im\phi}\sin^2\chi + \mathrm{e}^{in\phi}\cos^2\chi\right) \end{bmatrix} \begin{bmatrix} \cos\chi \\ e^{i\delta}\sin\chi \end{bmatrix} \\
&= \begin{bmatrix} \cos\chi \\ \mathrm{e}^{i(m\phi-\delta)}\sin\chi \end{bmatrix} \\
&= \mathrm{e}^{im\phi}\begin{bmatrix} \cos\chi \\ \mathrm{e}^{-i\delta}\sin\chi \end{bmatrix}
\end{aligned} \tag{E.4}$$

which is simply $\mathrm{e}^{im\phi}\left|(\lambda^+)^*\right\rangle$ and the device has produced the desired total angular momentum (TAM) state. The treatment for the orthogonal state is identical.

In the most general case, the input polarization can be any polarization state. As a result the output state will be a superposition of the two TAM states. Consider now any input polarization $\left|E_{\mathrm{in}}\right\rangle$ that is neither $\left|\lambda^+\right\rangle$ nor $\left|\lambda^-\right\rangle$. Since the two design polarizations are orthogonal, $\langle\lambda^+|\lambda^-|\lambda^+|\lambda^-\rangle = 0$, we can decompose the output in the following way

$$\begin{aligned}
\left|E_{\mathrm{out}}\right\rangle &= J\left|E_{\mathrm{in}}\right\rangle \\
&= \left[J\left|\lambda^+\right\rangle\left\langle\lambda^+|E_{\mathrm{in}}|\lambda^+|E_{\mathrm{in}}\right\rangle + J\left|\lambda^-\right\rangle\left\langle\lambda^-|E_{\mathrm{in}}|\lambda^-|E_{\mathrm{in}}\right\rangle\right] \\
&= \mathrm{e}^{im\phi}\left\langle\lambda^+|E_{\mathrm{in}}|\lambda^+|E_{\mathrm{in}}\right\rangle\left|(\lambda^+)^*\right\rangle + \mathrm{e}^{in\phi}\left\langle\lambda^-|E_{\mathrm{in}}|\lambda^-|E_{\mathrm{in}}\right\rangle\left|(\lambda^-)^*\right\rangle \\
&= \alpha\mathrm{e}^{im\phi}\left|(\lambda^+)^*\right\rangle + \beta\mathrm{e}^{in\phi}\left|(\lambda^-)^*\right\rangle
\end{aligned} \tag{E.5}$$

where we have simply inserted the projection operator $\left|\lambda^+\right\rangle\left\langle\lambda^+\right| + \left|\lambda^-\right\rangle\left\langle\lambda^-\right|$ and in the last step we have simply defined $\alpha \equiv \langle\lambda^+|E_{\mathrm{in}}|\lambda^+|E_{\mathrm{in}}\rangle$ and $\beta \equiv \langle\lambda^-|E_{\mathrm{in}}|\lambda^-|E_{\mathrm{in}}\rangle$. The coefficients α

and β are complex numbers that provide both a weight and a phase on the two TAM states.

Since the J-plate Jones matrix in Eq. E.3 is unitary, it is diagonalizable and therefore we can find its eigenvectors and eigenvalues. Additionally, the unitarity of J guarantees that the eigenvectors are orthonormal and its eigenvalues are complex exponentials. Thus, we can decompose the matrix into its canonical form $J = Q\Lambda Q^{-1}$ where Q is an orthonormal matrix whose columns are the eigenvectors and Λ is a diagonal matrix whose entries are the eigenvalues of J. Since we build the matrix in the linear polarization basis, the entries in Λ correspond to phase shifts along the x- and y-directions, δ_x and δ_y. Because we are working with a Jones matrix, the matrix Q that is composed of the eigenvectors, is simply a rotation matrix for the matrix Λ. In contrast to a normal linear birefringent waveplate rotated through some angle θ, the values of δ_x, δ_y and θ all depend on the spatial coordinate ϕ.

In the most general case, the eigenvalues and eigenvectors do not yield simple analytical solutions for the phase shifts and rotation angles but we can still find the solutions numerically for specific values of m, n, χ and δ. However, for the case where the input spin states are chosen to be circular polarizations, $\chi = \pi/4$ and $\delta = \pi/2$, but for general orbital angular momentum states m and n, we can find simple closed form solutions. In such a case, the matrix in Eq. E.3 reduces to

$$J = \frac{1}{2}\begin{bmatrix} \mathrm{e}^{im\phi} + \mathrm{e}^{in\phi} & -i\mathrm{e}^{im\phi} + i\mathrm{e}^{in\phi} \\ -i\mathrm{e}^{im\phi} + i\mathrm{e}^{in\phi} & -\mathrm{e}^{im\phi} - \mathrm{e}^{in\phi} \end{bmatrix} \tag{E.6}$$

from which we can find the eigenvalues as

$$\lambda_1 = \mathrm{e}^{\frac{i}{2}(m+n)\phi} \qquad \lambda_2 = \mathrm{e}^{\frac{i}{2}(m+n)\phi - \pi} \tag{E.7}$$

and eigenvectors as

$$|\mathrm{v}_1\rangle = \begin{bmatrix} \cos\frac{1}{4}\left(m-n\right)\phi \\ \sin\frac{1}{4}\left(m-n\right)\phi \end{bmatrix} \qquad |\mathrm{v}_2\rangle = \begin{bmatrix} -\sin\frac{1}{4}\left(m-n\right)\phi \\ \cos\frac{1}{4}\left(m-n\right)\phi \end{bmatrix} \tag{E.8}$$

Following the decomposition outlined above we can write the Jones matrix for circular polarization states mapped to two arbitrary values of OAM as

$$\begin{aligned} J(r,\phi) = &\begin{bmatrix} \cos\frac{1}{4}(m-n)\phi & \sin\frac{1}{4}(m-n)\phi \\ \sin\frac{1}{4}(m-n)\phi & -\cos\frac{1}{4}(m-n)\phi \end{bmatrix} \\ &\begin{bmatrix} \exp\left[\frac{i}{2}\left(m+n\right)\phi\right] & 0 \\ 0 & \exp\left[\frac{i}{2}\left(m+n\right)\phi-\pi\right] \end{bmatrix} \begin{bmatrix} \cos\frac{1}{4}(m-n)\phi & \sin\frac{1}{4}(m-n)\phi \\ \sin\frac{1}{4}(m-n)\phi & -\cos\frac{1}{4}(m-n)\phi \end{bmatrix}. \end{aligned} \tag{E.9}$$

Since we are in the linear polarization basis, we can easily see directly that the phase shifts are $\delta_x = 1/2(m+n)\phi$ and $\delta_y = 1/2(m+n)\phi - \pi$ and the rotation angle is $\theta = 1/4(m-n)\phi$.

Thus far we have been working in the linear polarization basis. However, if we take the matrix in Eq. E.6 and change to the basis of circular polarizations $\{|R\rangle, |L\rangle\}$, we can immediately gain insight into the action of the device. Carrying out this change of basis yields

$$J_{\text{circ}} = \begin{bmatrix} 0 & \mathrm{e}^{in\phi} \\ \mathrm{e}^{im\phi} & 0 \end{bmatrix} \tag{E.10}$$

where we have added the ‘circ’ subscript to show we are in the circular polarization basis. Only the off-diagonal elements remain in the matrix and the elements are exactly the designed azimuthal phase factors. This indicates the action of the J-plate is to flip the handedness of the input and add an azimuthal phase factor, just as we had found above for the more general case.

Thus far, we have only considered the simplest case of taking some input polarization $|E_{\text{in}}\rangle$, with zero OAM, as the input state to the J-plate. This case corresponds to a mapping from the Poincaré sphere of SAM (polarization) to the higher order Poincaré sphere (HOPS) that contains both SAM and OAM. However, the J-plate is equally capable of carrying out a transfer from one HOPS to a second, arbitrary HOPS.

Consider first, that the input state to a J-plate, J_2, is the output state of a previous J-plate, J_1. For simplicity we consider both of these devices to operate on circularly polarized eigenstates. A general output of the first device, following form above, can be written as

$$|\Psi_{\text{in}}\rangle = \alpha \mathrm{e}^{im\phi} |R\rangle + \beta \mathrm{e}^{in\phi} |L\rangle \tag{E.11}$$

where again, α and β are complex coefficients. If J_2 is designed to carry out the following transfer

$$\begin{aligned} |R\rangle &\rightarrow \mathrm{e}^{i\ell\phi} |L\rangle \\ |L\rangle &\rightarrow \mathrm{e}^{ip\phi} |R\rangle \end{aligned} \tag{E.12}$$

that is, the action of J_2 is to flip the circular polarization of a state and imprint OAM values of ℓ and p where for the most general case $m \neq n \neq \ell \neq p$. Passing the state in Eq. S12 through J_2 and using operator notation for brevity gives the final output of the J-plate as

$$\begin{aligned}|\Psi_{\text{out}}\rangle = J_2\,|\Psi_{\text{in}}\rangle &= \alpha \mathrm{e}^{im\phi} J_2\,|R\rangle + \beta \mathrm{e}^{in\phi} J_2\,|L\rangle \\ &= \alpha \mathrm{e}^{im\phi}\mathrm{e}^{i\ell\phi}\,|L\rangle + \beta \mathrm{e}^{in\phi}\mathrm{e}^{ip\phi}\,|R\rangle \\ &= \alpha \mathrm{e}^{i(m+\ell)\phi}\,|L\rangle + \beta \mathrm{e}^{i(n+p)\phi}\,|R\rangle\end{aligned} \tag{E.13}$$

Thus, since the values of ℓ and p are also arbitrary, the action of the J-plate is to carry an arbitrary input TAM state to any new input TAM state, which now has OAM of $(m + \ell)$ and $(n + p)$. For simplicity we have considered here the case where the all design input spin states are circular polarizations. However, this process can easily be generalized for elliptically-polarized design states. Thus, although we only considered in Chapter 6 the case of zero OAM for the input light the J-plate will, in general, act as a ladder in OAM. We can then represent the action of the device as

$$\begin{aligned}\left|\lambda^+\right\rangle|m\rangle &\to \left|\left(\lambda^+\right)^*\right\rangle|m+\ell\rangle \\ \left|\lambda^-\right\rangle|n\rangle &\to \left|\left(\lambda^-\right)^*\right\rangle|n+p\rangle\end{aligned} \tag{E.14}$$

where as in Chapter 6 we have taken the azimuthal phase factor that gives the field OAM and written this OAM explicitly as a state. The limiting factor when we extend this treatment to the case of general elliptically-polarized eigenstates, however, is that in order for the J-plate to simply add to the OAM of the input state, the polarization basis of the input state must be identical to the eigenstates of the J-plate it is passing through. That is, the input state must be of the form $|\Psi_{\text{in}}\rangle = \alpha \mathrm{e}^{im\phi}\,|\lambda^+\rangle + \beta \mathrm{e}^{in\phi}\,|\lambda^-\rangle$. Because the J-plate can be designed to perform SOC with any eigen-polarization, whereas previous devices only operate on input circular polarizations, one can also have two cascaded J-plates with unique eigen-polarizations which can lead to interesting new functionalities and will be the subject of future studies.

E.2 SPECIFIC CASE OF THE Q-PLATE FROM GENERAL TREATMENT

The design principle for we have implemented for arbitrary spin-to-orbital angular momentum conversion is a more general case than the specific Pancharatnam-Berry phase design[40], *q-plate*[41]. As such, if the target SOC parameters are set to be equivalent to the q-plate design, the more general case of the J-plate should collapse into the specific case of the q-plate.

For the q-plate the two values of OAM must be conjugates, requiring that $m = |\ell|$ and $n = -|\ell|$, and the design polarizations must be orthogonal circular polarizations, implying that $\chi = \pi/4$ and $\delta = \pi/2$. For such a case, the eigenpolarizations are left- and right-circular polarizations

$$\left|\lambda^{+}\right\rangle = |R\rangle = \frac{1}{\sqrt{2}}\begin{bmatrix} 1 \\ i \end{bmatrix} \tag{E.15}$$

$$\left|\lambda^{-}\right\rangle = |L\rangle = \frac{1}{\sqrt{2}}\begin{bmatrix} 1 \\ -i \end{bmatrix} \tag{E.16}$$

Entering these design polarizations into the matrix in Eq. E.2 yields the device matrix

$$J = \begin{bmatrix} \cos\ell\phi & \sin\ell\phi \\ \sin\ell\phi & -\cos\ell\phi \end{bmatrix}. \tag{E.17}$$

Following an identical treatment to Chapter 6 and above, the eigenvalues of this matrix provide the required phase shift, while the eigenvectors provide the rotation angle of each element at each point (r, ϕ). Upon carrying out this analysis, we can decompose the q-plate device matrix into a diagonal matrix whose entries are the eigenvalues and rotation matrices whose columns are the eigenvectors, yielding

$$J = \begin{bmatrix} \cos\frac{\ell}{2}\phi & \sin\frac{\ell}{2}\phi \\ \sin\frac{\ell}{2}\phi & -\cos\frac{\ell}{2}\phi \end{bmatrix} \begin{bmatrix} -1 & 0 \\ 0 & 1 \end{bmatrix} \begin{bmatrix} \cos\frac{\ell}{2}\phi & \sin\frac{\ell}{2}\phi \\ \sin\frac{\ell}{2}\phi & -\cos\frac{\ell}{2}\phi \end{bmatrix}. \tag{E.18}$$

Thus, for the case of conjugate angular momentum states and orthogonal circular polarization design states, the phase delay along the phase delays along the x- and y-directions are $\delta_x = -\delta_y = 1$. These phase delays are constants, i.e., independent of the azimuthal coordinate ϕ, and simply represent a half wave plate. Similarly examining the rotation angle we find that each element, which we have now shown to be a half wave plate, is rotated about its fast axis according to the equation $\theta = \ell\phi/2$. Following the convention[41] that $\ell = 2q$ we have that the rotation angle is given by $\theta(r, \phi) = q\phi$. This result is identical to the treatment of the q-plate[40,41], up to an arbitrary constant offset, and thus we see that this special case of SOC is contained in the more general form presented here.

E.3 DERIVATION OF OUTPUT FROM ROTATING QWP

The path taken on the poincare sphere and the general output state that is obtained for Fig. 6.3 of Chapter 6 can be derived in the following way. Beginning with the input from our laser, which is horizontally polarized, the beam passes through a QWP with a varying angle of the fast axis, β, followed by the J-plate that has been designed for the mapping of the form of Eq. S13. The output of the two cascaded elements can be found simply as

$$|E_{\text{out}}\rangle = JM(\beta)\,|E_{\text{in}}\rangle \tag{E.19}$$

where $M(\beta)$ is the standard Jones matrix for a QWP with rotated fast axis

$$M(\beta) = \begin{bmatrix} \cos^2(\beta) + i\sin^2(\beta) & (1-i)\cos(\beta)\sin(\beta) \\ (1-i)\cos(\beta)\sin(\beta) & i\cos^2(\beta) + \sin^2(\beta) \end{bmatrix} \tag{E.20}$$

J is the Jones matrix given in Eq. E.6 and $|E_{\text{in}}\rangle = |H\rangle = [1,0]'$.

Carrying out this matrix multiplication and changing to the left and right circular polarization basis we can directly decompose this result to give the general output. After applying trigonometric identities, this process yields the output as

$$|\Psi(\beta)\rangle = \sin\left(\frac{\pi}{4} - \beta\right)|\mathrm{L}\rangle\,|m\rangle + \mathrm{e}^{i2\beta}\cos\left(\frac{\pi}{4} - \beta\right)|\mathrm{R}\rangle\,|n\rangle \tag{E.21}$$

which is the value included in Chapter 6. Checking this equation for two cases where the angle of the QWP are $\beta = +45^{\mathrm{o}}$ and $\beta = -45^{\mathrm{o}}$, which should correspond to left and right circular polarizaed input states to the J-plate, we can see that the outputs are then pure states of $|\Psi(+45^{\mathrm{o}})\rangle = |\mathrm{R}\rangle\,|m\rangle$ and $|\Psi(-45^{\mathrm{o}})\rangle = |\mathrm{L}\rangle\,|n\rangle$. All other values of β will lead to a superposition of the two TAM state with weights and phases determined by Eq. E.21.

E.4 Simulation

The phase shifts, δ_x and δ_y for the linearly birefringent metasurface elements are determined using finite difference time domain software (FDTD, Lumerical Inc). A linearly polarized plane wave with $\lambda = 532$ nm is incident on an individual metasurface element with a fixed height of 600 nm and a refractive index of 2.42 (the value for amorphous $\mathrm{TiO_2}$ at this wavelength[108]). The phase shift, and transmission from this element is recorded as the width of the element is varied. We search for the range of widths that allow the library of elements to achieve any phase shift from $[0, 2\pi]$ and choose only the range of widths that provide a similar, high transmission efficiency.

E.5 FABRICATION

We have fully detailed the fabrication process and characterization of the TiO_2 nanostructures in ref[108] and we briefly summarize it here. We fabricated all devices on fused silica substrates. The substrates were spun coated with undiluted positive electron beam resist (EBR) (ZEP-520A; Zeon Chemicals). We spun the resist at 1,750 rpm to achieve the desired resist thickness of 600 nm. We then baked at 180 °C for 5 min. Subsequently, we coated the samples with ESPACER (Showa Denko K.K.), a conductive polymer, to avoid charging effects during the writing process. The patterns were exposed using an accelerating voltage of 125 kV (ELS-F125; Elionix Inc.), with a dose area of 880 $\mu C/cm^2$ and developed in o-Xylene (Sigma Aldrich) for 40 s under gentle agitation. We deposited the TiO_2 directly onto the exposed EBR using atomic layer deposition (Savannah; Cambridge Nanotech). A standard two-pulse system of water and *tetrakis(dimethylamido)titanium(IV)* precursor was used with a 0.2 s water pulse followed by a 7 s delay and a 0.4 s TDMAT pulse followed by a 10 s delay. The system was left under continuous 20 cm^3/min flow of N_2 carrier gas and was maintained at 90 ^oC throughout the process. This led to an overall deposition rate of 0.7 nm per cycle. This process ultimately leaves a blanket film of TiO_2 covering the entire device which must be removed to expose the individual metasurface units. We removed this film with reactive ion etching (Unaxis inductively coupled plasma) using a mixture of Cl_2 and BCl_3 gas (3 and 8 cm^3 /min, respectively) at a pressure of 4 mTorr, substrate bias of 150 V, and ICP power of

400 W. Etch rates were typically between 1.3 nm/s and 1.6 nm/s. After processing was complete, we removed the resist by placing the samples in Remover PG for 24 hrs, followed by a final clean in 2:1, sulfuric acid:H_2O_2.

E.6 Measurement

In order to fully characterize a vortex beams we need to measure *both* the intensity distribution and the phase fronts of the field. As such we used a Mach-Zehnder interferometer as shown in Fig. E.1. In this configuration, the horizontally-polarized source beam (a CW solid-state laser emitting at 532 nm with power of 4 mW) is split in two beams by means of a 50/50 beam splitter (BS). Half of the light is sent through the 'test arm' that contains the device and the other half of the light is sent through the 'reference arm'.

For the case of Fig. 6.2 and 6.3 in Chapter 6, where the two output states of the device are designed to propagate colinearly, we use the configuration shown in Fig. E.1A. In the test arm we place a halfwave plate (HWP) and quarter wave plate (QWP) before the J-plate. For the case where the input to the device in Fig. 6.2 of Chapter 5 is one of the circularly polarized eigenstates the HWP is removed and the horizontally-polarized laser beam is passed through QWP1. The fast axis of QWP1 is oriented at ±45° to produce a left- or right-circularly polarized beam incident on the J-plate. At the output, the vortex beam then passes through QWP2, which has its fast axis oriented at 90° with respect to QWP1 and the LP is in cross-polarization with respect to the laser. The purpose of QWP2 and LP are to filter out any light that is either unconverted by the J-plate or light that has not been incident on the device (the beam diameter is larger than the device aperture). Thus after QWP2 and LP only the OAM beam remains. In the reference arm, the beam passes through a HWP that rotates the polarization of the laser beam from horizontal to vertical and it then is sent to a 5x beam expander (BE). The reference beam and the OAM beam are then recombined via BS2 and imaged on a camera. The interference of the two beams, expanded reference beam and OAM beam, results in the measured characteristic spiral interference pattern (as seen in Fig. **??**D(i) and (vi)). We insert a beam block (BB) into the reference arm and thus eliminate the interference, to measure the intensity profile of the beam exiting the J-plate.

To create the equal superpositions of the two designed states, we simply remove QWP1 and 2 and insert the HWP into the test arm. Thus by passing the linearly-polarized laser through the HWP and varying the angle of the fast axis of the HWP, we change the angle of the linear polarization incident on the device with respect to the horizontal axis. Again, we insert or remove the BB in order to collect the intensity images or the interference images, respectively. This configuration is used to collect the images in Fig 6.2B and D (ii-v). To create a continual evolution from one pole of the HOPS to the opposite pole, as in Fig 6.3 of Chapter 6, we set the relative angle between the fast axis of QWP1 and 2 to 90° and then vary the angle of each fast axis in steps of 10°. The intensity and interference images are collected as above.

For the case of the device in Fig. 6.4 which exemplifies the most general case of SOC, we used the slightly altered configuration shown in Fig. E.1B . Because the device is designed to separate the two output states at angles of ±10° by the addition of a blazed grating phase profile, there is no need to filter out unconverted light. QWP1 and the HWP allow us to vary the input polarization to the device. Two additional mirrors are inserted after the device and a BB is placed in one of the output beam paths. The two mirrors direct the output OAM mode to BS2 where again it is sent to a camera to collect the intensity or interference image. We also measure the output power at each angle as the input polarization is varied (see discussion below). This is shown in the inset of Fig. E.1B, where an optical power meter is placed in each of the two beam paths to measure the output power.

E.7 Intensity calculation for superpositions of Laguerre-Gaussian beams

While in writing the output of the device in Chapter 6, we only considered the azimuthal phase dependence of the OAM beam, e.g., $e^{i\ell\phi}$, these beams will have different spatial distribution of their amplitudes for different values angular momentum ℓ. It is well established that Laguerre-Gaussian (LG) modes, which are solutions to the paraxial wave equation in cylindrical coordinates, carry an azimuthal phase dependence and therefore OAM[26]. The amplitudes of these LG beams are given by

$$u_{p,\ell}\left(r,\phi,z\right)=\sqrt{\frac{2p!}{\pi\left(p+|\ell|\right)}}\frac{1}{w(z)}\left(\frac{r\sqrt{2}}{w(z)}\right)^{|\ell|}L_p^{|\ell|}\left(\frac{2r^2}{w(z)^2}\right)\exp\left(\frac{-r^2}{w(z)^2}\right)\exp\left(\frac{-ikr^2}{2R(z)}\right)$$
$$\exp\left[-i(2p+|\ell|+1)\mathrm{arctan}\left(\frac{z}{z_R}\right)\right]\exp(i\ell\phi) \quad \text{(E.22)}$$

In general such LG beams can have both an radial and azimuthal index, given by p and ℓ, respectively. However, only ℓ alters the OAM content of the beam so we consider only beams with $p=0$. In such a case, the amplitude reduces to

$$u_{0,\ell}\left(r,\phi,z\right)=\sqrt{\frac{1}{\pi|\ell|}}\frac{1}{w(z)}\left(\frac{r\sqrt{2}}{w(z)}\right)^{|\ell|}L_0^{|\ell|}\left(\frac{2r^2}{w(z)^2}\right)\exp\left(\frac{-r^2}{w(z)^2}\right)\exp\left(\frac{-ikr^2}{2R(z)}\right)$$
$$\exp\left[-i(|\ell|+1)\mathrm{arctan}\left(\frac{z}{z_R}\right)\right]\exp(i\ell\phi) \quad \text{(E.23)}$$

Whenever the input polarization to the J-plate is any polarization that is *not* one of the eigen polarizations, the device forms a superposition of the form Eq. E.5. This amounts to a superposition of two OAM modes with amplitudes given by Eq. E.23. The relative phase shift and weights of these two OAM modes are then determined by the complex coefficients α and β, which are determined by the projection of the input polarization onto the two eigen-polarizations of the device (again as shown in Eq. E.23). Taking all of these factors together, we then produce the calculated plots of intensity shown in Fig. 6.2C(i-vi) using the following equation

$$\langle\Psi|\Psi|\Psi|\Psi\rangle = |\alpha u_{0,m}\left(r,\phi,z\right) + \beta u_{0,n}\left(r,\phi,z\right)|^2 \tag{E.24}$$

where m and n are the designed OAM values of the device. To calculate the phase plots in Fig. 6.2E(i-vi) we simply take the argument of the superposition.

E.8 Additional J-plate designs

Nothing about the design procedure that we have outlined here places limits on the values of OAM in the output beam, m and n. Thus, although we have shown the example of where $||m| - |n|| = 1$ in Chapter 6, the quantity $||m| - |n||$ is also arbitrary since no constraints are placed on m or n. We present here device design and measurements shown that are identical to those in Fig. 6.3 and 6.4 but instead with designed for the mappings $|R\rangle \rightarrow |{+6}\rangle\,|L\rangle$ and $|L\rangle \rightarrow |{+3}\rangle\,|R\rangle$. The design of this device is shown in Fig. E.2 and the measurement results of this device are shown in Fig. E.3 and Fig. E.4.

Note that, as discussed in Chapter 6, the equal superposition of these two OAM states results in $|m-n| = 3$ additional optical vortices that appear off-axis resulting in three additional zeros in the intensity located $360°/3 = 120°$ apart.

E.9 Device design for mapping from general input polarization

The device presented in Fig. 6.4 of Chapter 5, the most general demonstration of SOC not only imparts unique OAM onto two incident elliptically polarized beams but also adds an additional blazed grating to both of the beams in order to separate the outputs. To design this device, as discussed above, we solve for the eigenvectors and eigenvalues of the device matrix in Eq. E.3 for the specific numerical values of $\chi = \pi/3$, $\delta = 3\pi/10$, $m = -3$ and $n = +4$. The final device design is made up of a sum of two different devices, as shown in Fig. E.5. Figure E.5A shows the device design that would take the two input elliptical polarization eigenstates and map them to the two output TAM beams propagating co-linearly. Figure E.5B shows a device design which acts as blazed grating for two elliptical polarizations. Figure E.5C shows the sum of the previous two devices which is ultimately the fabricated device for the demonstration in Fig. 6.4. Figure E.5D shows an SEM image of the fabricated device. Unsurprisingly, adding a blazed grating profile to the two TAM states produces a device that resembles a forked hologram, which has traditionally been used to produce OAM beams. However, a critical difference between the device in Fig. E.5 and a traditional forked hologram is that the device in Fig. E.5 has spatially varying birefringence and orientation of the birefringence axis. Thus the device presented here and in Chapter 6 is the first instance of a forked hologram where the SAM is mapped to OAM and the OAM exiting the device on the two blazing angles can be designed to be any value. As stated in Chapter 6 this separation of the beam allows us to perform polarimetry on the device and experimentally confirm that the eigen-polarizations of the device are indeed elliptically-polarized.

E.10 STOKES POLARIMETRY FOR MEASURING INPUT DEVICE POLARIZATIONS

The present work sought to examine a more general form of spin-orbit coupling (SOC), one that is not bound by the usual device constraint of equal-and-opposite topological charges $\pm q$ for each circular polarization. To that end, using the formalism presented in Chapter 6, we designed and fabricated a J-plate intended to create vortex beams of arbitrary topological charge for a basis of arbitrarily chosen elliptical polarization states.

In order to demonstrate that the device as-fabricated performs the desired function, two facts must be confirmed experimentally:

1. That the vortex beams created are of the desired, designed topological charges m and n.
2. The polarization states producing pure vortex beams match the desired design elliptical polarization states.

For ease of verification, the vortex beam phase profiles were blazed at equal and opposite angles (as detailed in Chapter 6) so that the vortex beams would appear on different diffraction orders. This way, each of the polarization channels could be examined independently at separate locations in space, without one acting as a contaminating background for the other.

As discussed and shown in Chapter 6, the first item above is easily verified. Visual inspection of the beam on each diffraction order and its associated interference pattern readily reveals its topological charge.

The second point is somewhat more subtle. Suppose that the design elliptical polarization states are given by orthogonal Jones vectors $|\lambda^+\rangle$ and $|\lambda^-\rangle$. If a beam with a polarization state given by normalized Jones vector $|\ell\rangle$ and power P_0 is incident on the device, ideally the order associated with $|\lambda^+\rangle$ will have a power $P^+ = P_0|\langle\ell|\lambda^+|\ell|\lambda^+\rangle|^2$ and similarly the order associated with $|\lambda^-\rangle$ will have a power $P^- = P_0|\langle\ell|\lambda^-|\ell|\lambda^-\rangle|^2$ (assuming a lossless device). That is, when one design polarization is incident, the power on one order should be maximized and the other extinguished, and vice versa. How are these so-called maximally preferred polarization states to be determined for each order?

We can think of each diffraction order as having a characteristic polarization of its own – we denote these by Stokes vectors $\vec{S}^{\pm} = \begin{bmatrix} S_0^{\pm} & S_1^{\pm} & S_2^{\pm} & S_3^{\pm} \end{bmatrix}^T$ where + and − refer to the two diffraction orders. We need to determine $\vec{S}^{+}$ and $\vec{S}^{-}$. Each has its own degree of polarization (DOP) given by $p = \frac{\sqrt{S_1^2+S_2^2+S_3^2}}{S_0}$ and a state of polarization (SOP) given by $\{S_1, S_2, S_3\}$. Ideally, for each order, we would find $p = 1$ and that the SOP matches that of the design Jones vector, $|\lambda^{\pm}\rangle$. We note that the Jones vector and the SOP (pictorially represented on the Poincare sphere) are interchangeable representations of the polarization ellipse.

In order to experimentally determine $\vec{S}^{\pm}$, we perform a polarimetric measurement. We rely here on the Stokes representation as it is naturally tailored to such a measurement, given that the Stokes vector being based on intensities is experimentally measurable.

The measurement works as follows: We illuminate the device with six different test polarizations which are easy to prepare with a polarizer and quarter-wave plate. These are $|H\rangle$, $|V\rangle$, $|45°\rangle$, $|135°\rangle$, $|R\rangle$, and $|L\rangle$. For each polarization, the power of the illuminating beam is recorded (the laser has a strong preferred polarization). We denote this by $P_{\text{inc},|q\rangle}$ where $|q\rangle$ is the incident polarization state. For each test polarization, we record the power being directed into each diffraction order and denote this by $P^{\pm}_{|q\rangle}$ for each diffraction order + and −. Then we have, for each order:

$$\begin{bmatrix} P_{\text{inc},|H\rangle} & P_{\text{inc},|H\rangle} & 0 & 0 \\ P_{\text{inc},|V\rangle} & -P_{\text{inc},|V\rangle} & 0 & 0 \\ P_{\text{inc},|45°\rangle} & 0 & P_{\text{inc},|45°\rangle} & 0 \\ P_{\text{inc},|135°\rangle} & 0 & -P_{\text{inc},|135°\rangle} & 0 \\ P_{\text{inc},|R\rangle} & 0 & 0 & P_{\text{inc},|R\rangle} \\ P_{\text{inc},|L\rangle} & 0 & 0 & -P_{\text{inc},|L\rangle} \end{bmatrix} \begin{bmatrix} S_0^{\pm} \\ S_1^{\pm} \\ S_2^{\pm} \\ S_3^{\pm} \end{bmatrix} = \begin{bmatrix} P^{\pm}_{|H\rangle} \\ P^{\pm}_{|V\rangle} \\ P^{\pm}_{|45°\rangle} \\ P^{\pm}_{|135°\rangle} \\ P^{\pm}_{|R\rangle} \\ P^{\pm}_{|L\rangle} \end{bmatrix} \tag{E.25}$$

or, in short form:

$$A\vec{S}^{\pm} = \vec{P}^{\pm} \tag{E.26}$$

This equation is easily understood: Each row of the matrix A is the power-weighted Stokes vector of the test polarization. Each entry in the measured power vector $\vec{P}^{\pm}$ is then the inner product of the incident test polarization with the characteristic Stokes vector $\vec{S}^{\pm}$. $\vec{S}^{\pm}$ is determined by successive projection onto known polarization states.

The system is overdetermined (A is 6×4), so the system is solved in the least-squares sense. That is,

$$\vec{S}^{\pm} = (A^T A)^{-1} A^T \vec{P}^{\pm} \tag{E.27}$$

In Chapter 6, the SOPs obtained from $\vec{S}^{\pm}$ measured in this way are compared against the design states, showing reasonably close agreement.

It should be noted that measuring the polarization states $\vec{S}^{\pm}$ for the two diffraction orders is *not* akin to a measurement of the polarization state of light on this diffraction order. Indeed, $\vec{S}^{\pm}$ are the characteristic polarization states to which power directed into the order is selective, not the light's polarization state itself. In this way, $\vec{S}^{\pm}$ can be viewed as the eigenpolarizations of the diffraction orders.

The measured powers on each of the two OAM modes $|-3\rangle$ and $|+4\rangle$, for each of the input polarizations, are shown in Table S1. The setup and measurement procedure to collect these powers was already introduced in Fig. E.1B and the surrounding discussion in Section 6.

Table E.1: Measured power on each of the output beams for six input polarizations

	Input polarization					
	$\|H\rangle$	$\|45°\rangle$	$\|V\rangle$	$\|135°\rangle$	$\|R\rangle$	$\|L\rangle$
$\|-3\rangle$	4.8	1.4	1.0	5.1	2.0	4.2
$\|+4\rangle$	1.1	3.8	4.0	0.96	3.5	1.0

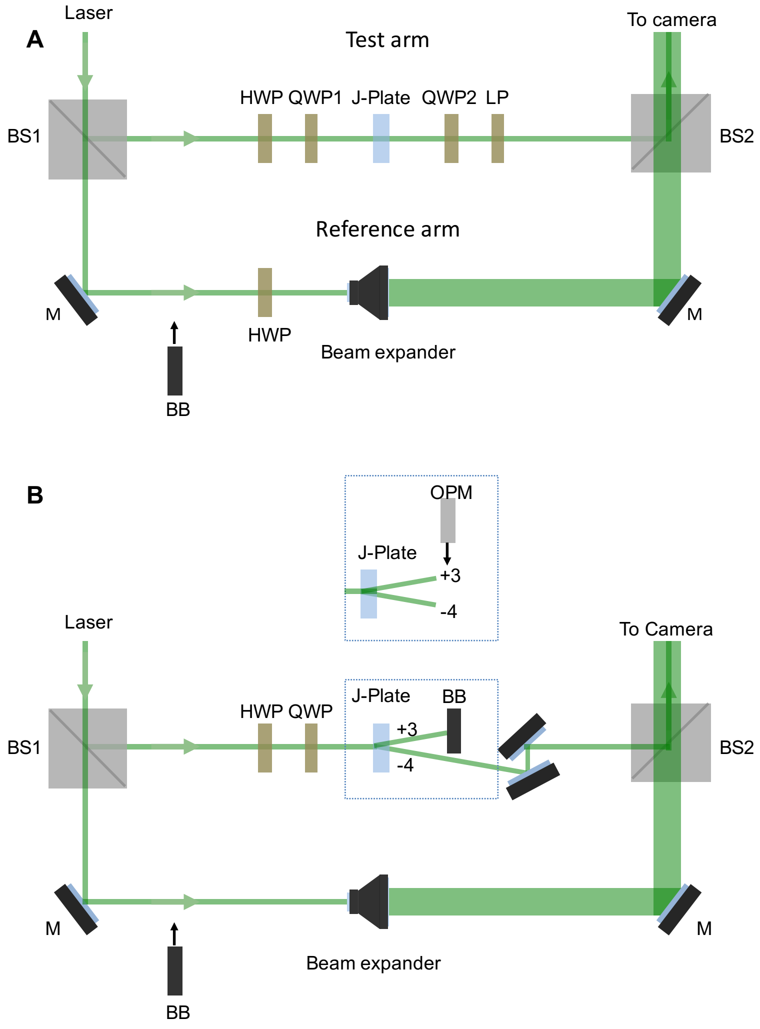

Figure E.1: Measurement setups for experimental verification of J-plate operation (**A**) Measurement setup for verification of the device corresponding to Fig. 6.2 and 6.3 in Chapter 6. (**B**) Measurement setup for the device corresponding to Fig. 6.4 in Chapter 6. BS = beamsplitter, M = mirror, HWP = halfwave plate, QWP = quarterwave plate, BB = beam block, LP = linear polarizer, OPM = optical power meter.

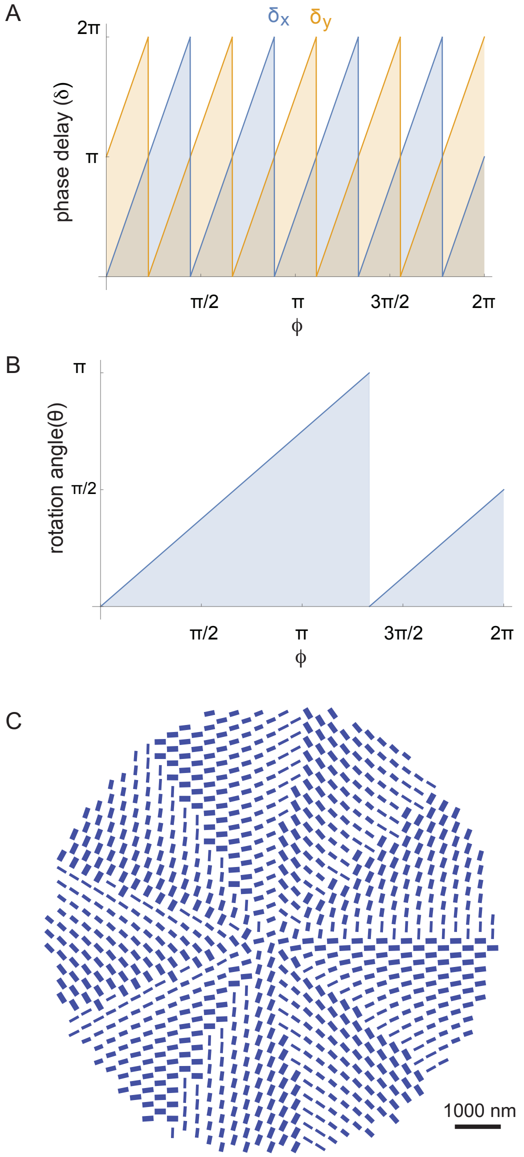

Figure E.2: Device design for mapping from circularly-polarized inputs to OAM with $m = +6$ and $n = +3$. (**A**). Phase delays δ_x (blue) and δ_y (yellow) as a function of azimuthal angle ϕ. (**B**) Rotation angle of the birefringent element as a function of azimuthal angle ϕ. (**C**) Actual device design after periodically sampling the two functions (A) and (B)

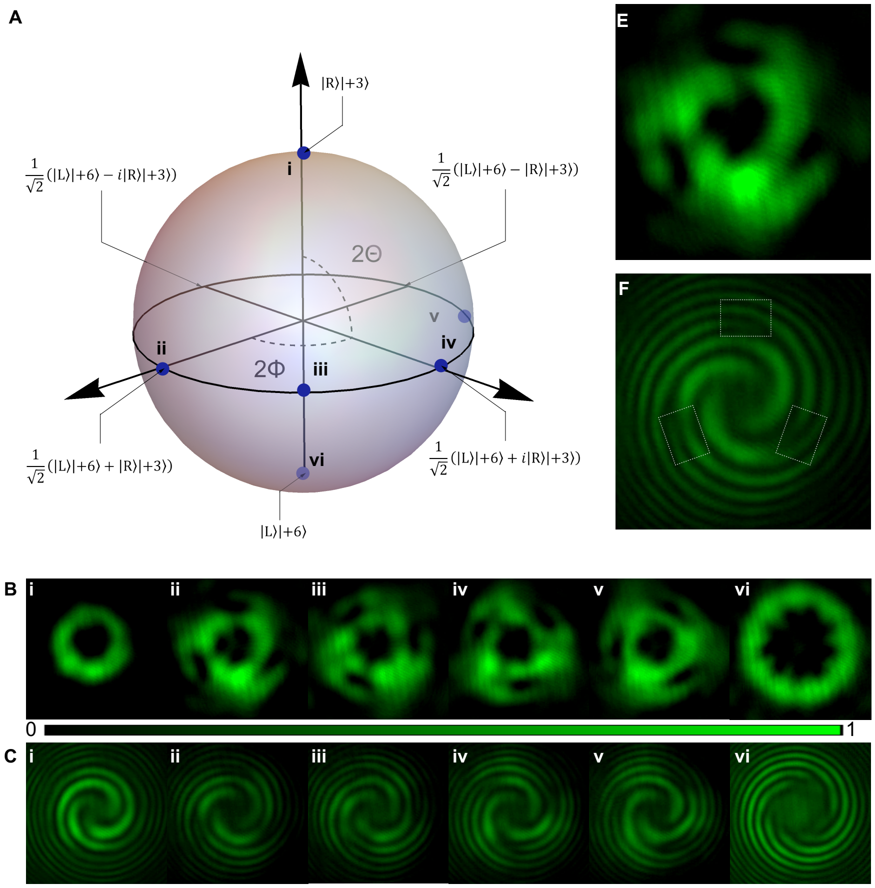

Figure E.3: Experimental demonstration of superposition of two arbitrary orbital angular momenta with circularly polarized eignestates.(**A**). Higher order Poincare sphere (HOP) representing all possible spin and orbital angular momentum states produced by a device that carries out the mapping $|R\rangle \rightarrow |L\rangle\,|+6\rangle$ and $|L\rangle \rightarrow |R\rangle\,|+3\rangle$. (**B**). Measured intensity of output state . (**C**) Measured interference of output state with a Guassian. The states in (B,C) i-vi are marked as blue circles on the HOP in (A). (**D**,**E**) Magnified view of measured intensity and interference of the states in (B)iii and (C)iii. The dashed boxes highlight an additional zero in intensity and phase discontinuity that results from the equal superposition of $|+3\rangle$ and $|+6\rangle$ states. This phase discontinuity results in an three off-axis zeros in the intensity pattern (F) and three additional forks in the interference pattern corresponding to the difference of OAM for the two states. The scale bar shows the value of phase

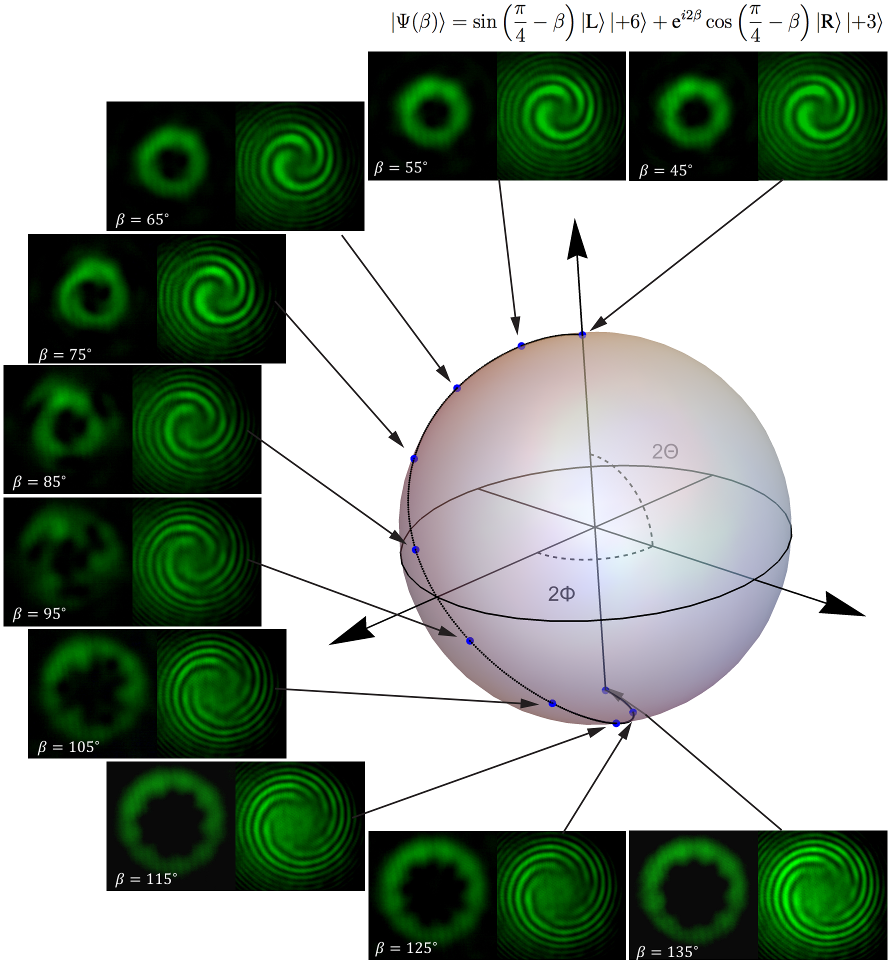

Figure E.4: Evolution of an arbitrary OAM superposition along a path on the higher order Poincare sphere. The images show measured output intensities (left) and interference (right) as the angle of the fast axis of a QWP is varied in front of a horizontally-polarized laser. The angle is varied from $\beta = 45^\text{o}$ to -45^o which transfers the output state from the north pole to the south pole while continuously changing both the weight and phase of the superposition state. The QWP angle for each intensity and interference image is displayed in the bottom left. The output state $|\Psi\rangle$ as a function of β, is shown at the top. The resulting path taken on the HOP is shown as the black line and the blue circles correspond to the measured points.

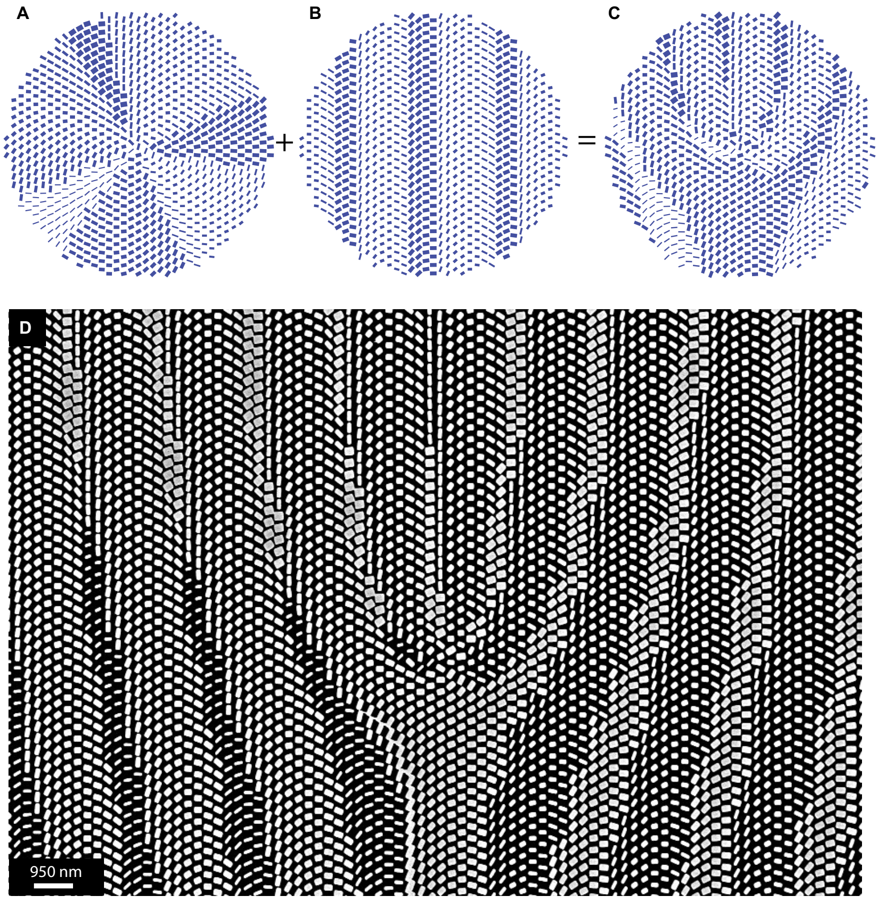

Figure E.5: Generalized design for elliptical polarization SOC and mode separation (**A**) Device design for mapping from elliptically polarized inputs with $\chi = \pi/6$ and $\delta = 3\pi/10$. This device design would produce both output beams co-linearly. (**B**) Device design for a blazed grating that deflects the two beams produced by the device in (A) to $\pm 10^\circ$ away from the input beam optical axis. (**C**) Sum of the designs in (A) and (B) which is the device used in Fig. 4 of Chapter 6. (**D**). Scanning electron microscope image of the fabricated device.

References

[1] Herzberger, M. Optics from euclid to huygens. *Applied Optics* **5**, 1383–1393 (1966).

[2] Bardeen, J. & Brattain, W. H. The transistor, a semi-conductor triode. *Physical Review* **74**, 230 (1948).

[3] Joannopoulos, J. D., Villeneuve, P. R. & Fan, S. Photonic crystals: putting a new twist on light. *Nature* **386**, 143 (1997).

[4] Jackson, J. D. *Classical electrodynamics* (John Wiley & Sons, 2007).

[5] Kittel, C. *Introduction to solid state physics* (Wiley, 2005).

[6] Pendry, J. B., Holden, A. J., Robbins, D. & Stewart, W. Magnetism from conductors and enhanced nonlinear phenomena. *IEEE transactions on microwave theory and techniques* **47**, 2075–2084 (1999).

[7] Veselago, V. G. The electrodynamics of substances with simultaneously negative values of |[epsi]| and |[mu]|. *Sov. Phys. Uspekhi* **10**, 509–514 (1968).

[8] Smith, D. R., Pendry, J. B. & Wiltshire, M. C. K. Metamaterials and negative refractive index. *Science* **305**, 788–792 (2004). URL `http://science.sciencemag.org/content/305/5685/788`. `http://science.sciencemag.org/content/305/5685/788.full.pdf`.

[9] Pendry, J. B. Negative refraction makes a perfect lens. *Phys. Rev. Lett.* **85**, 3966–3969 (2000). URL `https://link.aps.org/doi/10.1103/PhysRevLett.85.3966`.

[10] Grbic, A., Jiang, L. & Merlin, R. Near-field plates: Subdiffraction focusing with patterned surfaces. *Science* **320**, 511–513 (2008).

[11] Shalaev, V. M. Optical negative-index metamaterials. *Nat Photon* **1**, 41–48 (2007). URL `http://dx.doi.org/10.1038/nphoton.2006.49`.

[12] Agranovich, V. & Kravtsov, V. Notes on crystal optics of superlattices. *Solid State Communications* **55**, 85 – 90 (1985). URL `http://www.sciencedirect.com/science/article/pii/0038109885911111`.

[13] Poddubny, A., Iorsh, I., Belov, P. & Kivshar, Y. Hyperbolic metamaterials. *Nat Photon* **7**, 948–957 (2013). URL `http://dx.doi.org/10.1038/nphoton.2013.243`.

[14] Yu, N. *et al.* Light propagation with phase discontinuities: generalized laws of reflection and refraction. *science* **334**, 333–337 (2011).

[15] Herzig, H. P. *Micro-optics: elements, systems and applications* (CRC Press, 1997).

[16] Arbabi, A., Horie, Y., Bagheri, M. & Faraon, A. Dielectric metasurfaces for complete control of phase and polarization with subwavelength spatial resolution and high transmission. *Nature Nanotechnology* **10** (2015).

[17] Balthasar Mueller, J. P., Rubin, N. A., Devlin, R. C., Groever, B. & Capasso, F. Metasurface polarization optics: Independent phase control of arbitrary orthogonal states of polarization. *Phys. Rev. Lett.* **118**, 113901 (2017). URL https://link.aps.org/doi/10.1103/PhysRevLett.118.113901.

[18] Aieta, F. *et al.* Aberration-free ultrathin flat lenses and axicons at telecom wavelengths based on plasmonic metasurfaces. *Nano letters* **12**, 4932–4936 (2012).

[19] Yu, N. & Capasso, F. Flat optics with designer metasurfaces. *Nature materials* **13**, 139 (2014).

[20] Jahani, S. & Jacob, Z. All-dielectric metamaterials. *Nature nanotechnology* **11**, 23 (2016).

[21] Lin, D. Dielectric gradient metasurface optical elements. *Science* **345**, 298–302 (2014).

[22] Maxwell, J. C. A dynamical theory of the electromagnetic field. *Philosophical transactions of the Royal Society of London* **155**, 459–512 (1865).

[23] Poynting, J. H. The wave motion of a revolving shaft, and a suggestion as to the angular momentum in a beam of circularly polarised light. *Proceedings of the Royal Society of London A: Mathematical, Physical and Engineering Sciences* **82**, 560–567 (1909). URL http://rspa.royalsocietypublishing.org/content/82/557/560. http://rspa.royalsocietypublishing.org/content/82/557/560.full.pdf.

[24] Beth, R. A. Mechanical detection and measurement of the angular momentum of light. *Physical Review* **50**, 115 (1936).

[25] Darwin, C. Notes on the theory of radiation. *Proceedings of the Royal Society of London. Series A, Containing Papers of a Mathematical and Physical Character* **136**, 36–52 (1932).

[26] Allen, L., Beijersbergen, M. W., Spreeuw, R. J. C. & Woerdman, J. P. Orbital angular momentum of light and the transformation of laguerre-gaussian laser modes. *Phys. Rev. A* **45**, 8185–8189 (1992). URL https://link.aps.org/doi/10.1103/PhysRevA.45.8185.

[27] Griffiths, D. J. *Introduction to quantum mechanics* (Cambridge University Press, 2016).

[28] Bliokh, K. Y., Rodriguez-Fortuno, F. J., Nori, F. & Zayats, A. V. Spin-orbit interactions of light. *Nat Photon* **9**, 796–808 (2015). URL `http://dx.doi.org/10.1038/nphoton.2015.201`.

[29] Winkler, R. Origin of spin–orbit coupling effects. *Spin–Orbit Coupling Effects in Two-Dimensional Electron and Hole Systems* 61–68 (2003).

[30] Wang, J. *et al.* Terabit free-space data transmission employing orbital angular momentum multiplexing. *Nat Photon* **6**, 488–496 (2012). URL `http://dx.doi.org/10.1038/nphoton.2012.138`.

[31] Leach, J. *et al.* Quantum correlations in optical angle–orbital angular momentum variables. *Science* **329**, 662–665 (2010).

[32] Fickler, R. *et al.* Quantum entanglement of high angular momenta. *Science* **338**, 640–643 (2012).

[33] Götte, J., Franke-Arnold, S., Zambrini, R. & Barnett, S. M. Quantum formulation of fractional orbital angular momentum. *Journal of Modern Optics* **54**, 1723–1738 (2007).

[34] Nye, J. F. & Berry, M. V. Dislocations in wave trains. *Proceedings of the Royal Society of London A: Mathematical, Physical and Engineering Sciences* **336**, 165–190 (1974). URL `http://rspa.royalsocietypublishing.org/content/336/1605/165`. `http://rspa.royalsocietypublishing.org/content/336/1605/165.full.pdf`.

[35] Padgett, M., Courtial, J. & Allen, L. Light's orbital angular momentum. *Physics Today* **57**, 35–40 (2004).

[36] Hell, S. W. & Wichmann, J. Breaking the diffraction resolution limit by stimulated emission: stimulated-emission-depletion fluorescence microscopy. *Opt. Lett.* **19**, 780–782 (1994). URL `http://ol.osa.org/abstract.cfm?URI=ol-19-11-780`.

[37] Hell, S. W. Nanoscopy with focused light. *Annalen der Physik* **527**, 423–445 (2015).

[38] Friese, M. E. J., Nieminen, T. A., Heckenberg, N. R. & Rubinsztein-Dunlop, H. Optical alignment and spinning of laser-trapped microscopic particles. *Nature* **394**, 348–350 (1998). URL `http://dx.doi.org/10.1038/28566`.

[39] Yang, Y. *et al.* Dielectric meta-reflectarray for broadband linear polarization conversion and optical vortex generation. *Nano Letters* **14**, 1394–1399 (2014). URL `http://dx.doi.org/10.1021/nl4044482`. PMID: 24547692, `http://dx.doi.org/10.1021/nl4044482`.

[40] Biener, G., Niv, A., Kleiner, V. & Hasman, E. Formation of helical beams by use of pancharatnam–berry phase optical elements. *Opt. Lett.* **27**, 1875–1877 (2002). URL http://ol.osa.org/abstract.cfm?URI=ol-27-21-1875.

[41] Marrucci, L., Manzo, C. & Paparo, D. Optical spin-to-orbital angular momentum conversion in inhomogeneous anisotropic media. *Phys. Rev. Lett.* **96**, 163905 (2006). URL https://link.aps.org/doi/10.1103/PhysRevLett.96.163905.

[42] Bliokh", K. Y. Angular momenta and spin-orbit interaction of nonparaxial light in free space. *Physical Review A* **82** (2010).

[43] Johnson, P. B. & Christy, R. W. Optical constants of the noble metals. *Phys. Rev. B* **6**, 4370–4379 (1972). URL https://link.aps.org/doi/10.1103/PhysRevB.6.4370.

[44] Shelby, R. A., Smith, D. R. & Schultz, S. Experimental verification of a negative index of refraction. *Science* **292**, 77–79 (2001). URL http://science.sciencemag.org/content/292/5514/77. http://science.sciencemag.org/content/292/5514/77.full.pdf.

[45] Salandrino, A. & Engheta, N. Far-field subdiffraction optical microscopy using metamaterial crystals: Theory and simulations. *Phys. Rev. B* **74**, 075103 (2006). URL https://link.aps.org/doi/10.1103/PhysRevB.74.075103.

[46] Liu, Z., Lee, H., Xiong, Y., Sun, C. & Zhang, X. Far-field optical hyperlens magnifying sub-diffraction-limited objects. *Science* **315**, 1686–1686 (2007). URL http://science.sciencemag.org/content/315/5819/1686. http://science.sciencemag.org/content/315/5819/1686.full.pdf.

[47] Pors, A. & Bozhevolnyi, S. I. Plasmonic metasurfaces for efficient phase control in reflection. *Opt. Express* **21**, 27438–27451 (2013). URL http://www.opticsexpress.org/abstract.cfm?URI=oe-21-22-27438.

[48] Naik, G. V. *et al.* Epitaxial superlattices with titanium nitride as a plasmonic component for optical hyperbolic metamaterials. *Proceedings of the National Academy of Sciences* **111**, 7546–7551 (2014). URL http://www.pnas.org/content/111/21/7546.abstract. http://www.pnas.org/content/111/21/7546.full.pdf.

[49] Esfandyarpour, M., Garnett, E. C., Cui, Y., McGehee, M. D. & Brongersma, M. L. Metamaterial mirrors in optoelectronic devices. *Nat Nano* **9**, 542–547 (2014). URL http://dx.doi.org/10.1038/nnano.2014.117.

[50] Kildishev, A., Boltasseva, A. & Shalaev, V. Planar photonics with metasurfaces. *Science* **339** (2013).

[51] Liu, Y. & Zhang, X. Metasurfaces for manipulating surface plasmons. *Applied Physics Letters* **103**, 141101 (2013). URL `http://dx.doi.org/10.1063/1.4821444`. `http://dx.doi.org/10.1063/1.4821444`.

[52] Lin, J. *et al.* Polarization-controlled tunable directional coupling of surface plasmon polaritons. *Science* **340**, 331–334 (2013). URL `http://science.sciencemag.org/content/340/6130/331`. `http://science.sciencemag.org/content/340/6130/331.full.pdf`.

[53] Rodríguez-Fortuño, F. *et al.* Near-field interference for the unidirectional excitation of electromagnetic guided modes. *Science* **340**, 328–330 (2013).

[54] Kapitanova, P. V. *et al.* Photonic spin hall effect in hyperbolic metamaterials for polarization-controlled routing of subwavelength modes. *Nature communications* **5** (2014).

[55] Petersen, J., Volz, J. & Rauschenbeutel, A. Chiral nanophotonic waveguide interface based on spin-orbit interaction of light. *Science* **346**, 67–71 (2014). URL `http://science.sciencemag.org/content/346/6205/67`. `http://science.sciencemag.org/content/346/6205/67.full.pdf`.

[56] Baski, A. & Fuchs, H. Epitaxial growth of silver on mica as studied by afm and stm. *Surface Science* **313**, 275 – 288 (1994). URL `http://www.sciencedirect.com/science/article/pii/0039602894900485`.

[57] Park, J. H. *et al.* Single-crystalline silver films for plasmonics. *Advanced Materials* **24**, 3988–3992 (2012). URL `http://dx.doi.org/10.1002/adma.201200812`.

[58] Palik, E. D. *Handbook of optical constants of solids*, vol. 3 (Academic press, 1998).

[59] Wu, Y. *et al.* Intrinsic optical properties and enhanced plasmonic response of epitaxial silver. *Advanced Materials* **26**, 6106–6110 (2014). URL `http://dx.doi.org/10.1002/adma.201401474`.

[60] Fan, X., Wang, G. P., Lee, J. C. W. & Chan, C. T. All-angle broadband negative refraction of metal waveguide arrays in the visible range: Theoretical analysis and numerical demonstration. *Phys. Rev. Lett.* **97**, 073901 (2006). URL `https://link.aps.org/doi/10.1103/PhysRevLett.97.073901`.

[61] Smith, D. R. & Schurig, D. Electromagnetic wave propagation in media with indefinite permittivity and permeability tensors. *Phys. Rev. Lett.* **90**, 077405 (2003). URL `https://link.aps.org/doi/10.1103/PhysRevLett.90.077405`.

[62] Lee, S.-Y. *et al.* Role of magnetic induction currents in nanoslit excitation of surface plasmon polaritons. *Phys. Rev. Lett.* **108**, 213907 (2012). URL `https://link.aps.org/doi/10.1103/PhysRevLett.108.213907`.

[63] Huang, L. *et al.* Helicity dependent directional surface plasmon polariton excitation using a metasurface with interfacial phase discontinuity. *Light Sci Appl* **2**, e70– (2013). URL http://dx.doi.org/10.1038/lsa.2013.26.

[64] Bychkov, Y. A. & Rashba, E. I. Oscillatory effects and the magnetic susceptibility of carriers in inversion layers. *Journal of physics C: Solid state physics* **17**, 6039 (1984).

[65] Onoda, M., Murakami, S. & Nagaosa, N. Hall effect of light. *Phys. Rev. Lett.* **93**, 083901 (2004). URL https://link.aps.org/doi/10.1103/PhysRevLett.93.083901.

[66] Raether, H. *Surface plasmons on smooth and rough surfaces and on gratings*, vol. 111 (Springer, 2006).

[67] Silva, A. *et al.* Performing mathematical operations with metamaterials. *Science* **343**, 160–163 (2014). URL http://science.sciencemag.org/content/343/6167/160. http://science.sciencemag.org/content/343/6167/160.full.pdf.

[68] Huang, K. C. Y. *et al.* Electrically driven subwavelength optical nanocircuits. *Nat Photon* **8**, 244–249 (2014). URL http://dx.doi.org/10.1038/nphoton.2014.2.

[69] Hafezi, M., Demler, E. A., Lukin, M. D. & Taylor, J. M. Robust optical delay lines with topological protection. *Nature Physics* **7**, 907–912 (2011).

[70] Ambrosio, A., Devlin, R. C., Capasso, F. & Wilson, W. L. Observation of nanoscale refractive index contrast via photoinduced force microscopy. *ACS Photonics* **4**, 846–851 (2017).

[71] Chen, W. T. *et al.* Immersion meta-lenses at visible wavelengths for nanoscale imaging. *Nano Letters* **17**, 3188–3194 (2017).

[72] Devlin, R. C. *et al.* Spin-to-orbital angular momentum conversion in dielectric metasurfaces. *Optics express* **25**, 377–393 (2017).

[73] Devlin, R. C. *et al.* Spin-to-orbital angular momentum conversion in dielectric metasurfaces. *Opt. Express* **25**, 377–393 (2017). URL http://www.opticsexpress.org/abstract.cfm?URI=oe-25-1-377.

[74] Groever, B., Chen, W. T. & Capasso, F. Meta-lens doublet in the visible. *Nano Letters* (2017).

[75] Khorasaninejad, M. *et al.* Metalenses at visible wavelengths: Diffraction-limited focusing and subwavelength resolution imaging. *Science* **352**, 1190–1194 (2016).

[76] Khorasaninejad, M. *et al.* Multispectral chiral imaging with a metalens. *Nano letters* **16**, 4595–4600 (2016).

[77] Khorasaninejad, M. *et al.* Polarization-insensitive metalenses at visible wavelengths. *Nano letters* **16**, 7229–7234 (2016).

[78] Khorasaninejad, M. *et al.* Achromatic metalens over 60 nm bandwidth in the visible and metalens with reverse chromatic dispersion. *Nano Letters* **17**, 1819–1824 (2017).

[79] Mueller, J. B., Rubin, N. A., Devlin, R. C., Groever, B. & Capasso, F. Metasurface polarization optics: Independent phase control of arbitrary orthogonal states of polarization. *Physical Review Letters* **118**, 113901 (2017).

[80] Zhu, A. Y. *et al.* Ultra-compact visible chiral spectrometer with meta-lenses. *APL Photonics* **2**, 036103 (2017).

[81] Zhan, A. *et al.* Low-contrast dielectric metasurface optics. *ACS Photonics* **3**, 209–214 (2016).

[82] Gutruf, P. *et al.* Mechanically tunable dielectric resonator metasurfaces at visible frequencies. *ACS nano* **10**, 133–141 (2015).

[83] Lalanne, P., Astilean, S., Chavel, P., Cambril, E. & Launois, H. Design and fabrication of blazed binary diffractive elements with sampling periods smaller than the structural cutoff. *JOSA A* **16**, 1143–1156 (1999).

[84] Sun, S. *et al.* High-efficiency broadband anomalous reflection by gradient meta-surfaces. *Nano letters* **12**, 6223–6229 (2012).

[85] Sun, S. *et al.* Gradient-index meta-surfaces as a bridge linking propagating waves and surface waves. *Nature materials* **11**, 426 (2012).

[86] Wen, D. *et al.* Helicity multiplexed broadband metasurface holograms. *Nature communications* **6**, 8241 (2015).

[87] Zheng, G. *et al.* Metasurface holograms reaching 80% efficiency. *Nature nanotechnology* **10**, 308–312 (2015).

[88] Xie, Q. *et al.* Atomic layer deposition of ti o 2 from tetrakis-dimethyl-amido titanium or ti isopropoxide precursors and h 2 o. *Journal of applied physics* **102**, 083521 (2007).

[89] George, S. M. Atomic layer deposition: an overview. *Chem. Rev* **110**, 111–131 (2010).

[90] High, A. A. *et al.* Visible-frequency hyperbolic metasurface. *Nature* **522**, 192 (2015).

[91] Aarik, J., Aidla, A., Kiisler, A.-A., Uustare, T. & Sammelselg, V. Effect of crystal structure on optical properties of tio2 films grown by atomic layer deposition. *Thin Solid Films* **305**, 270–273 (1997).

[92] Jellison Jr, G. & Modine, F. Parameterization of the optical functions of amorphous materials in the interband region. *Applied Physics Letters* **69**, 371–373 (1996).

[93] Eufinger, K., Poelman, D., Poelman, H., De Gryse, R. & Marin, G. Photocatalytic activity of dc magnetron sputter deposited amorphous tio 2 thin films. *Applied surface science* **254**, 148–152 (2007).

[94] Apetz, R. & Bruggen, M. P. Transparent alumina: A light-scattering model. *Journal of the American Ceramic Society* **86**, 480–486 (2003).

[95] King, J. S., Graugnard, E. & Summers, C. J. Tio2 inverse opals fabricated using low-temperature atomic layer deposition. *Advanced Materials* **17**, 1010–1013 (2005).

[96] Sander, M. S., Cote, M. J., Gu, W., Kile, B. M. & Tripp, C. P. Template-assisted fabrication of dense, aligned arrays of titania nanotubes with well-controlled dimensions on substrates. *Advanced Materials* **16**, 2052–2057 (2004).

[97] Berry, M. V. Quantal phase factors accompanying adiabatic changes. In *Proceedings of the Royal Society of London A: Mathematical, Physical and Engineering Sciences*, vol. 392, 45–57 (The Royal Society, 1984).

[98] Bhandari, R. Polarization of light and topological phases. *Physics Reports* **281**, 1–64 (1997).

[99] Pancharatnam, S. Generalized theory of interference, and its applications. In *Proceedings of the Indian Academy of Sciences-Section A*, vol. 44, 247–262 (Springer, 1956).

[100] Bomzon, Z., Kleiner, V. & Hasman, E. Pancharatnam–berry phase in space-variant polarization-state manipulations with subwavelength gratings. *Opt. Lett.* **26**, 1424–1426 (2001). URL `http://ol.osa.org/abstract.cfm?URI=ol-26-18-1424`.

[101] Chen, W. T. *et al.* High-efficiency broadband meta-hologram with polarization-controlled dual images. *Nano letters* **14**, 225–230 (2013).

[102] Luo, W., Xiao, S., He, Q., Sun, S. & Zhou, L. Photonic spin hall effect with nearly 100% efficiency. *Advanced Optical Materials* **3**, 1102–1108 (2015).

[103] (2016). URL `https://www.strategyanalytics.com/strategy-analytics/blogs/smart-phones/2016/12/21/44-of-world-population-will-own-smartphones-in-2017#.WXodINPytp8`.

[104] Aieta, F., Kats, M. A., Genevet, P. & Capasso, F. Multiwavelength achromatic metasurfaces by dispersive phase compensation. *Science* **347**, 1342–1345 (2015).

[105] Arbabi, A., Horie, Y., Ball, A. J., Bagheri, M. & Faraon, A. Subwavelength-thick lenses with high numerical apertures and large efficiency based on high-contrast transmitarrays. *Nature Communications* **6** (2015).

[106] Chang-Hasnain, C. J. High-contrast gratings as a new platform for integrated optoelectronics. *Semiconductor Science and Technology* **26**, 014043 (2010).

[107] Chong, K. E. *et al.* Polarization-independent silicon metadevices for efficient optical wavefront control. *Nano letters* **15**, 5369–5374 (2015).

[108] Devlin, R. C., Khorasaninejad, M., Chen, W. T., Oh, J. & Capasso, F. Broadband high-efficiency dielectric metasurfaces for the visible spectrum. *Proceedings of the National Academy of Sciences* **113**, 10473–10478 (2016). URL `http://www.pnas.org/content/113/38/10473.abstract`. `http://www.pnas.org/content/113/38/10473.full.pdf`.

[109] Fattal, D., Li, J., Peng, Z., Fiorentino, M. & Beausoleil, R. G. Flat dielectric grating reflectors with focusing abilities. *Nature Photonics* **4**, 466–470 (2010).

[110] Khorasaninejad, M., Zhu, W. & Crozier, K. Efficient polarization beam splitter pixels based on a dielectric metasurface. *Optica* **2**, 376–382 (2015).

[111] Khorasaninejad, M. & Crozier, K. B. Silicon nanofin grating as a miniature chirality-distinguishing beam-splitter. *Nature communications* **5**, 5386 (2014).

[112] Khorasaninejad, M. *et al.* Achromatic metasurface lens at telecommunication wavelengths. *Nano letters* **15**, 5358–5362 (2015).

[113] Larouche, S., Tsai, Y.-J., Tyler, T., Jokerst, N. M. & Smith, D. R. Infrared metamaterial phase holograms. *Nature materials* **11**, 450 (2012).

[114] Liu, S. *et al.* Optical magnetic mirrors without metals. *Optica* **1**, 250–256 (2014).

[115] Merlin, R. Radiationless electromagnetic interference: evanescent-field lenses and perfect focusing. *Science* **317**, 927–929 (2007).

[116] Monticone, F., Estakhri, N. M. & Alù, A. Full control of nanoscale optical transmission with a composite metascreen. *Physical review letters* **110**, 203903 (2013).

[117] Ni, X., Emani, N. K., Kildishev, A. V., Boltasseva, A. & Shalaev, V. M. Broadband light bending with plasmonic nanoantennas. *Science* **335**, 427–427 (2012).

[118] Rogers, E. T. *et al.* A super-oscillatory lens optical microscope for subwavelength imaging. *Nature materials* **11**, 432 (2012).

[119] Spinelli, P., Verschuuren, M. & Polman, A. Broadband omnidirectional antireflection coating based on subwavelength surface mie resonators. *Nature communications* **3**, 692 (2012).

[120] Berry, M. V. The adiabatic phase and pancharatnam's phase for polarized light. *Journal of Modern Optics* **34**, 1401–1407 (1987).

[121] Aieta, F., Genevet, P., Kats, M. & Capasso, F. Aberrations of flat lenses and aplanatic metasurfaces. *Optics express* **21**, 31530–31539 (2013).

[122] Mair, A., Vaziri, A., Weihs, G. & Zeilinger, A. Entanglement of the orbital angular momentum states of photons. *Nature* **412**, 313–316 (2001). URL `http://dx.doi.org/10.1038/35085529`.

[123] Dennis, M. R., O'Holleran, K. & Padgett, M. J. Chapter 5 singular optics: Optical vortices and polarization singularities. *Progress in Optics* **53**, 293 – 363 (2009). URL `http://www.sciencedirect.com/science/article/pii/S0079663808002059`.

[124] Padgett, M. & Bowman, R. Tweezers with a twist. *Nature Photonics* **5**, 343–348 (2011).

[125] Simpson, N., Dholakia, K., Allen, L. & Padgett, M. Mechanical equivalence of spin and orbital angular momentum of light: an optical spanner. *Optics letters* **22**, 52–54 (1997).

[126] Ambrosio, A., Piccirillo, B., Sasso, A. & Santamato, E. Experimental and theoretical study of the transient rotation of isotropic transparent microparticles in astigmatic optical tweezers. *Optics communications* **230**, 337–345 (2004).

[127] Ambrosio, A., Marrucci, L., Borbone, F., Roviello, A. & Maddalena, P. Light-induced spiral mass transport in azo-polymer films under vortex-beam illumination. *Nature communications* **3**, 989 (2012).

[128] Lin, J., Genevet, P., Kats, M. A., Antoniou, N. & Capasso, F. Nanostructured holograms for broadband manipulation of vector beams. *Nano letters* **13**, 4269–4274 (2013).

[129] Bouchard, F., Mand, H., Mirhosseini, M., Karimi, E. & Boyd, R. W. Achromatic orbital angular momentum generator. *New Journal of Physics* **16**, 123006 (2014).

[130] Machavariani, G. *et al.* Efficient conversion of a gaussian beam to a high purity helical beam. *Optics communications* **209**, 265–271 (2002).

[131] Milione, G., Sztul, H., Nolan, D. & Alfano, R. Higher-order poincaré sphere, stokes parameters, and the angular momentum of light. *Physical review letters* **107**, 053601 (2011).

[132] Biener, G., Niv, A., Kleiner, V. & Hasman, E. Formation of helical beams by use of pancharatnam–berry phase optical elements. *Optics letters* **27**, 1875–1877 (2002).

[133] Niv, A., Biener, G., Kleiner, V. & Hasman, E. Spiral phase elements obtained by use of discrete space-variant subwavelength gratings. *Optics communications* **251**, 306–314 (2005).

[134] Nagali, E. *et al.* Optimal quantum cloning of orbital angular momentum photon qubits through hong-ou-mandel coalescence. *Nat Photon* **3**, 720–723 (2009). URL `http://dx.doi.org/10.1038/nphoton.2009.214`.

[135] Huang, H. *et al.* Mode division multiplexing using an orbital angular momentum mode sorter and mimo-dsp over a graded-index few-mode optical fibre. *Scientific reports* **5** (2015).

[136] Marrucci, L., Manzo, C. & Paparo, D. Pancharatnam-berry phase optical elements for wave front shaping in the visible domain: switchable helical mode generation. *Applied Physics Letters* **88**, 221102 (2006).

[137] Milione, G. *et al.* 4× 20 gbit/s mode division multiplexing over free space using vector modes and a q-plate mode (de) multiplexer. *Optics letters* **40**, 1980–1983 (2015).

[138] Gorodetski, Y., Biener, G., Niv, A., Kleiner, V. & Hasman, E. Optical properties of polarization-dependent geometric phase elements with partially polarized light. *Optics communications* **266**, 365–375 (2006).

[139] Shalaev, M. I. *et al.* High-efficiency all-dielectric metasurfaces for ultracompact beam manipulation in transmission mode. *Nano letters* **15**, 6261–6266 (2015).

[140] Bouchard, F. *et al.* Optical spin-to-orbital angular momentum conversion in ultra-thin metasurfaces with arbitrary topological charges. *Applied Physics Letters* **105**, 101905 (2014).

[141] Hakobyan, D., Magallanes, H., Seniutinas, G., Juodkazis, S. & Brasselet, E. Tailoring orbital angular momentum of light in the visible domain with metallic metasurfaces. *Advanced Optical Materials* **4**, 306–312 (2016).

[142] Karimi, E. *et al.* Generating optical orbital angular momentum at visible wavelengths using a plasmonic metasurface. *Light: Science and Applications* **3**, e167 (2014).

[143] Li, G. *et al.* Spin-enabled plasmonic metasurfaces for manipulating orbital angular momentum of light. *Nano letters* **13**, 4148–4151 (2013).

[144] Mehmood, M. *et al.* Visible-frequency metasurface for structuring and spatially multiplexing optical vortices. *Advanced Materials* **28**, 2533–2539 (2016).

[145] Pu, M. *et al.* Catenary optics for achromatic generation of perfect optical angular momentum. *Science advances* **1**, e1500396 (2015).

[146] Bauer, T. *et al.* Observation of optical polarization möbius strips. *Science* **347**, 964–966 (2015).

[147] D'ambrosio, V. *et al.* Photonic polarization gears for ultra-sensitive angular measurements. *Nature communications* **4** (2013).

[148] Giovannini, D., Nagali, E., Marrucci, L. & Sciarrino, F. Resilience of orbital-angular-momentum photonic qubits and effects on hybrid entanglement. *Physical Review A* **83**, 042338 (2011).

[149] Slussarenko, S. *et al.* Tunable liquid crystal q-plates with arbitrary topological charge. *Optics express* **19**, 4085–4090 (2011).

[150] Yan, L. *et al.* Q-plate enabled spectrally diverse orbital-angular-momentum conversion for stimulated emission depletion microscopy. *Optica* **2**, 900–903 (2015).

[151] Khorasaninejad, M., Ambrosio, A., Kanhaiya, P. & Capasso, F. Dispersion-compensated meta-holograms based on detour phase. *arXiv preprint arXiv:1601.01415* (2016).

[152] Berry, M. Optical vortices evolving from helicoidal integer and fractional phase steps. *Journal of Optics A: Pure and Applied Optics* **6**, 259 (2004).

[153] Leach, J., Yao, E. & Padgett, M. J. Observation of the vortex structure of a non-integer vortex beam. *New Journal of Physics* **6**, 71 (2004).

[154] Oemrawsingh, S., Aiello, A., Eliel, E., Nienhuis, G. & Woerdman, J. How to observe high-dimensional two-photon entanglement with only two detectors. *Physical review letters* **92**, 217901 (2004).

[155] Oemrawsingh, S. *et al.* Experimental demonstration of fractional orbital angular momentum entanglement of two photons. *Physical review letters* **95**, 240501 (2005).

[156] Mero, M., Liu, J., Rudolph, W., Ristau, D. & Starke, K. Scaling laws of femtosecond laser pulse induced breakdown in oxide films. *Physical Review B* **71**, 115109 (2005).

[157] Leach, J., Padgett, M. J., Barnett, S. M., Franke-Arnold, S. & Courtial, J. Measuring the orbital angular momentum of a single photon. *Physical review letters* **88**, 257901 (2002).

[158] Barnett, S. M. & Allen, L. Orbital angular momentum and nonparaxial light beams. *Optics Communications* **110**, 670–678 (1994). URL `http://www.sciencedirect.com/science/article/pii/0030401894902690`.

[159] O'Neil, A. T., MacVicar, I., Allen, L. & Padgett, M. J. Intrinsic and extrinsic nature of the orbital angular momentum of a light beam. *Phys. Rev. Lett.* **88**, 053601 (2002). URL `https://link.aps.org/doi/10.1103/PhysRevLett.88.053601`.

[160] Padgett, M. J. Orbital angular momentum 25 years on. *Opt. Express* **25**, 11265–11274 (2017). URL `http://www.opticsexpress.org/abstract.cfm?URI=oe-25-10-11265`.

[161] Gibson, G. *et al.* Free-space information transfer using light beams carrying orbital angular momentum. *Opt. Express* **12**, 5448–5456 (2004). URL `http://www.opticsexpress.org/abstract.cfm?URI=oe-12-22-5448`.

[162] Bozinovic, N. *et al.* Terabit-scale orbital angular momentum mode division multiplexing in fibers. *Science* **340**, 1545–1548 (2013).

[163] He, H., Friese, M. E. J., Heckenberg, N. R. & Rubinsztein-Dunlop, H. Direct observation of transfer of angular momentum to absorptive particles from a laser beam with a phase singularity. *Phys. Rev. Lett.* **75**, 826–829 (1995). URL https://link.aps.org/doi/10.1103/PhysRevLett.75.826.

[164] Vaziri, A., Weihs, G. & Zeilinger, A. Experimental two-photon, three-dimensional entanglement for quantum communication. *Phys. Rev. Lett.* **89**, 240401 (2002). URL https://link.aps.org/doi/10.1103/PhysRevLett.89.240401.

[165] Dada, A. C., Leach, J., Buller, G. S., Padgett, M. J. & Andersson, E. Experimental high-dimensional two-photon entanglement and violations of generalized bell inequalities. *Nat Phys* **7**, 677–680 (2011). URL http://dx.doi.org/10.1038/nphys1996.

[166] Beijersbergen, M., Allen, L., van der Veen, H. & Woerdman, J. Astigmatic laser mode converters and transfer of orbital angular momentum. *Optics Communications* **96**, 123 – 132 (1993). URL http://www.sciencedirect.com/science/article/pii/003040189390535D.

[167] Bazhenov, V. Y., Vasnetsov, M. & Soskin, M. Laser beams with screw dislocations in their wavefronts. *Jetp Lett* **52**, 429–431 (1990).

[168] Beijersbergen, M., Coerwinkel, R., Kristensen, M. & Woerdman, J. Helical-wavefront laser beams produced with a spiral phaseplate. *Optics Communications* **112**, 321–327 (1994).

[169] Naidoo, D. *et al.* Controlled generation of higher-order poincarã©sphere beams from a laser. *Nat Photon* **10**, 327–332 (2016). URL http://dx.doi.org/10.1038/nphoton.2016.37.

[170] See supplementary materials for more information on device design, additional demonstrations, measurements and methods.

[171] Jones, R. C. A new calculus for the treatment of optical systemsi. description and discussion of the calculus. *J. Opt. Soc. Am.* **31**, 488–493 (1941). URL http://www.osapublishing.org/abstract.cfm?URI=josa-31-7-488.

[172] Milione, G., Sztul, H. I., Nolan, D. A. & Alfano, R. R. Higher-order poincaré sphere, stokes parameters, and the angular momentum of light. *Phys. Rev. Lett.* **107**, 053601 (2011). URL https://link.aps.org/doi/10.1103/PhysRevLett.107.053601.

[173] Milione, G., Evans, S., Nolan, D. A. & Alfano, R. R. Higher order pancharatnam-berry phase and the angular momentum of light. *Phys. Rev. Lett.* **108**, 190401 (2012). URL https://link.aps.org/doi/10.1103/PhysRevLett.108.190401.

[174] Baumann, S. M., Kalb, D. M., MacMillan, L. H. & Galvez, E. J. Propagation dynamics of optical vortices due to gouy phase. *Opt. Express* **17**, 9818–9827 (2009). URL `http://www.opticsexpress.org/abstract.cfm?URI=oe-17-12-9818`.

[175] Kolkowitz, S. *et al.* Spinâ€“orbit-coupled fermions in an optical lattice clock. *Nature* **542**, 66–70 (2017). URL `http://dx.doi.org/10.1038/nature20811`.

[176] Chang, D. E., Sørensen, A. S., Hemmer, P. & Lukin, M. Strong coupling of single emitters to surface plasmons. *Physical Review B* **76**, 035420 (2007).